ADDITIVE MANUFACTURING-DRIVEN THIN FILM ULTRASOUND SENSORS: FROM SENSING INK DEVELOPMENT TO APPLICATIONS IN ULTRASONICS-BASED STRUCTURAL HEALTH MONITORING

PENGYU ZHOU

PhD

The Hong Kong Polytechnic University

2021

The Hong Kong Polytechnic University

Department of Mechanical Engineering

Additive Manufacturing-driven Thin Film Ultrasound Sensors: from Sensing Ink Development to Applications in Ultrasonics-based Structural Health Monitoring

Pengyu Zhou

A thesis submitted in partial fulfilment of the requirements

for the degree of Doctor of Philosophy

June 2021

CERTIFICATE OF ORIGINALITY

I hereby declare that this thesis is my own work and that, to the best of my knowledge and belief, it reproduces no material previously published or written, nor material that has been accepted for the award of any other degree or diploma, except where due acknowledgment has been made in the text.

_____

ZHOU Pengyu

ABSTRACT

Structural health monitoring (SHM), a bionic paradigm inspired by the manner of information perception and decision-making of human beings, has shown appealing promise in safeguarding engineering assets. Amidst diverse SHM approaches, the acousto-ultrasonic wave-driven SHM, which leverages numerous merits of acousto-ultrasonic waves, strikes a balance among resolution, detectability, practicality, and cost, well corroborating the concept of *in situ* SHM. Central to the realization of *in situ* acousto-ultrasonic wave-driven SHM is the acquisition of acousto-ultrasonic wave signals. Nevertheless, for most of the prevailing sensors that are developed for entertaining such a demand, a challenge remains: how to compromise "sensing effectiveness" with "sensing cost"?

In this PhD study, a series of thin film ultrasound sensors are developed by virtue of a direct-write additive manufacturing (AM) approach – inkjet-printing. The sensing inks and printed sensors are morphologically tuned at nano scales, driving the sensors to be highly sensitive to acousto-ultrasonic waves in a broad band regime, from static strain to high-frequency ultrasound of frequencies up to 1.6 MHz. Being ultra-thin and lightweight, the sensors feature a homogenous, consolidated nanostructure, with which transient change of the tunneling resistance among adjacent electrical-conductive nanoplatelets in the polymeric matrix can be triggered, when the sensors are loaded with dynamic strains induced by acousto-ultrasonic waves. It is the triggered quantum tunneling effect that endows the sensors with capability to respond to dynamic acousto-ultrasonic signals of high frequencies with excellent fidelity and accuracy.

Based on the mechanism study, a nanocomposite-based sensing ink, formulated with carbon black (CB) nanoparticles and polyvinyl pyrrolidone (PVP), is developed. The sensing ink is rigorously designed and morphologically optimized to be stable, printable and wettable. By directly depositing the sensing ink on flexible polyimide (PI) substrates, ultralight, flexible, nanocomposite thin film ultrasound sensors are produced via drop-on-demand inkjet printing. With the quantum tunneling effect triggered among CB nanoparticles, the printed CB/PVP film sensors have proven capability of *in situ*, precisely responding to dynamic strains in a broad range from quasi-static strain, through medium-frequency vibration, to strain induced by acousto-ultrasonic waves up to 500 kHz. Notably, the sensitivity of the sensors can be tuned by adjusting the degree of sensor conductivity via controlling the printed passes, endowing the sensors with capacity of resonating to strains of a particular frequency, authenticating that inkjet-printed thin film ultrasound sensors can be tailor-made to accommodate specific signal acquisition demands.

To further enhance the sensitivity and expanding responsive range of the sensors, morphologically optimized NGP/poly (amic acid) (PAA) hybrid-based nanocomposite ink is synthesized, with which nanographene platelets (NGP)/PI sensors are fabricated. The ink is produced with high-shear liquid phase exfoliation (LPE) from inexpensive bulk graphite, manifesting good printability and graphene concentration as high as 13.1 mg mL^{-1}. Featuring an ultra-thin thickness (~ 1 μm only), the inkjet-printed NGP/PI film sensors are demonstrated to possess excellent thermal stability and high adhesive strength reaching the American Society for Testing and Materials (ASTM) 5B level. The uniform and consolidated NGP/PI nanostructure in the sensors enables

the formation of π-π interactions between NGPs and PI polymer matrix, and consequently the quantum tunneling effect is triggered among NGPs when acousto-ultrasonic waves traverse the sensors. This sensing mechanism facilitates the NGP/PI sensors with comparable performance as prevailing commercial ultrasound sensors such as piezoelectric sensors. The film sensors demonstrate a gauge factor as high as 739, when sensing ultrasound at 175 kHz, and a ultrabroad responsive spectrum up to 1.6 MHz. This is first ever that an inkjet-printed thin film ultrasound sensor responds to dynamic strains in such a broad band and acousto-ultrasonic waves of such a high frequency.

To examine the effects of aggressive environmental exposures to the inkjet-printed thin film ultrasound sensors, the sensing performance of the sensors in acquiring broadband acousto-ultrasonic wave signals is scrutinized in an extensive regime of temperature variation from –60 to 150 ºC, which spans the thermal extremes undergone by most aircraft and spacecraft. Under high-intensity thermal cycles from –60 to 150 ºC, the sensors exhibit stability and accuracy in responding to signals in a broad band as well. Compared against conventional ultrasound sensors such as piezoelectric wafers, inkjet-printed film sensors avoid the influence of increased dielectric permittivity during the measurement of high-frequency signals at elevated temperatures.

With proven sensitivity, sensing accuracy and stability, the inkjet-printed thin film ultrasound sensors are further developed into an all-printed nanocomposite sensor array (APNSA), in lieu of conventional ultrasonic phased array which is of a low degree of integrity with composites, to ameliorate ultrasonic imaging of composites. Individual sensing elements of APNSA are inkjet printed by directly writing sensing

inks on Kapton film substrates. Compared with a conventional ultrasonic phased array, APNSA can be fully integrated with the inspected composites. In conjunction with the use of the additively manufactured APNSA, ultrasonic imaging of composites can be implemented, spotlighting a nature of full integration of APNSA with composites for *in situ* SHM and anomaly detection, yet without degrading the original integrity of the composites.

In conclusion, starting from mechanism study, through design to fabrication of sensing inks, new breeds of thin film ultrasound sensors are developed via inkjet printing. Successful application paradigms of the thin film ultrasound sensors have accentuated the alluring potentials of the new sensors in fulfilling real-world *in situ* acousto-ultrasonic wave-driven SHM.

PUBLICATIONS ARISING FROM THE THESIS

Refereed Journal Papers

1. **Zhou, P.**, Liao, Y., Yang, X., Su, Y., Yang, J., Xu, L., Wang, K., Zeng, Z., Zhou, L.-M., Zhang, Z. and Su, Z.* 'Thermally stable, adhesively strong graphene/polyimide films for inkjet printing ultrasound sensors', *Carbon*, 2021;**184**:64-71.

2. **Zhou, P.**, Yang, X., Su, Y., Yang, J., Xu, L., Liao, Y., Wang, K., Zhou, L.-M. and Su, Z.* 'Direct-write nanocomposite sensor array for ultrasonic imaging of composites', *Composites Communications*, 2021;**28**:100937

3. **Zhou, P.**, Cao, W., Liao, Y., Wang, K., Yang, X., Yang, J., Su, Y., Xu, L., Zhou, L.-M., Zhang, Z. and Su, Z.* 'Temperature effect on all-inkjet-printed nanocomposite piezoresistive sensors for ultrasonics-based health monitoring', *Composites Science and Technology*, 2020;**197**:108273.

4. **Zhou, P.**, Liao, Y., Li, Y., Pan, D., Cao, W., Yang, X., Zou, F., Zhou, L.-M., Zhang, Z. and Su, Z.* 'An inkjet-printed, flexible, ultra-broadband nanocomposite film sensor for in-situ acquisition of high-frequency dynamic strains', *Composites Part A: Applied Science and Manufacturing*, 2019;**125**:105554.

5. Liao, Y., **Zhou, P.**, Pan, D., Zhou, L.-M. and Su, Z.* 'An ultra-thin printable nanocomposite sensor network for structural health monitoring', *Structural Health Monitoring: An International Journal*, 2021;**20**(3):894-903. **(Co-first author)**

6. Cao, W., **Zhou, P.**, Liao, Y., Yang, X., Pan, D., Li, Y., Pang, B., Zhou, L.-M. and Su, Z.* 'A spray-on, nanocomposite-based sensor network for in-situ active structural health monitoring', *Sensors*, 2019;**19**(9):2077. **(Co-first author)**

7. Yang, X., Wang, K., **Zhou, P.**, Xu, L. and Su, Z.* 'Imaging damage in plate waveguides using frequency-domain multiple signal classification (F-MUSIC)', ***Ultrasonics***, 2022;**119**:106607.

8. Yang, X., Wang, K., **Zhou, P.**, Xu, L., Liu, J., Sun, P. and Su, Z.* 'Ameliorated-multiple signal classification (Am-MUSIC) for damage imaging using a sparse sensor network', ***Mechanical Systems and Signal Processing***, 2022;**163**:108154.

9. Su, Y., Xu, L., **Zhou, P.**, Yang, J., Wang, K., Zhou, L.-M. and Su, Z.* 'Carbon nanotube-decorated glass fibre bundles for cure self-monitoring and load self-sensing of FRPs', ***Composites Communications***, 2021;**27**:100899.

10. Cao, W., Wang, K., **Zhou, P.**, Yang, X., Xu, L., Liu, M., Fromme, P., Pang, B., Chi, R. and Su, Z.* 'Nonlinear ultrasonic evaluation of disorderedly clustered pitting damage using an in-situ sensor network', *Structural Health Monitoring: An International Journal*, 2020;**19**(6):1989-2006.

11. Cao, W., Wang, Y., **Zhou, P.**, Yang, X., Wang, K., Pang, B., Chi, R. and Su, Z.* 'Microstructural material characterization of hypervelocity-impact-induced pitting damage', *International Journal of Mechanical Sciences*, 2019;**163**:105097.

12. Su, Y., Yang, J., Liao, Y., **Zhou, P.**, Xu, L., Zhou, L.-M. and Su, Z.* 'An implantable, compatible and networkable nanocomposite piezoresistive sensor for in situ acquisition of dynamic responses of CFRPs', *Composites Science and Technology*, 2021;**208**:108747.

13. Weng, Z., Guan, R., Zou, F. *, **Zhou, P.**, Liao, Y., Su, Z. Huang, L. and Liu, F. 'A highly sensitive polydopamine@hybrid carbon nanofillers based nanocomposite sensor for acquiring high-frequency ultrasonic waves', *Carbon*, 2020;**170**:403-413.

14. Guan, R., Zou, F. *, Weng, Z., **Zhou, P.**, Liao, Y., Su, Z. and Huang, L. 'On a highly reproducible, broadband nanocomposite ultrasonic film sensor fabricated by ultrasonic atomization-assisted spray coating', *Advanced Engineering Materials*, 2020;**22**:2000462.

15. Li, Y., Wang, K., Wang, Q., Yang, J., **Zhou, P.**, Su, Y., Guo, S. and Su, Z.* 'Acousto-ultrasonics-based health monitoring for nano-engineered composites using a dispersive graphene-networked sensing system', *Structural Health Monitoring: An International Journal*, 2021;**20**(1):240-254.

16. Wang, K., Cao, W., Liu, M., Li, Y., **Zhou, P.** and Su, Z.* 'Advancing elastic wave imaging using thermal susceptibility of acoustic nonlinearity', *International Journal of Mechanical Sciences*, 2020;**175**:105509.

17. Xu, L., Wang, K., Yang, X., Su, Y., Yang, J., Liao, Y., **Zhou, P.** and Su, Z.* 'Model-driven fatigue crack characterization and growth prediction: A two-step, 3-D fatigue damage modeling framework for structural health monitoring', *International Journal of Mechanical Sciences*, 2021;**195**:106226.

18. Yang, J., Su, Y., Liao, Y., **Zhou, P.**, Xu, L. and Su, Z.* 'Ultrasound tomography for health monitoring of carbon fibre–reinforced polymers using implanted nanocomposite sensor networks and enhanced reconstruction algorithm for the probabilistic inspection of damage imaging' (Accepted by *Structural Health Monitoring: An International Journal*, in press).

Refereed Conference Papers

1. **Zhou, P.**, Liao, Y., Li, Y., Pan, D., Cao, W., Zhou, L.-M. and Su, Z. 'A nanocomposites-based, all-inkjet-printed, flexible, ultra-broadband film sensor for *in-situ* acquisition of dynamic strain', in *Proceedings of the 22nd International Conference on Composite Materials* (ICCM-22), edited by Mouritz, A., Wang, C. and Bronwyn, F., Paper ID: 1210-1, 11-16, August, 2019, Melbourne, Australia.

2. Cao, W., **Zhou, P.**, Wang, K., Wang, Y., Chi, R., Pang, B. and Su, Z. 'Quantitative characterization of hypervelocity debris cloud-induced pitting damage in AL-Whipple shields using nonlinear ultrasonic waves', in *Structural Health Monitoring 2019: Enabling Intelligent Life-cycle Health Management for Industry Internet of Things* (IIOT) - *Proceedings of the 12th International*

Workshop on Structural Health Monitoring (IWSHM-12), edited by Chang, F.-K. and Kopsaftopoulos, F., Lancaster: DEStech Publications, Inc., ISBN: 978-1-60595- 601-5, pp. 2299-2307, 10-12, September, 2019, Stanford, CA., USA.

3. Li, Y., **Zhou, P.**, Liao, Y. and Su, Z. 'Nano-engineered graphene polymer composites with self-health monitoring', in *Proceedings of the 22nd International Conference on Composite Materials* (ICCM-22), edited by Mouritz, A., Wang, C. and Bronwyn, F., Paper ID: 2412-5, 11-16, August, 2019, Melbourne, Australia.

4. Liao, Y., **Zhou, P.**, Zhou, L.-M. and Su, Z. 'An inkjet-printed, nanocomposites-inspired sensor network for acousto-ultrasonics-based structural health monitoring', in *Proceedings of the 9th European Workshop on Structural Health Monitoring* (EWSHM-9), edited by Soutis, C. and Gresil, M., 10-13, July, 2018, Manchester, UK.

5. Cao, W., Wang, K., Xu, L., **Zhou, P.**, Yang, X., Pang, B., Fromme, P. and Su, Z. 'Modally selective nonlinear ultrasonic waves for characterization of pitting damage in Whipple shields of spacecraft', in *Proceedings of the SPIE* (Vol. 11381, *Proceedings of SPIE Conference on Smart Structures/NDE* (Health Monitoring of Structural and Biological Systems XIV)), edited by Fromme, P. and Su, Z., pp. 113811M-1-16, 27, April-1, May, 2020 (online conference), CA., USA.

ACKNOWLEDGEMENTS

First and foremost, I would like to express my sincere gratitude to my chief supervisor, Prof. Zhongqing Su. Without his vast knowledge, kind guidance and invaluable help, it would be impossible for me to accomplish the contents presented here. He is not just my academic supervisor, but also a great mentor in all aspects. Whenever I faced problems or felt anxious, he always told me not to worry. I still remember the first day I registered as an RPg student in PolyU, he said: “Don’t rush to your research, and discover Hong Kong first! One can only be productive when he loves where he lives.” He often shared his travel experience, not only in Hong Kong but all over the world, which broadens my horizons and brings a lot of references for me. Thanks to him, now I have accomplished my PhD thesis, and fell in love with this surprising and gorgeous city, even after a few difficult moments of this city.

I also wish to thank my co-supervisor, Prof. Li-min Zhou, for his guidance and support. In the meantime, I would like to express my appreciation to Prof. Lei Qiu at Nanjing University of Aeronautics and Astronautics and Prof. Qiang Wang at Nanjing University of Posts and Telecommunications, who helped me a lot in experimental equipment and solving problems of signal acquisition.

I would like to convey my profound gratitude to Ms. Joyce Lau and Dr. Terence Wong from the Cleanroom, as they provided me with crucial technical support on inkjet printing. Many thanks to Ms. Pendy Ho and Dr. Hardy Lui from the Materials Research Centre, and Dr. Pai Wong from the Department of Applied Physics, for their help in

material characterizations. I would also like to thank Ms. Lily Tam, Mrs. Michelle Lai, Mr. Benny Leung, Dr. Stephen Ng, and Mr. Sky Tse from the Department of Mechanical Engineering, for their work on general affairs and lab management.

Next, I would like to appreciate my colleagues, peers, and friends in the Department of Mechanical Engineering. With help from Dr. Yaozhong Liao and Dr. Yehai Li, I could quickly become familiar with my research field and the lab at the very beginning. I am indebted to Dr. Kai Wang, for his suggestions regarding to ultrasonic waves and personal career development. I am also grateful to Mr. Xiongbin Yang, Mr. Yiyin Su, Mr. Lei Xu, Mr. Jianwei Yang, Mr. Yi He, Ms. Tianhui Lu and Mr. Xinze Guo. We shared a lot, which has enriched my postgraduate study experience with friendship. Additional thanks to Dr. Yafeng Wang, Dr. Wuxiong Cao and Dr. Guangzhe Li: They are not only my colleagues and friends in the Department of Mechanical Engineering, but also my alumni of Harbin Institute of Technology – similar campus experiences let us have many common topics, and we spent a lot of happy time together.

Special thanks to beloved Miss Xueyin Chen, as well as her family. Thanks very much for your patience! We have not seen each other in person for more than one year when this thesis was completed, because of the lockdown and border control due to the COVID-19 pandemic. Looking forward to seeing you soon!

Last but not least, I would like to express my deepest appreciation to my family, for their love, care, and patience at all times. Their encouragement and support help me overcome various obstacles in pursuing my PhD degree.

NOMENCLATURE

Acronyms and Initialisms

AFM	Atomic Force Microscopy
AIP	All-inkjet-printed
AM	Additive Manufacturing
APNSA	All-printed Nanocomposite Sensor Array
ASTM	American Society for Testing and Materials
BSS	Baseline Signal Stretch
CB	Carbon Black
CVD	Chemical Vapor Deposition
EC	Ethyl Cellulose
EG	Ethylene Glycol
EMAS	Electromagnetic Acoustic Sensor
FBG	Fibre Bragg Grating
FESEM	Field Emission Scanning Electron Microscopy
FRP	Fibre-reinforced Plastic
FTIR	Fourier-transform Infrared Spectroscopy
GFRP	Glass Fibre-reinforced Plastic
GO	Graphene Oxide

LPE	Liquid Phase Exfoliation
MFC	Macrofibre Composite
MUSIC	Multiple Signal Classification
NASA	National Aeronautics and Space Administration, U.S.A.
NDT	Non-destructive Testing
NGP	Nanographene Platelets
NMP	N-methyl-2-pyrrolidone
OBS	Optimal Baseline Selection
PAA	Poly(amic acid)
PDI	Probability-based Diagnostic Imaging
PI	Polyimide
PDMS	Polydimethylsiloxane
PSN	Lead Stibium Niobium
PVDF	Polyvinylidene Fluoride
PVDF-CTFE	Poly(vinylidene fluoride-co-chlorotrifluoroethylene)
PVDF-HFP	Poly(vinylidene fluoride-co-hexafluoropropene)
PVDF-TrFE	Poly(vinylidene fluoride-trifluoroethylene)
PVDF-TrFE-CTFE	Poly(vinylidene fluoride-trifluoroethylene-chlorotrifluoroethylene)
PVP	Polyvinyl Pyrrolidone
PWAS	Piezoelectric Wafer Active Sensor

PZT	Lead Zirconate Titanate
RAPID	Reconstruction Algorithm for Probabilistic Inspection of Defects
RFID	Radio Frequency Identification
rGO	Reduced Graphene Oxide
R-V	Resistance-voltage
SBS	Poly(styrene-butadiene-styrene)
SDBS	Sodium Dodecylbenzenesulfonate
SEM	Scanning Electron Microscopy
SHM	Structural Health Monitoring
SLG	Single-layer Graphene
ToF	Time of Flight
XPS	X-ray Photoelectron Spectroscopy
0D	Zero-dimensional
1D	One-dimensional
2D	Two-dimensional
3D	Three-dimensional

Symbols

$\vec{u}$	Displacement vector
$\vec{f}$	Body force
E	Young's modulus
v	Poisson's ratio
λ_e	Lame's constant
μ_e	Shear modulus
k	Wavenumber
ω	Angular frequency of Lamb waves
c_T	Transverse propagating velocity of Lamb waves
c_L	Longitudinal propagating velocity of Lamb waves
S_{ij}	Mechanical strain
T_{kl}	Mechanical stress
D_j	Electric displacement
E_k	Electrical field
d_{kij}	Piezoelectric coefficient of PWAS
s_{ijkl}	Material compliance
ε_{jk}	Dielectric permittivity
Q_e	Charge of PWAS
C	Internal capacitance of PWAS

C_e	Capacitance of PWAS
V	Voltage
A_e	Area of PWAS electrodes
λ_B	Central wavelength of reflected narrowband spectrum of FBG sensor
k_{31}	Electromechanical coupling coefficient
Λ	Grating period of FBG sensor
n_f	Effective refractive index of FBG sensor
K_f	Theoretical gauge constant of FBG sensor
ε	Strain
Z	Figure of merit of inkjet printing
η	Viscosity
γ	Surface tension
ρ	Density
d	Diameter
h	Half-thickness of plate
R_e	Reynolds number
W_e	Weber number
O_h	Ohnesorge number
K	Gauge factor
R	Resistance

h_p	Plank's constant
s	Distance between conductive particles
Q	Number of particles forming a single conducting path
A^2	Effective cross-section of a tunneling current
N	Number of conducting paths
m	Mass
α_c	Constant related to status of conducting path
β_c	Constant related to status of conducting path
δ_c	Constant related to status of conducting path
τ_c	Constant related to status of conducting path
c_1	Constant linked to resistance change
c_2	Constant linked to resistance change
c_3	Constant linked to resistance change
c_4	Constant linked to resistance change
U	Uncertainty of resistance changing ratio
C^2	Coefficients of determination
D	Deflection
t	Thickness
l	Length
M	Circuit parameter
A_λ	UV-vis absorption at wavelength λ

α_λ	UV-vis absorption coefficient at wavelength λ
c	Concentration
d_{31}	In-plane piezoelectric coefficient
T	Temperature
v	Velocity
P	Pressure
Δt_i	Damage-induced ToF
L	Distance between actuator, sensor, or damage
$S_0^{Anomaly}$	Anomaly-scattered S_0 mode
$\boldsymbol{R}^{S_0^{Anomaly}}(t)$	Covariance matrix of signals
$r_m(t)$	Anomaly-scattered S_0 mode captured via the m^{th} sensing element
$\boldsymbol{A}$	Steering vector of sensor array
a_m	Steering vector of the m^{th} sensing element
τ_m	Wave propagation time difference
c_w	Wave propagation velocity
P	Pixel value of spatial spectrum

TABLE OF CONTENTS

LIST OF FIGURES

LIST OF TABLES

CHAPTER 1

Introduction

1.1 Background and Motivation

The structural health status remains the most critical yet paramount factor of an in-service engineering structure to warrant its operation safety, structure durability, and financial benefits. Tiny and barely visible, embryonic damage in engineering structures can deteriorate to a critical level, if damage of such a level is “overlooked”, which may ultimately lead to irretrievable and catastrophic consequences [1]. With safety being the paramount concern in engineering practice, it is of vital significance to warrant the structural integrity and reliability, and prevent any possible failure of engineering structures.

The manner that human beings perceive environmental fluctuation and sense self-body status, as well as the behaviour of decision making, has provided a superior model for developing new genres of sensing systems to accommodate engineering practice [2-4]. Inspired by natural biological nervous systems, structural health monitoring (SHM) – an emerging technique that is aimed at enhancing structural safety while in the meantime driving down exorbitant maintenance cost, is a bionic attempt that expands the concept of biological sensing philosophy to engineering structures,

and based on the sensed structural responses and ambient parameters, the structural health and integrity status can be accessed in a real-time manner. The sophisticated structural health-enhancement technique trans-disciplinarily embraces state-of-the-art scientific advances and technological breakthroughs in mechanics, material science, informatics, big data, sensing technology and additive manufacturing (AM).

Amidst diverse SHM approaches, those using acousto-ultrasonic waves are intensively explored and have gained prominence in safeguarding the structural health and improving reliability. Leveraging numerous merits of acousto-ultrasonic waves, acousto-ultrasonic wave-driven SHM has ushered in a new avenue to strike a balance among resolution, detectability, practicality, and cost, corroborating the concept of *in situ* SHM.

Sensing remains the most elementary yet pivotal constituent in non-invasive or non-intrusive health care for human beings, as well as *in situ* SHM. Central to the implementation of *in situ* SHM is sensing acousto-ultrasonic wave signals. In an *in situ* SHM system, a certain number of sensors are utilized in either dense or sparse configurations, and immobilized in the inspected structures, to acquire desired acousto-ultrasonic wave signals (Figure 1.1). By extracting and interpreting variations of subtle acousto-ultrasonic wave features, multiscale damage or faults in the inspected structures can be pinpointed and characterized, either qualitatively or quantitatively.

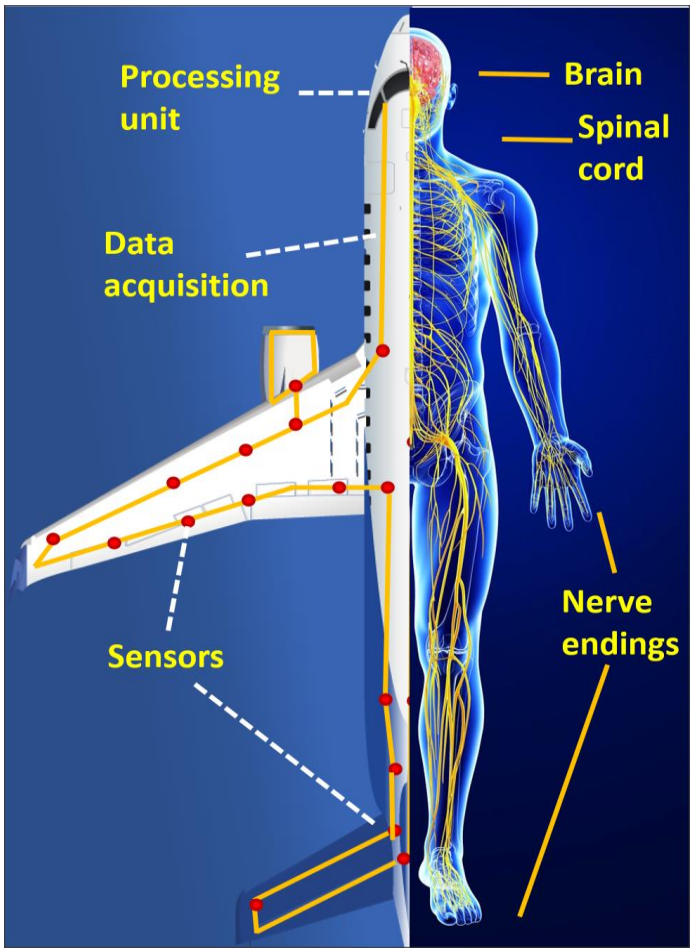

Figure 1.1 SHM system implemented in an aeroplane structure and the biological nervous system of a human body.

Taking advantages of such bionic concept, structural integrity information can be accurately and quantitatively monitored in a real-time, smart, and intelligent, but cost-effective manner. In an acousto-ultrasonic wave-driven SHM system, the configured sensors act as nerve endings in a human body, to achieve faithful sensing and enable precise perception of structural responses. Commercially available sensors for SHM are in a diversity of modalities, as typified by metal-foil strain gauges [5], piezoelectric wafers (typically lead zirconate titanate (PZT)) [6], optical fibres [7], electromagnetic

acoustic sensors (EMASs) [8], and piezoelectric polymeric sensors (*e.g.*, polyvinylidene fluoride (PVDF) and its copolymers) [9, 10].

Amid these prevailing sensors, the sensitivity of strain gauges is often limited by their intrinsic capacity of only responding to dynamic strain signals in a spectrum of low frequencies [11]; piezoelectric wafers are known rigid and unwieldy, presenting difficulty in conforming to a curved surface; optical fibre-based sensors are brittle, and embedding optical fibres into structures such as laminated composites may not only complicate fabrication process but degrade local strength of the composites; PVDF enables large area coverage and good adaption to a curved surface, but its piezoelectric coefficients are usually low, which implies inferior sensitivity to acousto-ultrasonic wave signals of high frequency [12].

As mentioned earlier in this chapter, to implement *in situ* SHM in engineering structures, a certain number of sensors are to be configured and immobilized in the inspected structures. Nevertheless, most genres of the sensors feature a low degree of integrity with the inspected structures – irrespective of the intention of discovering damage and monitoring their progress, the deployment of sensors and their supporting systems on the inspected structures possibly introduce defect, stress concentration and incompatibility between sensors and the host structures, and in addition they impose remarkable weight and volume penalty to the inspected structures. This concern is particularly accentuated when stiff yet brittle sensors such as piezoceramic wafers are networked in a dense formality [13], and the inspected structures are manipulated in a cruel environment.

Recognizing the deficiencies that prevailing sensors are facing, to configure sensors and achieve acousto-ultrasonic wave-driven SHM of engineering structures, four issues are borne in mind, so as to strike a balance between "sensing effectiveness" and "sensing cost":

(i) Sensors for *in situ* SHM should be of adequate sensitivity to acousto-ultrasonic waves, as well as desired level of reliability and durability under extremely atrocious ambient conditions;
(ii) If SHM systems are developed with a dense grid of sensors, not only will extra weight penalty be added to the host structures, but the cost of sensors and maintenance expenditure also become exorbitant;
(iii) Sparsely configured sensors may sometimes "overlook" the damage status of the structures because the information acquired by only a few sensors can be inadequate;
(iv) Sensors in SHM systems should be of an appropriate degree of integrity with the host structures, without degrading their original structural integrity.

Nevertheless, for most of the existing sensors for acousto-ultrasonic wave-driven SHM, it is a challenging task to strike such a balance. Driven by the recent advances and technological break-throughs in material science, a great deal of effort has been dedicated to developing functionalized nanocomposites to accommodate specific structural or functional requirements, which has blazed a trail for new generation of sensing devices. A variety of carbon nanofillers, represented by graphene and multi-walled carbon nanotubes, are readily available, combing which with polymers leads to nanocomposites with the merits of both the nanofillers and polymers, such as low

density, good flexibility, environmental and chemical stability, along with improved electrical and mechanical profiles. Central to the interest in using nanocomposites to develop sensing devices is the nanocomposite-based piezoresistive sensors. However, when extended to the acquisition of high-frequency dynamic strains induced by acousto-ultrasonic waves in an ultrasound regime (several kHz or above), majority of the prevailing nanocomposite-based sensors fail to respond, whereby being uncapable to meet the requirements of sensors for *in situ* SHM.

On the other hand, in the past decade, AM has paved a promising way towards the development of various innovative electronics and devices. AM is defined with seven categories by the American Society for Testing and Materials (ASTM) Committee F42 on Additive Manufacturing Technologies: vat photopolymerization, material jetting, binder jetting, material extrusion, powder bed fusion, sheet lamination, and direct energy deposition [14]. Among flourishing addictive manufacturing techniques, ink-based material jetting approaches, as typified by inkjet printing, spray coating, aerosol jet printing, direct ink writing, and embedded printing, have gained increased preference for large-scale fabrication of flexible electronics [15].

Inspired by the booming nanotechnology and AM techniques, leveraging quantum tunneling effect, nanocomposite-inspired spray-coated sensors have been developed by the research group to which the candidate belongs. These sensors have proven effectiveness in faithfully perceiving dynamic strains with a broad frequency bandwidth (the bandwidth is referred to as the range of strain frequency that the sensors can perceive), from static strain, through medium-frequency vibration, to high-frequency acousto-ultrasonic waves [11, 16, 17]. The sensors can further be networked

for implementing acousto-ultrasonic wave-driven *in situ* SHM. However, although the fabrication of such sensors using manually manipulated spray coating is yet cost-effective, the manual manipulation introduces discrepancy among individual sensors, which is not to be neglectable in some high-precision measurement applications, in particular when a batch of such sensors are needed to form a dense sensor network at a large scale.

As a computer-aided, drop-on-demand AM approach, inkjet printing features versatility, simplicity, controllability, automaticity with high precision yet low cost. When used for fabricating sensing devices, inkjet printing makes it possible to customize sensor patterns, by precisely regulating the placement of picolitre volumes of ink droplets [18, 19]. The inkjet-printed sensors take advantages of good flexibility, light weight, and ease of processability. A broad range of electronic devices have been developed using inkjet printing, showing enhanced properties and performance when compared against those prepared using conventional manufacturing approaches.

In summary, sensors play a rudimentary yet critical role in acousto-ultrasonic wave-driven SHM. Although *in situ* SHM has been demonstrated as a promising technique to warrant the integrity and reliability of engineering structures, it is still a challenging issue for the prevailing sensors to strike a balance between "sensing effectiveness" and "sensing cost", which has posed barriers to practical implementation of "on-line" and real-time SHM. Direct-write AM approaches such as inkjet printing with a high degree of automation and fabrication accuracy are of proven effectiveness in producing new electronics and devices, but sensors that are produced by AM approaches with

outstanding acousto-ultrasonic wave sensing performance, and can be further applied to *in situ* SHM are still rare.

1.2 Research Objectives

In recognition of the drawbacks of prevailing sensors for acousto-ultrasonic wave-driven SHM as commented in the above, and motivated by the emerging direct-write AM techniques, this PhD study is dedicated at developing new breeds of nanocomposite-based thin film ultrasound sensors by using direct-write AM (a drop-on-demand inkjet printing approach), from sensing ink formulation, through sensor fabrication, to applications of *in situ* acousto-ultrasonics-based SHM. The sensors are to be designed and fabricated with merits of superb ultrasound sensitivity, light weight, good flexibility, and excellent stability to aggressive environmental exposures. To achieve the above aims and address the inefficiencies of existing methods as briefed above, the following specific objectives are set:

(i) To design, formulate and produce nanocomposite-based sensing inks with good printability, wettability, storage stability, and functionality;
(ii) To fabricate inkjet-printed nanocomposite-based thin film ultrasound sensors that are responsive and sensitive to acousto-ultrasonic waves up to megahertz;
(iii) To conduct morphological and microstructural characterizations of the printed thin film ultrasound sensors, and optimize the nanostructure of the sensors;
(iv) To evaluate the sensing capability, sensitivity, fidelity and accuracy of the printed thin film ultrasound sensors to high frequency acousto-ultrasonic waves;

(v) To optimize the ultrasound sensing performance of the printed thin film ultrasound sensors;

(vi) To scrutinize the sensing performance of the printed thin film ultrasound sensors in acquiring broadband acousto-ultrasonic wave signals under atrocious ambient conditions;

(vii) To apply the developed thin film ultrasound sensors, by configuring sensor networks or sensor arrays, to implement acousto-ultrasonic wave-driven SHM on engineering structures.

1.3 Scope of the Thesis

This PhD study aspires to develop new genres of nanocomposite-based thin film ultrasound sensors for acousto-ultrasonic wave-driven SHM applications through direct-write AM. The developed sensors are expected to feature merits of extraordinary ultrasound sensitivity, light weight, good flexibility, and excellent stability to aggressive environmental exposures. This thesis is systematically organized in the order of sensor design philosophy, sensing ink fabrication, sensor printing, sensing capability validation, environmental exposure performance examination, and proof-of-concept application paradigms.

A brief literature review that concerns acousto-ultrasonic wave-driven SHM, sensors for SHM, and AM in fabrication of electronic devices is presented in Chapter 2. The basic concept of SHM and fundamentals of acousto-ultrasonic waves are recapped, and various types of ultrasound sensors for SHM are compared in terms of pros and

cons. Previous studies regarding to ink-based AM, and inkjet-printed electronic devices are also commented.

Chapter 3 is pertaining to the development of ultra-thin, flexible, and printable carbon black (CB)/polyvinyl pyrrolidone (PVP) nanocomposite-based ultrasound sensors for *in situ* acquisition of high-frequency acousto-ultrasonic wave signals. Leveraging drop-on-demand AM (inkjet printing), the produced sensors precisely respond to dynamic strains in a broad range from quasi-static strain, through medium-frequency vibration, to acousto-ultrasonic waves up to 500 kHz. Interestingly, the sensitivity of the inkjet-printed sensors can be fine-tuned by adjusting the degree of conductivity via controlling the printed passes, endowing the sensors with a capacity of resonating to strains of a particular frequency.

In Chapter 4, to further enhance the sensing performance of inkjet-printed nanocomposite-based ultrasound sensors, by leveraging high-shear liquid phase exfoliation (LPE) and inkjet printing, nanographene platelets (NGP)/polyimide (PI) sensors are fabricated with morphologically optimized poly(amic acid) (PAA) hybrid-based nanocomposite ink, which is produced from inexpensive bulk graphite. The sensing ink possesses superb graphene concentration as high as 13.1 mg mL^{-1}. The produced NGP/PI film sensors feature an ultra-thin thickness (~ 1 μm only), and the sensors are demonstrated with prominent thermal stability and superior adhesive strength that reaches ASTM 5B level. The sensors have a proven gauge factor as high as 739 (when sensing acousto-ultrasonic waves at 175 kHz), along with an ultra-broad responsive band up to 1.6 MHz. This chapter has also unveiled the unique sensing mechanism of the NGP/PI ultrasound sensors. With a highly consolidated NGP/PI

nanostructure in the sensors, quantum tunneling effect is triggered among NGPs and π-π interaction is formed between NGPs and PI polymer matrix. Such a trait endows the sensors superior sensing performance to high frequency acousto-ultrasonic waves.

Upon sensor fabrication, characterization, and sensing performance examination, temperature effect on ultralight and flexible inkjet-printed thin film ultrasound sensors in acquiring broadband acousto-ultrasonic wave signals is examined in Chapter 5. The developed thin film ultrasound sensors are further inkjet-printed with electrodes and insulating layers, to form all-inkjet-printed (AIP) sensors. Under high-intensity thermal cycles which span the thermal extremes undergone by most aircraft and spacecraft (from –60 to 150 °C), the sensors have proven stability and accuracy in responding to signals in a broad band from static to half a megahertz. Specifically, compared to piezoelectric sensors, the AIP sensors can avoid the negative influence of increased dielectric permittivity during the measurement of high-frequency signals at elevated temperatures.

In Chapter 6, the inkjet-printed thin film ultrasound sensors are extended to all-printed nanocomposite sensor array (APNSA) for ultrasonic imaging of composites. With the additively manufactured nanocomposite sensor array, ultrasonic imaging of anomaly in composites is implemented, manifesting the alluring application potentials of the APNSA in fulfilling *in situ* SHM of composites. It is noteworthy that the APNSA can be fully integrated with the inspected composites, authenticating an additional merit of the APNSA over conventional ultrasonic phased array in *in situ* SHM for composites.

Chapter 7 serves as the conclusion of the thesis, where recommendations for future

research are also made.

CHAPTER 2

State of the Art: A Literature Review

2.1 Introduction

With the motivation to enhance structural safety, and drive down exorbitant maintenance cost of engineering structures, this PhD study is dedicated to developing thin film ultrasound sensors for *in situ* SHM through AM approaches. This chapter reviews the state of the art of some key aspects of acousto-ultrasonic wave-driven SHM and AM techniques that are related to this PhD study.

To start with, the basic concept of guided ultrasonic wave-based SHM – a non-invasive and real-time technique of monitoring the integrity of engineering structures, is introduced, and the theoretical fundamentals of guided ultrasonic waves are briefly summarized. Central to the realization of acousto-ultrasonic wave-driven SHM is extracting structural health information from acquired wave signals. Ultrasonic wave signals are acquired by ultrasound sensors, and thus ultrasound sensors play the irreplaceable yet paramount role in an SHM system. Various categories of sensors for this purpose are surveyed and summarized. Targeting developing new ultrasound sensors through AM approaches, ink-based AM approaches in fabrication of electronic devices, especially inkjet printing, are also reviewed.

2.2 Acousto-ultrasonic Wave-driven Structural Health Monitoring

2.2.1 Basic Concept of Structural Health Monitoring

The past decades have witnessed unprecedented prosperity of transportation industry globally, particularly the aviation industry and high-speed railway. The rapid conveyance capability and reduced cost have provided people with possibilities to travel more conveniently than ever before. However, the potential threats behind the prosperity must be envisaged. The longer a high-speed train is in service, the more critical defects it may develop. The defects are usually initiated by imperceptible fatigue cracks in train bogies. As an example, Figure 2.1 shows a fatigue crack found in the bogie of a Shinkansen bullet train (JR West N700 series, “Nozomi” train bound for Tokyo station) in December 2017. The crack in the frame was 44 cm, and a further cracking of 3 cm would result in the break of the entire bogie [20]. Damage in such a scale usually would not arouse sufficient attention until it deteriorates to an irretrievable level, so it is of vital significance to detect and identify these defects at their early stages.

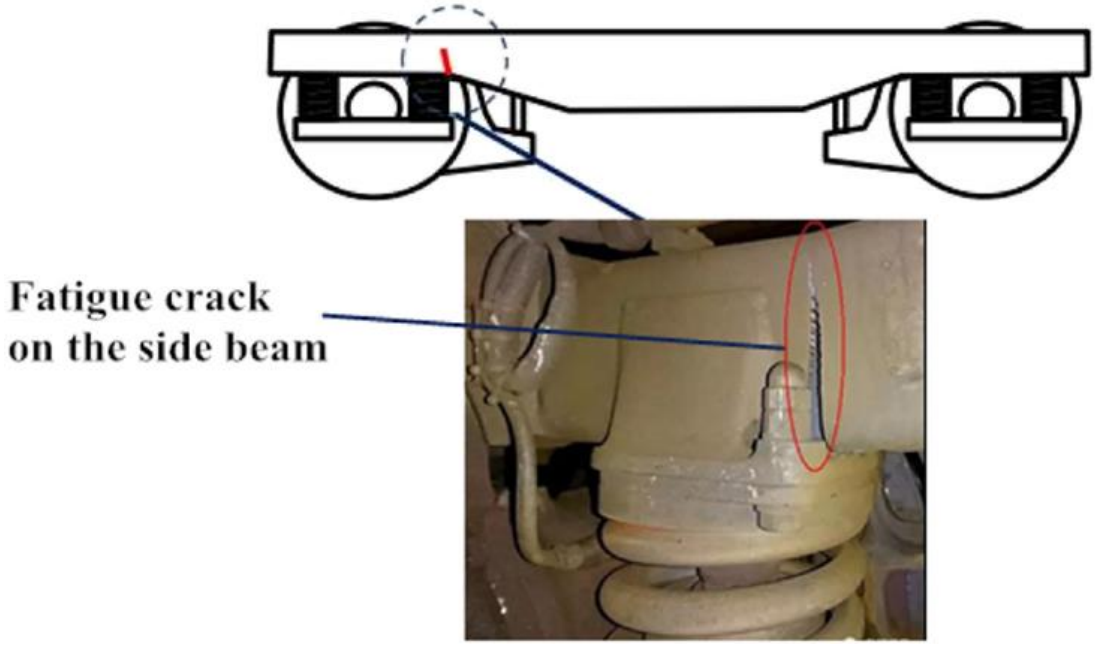

Figure 2.1 A fatigue crack found in a Shinkansen bullet train bogie [20].

To warrant that engineering structures can be operated safely and fulfil all scheduled work with adequate reliability, non-destructive testing (NDT) techniques have been entailed [21-23]. NDT is developed and conducted to identify and characterize any defect or damage in the surface or inferior part of the structure, which is a non-invasive technique that does not cause changes or alterations to the system structures.

There have been various approaches to conduct NDT on engineering structures, and representative NDT methods include ultrasonic testing [24], electromagnetic testing [25], radiography testing [26], optical testing [27] and thermal testing [28], to name a few. Nevertheless, in real-world engineering practice, restricted by the "off-line" nature of NDT, NDT must be scheduled and carried out on a regular basis, and NDT-based inspection can only be carried out after terminating the normal operation of the system. Components must be dismantled from the main system before being inspected,

and these components also need to be cleaned before and after NDT-based inspection, to warrant the inspection accuracy and keep their operation performance after inspection. In addition, human factors on NDT system manipulation and subjective analysis of inspection results also have non-neglectable influence on the practical effectiveness of NDT.

All the factors mentioned in the above have made NDT costly, laborious, and time-consuming. In recognition of this, SHM techniques have been motivated, and entailed as an emerging approach to detect damage at its embryo stage without terminating the normal operation of the system [29]. Such sophisticated structural integrity-enhancement techniques trans-disciplinarily embrace state-of-the-art scientific advances and technological breakthroughs in mechanics, material science, informatics, big data, sensing technology and additive manufacturing. SHM provides real-time surveillance of the health status of engineering structures, enabling the structures to strictly meet reliability, integrity safety and durable criteria.

An SHM strategy can be implemented by either passive or active approaches, in terms of the means of sensing, *i.e.*, passive SHM and active SHM [30]. For passive SHM techniques, various operational parameters, such as the magnitude of a load applied to the structure, and ambient information are collected by the SHM systems, whereby to evaluate the structural integrity status with modelling analysis and signal processing. For example, impact monitoring of an aircraft can be implemented through a passive SHM system, by acquiring acoustic emission signals induced by the impacts from external objects. With perceived data and specific diagnostic algorithms, the impact positions can be precisely identified, and the impact characteristics can be further

estimated [31]. Although passive SHM has been proven effective in various application scenarios, the disadvantages of passive SHM are also obvious: it can only "listen" to the reactions of structures to external alterations with a low degree of controllability, and it also suffers from problems such as low signal-to-noise ratio (SNR), and broadband noise interference [32].

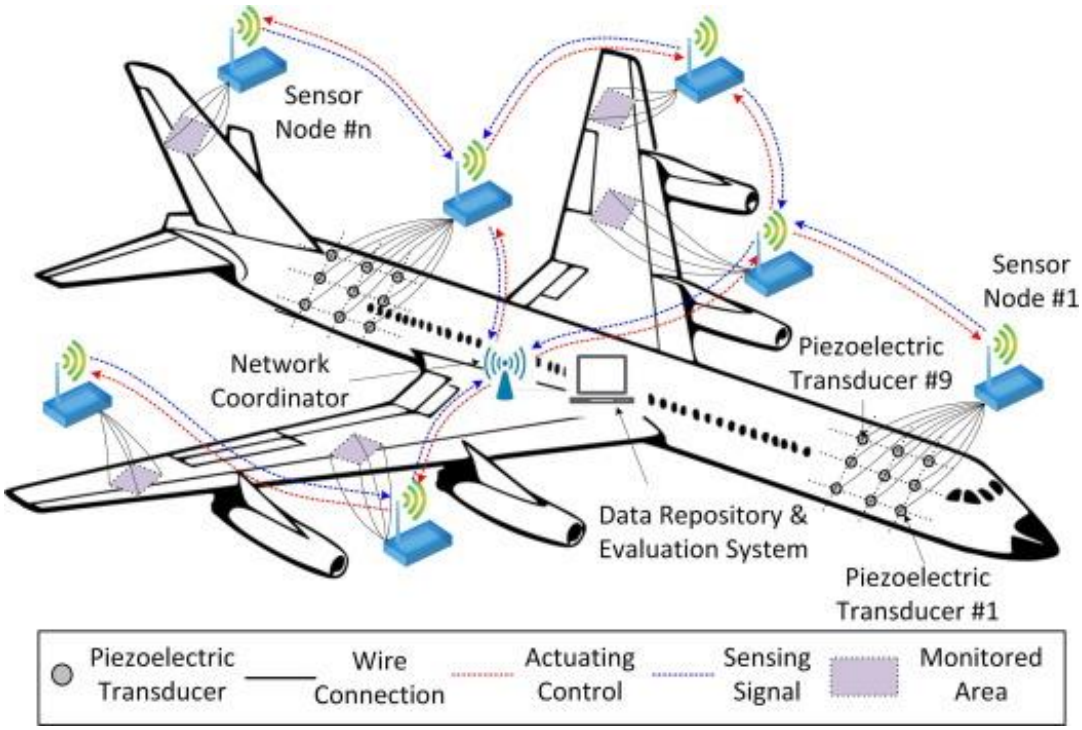

Figure 2.2 A typical active SHM system of an aeroplane [33].

As another strategy of SHM, active SHM which leverages numerous merits of acousto-ultrasonic waves, has ushered in a new avenue to strike a balance among detectability, practicality, resolution, and cost, well corroborating the concept of *in situ* SHM. In acousto-ultrasonic wave-based SHM, the sensor networks or sensor arrays, either externally attached on a structural surface or internally embedded in the structure, play

a rudimentary yet critical role in perceiving environmental variations and feature changes of waves guided by the inspected structure, in a real-time and *in situ* manner [17, 34-36], on which basis diagnosis and prognosis can be implemented [11, 37-40]. Active SHM systems can be permanently installed onto structures, and integrity information be accurately accessed and provided on-demand [30].

Compared with passive SHM approaches based on perceiving external source-triggered signals, active SHM systems utilize actively generated acousto-ultrasonic wave signals of specific frequencies and magnitudes. Such an active manner effectively minimizes the negative influence of signal noise, and enhances the system controllability and diagnosis accuracy. By interpreting changes of subtle acousto-ultrasonic wave features, multiscale damage or faults in an inspected structure can be pinpointed and characterized, either qualitatively or quantitatively, and the remaining service life of the system can also be derived.

2.2.2 Fundamentals of Guided Ultrasonic Waves

In 1889, the Lord Rayleigh studied wave propagation along a free semi-infinite guided surface of solid, which was the first time that the concept of guided waves was reported [41]. While in 1917, British applied mathematician Horace Lamb mathematically investigated the elastic waves that propagate in thin-plate- and shell-like structural configurations, and established the theoretical fundamentals of such waves [42]. Having been developed for more than a century, the waves discovered by Horace Lamb, which are known as Lamb waves, now have been utilized in various engineering application scenarios.

As another kind of ultrasonic waves, bulk ultrasonic waves are widely applied in NDT inspection [43]. Bulk waves traverse in infinite media without boundaries, being substantially different from guided waves that require boundaries to guide their propagation in solid media [44]. As shown in Figure 2.3, due to the "no-boundary" nature of bulk ultrasonic waves, bulk-wave-based NDT inspection can only provide structural integrity information of the position beneath the ultrasonic probe, so the probe must be moved along the surface if a scan of the entire sample is required. Such an inevitable action has made the bulk-wave-based NDT laborious.

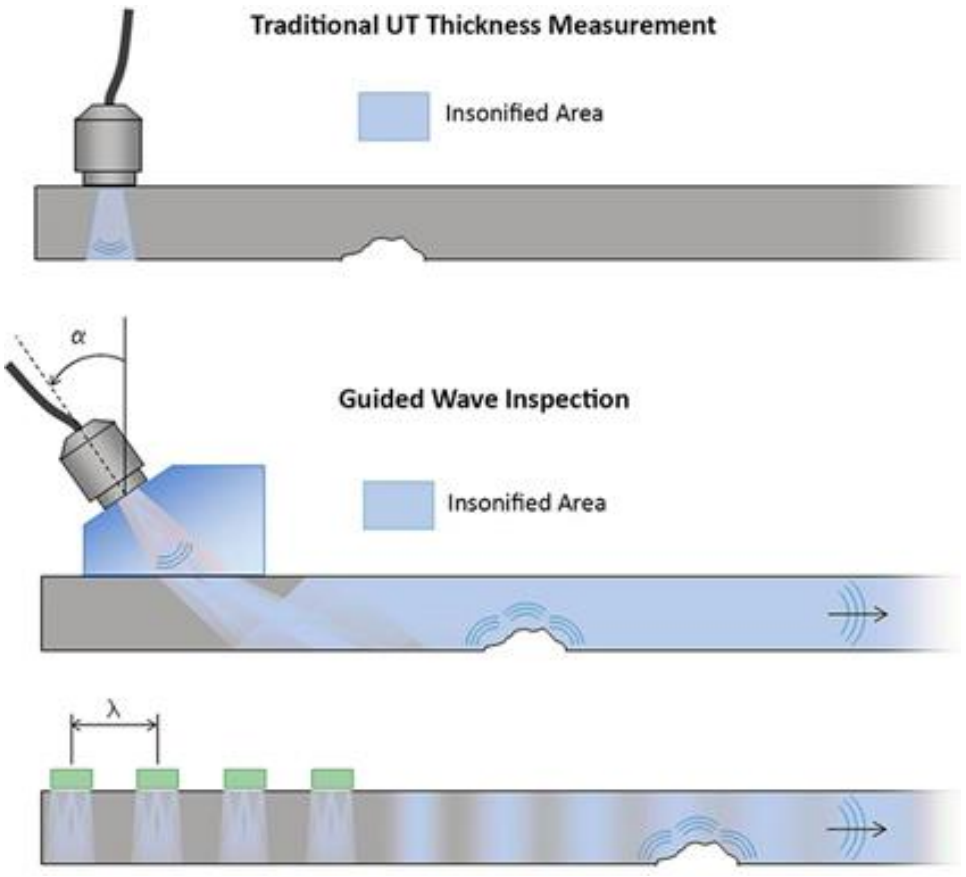

Figure 2.3 Comparison of bulk wave- and guided wave-based inspections [44].

Guided wave-based inspection has attracted extensive attention in the field of NDT and SHM. When compared to bulk waves, guided ultrasonic waves can propagate along boundaries, the structural and material status information of a specific area can be reflected with only one probe point, and thus manual scanning of the whole structure is no longer needed, which has made guided wave-based inspection more laboursaving and effective.

Taking advantage of merits of Lamb waves such as high sensitivity to damage of small dimension and long-distance probing, the quantitative information of damage can be derived from the Lamb wave signals, on which basis damage identification and health status perception in different structures can be achieved *in situ* with high accuracy. Fundamentals of Lamb waves are recapped here. Consider an infinite isotropic plate (Figure 2.4), and the Lamb wave motion in the plate is governed by Cartesian tensor notion [45]

$$(\lambda_e + \mu_e)\nabla(\nabla\vec{u}) + \mu_e\nabla^2\vec{u} + \rho\vec{f} = \rho\ddot{\vec{u}}, \tag{2.1}$$

where

$$\lambda_e = \frac{Ev}{(1+v)(1-2v)}, \tag{2.2}$$

$$\mu_e = \frac{E}{2(1+v)}. \tag{2.3}$$

In the above, $\vec{u}$ denotes the displacement vector, $\vec{f}$ the body force, ρ the waveguide density, μ_e the shear modulus of the waveguide. λ_e signifies the Lame's constant that is related to the Young's modulus E and Poisson's ratio v. $\nabla = \frac{\partial}{\partial x_1} + \frac{\partial}{\partial x_2} + \frac{\partial}{\partial x_3}$, and $\nabla^2 = \frac{\partial^2}{\partial {x_1}^2} + \frac{\partial^2}{\partial {x_2}^2} + \frac{\partial^2}{\partial {x_3}^2}$.

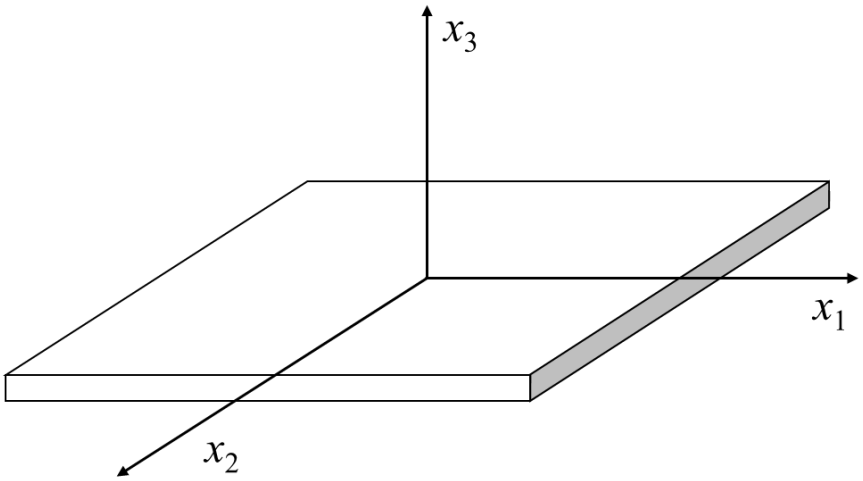

Figure 2.4 An infinite isotropic thin plate.

Lamb waves are guided to propagate in the plate, and consist of symmetric (in-plane motion) and anti-symmetric modes (out-of-plane motion) (Figure 2.5). Both symmetric and anti-symmetric modes are of dispersive nature, showing strong dependence on wave excitation frequency, and Lamb waves can be expressed by Rayleigh-Lamb equations [46]

$$\frac{\tanh(qh)}{\tanh(ph)} = -\frac{4k^2pq}{(q^2-k^2)^2}, \tag{2.4}$$

$$\frac{\tanh(qh)}{\tanh(ph)} = -\frac{(q^2-k^2)^2}{4k^2pq}, \tag{2.5}$$

where

$$p = \sqrt{(\omega / c_L)^2 - k^2}, \tag{2.6}$$

$$q = \sqrt{(\omega / c_T)^2 - k^2}. \tag{2.7}$$

Equation (2.4) is for the symmetric modes while Equation (2.5) is for the

antisymmetric modes. In Equations (2.4)-(2.7), ω is the angular frequency of the Lamb waves. k denotes the wavenumber, and h is the half-thickness of the plate. c_T is the bulk transverse propagating velocity of the Lamb waves and c_L represents the longitudinal propagating velocity of the Lamb waves. c_T and c_L are defined as

$$c_T = \sqrt{\frac{E}{2\rho(1+\nu)}}, \tag{2.8}$$

$$c_L = \sqrt{\frac{E(1-\nu)}{\rho(1+\nu)(1-2\nu)}}. \tag{2.9}$$

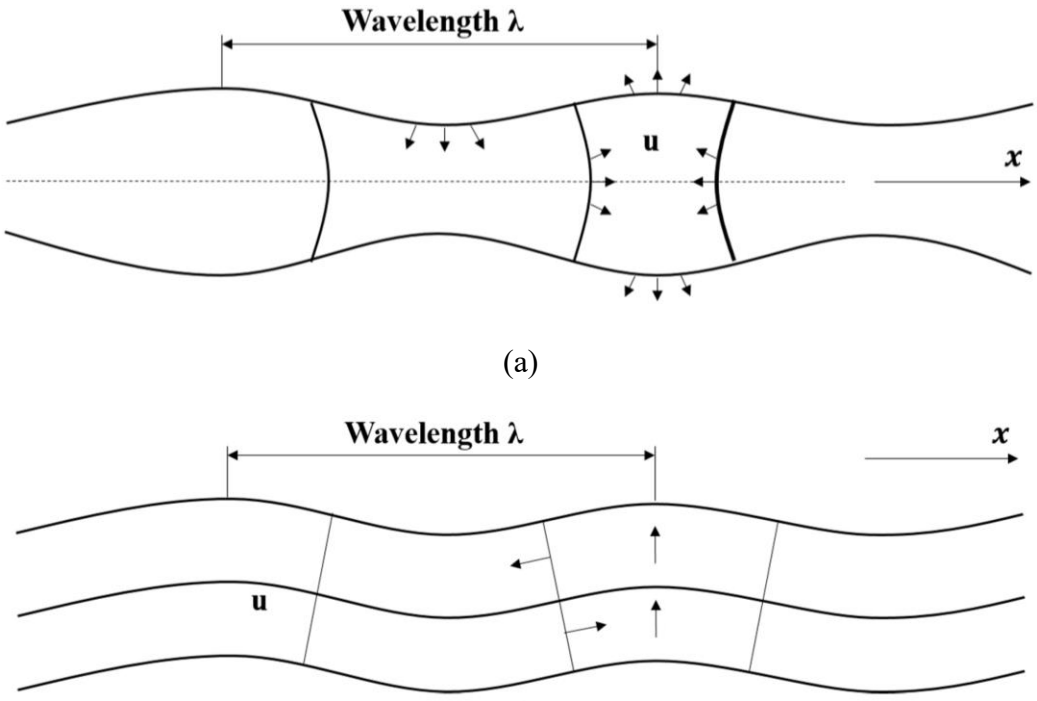

Figure 2.5 Mode shapes of (a) symmetric and (b) anti-symmetric Lamb wave modes [47].

By solving the Rayleigh-Lamb equations, the dispersion curves for an Al-7075-T651 plate with the thickness of 2 mm in terms of the phase and group velocities of the

waves, as an example, are shown in Figure 2.6, indicating the dispersion natures of Lamb waves. The phase velocity is referred to the propagation speed of the phase of a particular frequency contained in the waves, while the group velocity is the velocity with which the overall shape of the wave amplitude, which is the actual velocity captured in experiment [48].

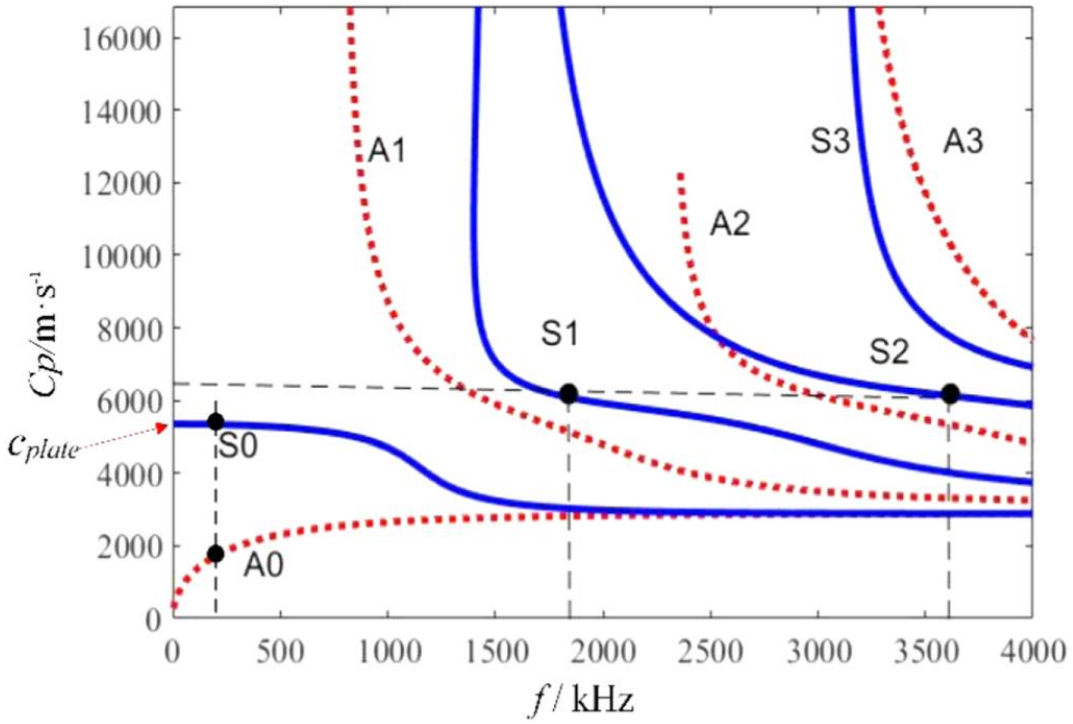

(a)

Figure 2.6 Dispersion curves for an Al-7075-T651 plate with the thickness of 2 mm: (a) phase velocity and (b) group velocity [49].

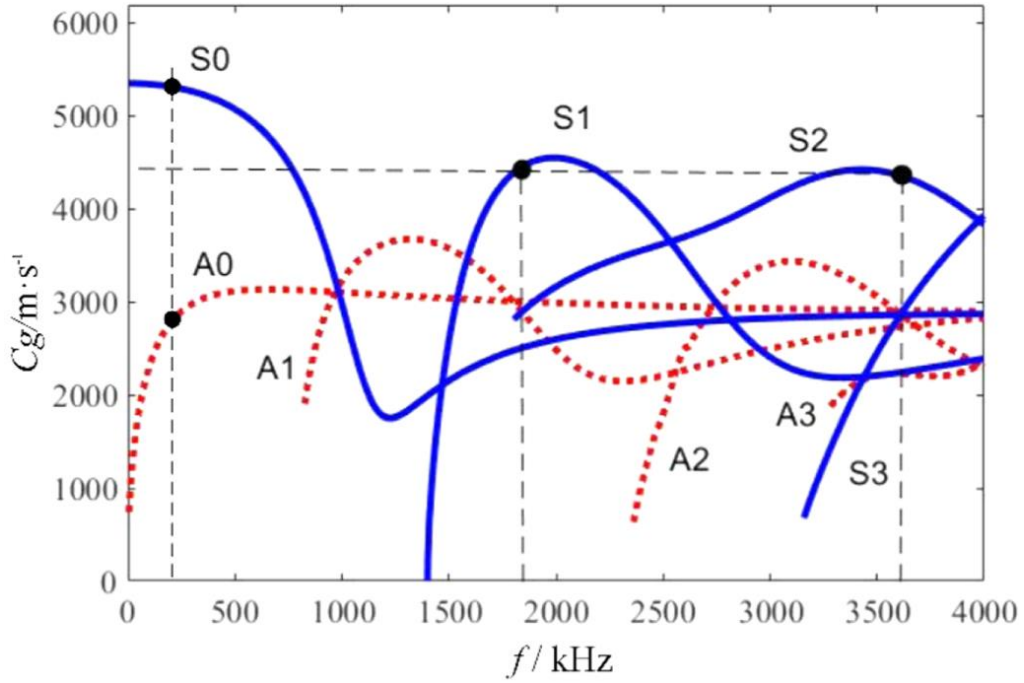

(b)

Figure 2.6 *Cont.*

When propagating, interactions between Lamb waves and damage cause unique scattering and mode conversion of the waves. Targeting accurate and quantitative identification and localization of damage with Lamb wave-based active SHM, a number of Lamb wave-based damage imaging methods have been proposed, such as delay-and-sum algorithm [50], probability based diagnostic imaging (PDI) algorithm [51, 52], time reversal-based imaging method [53], and reconstruction algorithm for probabilistic inspection of defects (RAPID) [54]. The above-mentioned approaches are based on characteristic changes in Lamb wave signals, either in a linear domain [55-57], or in a nonlinear domain [58, 59].

2.3 Sensors for Acousto-ultrasonic Wave-based Structural Health Monitoring

As mentioned in the sections above, acquisition of acousto-ultrasonic wave signals plays the most critical role in acousto-ultrasonic wave-driven SHM. Hitherto, there have been various sorts of ultrasound sensors developed for SHM and applied in real-world engineering practice, and this section gives a brief review on the state-of-the-art of sensors for SHM.

2.3.1 Piezoelectric Sensors

Piezoelectric sensors are the most commonly selected sensors to implement generation of acousto-ultrasonic waves-driven SHM techniques. By virtue of the piezoelectric effect, piezoelectric sensors convert mechanical energy (strain or stress energy) to electrical energy, *i.e.*, when mechanical strain or stress is applied onto a piezoelectric sensor, electrical filed can be generated in the sensor, and the strain or stress can be reflected in terms of variation in the output voltage magnitude of the sensor. For piezoelectric materials that are suitable to develop and produce piezoelectric ultrasonic sensors, they have to be non-centrosymmetric, poorly conductive under externally applied mechanical strain or stress, and their dipole moment magnitude should also be capable to be altered [60].

Piezoelectric wafer active sensors (PWASs) are among successful applications of piezoelectric sensors for SHM. Using PWAS as an example to illustrate the sensing principles of piezoelectric sensors (Figure 2.7(a)). The mechanical strain S_{ij} and electric displacement D_j of a PWAS under mechanical stress T_{kl} and electrical field E_k

is ascertained through the tensorial piezoelectric constitutive equation [61]

$$S_{ij} = s^{E}_{ijkl} T_{kl} + d_{kij} E_k , \tag{2.10}$$

$$D_j = d_{jkl} T_{kl} + \varepsilon^{T}_{jk} E_k , \tag{2.11}$$

where d_{kij} and d_{jkl} signify the piezoelectric coefficients, s^{E}_{ijkl} the material compliance at zero electrical field (*i.e.*, $E = 0$), and ε^{T}_{jk} the dielectric permittivity at zero stress (*i.e.*, $T = 0$).

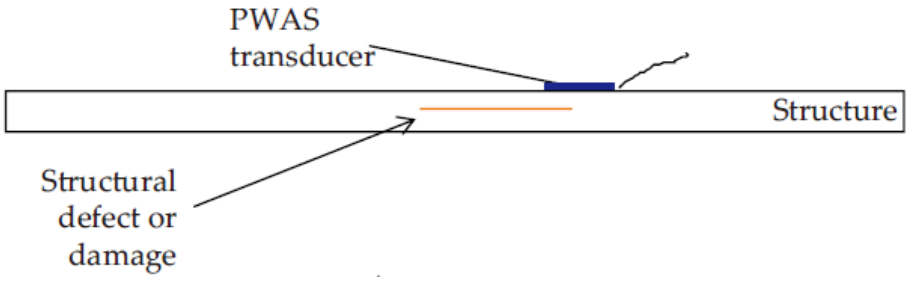

(a)

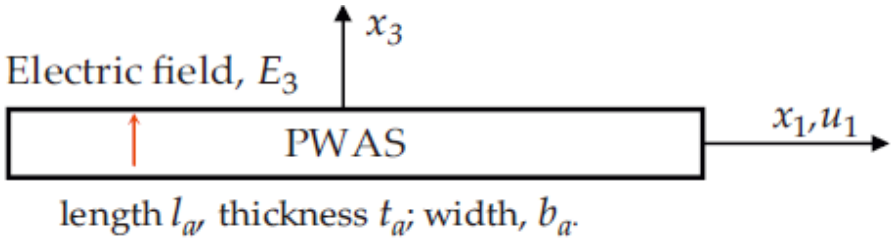

(b)

Figure 2.7 (a) Schematic of damage detection with a PWAS and (b) a PWAS of 1D assumption [61].

To simplify the model, considering a one-dimensional (1D) condition, as shown in Figure 2.7(b), Equations (2.10) and (2.11) can be simplified as

$$S_1 = s_{11}^E T_1 + d_{31} E_3 , \tag{2.12}$$

$$D_3 = d_{31} T_1 + \varepsilon_{33}^T E_3 . \tag{2.13}$$

For a PWAS, when it is subject to external stress, the charge Q_e produced on the sensor is given by

$$Q_e = D_3 A_e , \tag{2.14}$$

where A_e is the area of electrodes. The relationship between the electric displacement D_3, charge Q, capacitance C_e, and output voltage V is

$$D_3 = \frac{Q_e}{A_e} = \frac{C_e}{A_e} V , \tag{2.15}$$

and the relationship between the applied electric field E_3 and output voltage V is

$$E_3 = -\frac{V}{t_a}, \tag{2.16}$$

where t_a signifies the thickness of the PWAS. Substituting Equations (2.15) and (2.16) into (2.13) yields

$$V(C_e + \varepsilon_{33}^T \frac{A_e}{t_a}) = A_e d_{31} T_1 . \tag{2.17}$$

It is also known that the internal capacitance C of the PWAS can be presented as

$$C = \varepsilon_{33}^T \frac{A_e}{t_a} . \tag{2.18}$$

By substituting Equation (2.18) into (2.17), the output signal V of PWAS under stress T_3 can be ascertained as

$$V = \frac{A_e d_{31}}{C_e + C} T_1 . \tag{2.19}$$

When the PWAS is subject to in-plane strain S_1, by combing Equations (2.12), (2.13), (2.15) and (2.16)

$$d_{31}S_1 - s_{11}^E \frac{C_e}{A_e} V = (1-k_{31}^2) s_{11}^E \varepsilon_{33}^T \frac{V}{t_a}. \tag{2.20}$$

In Equation (2.20), k_{31} is the electromechanical coupling coefficient of the PWAS, which is defined by

$$k_{31}^2 = \frac{d_{31}^2}{s_{11}^E \varepsilon_{33}^T}. \tag{2.21}$$

By rearranging Equations (2.20) with (2.18), the output signal magnitude V of the PWAS under strain S_1 can be ascertained as

$$V = \frac{1}{C_e + (1-k_{31}^2)C} \frac{A_e d_{31}}{s_{11}^E} S_1. \tag{2.22}$$

Having understood the sensing mechanism of piezoelectric sensors, representative piezoelectric sensors for acousto-ultrasonic wave-driven SHM are introduced in this section. Amid diverse piezoelectric sensors, PZT ceramic wafers are the most commonly used piezoelectric sensors in SHM. PZT wafers are capable of generating and receiving signals of ultrasonic waves, *i.e.*, PZT wafers can serve as both wave actuators and receivers in an SHM system. When compared to conventional bulk piezoelectric sensors used in NDT (Figure 2.8(a)), PZT wafers are much lighter and handier (Figure 2.8(b)), and can be directly adhered or mounted onto the surface of structures, to conduct *in situ* and real-time SHM with a high degree of automation.

(a)

(b)

Figure 2.8 (a) A conventional bulk piezoelectric ultrasonic sensor used in NDT; and (b) PZT wafers in various shapes and dimensions for acousto-ultrasonic wave-driven SHM [62].

PZT wafers feature advantages of high sensitivity, broad sensing band, and low manufacturing cost. To further accommodate the demands of *in situ* SHM, PZT wafers need to be networked to derive adequate structural and material information.

Representatively, the SMART Layer® based on a built-in PZT wafer network on polymer film was developed at NASA Marshall Space and Flight Center [63], and *in situ* monitoring of structural integrity of filament wound composite structures were successfully implemented with the SMART Layer® (Figure 2.9(a)) [64]. Figure 2.9(b) shows a lightweight diagnostic film developed with PZT sensors/actuators, which is integrated with multiple wiring paths fabricated by inkjet printing [65]. Recently, a piezoelectric sensor network based on PZT wafers was reported [66]. As show in Figure 2.9(c), the PZT layer was manufactured by the Flexible Printed Circuit process with shared signal transmission wires, and this PZT layer was verified reliable in damage monitoring.

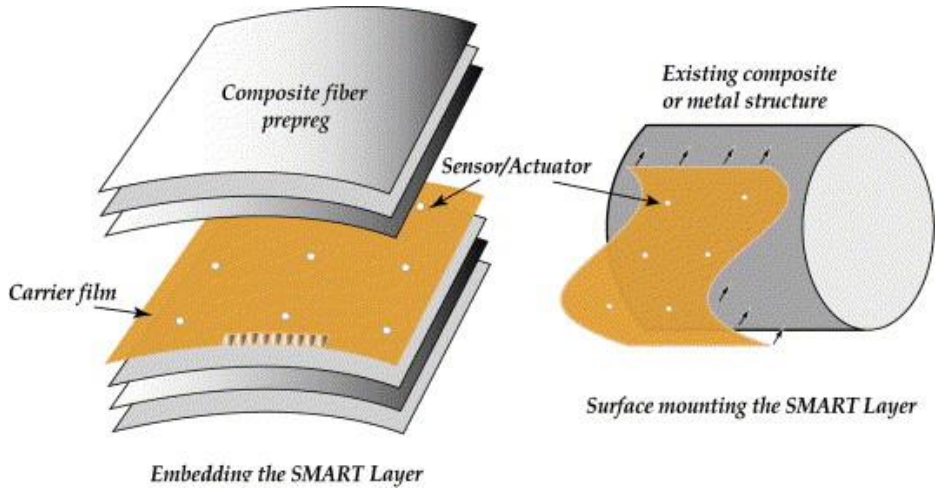

(a)

Figure 2.9 (a) Concept of SMART Layer® [64]; (b) diagnostic film developed with PZT sensors/actuators [65]; and (c) piezoelectric sensor network layer based on PZT wafers [66].

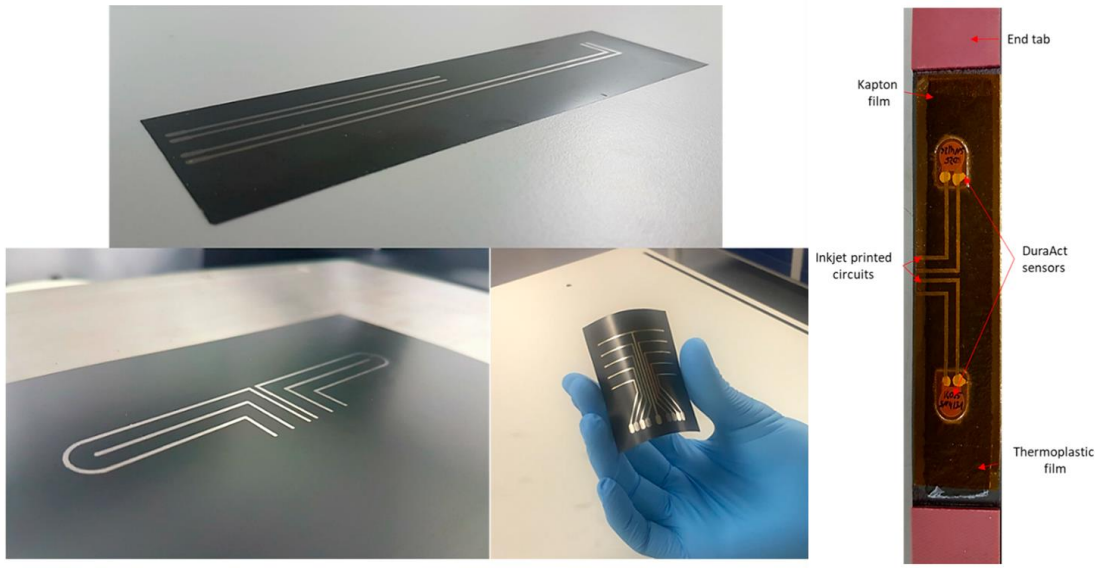

(b)

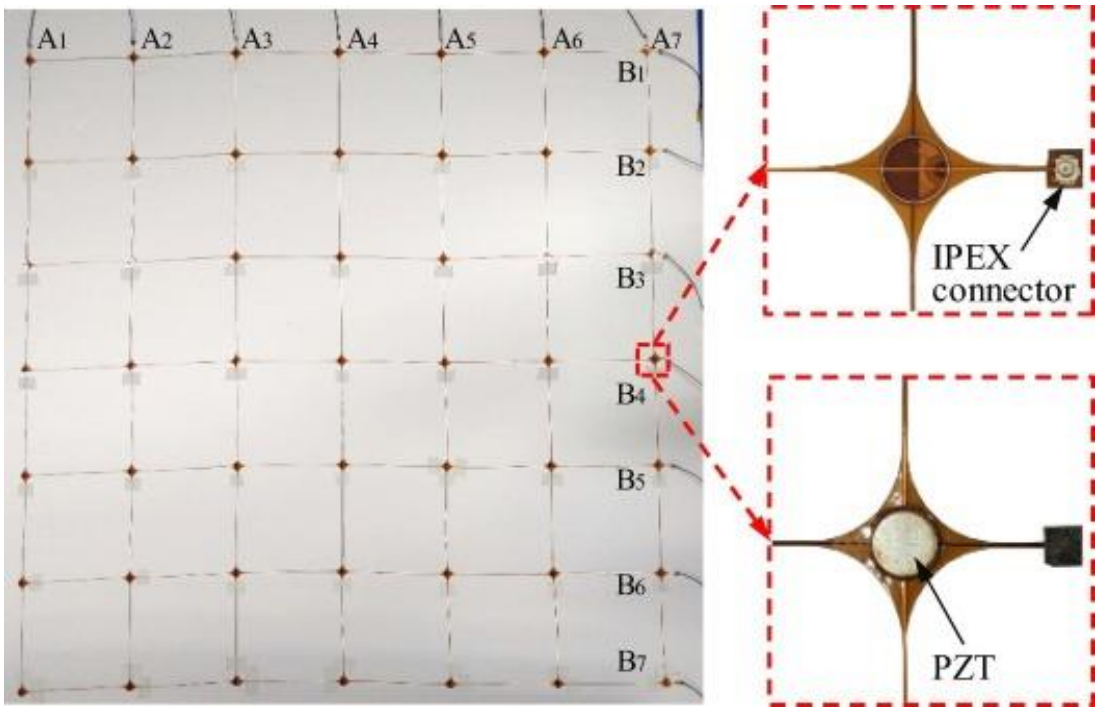

(c)

Figure 2.9 *Cont.*

However, there are also some drawbacks of PZT wafers. PZT wafers are in general rigid and unwieldy, presenting difficulty conforming to a curved surface. In addition, the use of a large number of PZT wafers to form a dense sensor network introduces

remarkable weight and volume penalty to the inspected structures.

Apart from piezoelectric ceramic wafers, piezoelectric polymer sensors are recognized as an alternative to piezoelectric ceramic sensors. PVDF (Figure 2.10(a)) is the most representative piezoelectric polymer material. β-phase PVDF with all trans planar zigzag conformation (TTTT) and semi-polar γ-phase PVDF (TTTGTTTG') [67], as well as copolymers of PVDF including poly(vinylidene fluoride-trifluoroethylene) (PVDF-TrFE) [68], all of these exhibit attractive piezoelectric properties. The good flexibility, light weight, long-term stability and easy processability of PVDF and its copolymers have made them highly desirable for developing ultrasound sensors [69].

In recent years, coatings of PVDF-TrFE ultrasonic sensor arrays via aerosol spraying on metal plates were reported by researchers (Figure 2.10(b)), and the sprayed arrays are demonstrated capable of generating and detecting ultrasonic waves [46]. There are also some other polymeric materials that have been proven with piezoelectric properties, such as some other copolymers of PVDF – poly(vinylidene fluoride-co-chlorotrifluoroethylene) (PVDF-CTFE) [70] and poly(vinylidene fluoride-co-hexafluoropropene) (PVDF-HFP) [71], and terpolymer of PVDF – poly(vinylidene fluoride-trifluoroethylene-chlorotrifluoroethylene) (PVDF-TrFE-CTFE) [72], and Nylon-11 [73], to name but a few. However, for most of the polymeric piezoelectric sensors towards acousto-ultrasonic wave-driven SHM applications, the response intensity of acousto-ultrasonic waves of high frequency is still inferior, as a result of their lower piezoelectric coefficients compared with piezoelectric ceramic sensors.

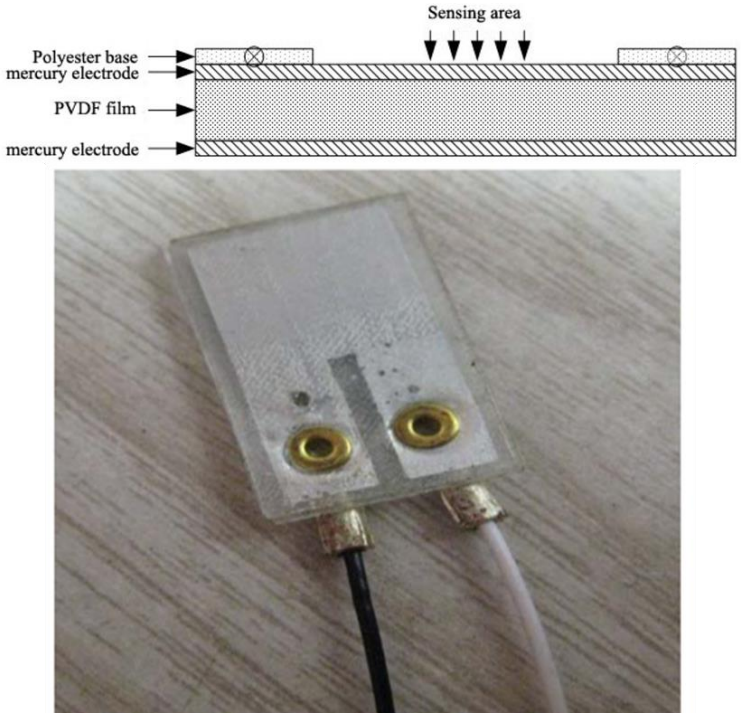

(a)

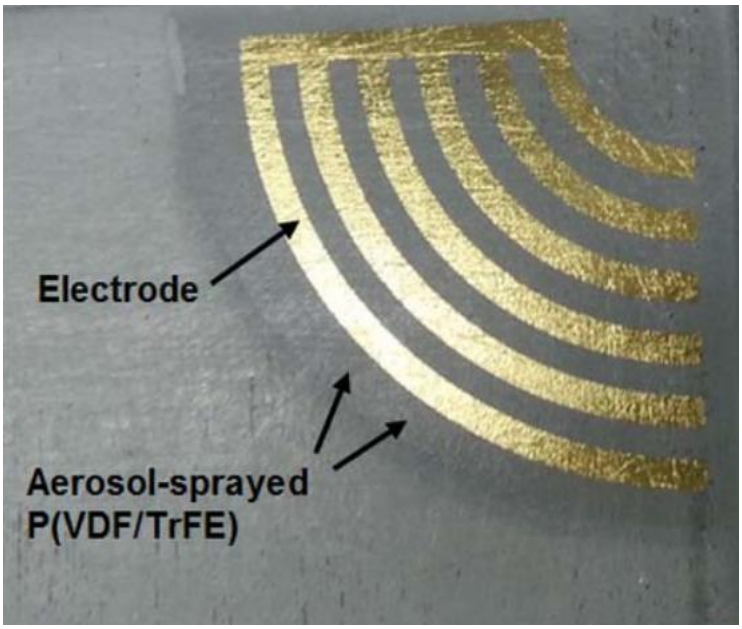

(b)

Figure 2.10 (a) A PVDF piezoelectric sensor [74]; and (b) aerosol-sprayed PVDF-TrFE sensors with electrodes [46].

2.3.2 Fibre Optic Sensors

Optical fibre techniques have attracted a great deal of research interest, especially in the field of telecommunication, and development of sensing systems. Optical fibres are good for its immunity to electromagnetic interference. In addition to that, optical fibres also feature advantages of long lifespan, low cost, light weight, broad bandwidth, and small physical size [75]. As a large amount of information can be transferred with superior efficiency through optical fibres, optical fibre-based telecommunication facilitates faster communication speed with less signal degradation.

Fibre Bragg Grating (FBG) sensors have demonstrated their promising application potentials in acousto-ultrasonic wave-driven SHM, especially for the *in situ* monitoring of fibre-reinforced plastics (FRPs): fibre optic sensors can be embedded and immobilized into FRP structures during the manufacturing process, and health status of the FRP structures can be monitored through the fibre optic sensors within the whole service cycle of FRPs.

The acousto-ultrasonic wave sensing mechanism of FBG sensors is dominantly based on the Bragg wavelength shift (Figure 2.11). When broadband light is transmitted through a FBG sensor, the Bragg wavelength of the FBG sensor, *i.e.*, the central wavelength of reflected narrowband spectrum, λ_B, is determined as [76]

$$\lambda_B = 2n_f \Lambda, \tag{2.23}$$

where n_f is the effective refractive index in the grating region, and Λ the grating period.

When the FBG sensors are subject to strains induced by acousto-ultrasonic waves (strains are within that gauge length), the effective refractive index and grating period are altered by the dynamic strains, and shift of Bragg wavelength occurs. Considering that the temperature effect is negligible, the shift of Bragg wavelength under strain variation $\Delta\varepsilon$ is given as

$$\Delta\lambda_{\mathrm{B}} = K_f \Delta\varepsilon\,, \tag{2.24}$$

where K_f is the theoretical gauge constant of FBG sensors.

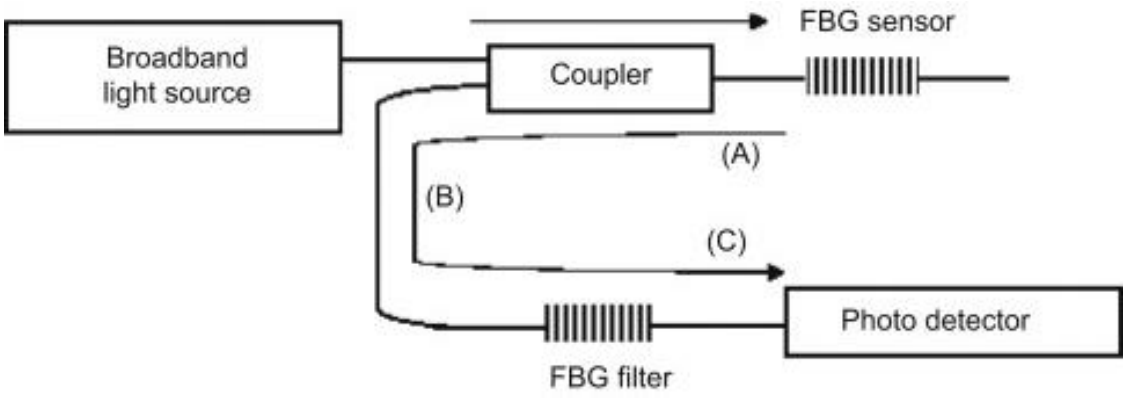

(a)

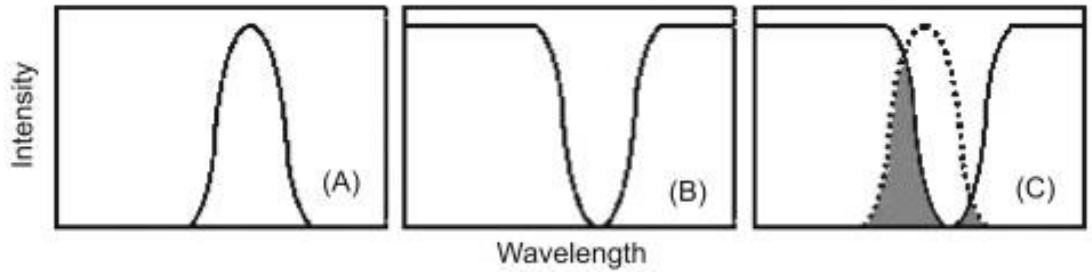

(b)

Figure 2.11 (a) Signal acquisition system of FBG sensor-based SHM; and (b) schematic diagram of the strain-light conversion [76].

FBG sensor-based *in situ* SHM can be implemented onto various materials and structures such as aluminium-based structures [77] and CFRP composites [78]. FBG sensors for acousto-ultrasonic wave-based damage identification on aerospace structures have been widely reported [79]. A PZT/FBG hybrid sensing diagnostic system was developed for long term health monitoring of aerospace vehicle structures [75, 79]. Nevertheless, due to the additional interfaces introduced by FBG sensors, embedding optical fibres into engineering structures such as laminated composites may cause delamination of the composites. Minimizing the negative impact of FBG sensors on structural integrity still remains to be studied in the future.

2.3.3 Electromagnetic Acoustic Sensors

Piezoelectric wafers, when used as sensors in an acousto-ultrasonic wave-driven SHM system, may present inferior sensing performance as a result of the mechanical coupling between sensors and host structures. In addition, material fatigue or structures, or acute change of ambient conditions may progressively degrade the strength of adhesive layers, potentially leading to exfoliation of sensors from the host structures [80]. As a non-contact monitoring method, utilizing EMASs can effectively avoid these problems.

EMASs perceive acousto-ultrasonic wave signals with electromagnetic approaches, either the Lorentz force (known as periodic permanent magnet EMASs) [81, 82] or magnetostrictive effects (known as magnetostrictive EMASs) [83, 84]. EMASs render SHM capable of being implemented in a non-contact manner. Figure 2.12 comparably shows the working conditions of conventional piezoelectric ultrasonic sensors and

EMASs. Compared with contact piezoelectric sensors, the energy conversion efficiency of non-contact EMASs is fairly low, leading to a lower SNR [85]. When being employed for SHM applications, EMASs require high power excitation, and the utility of EMASs is only restricted to conductive materials due to their electromagnetic working principles [32].

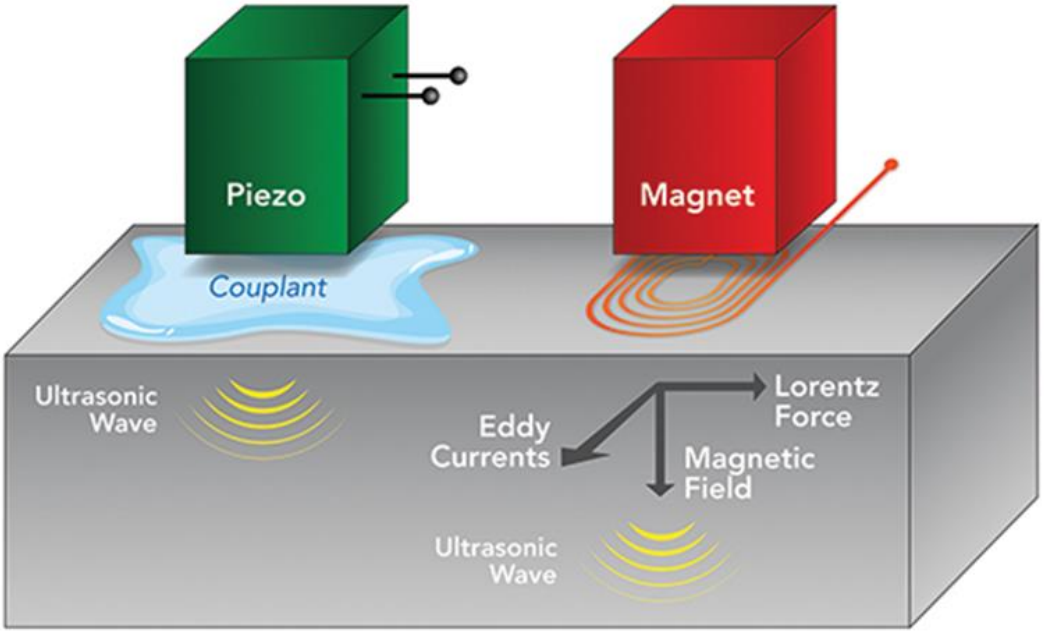

Figure 2.12 Comparison of a piezoelectric ultrasonic sensor and an EMAS [86].

2.3.4 Nanocomposite-based Piezoresistive Sensors

Driven by the recent advances and technological break-throughs in nanomaterials, a great deal of effort has been dedicated to develop functionalized nanocomposites to accommodate specific structural or functional requirements, which has blazed a trail for new generations of human-machine interfaces including sensing devices [87-91]. A variety of carbon nanofillers, represented by graphene and multi-walled carbon nanotubes, are readily available, combing which with polymers leads to

nanocomposites with the merits of both the nanofillers and polymers such as low density, good flexibility, environmental and chemical stability, along with improved electrical and mechanical profiles.

Central to the interest in using nanocomposites to develop sensing devices is the piezoresistive strain sensors [92]. Representatively, Spinelli *et al*. fabricated a nanocomposite compound with multi-walled carbon nanotubes and structural thermosetting epoxy resin, and demonstrated its use in SHM [93]. Qin *et al*. reported a type of graphene/PI nanocomposites that showed enhanced sensitivity to structural deformation under compression, bending, stretching and torsion (Figure 2.13(a)) [94]. Wu *et al*. designed piezoresistive strain sensors consisting of vertical graphene nanosheets that were arranged in a maze-like network and sandwiched between two polydimethylsiloxane substrates, and the sensors presented good stretchability, excellent linearity and high sensitivity to dynamic strains when compared with conventional metal-foil strain sensors [95]. Qiu *et al*. fabricated graphene-based cellular elastomers with reduced graphene oxide (rGO), and thus-produced elastomers could provide instantaneous and high-fidelity electrical response to dynamic pressures up to 2 kHz [96]. Liu *et al*. produced graphene oxide (GO)/graphene resistive pressure sensors, with proven capability of responding to transient signals up to 10 kHz (Figure 2.13(b)) [97]. These studies are among pioneering explorations in recent years, which have affirmed the capability of graphene-based nanocomposites in sensing dynamic strains, and paved a solid path leading to flexible, functional devices for acquiring high frequency ultrasonic wave signals.

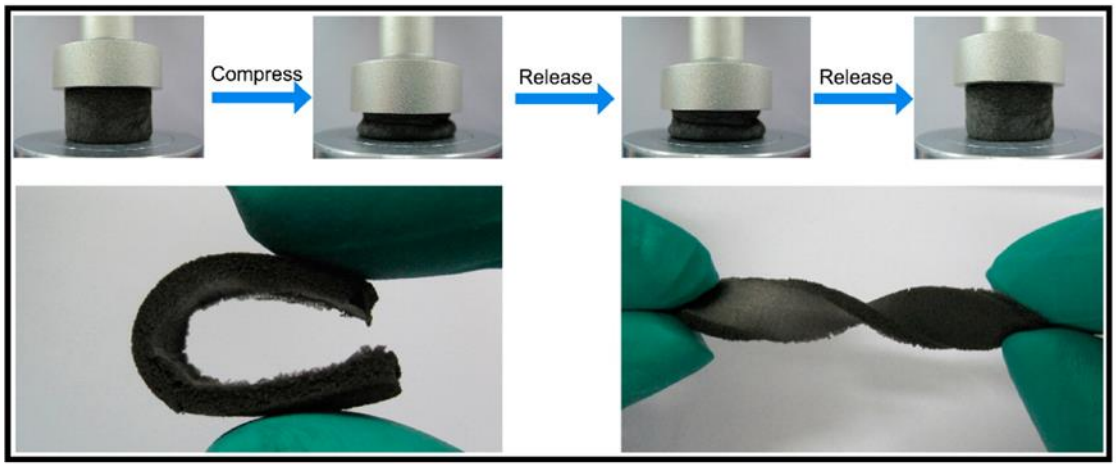

(a)

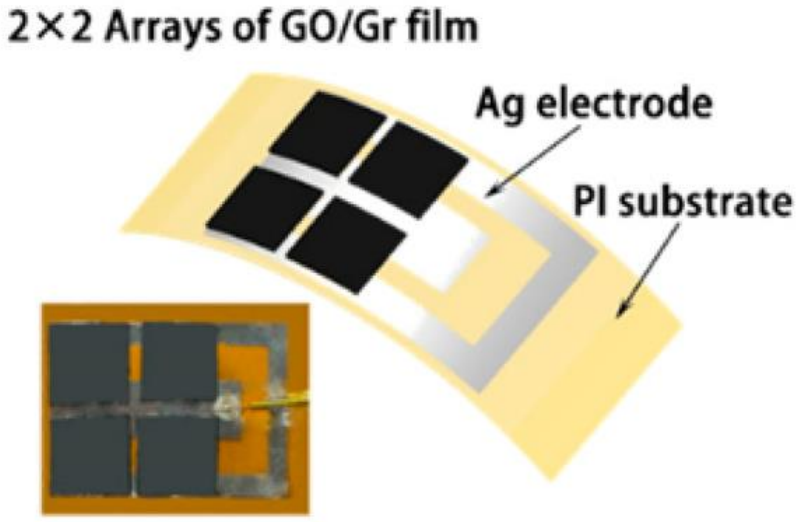

(b)

Figure 2.13 (a) Flexible graphene/PI nanocomposite foam strain sensors [94]; and (b) GO/graphene resistive pressure sensors [97].

In recent years, a new genre of nanocomposite-inspired sensors, have been developed and fabricated, with proven effectiveness in faithfully perceiving dynamic strains with a broad frequency bandwidth, from static strain, through medium-frequency vibration, to high-frequency ultrasonic waves up to 400 kHz [16, 98-100]. Under acousto-

ultrasonic wave-induced strains, quantum tunneling effect generated in the formed nanofiller conductive network of the sensors induces a dynamic alteration in the electrical conductivity and thus the piezoresistivity of the sensors, endowing the sensors with capacity in perceiving acousto-ultrasonic wave signals.

This type of sensors can be sprayed to various structural surfaces [17, 101], and further be networked for implementing acousto-ultrasonic wave-based passive or active SHM. Although the fabrication of such sensors using manually manipulated approaches such as spray coating is facile and cost-effective, the manual manipulation of spray coating lacks controllability and automaticity, which may incur discrepancy among individual sensors. Such a drawback cannot be neglectable in high-precision measurement applications, in particular when a batch of such sensors are needed to configure sensor networks at a large scale in SHM applications.

2.4 Additive Manufacturing in Electronic Device Fabrication

The past decade has witnessed the rapid development of AM techniques, and now AM has been a major approach for manufacturing electronics including sensing devices. Ink-based material jetting AM is capable of directly printing solution-processed functional inks onto substrates with a spatially controlled manner, and has gained increased preference for large-scale fabrication of flexible electronics. In this section,

ink-based AM techniques for developing innovative electronic devices are summarized, and fundamentals of inkjet printing are introduced.

2.4.1 Ink-based Additive Manufacturing

Figure 2.14 illustrates various ink-based AM techniques, as represented by spray coating, inkjet printing, aerosol jet printing, direct ink writing, and embedded printing [15]. Being the most cost-effective and convenient method, the airbrush spray coating deposits inks directly onto substrates under compressed gas flow, and is widely utilized to produce films [102]. Other approaches of spray coating consist of ultrasonic spray deposition [103] and electrospray deposition [104], to name a few. Inkjet printing renders ink droplets to be spatially jetted at designated positions by an applied pressure through the printhead [105]. The fundamentals of inkjet printing are to be introduced in detail in the next section. For aerosol jet printing, the functional inks are firstly atomized by the aerosol actuator, and then the aerosol beam is jetted by gas flow onto substrates with desired patterns [106]. Aerosol printing techniques are feasible for inks with high viscosity up to 2500 cP, while direct ink writing is capable of printing semisolid materials in a layer-to-layer manner [107]. Embedded three-dimensional (3D) printing is a combination of fabrication and packaging, allowing viscoelastic functional inks to be directly deposited into an elastomeric polymer matrix [108].

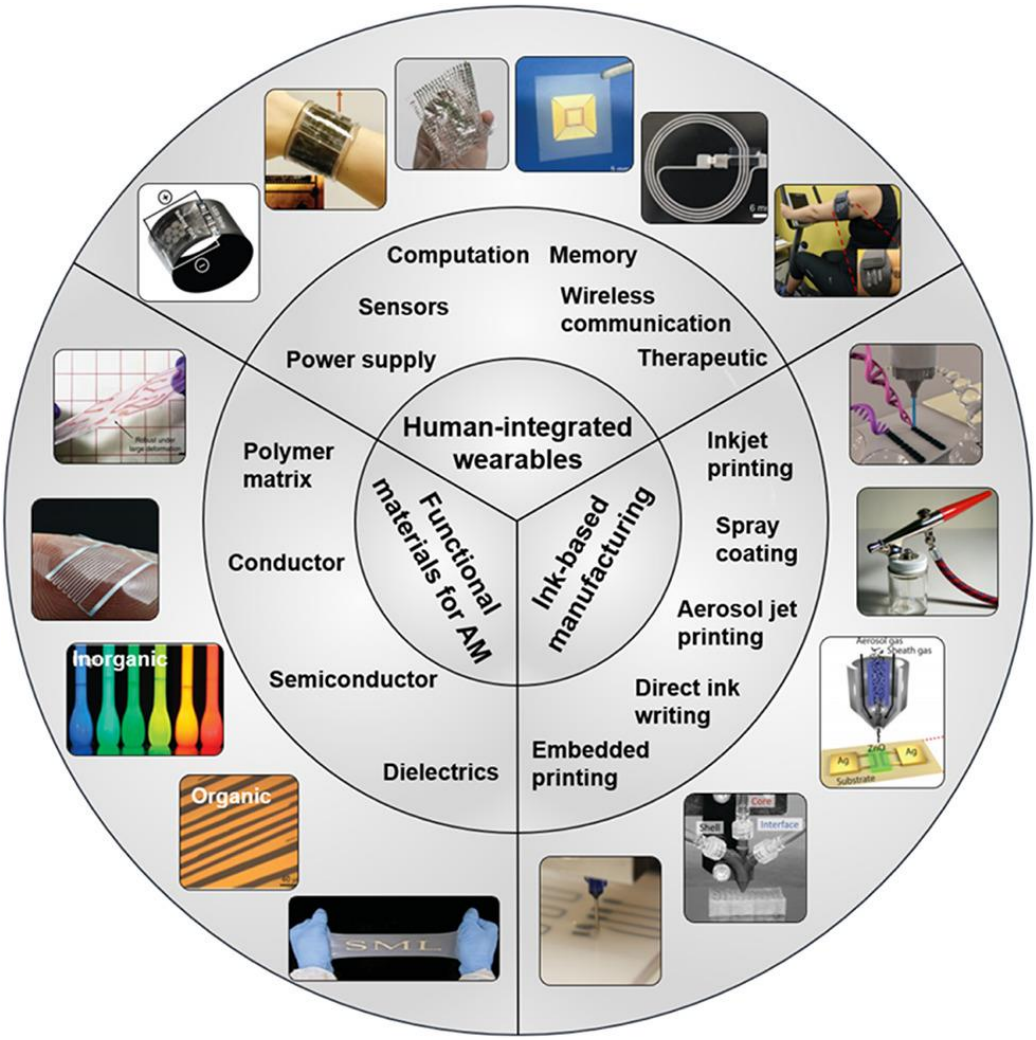

Figure 2.14 A summary of Ink-based AM techniques [15].

2.4.2 Fundamentals of Inkjet Printing

Amongst diverse options of AM, the inkjet printing has gained prominence towards fabrication of electronic devices in a large-scale and cost-effective manner. Being a computer-aided, and drop-on-demand AM approach, the inkjet printing features versatility, simplicity, controllability, automaticity with high precision yet low cost. When used for fabricating electronic devices, inkjet printing makes it possible to customize the device patterns, by precisely regulating the placement of picolitre volumes of ink droplets [18, 19].

Inkjet-printed sensors take advantages of good flexibility, light weight, and ease of processability. A broad range of electronic devices have been developed using inkjet printing, showing enhanced properties and performance when compared against those prepared with conventional manufacturing approaches. Amid successful paradigms are strain gauges [109], transistors [110, 111], humidity sensors [112, 113], large-area thermoelectric devices [114, 115], solar cells [116, 117], radio frequency identification (RFID) devices [118, 119], and battery electrodes [120, 121], to name a few.

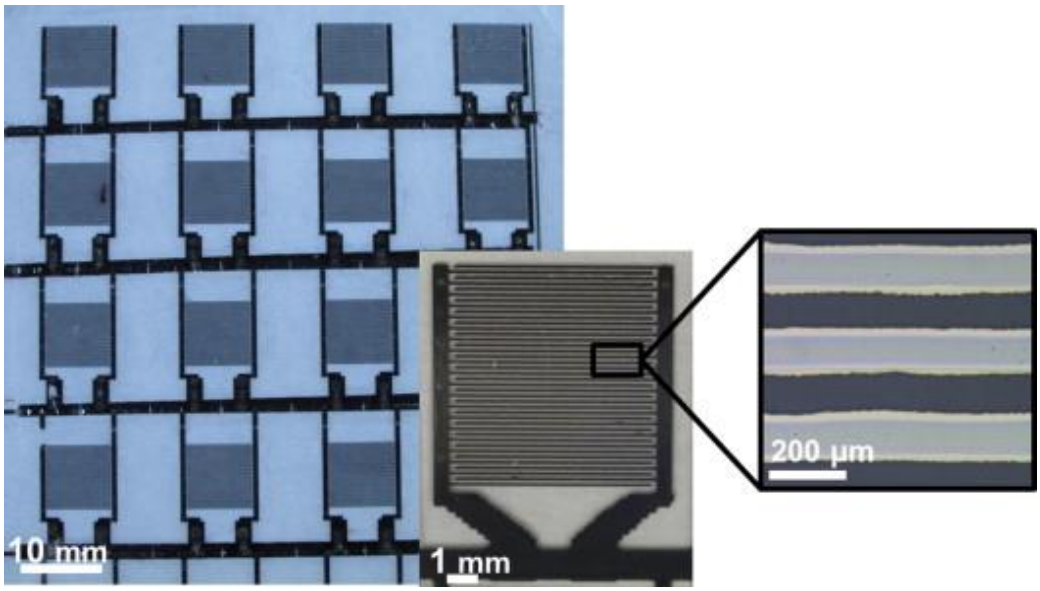

(a)

Figure 2.15 (a) Inkjet-printed interdigitated electrode capacitors [113]; and (b) inkjet-printed thermoelectric devices [114].

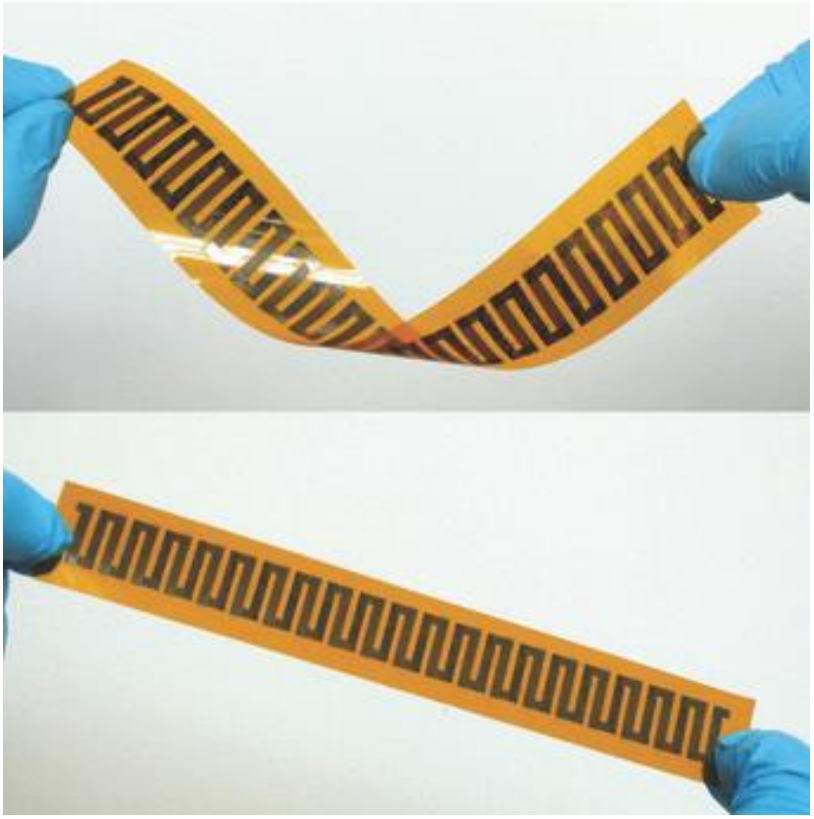

(b)

Figure 2.14 *Cont.*

Generally, inkjet printing can be classified in two main categories, *i.e.*, continuous inkjet printing and drop-on-demand inkjet printing. Continuous inkjet printing generates continuous droplet streams, and unwanted droplets are deflected by electrical field and then recycled, while drop-on-demand inkjet printing only generates the required individual droplets [122]. In the continuous inkjet printing process, as though unwanted inks can be recycled, the exposure of inks to the ambient environment may pose threat to the ink functionality and stability [123]. When compared with continuous inkjet printing, drop-on-demand inkjet printing can effectively prevent potential waste of inks. For drop-on-demand inkjet printing, ink droplets are formed and ejected by vapor bubbles (namely thermal drop-on-demand

printing) or piezoelectric actuators (namely piezoelectric drop-on-demand printing) with specific jetting waveforms and frequencies, which is based on the working principle of the inkjet printer nozzles, as exhibited in Figure 2.16.

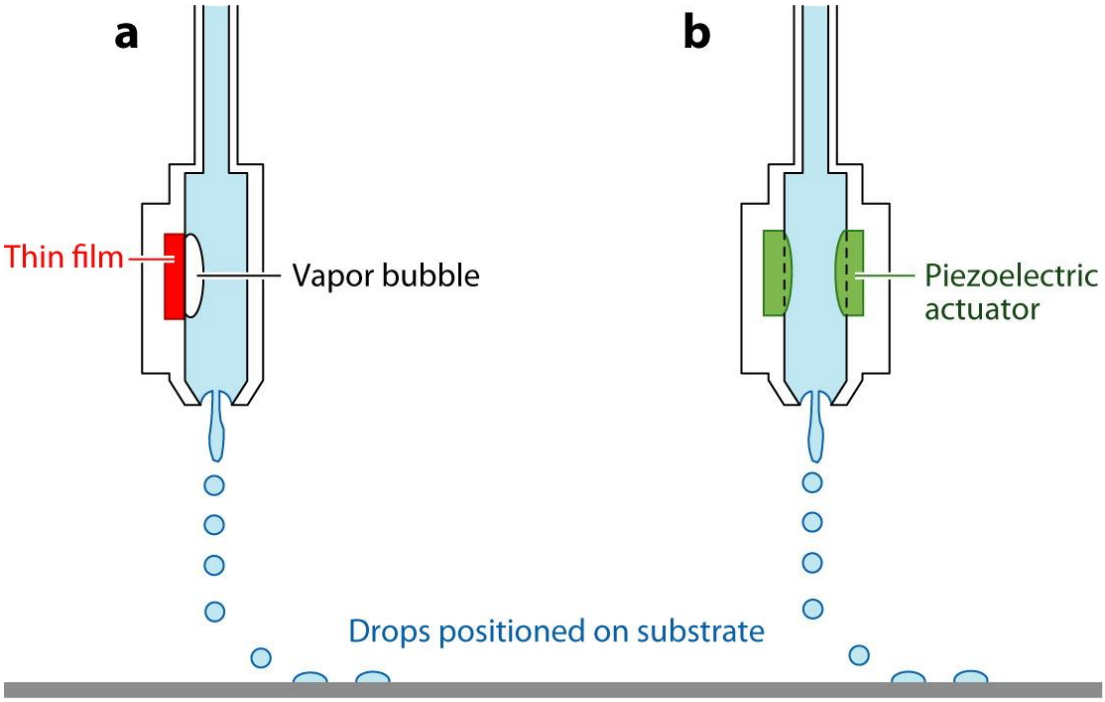

Figure 2.16 A comparison between thermal and piezoelectric drop-on-demand inkjet printing [123].

It is also noteworthy that when the ink droplets are squeezed out from the nozzle orifice, the non-Newtonian rheological properties of ink droplets are likely to block and clog the inkjet printing nozzle [124]. The functional inks for inkjet printing should thus be rigorously designed and optimized, and the ink printability can be ascertained by a figure of merit Z [125]

$$Z = \frac{(\gamma \rho d)^{1/2}}{\eta}, \tag{2.25}$$

where η is the viscosity of the ink, γ the surface tension and ρ the density of the ink,

and d the printer nozzle diameter. If $Z < 1$, viscous dissipation of the ink prevents drop ejection from the nozzle, while ink droplets are accompanied by unwanted satellite drops when $Z > 14$. Only when Z is in a range of (0, 10) [126] or (4, 14) [127], stable ink droplets can be formed.

2.5 Summary

In this chapter, basic concept of SHM is briefly recapitulated. Acousto-ultrasonic wave-driven SHM provides a strategy to implement *in situ* and real-time surveillance of the health status of engineering structures. The propagation characteristics of Lamb waves, as well as the principles of damage identification of Lamb wave-based SHM are introduced. As the most rudimentary and prominent building block of SHM, prevailing sensors for SHM are summarized in this chapter, including piezoelectric sensors, fibre optic sensors, EMASs and nanocomposite-based piezoresistive sensors. The review of sensors addresses their sensing mechanisms, and pros and cons.

In brief, piezoelectric ceramic wafers with excellent sensing performance are rigid and unwieldy, presenting difficulty conforming to a curved surface potentially, and may add extra weight penalty to the host structures; Lightweight and flexible piezoelectric polymer sensors render good sensing coverage over an extended area, and can adapt to curved surfaces, but their response intensity of acousto-ultrasonic wave signals of high frequency is inferior; Fibre optic sensors are of good immunity to electromagnetic interference with long lifespan, but fibre optic sensors are brittle, and installation of fibre optic sensors may cause degradation to structural strength; Employing EMASs

in SHM can effectively avoid the problem of sensor-structure coupling, and sensor exfoliation, but the use of EMASs is constrained to specific materials; New breeds of nanocomposite-based piezoresistive sensors pave a new solid path to the development of sensors for SHM, but the exploration is still in its preliminary stage, and there are still great opportunities to improve the design, manufacturing process, responsivity, and sensing bandwidth of nanocomposite-based sensors.

As an emerging and prominent technique in fabricating novel electronic devices, ink-based AM is briefly introduced, and emphases are placed on the fundamentals of inkjet printing, including the categories, principles, and ink printability of inkjet printing. Driven by the state of the art reviewed above, developing innovative nanocomposite-based thin film ultrasound sensors for acousto-ultrasonic wave-driven SHM using direct-write inkjet printing becomes the main objective of this PhD study.

CHAPTER 3

Inkjet-printed CB/PVP Ultrasound Sensors

3.1 Introduction

Ultralight, flexible, CB/PVP thin film ultrasound sensors are manufactured using drop-on-demand inkjet printing approach which deposits the integrated ink directly on flexible substrates (PI films). The rigorously designed ink, made of CB and PVP, is morphologically optimized towards enhanced stability and printability. The inkjet-printed CB/PVP thin film ultrasound sensors feature a thickness of only ~1 μm that is remarkably thinner than a hot-pressed CB/PVDF senor (~200 μm) that developed before by the group to which the candidate belongs. The new sensors show additional merits including remarkably enhanced sensitivity and signal stability when used to acquire broadband acousto-ultrasonic wave signals. Notably, conductivity and sensitivity of the sensors can be fine-tuned by precisely controlling the number of printed passes (*i.e.,* printed layers), endowing the sensors with a capacity to resonate to strains of a particular frequency. The inkjet-printed CB/PVP sensors have proven responsivity to dynamic strains in a broad frequency range from quasi-static strain, through medium-frequency vibration, to acousto-ultrasonic waves up to 500 kHz.

3.2 Ink Preparation and Sensor Fabrication

3.2.1 Selection of Nanofillers and Matrix

To develop inkjet-printed sensors responsive to broadband dynamic strains, CB is chosen as the nanofiller and PVP as the polymer matrix to prepare a nanocomposite hybrid. Such selection is made based on twofold consideration:

(i) CB, the nanofiller with a low-aspect ratio yet high specific surface area can be evenly dispersed in the polymer matrix with mitigated aggregates and reduced amount of nanoparticle entanglement. Such a trait is beneficial to minimize the blockage and clogging of the inkjet printing nozzle [99, 128, 129]. It is also conducive to the initial formation of a conductive network in the hybrid and the trigger of tunneling current when the nanofiller contents reach their percolation threshold [16];

(ii) PVP is soluble in both aqueous and organic solvents, and it can be utilized as a stabilizer for nano-scalar dispersion owing to its amphiphilic groups [114]. PVP presents desirable adhesive, cohesive, and dispersive properties with good wettability, enhancing the stability of the fabricated nanocomposite inks.

3.2.2 Ink Preparation and Substrate Pre-treatment

The creation of ink droplets in the micro-sized capillaries of the nozzle deserves particular attention, and property optimization of the CB/PVP hybrid is a key issue in the printing process (to be detailed in subsequent sections). Bearing that in mind, the

nanocomposite ink is formulated by mixing CB powder (CABOT® Black Pearl 2000, morphology of which can be referred to [130]); average particle diameter: 30 nm; 0.28 g) with PVP (PVP K-30, Sigma-Aldrich; 0.56 g) in N-methyl-2-pyrrolidone (NMP, J&K Scientific; 40 mL), to which 0.08 g sodium dodecylbenzenesulfonate (SDBS, Sigma-Aldrich) is added as surfactant, to stabilize the dispersions of CB and decrease the surface tension of the ink. The mixture is mechanically stirred at a room temperature (25 ºC) for 2 hours at 400 rpm and sonicated for 1 hour in an ultrasonic bath (Brandson® 5800 Ultrasonic Cleaner; 40 kHz), to warrant even dispersion of CB powder in PVP matrix. Before being filled into the cartridge, the as-prepared CB/PVP dispersions are filtered through a 0.45 μm-diameter PVDF micropore sieve to screen larger CB particle agglomerates. Via such a process, the physical properties and parameters of the ink are regulated to best fit the inkjet printing process. This series of process leads to stable ink droplets, with minimizes possibility of nozzle blockage and clogging.

PI films with a thickness of 25 μm are used as the substrate, on which the nanocomposite hybrid is inkjet-printed, owing to the desirable resistance to high temperature of the PI films and their good flexibility. Printed on the flexible PI films, the sensors can adapt to a curved structural surface. PI films are pre-treated using a plasma cleaner (PDC-002, Harrick Plasma, Inc.), and in the pre-treatment O_2 plasma is generated at a radio frequency power of 30 W and 450 mTorr for 2 minutes, to enlarge the surface energy of the films and consequently improve wettability of the ink printed on the films. The prepared ink is then directly deposited on the surface of a PI film.

3.2.3 Sensor Printing

The inkjet printing is implemented on an inkjet printing platform. The platform consists mainly of a PiXDRO LP50 inkjet printer (OTB Solar-Roth & Rau), Figure 3.1, equipped with a DMC-11610 cartridge (Dimatix-Fujifilm Inc.) which produces droplets with a volume of 10 pL, through 16 parallel piezoelectric actuated nozzles with a diameter of 21.5 μm for each. The pattern of the sensor is designed to be a rectangle, with a dimension of 10.0 mm in width and 20.0 mm in length.

Figure 3.1 PiXDRO LP50 inkjet printer.

The PVDF micropore sieve-filtered ink (1.5 mL) is filled in the cartridge, and the piezoelectric actuated nozzles, under a driving voltage of 28 V, print the ink on the pre-treated PI films with a 4 kHz printing frequency. The printing resolution, calibrated by

the number of ink drops printed along a line of 25.4 mm (1 inch), is set as 500 dpi in both the cross-scan and in-scan directions, so that the drop spacing is ~50 μm in both directions. The plasma-treated PI films are fixed on a substrate plate with a substrate vacuum pump, and the film is heated to 45 ºC during the printing process, to gain a solution evaporation rate that is higher than that rate under a room temperature (so as to prevent the lateral flow of the printed ink and create a reduced "coffee-stain" effect [131]). Such printed sensors are displayed in Figure 3.2.

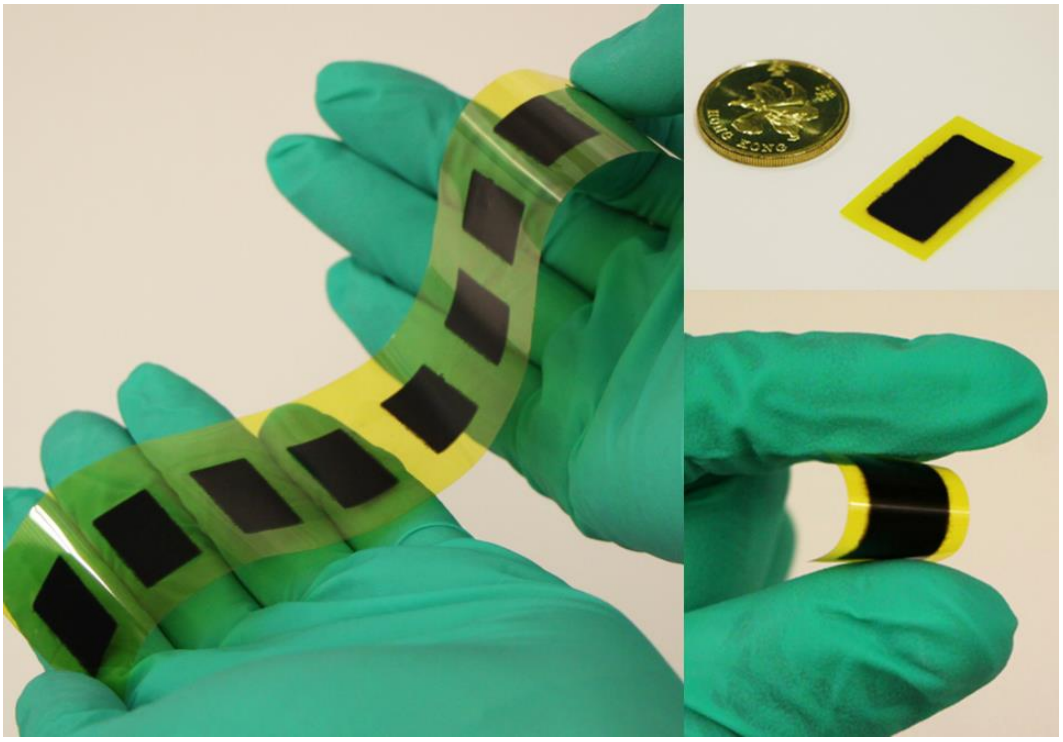

Figure 3.2 Pictured CB/PVP hybrids that are inkjet-printed and directly deposited on PI films.

3.3 Material Morphological Characterization

3.3.1 Inks and Substrates

The density of the CB/PVP nanocomposite ink, estimated by weighing a certain volume of the filtered ink using a pipette, is 1.12 g cm^{-3}. A viscosimeter (NDJ-5S, Lichen Technology) is used to measure the viscosity of the ink, and 0 # rotor is chosen with a rotation speed of 6 rpm (for measurement of liquids with viscosity lower than 10 mPa s). The surface tension measurement of the ink is implemented with a force tensiometer (KRÜSS® K100). The force tensiometer is calibrated by de-ionized water before measurement. A platinum loop is immersed into the liquid and then withdrawn, and the maximum of pull-out force is recorded. To evaluate the effect of plasma treatment on the PI film substrates, as well as the surface matching between the substrates and the inks, 1 μL deionized water with ethylene glycol (EG, Sigma-Aldrich) are dropped through a stainless needle respectively onto the plasma-treated and untreated PI films for comparison, and the contact angles in two cases are measured with an imaging system (ramé-hart, Inc.). The surface energy of the PI films is calculated in terms of the interfacial energy and the measured contact angles of water and EG using DROPimage software (ramé-hart, Inc.).

To warrant good printability of the CB/PVP ink, both the physical properties and fluid mechanics of the ink are worthy of optimization. During the printing process, the viscosity η, surface tension γ, density ρ of the ink, and the nozzle diameter d, are key parameters controlling the quality of liquid drops. With these parameters, dimensionless physical constants, such as the Reynolds (R_e), Weber (W_e) and

Ohnesorge (O_h) numbers of the ink, can be ascertained by [123]

$$R_e = \frac{v\rho d}{\eta}, \tag{3.1}$$

$$W_e = \frac{v^2 \rho d}{\gamma}, \tag{3.2}$$

$$O_h = \frac{\sqrt{W_e}}{R_e} = \frac{\eta}{(\gamma\rho d)^{1/2}}, \tag{3.3}$$

where v signifies the drop velocity. A figure of merit, Z – the reciprocal of O_h, is used to identify the appropriateness of the ink for printing as [125]

$$Z = \frac{1}{O_h} = \frac{(\gamma\rho d)^{1/2}}{\eta}. \tag{3.4}$$

It has been demonstrated that the fluid is printable only when $Z > 2$ [132], and a stable droplet can be formed when Z is in a range of (0, 10) [126] or (4, 14) [127], which warrants the single-drop formability, the minimum stand-off distance, position accuracy, and maximum allowable jetting frequency. In the case that $Z < 1$, viscous dissipation prevents drop ejection from the nozzle, while droplets are accompanied by unwanted satellite drops when $Z > 14$.

In this study, η of the CB/PVP ink is measured to be 2.42 mPa s with the viscometer. Knowing γ = 43.9 mN m^{-1} and ρ = 1.12 g cm^{-3}, Z value of the ink is calculated to be 13.5 according to Equation (3.4), with a nozzle diameter of 21.5 μm. Such a value of Z falls in the optimal range of [1, 14], indicating that the CB/PVP ink can form stable droplets. This can further be demonstrated in the droplet screenshot, Figure 3.3, which is captured with a stroboscopic camera equipped on the inkjet printer. Figure 3.3 compares the droplets generated by five successive nozzles of the cartridge, all of

which are observed stable without any tail or satellite drop.

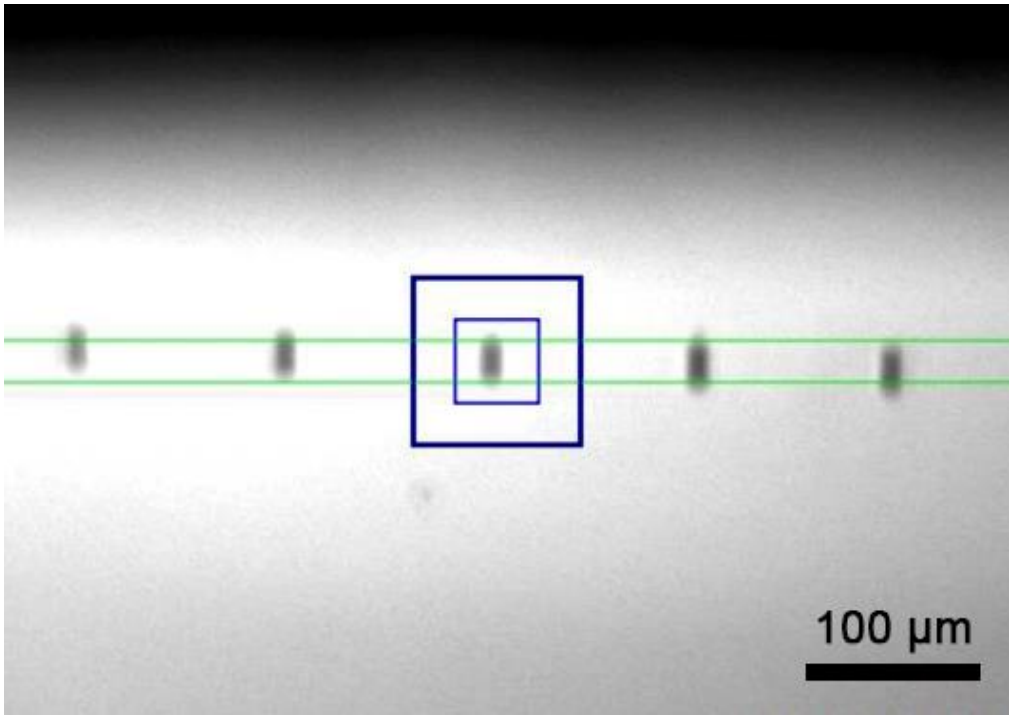

Figure 3.3 CB/PVP ink droplets generated by five successive nozzles of the cartridge.

For the polymeric substrates, the low surface energy makes it challenging for a printed droplet to form a uniform layer because the droplet tends to bead up [133]. Good adhesion can be achieved by using a swelling polymer layer, a porous layer or a roughened surface [134], whereby a higher surface energy of the substrate can be obtained. Figure 3.4 compares the contact angles of water drops on the PI film substrate before and after plasma pre-treatment, to observe a decrease in the angle from 48º to 7º – suggesting improved wettability of the printed CB/PVP ink on the PI films upon plasma treatment. The surface energy is calculated to increase from 50.62 (before plasma treatment) to 86.93 mJ m^{-2} (after plasma treatment). The imide groups in the

PI films are modified to secondary amide and carboxylate groups after being exposed to O_2 plasma [135], and the formation of these polar components increases the surface energy.

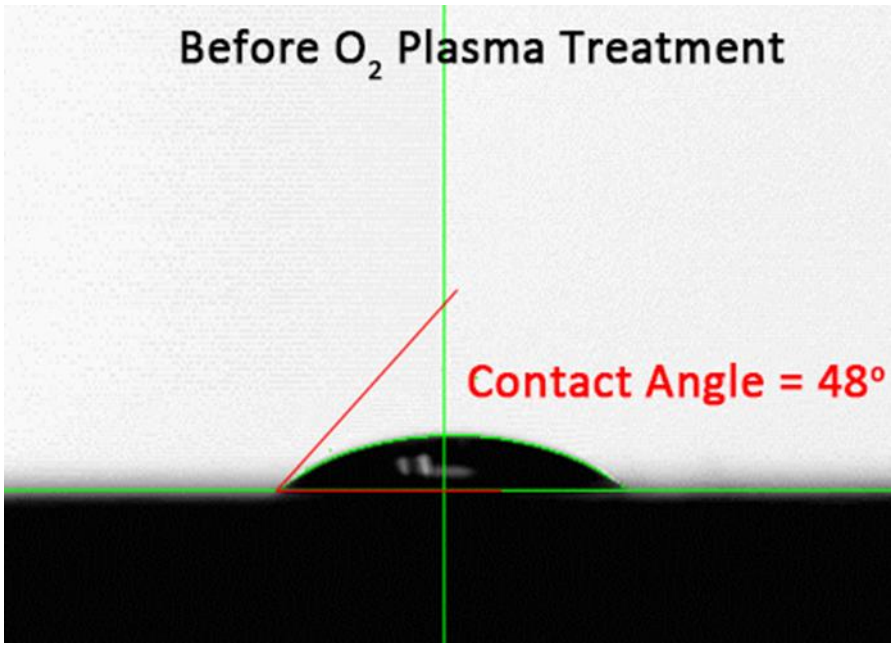

(a)

Figure 3.4 Contact angle of water drops on PI film substrates: (a) before and (b) after O_2 plasma treatment.

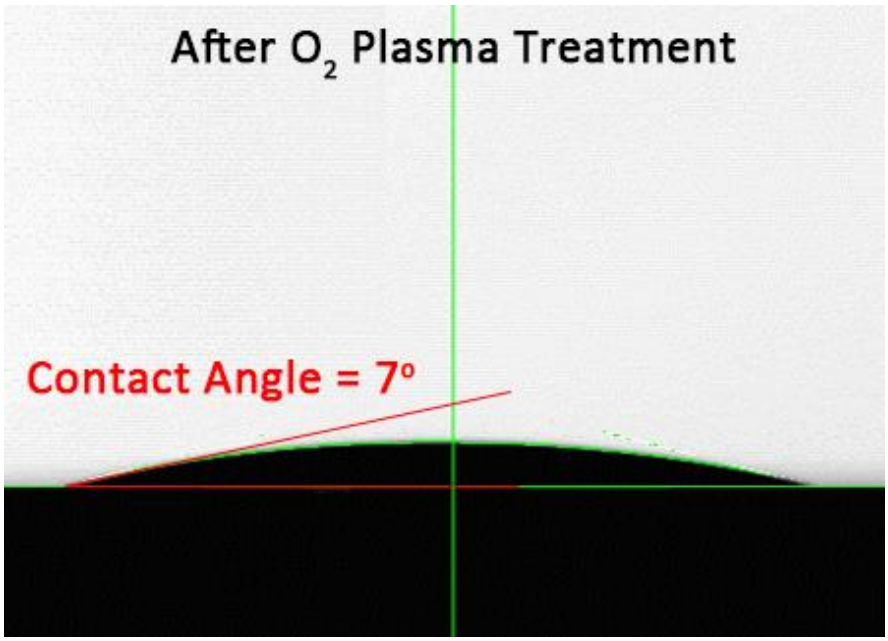

(b)

Figure 3.4 *Cont.*

3.3.2 Inkjet-printed CB/PVP Ultrasound Sensors

With the same printing approach, a series of sensors are comparatively fabricated, featuring different numbers of printed passes (6, 9, 12 and 15, respectively), whereby to determine the most suitable number of printed passes leading to high sensitivity of the sensor to high-frequency dynamic strains. The thickness of each sensor is measured with a surface profiler (DektakXT Surface Optical Profiler, Bruker®). Morphological characterization of the printed sensors that are sputter-coated with a thin layer of gold is performed on a scanning electron microscopy (SEM) platform (TESCAN® Vega 3). The electrical resistance (R) of each sensor is measured using a four-probe method with a dynamic digital multimeter (Keithley® DMM 7510). The measurement is conducted with the "4-wire resistance" mode of the multimeter, and the four probe points are equally arranged in a line on the sensor. The distance between two

neighbouring measurement points is 4.0 mm and the voltage-to-current ratio of the inner two probe points is calibrated by the multimeter. R is calculated according to the voltage-to-current ratio with a correction factor of 2.3532 [136]. The conductivity (σ) is calculated via $\sigma = l/(R \cdot A)$, where l and A are the length of the sensor and effective cross-section area of the sensor, respectively. With R, the relationship between σ of a sensor and the number of printed passes can be ascertained. Raman spectra are obtained to show the microstructural properties of the sensors at a room temperature, with a Raman spectrometer (LabRAM HR 800, HORIBA®) (a 488 nm excitation laser wavelength and 50 mW laser power in the range of 1100-2000 cm^{-1}).

No obvious discrepancy in the morphological characteristics can be observed among the inkjet-printed sensors of different printed passes (6, 9, 12 and 15, respectively), and Figure 3.5 shows a typical surface pattern of the sensor of 15 layers. The morphological characteristic of the sensors is observed to be of good homogeneity. As can be seen from the SEM image, the CB/PVP aggregates densely and evenly distribute, creating a highly consolidated nanostructure that is a building block to form a uniform electrical-conductive network in the sensor.

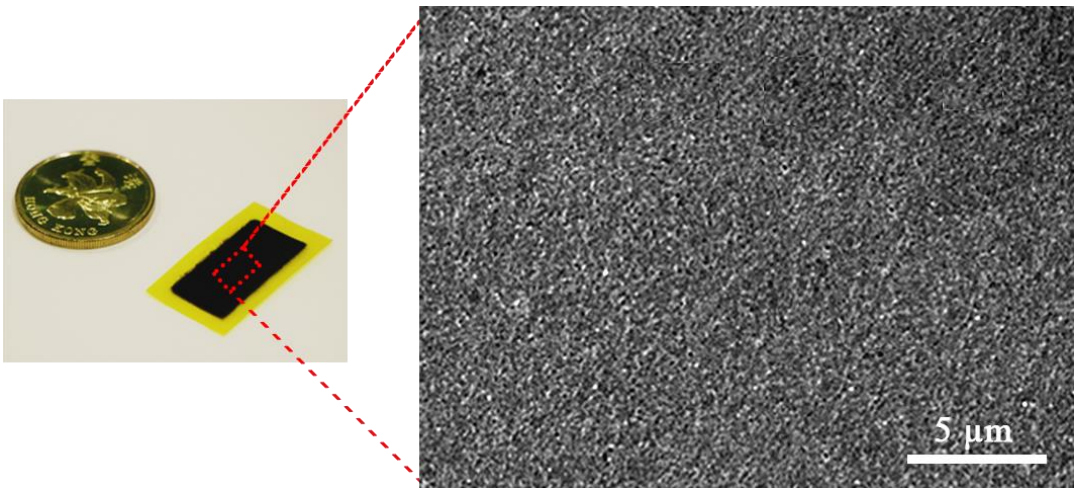

Figure 3.5 SEM (12.00 k× magnification) image of the inkjet-printed CB/PVP sensor of 15 printed passes.

To further examine the geometrical uniformity and consistency of the printed sensors, the sensor thickness against the number of printed passes is presented in Figure 3.6(a). It is apparent that the average sensor thickness increases linearly with the number of printed layers (the red line). Exemplarily, the average thickness of the sensors of 6 layers is 410 nm only and that of 15 layers is 1.3 µm, both of which are much thinner than that (~200 µm) of the nanocomposite sensors manufactured using conventional melt-mixing and pressing [16, 99]. The black curve in Figure 3.6(b) argues an increase in the measured electrical conductivity of the sensors with the number of printed passes. It is noteworthy that from 12 to 15 layers, the electrical conductivity witnesses a remarkable leap from 0.35 S m^{-1} to 0.63 S m^{-1}, which can be attributable to the decrease of the roughness-to-thickness ratio of the sensors with an increase in the layer number [137]. As the ink for fabricating the nanocomposite sensor is rigorously designed and optimized, and the manufacturing process is precisely controlled, the electrical conductivity of all the printed sensors, regardless of the number of printed passes, is

within the regime of the percolation threshold of the nanofiller [138]. At the percolation threshold, the accordingly prepared nanocomposite sensors exhibit the highest sensitivity to external strains (*e.g.*, the strain induced by acousto-ultrasonic waves), as a result of the tunneling current in the conductive network induced by particulate movement [11].

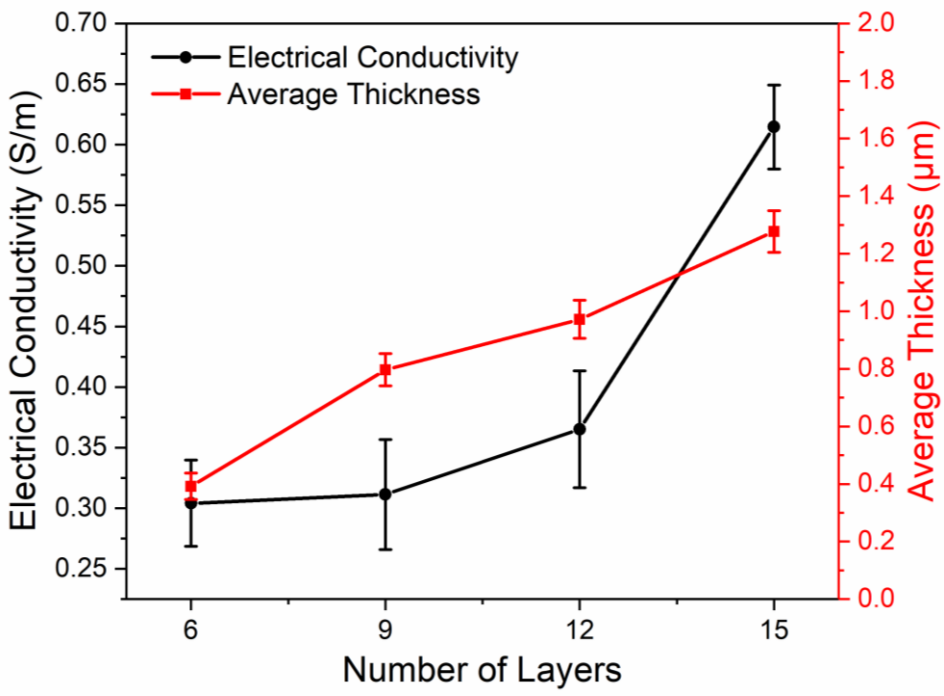

(a)

Figure 3.6 (a) Average sensor thickness (red line) and electrical conductivity of the sensors (black line) with respect to number of printed passes; and (b) Raman spectra of printed sensors of different printed passes.

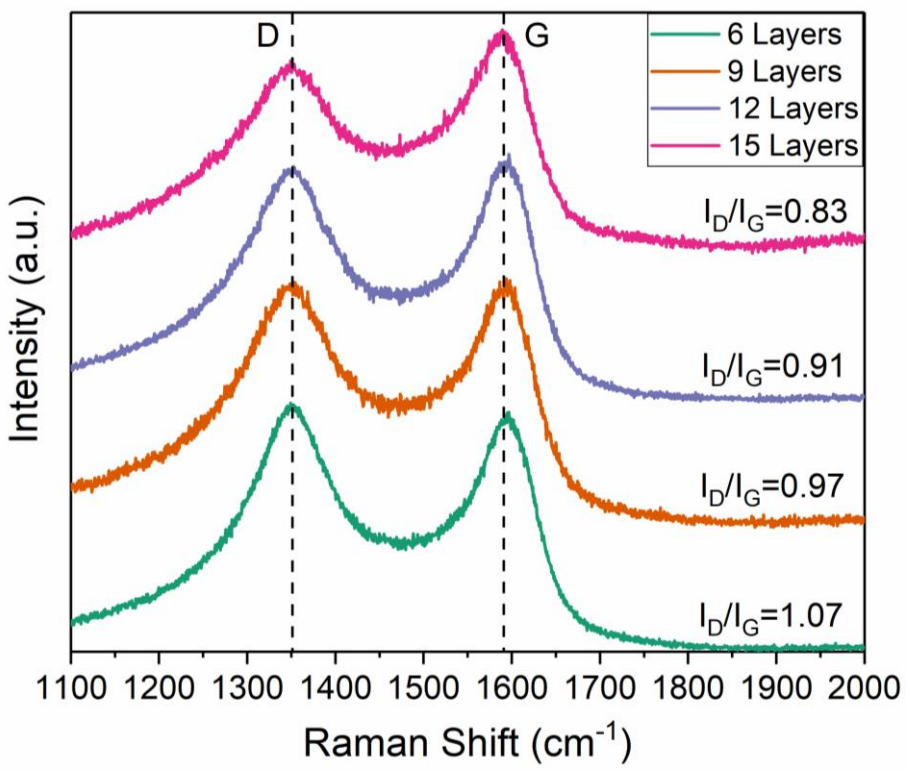

(b)

Figure 3.6 *Cont.*

The primary spherical particles of CB in the nanocomposite ink comprise graphitic and amorphous-like domains, and the graphitic-like domains typically consist of 3-4 turbostratically stacked carbon polyaromatic layers [139]. The obtained Raman spectra of the printed sensors of different passes are shown in Figure 3.6(b), in which two peaks are observed, namely, the *D* peak at ~1355 cm^{-1} and *G* peak at ~1586 cm^{-1}. The former peak indicates the structural defects ascribed to the structural edge effect, while the latter asserts the tangential mode vibration of the *C* atoms in the graphite structure [140]. It is the structural defects in the graphite structure that affects the electrical conductivity of the conductive network formed in the printed sensors. For the nanocomposite sensors, if the intensity ratio of the *D* peak and *G* peak (I_D/I_G) calculated from the Raman spectra is exceptionally high, a large quantity of intrinsic

microstructural defects will be present in the sensors, indicating a low local conductivity which is not conducive to electron movement; on the other hand, an exceptionally low I_D/I_G will result in a highly dense and saturated conductive network, and under that circumstance the nanofiller has little tunneling effect when the sensors are subject to external strains.

Subsequently, I_D/I_G of the printed sensors is calculated from the Raman spectra, and exemplarily it is 1.07 when the sensors have 6 printed passes. I_D/I_G of the printed sensors decreases with the printed passes, and it is 0.83 for the sensors of 15 layers. A lower intensity ratio suggests a weaker *D* peak induced by the defect and thus a better electrical-conductive carbon aromatic structure (this resulting in a more compact conductive network in the sensor), and this speculation agrees with the increasing tendency of the electrical conductivity measured and shown in Figure 3.6(a). For the sensors of different printed passes (6, 9, 12 and 15, respectively), I_D/I_G varies from 0.83 to 1.07, while the electrical conductivities are within the regime of percolation threshold, indicating that I_D/I_G of the printed sensors should be kept at around 0.95, and tunneling effect can be triggered among CB particles in the conductive network when the sensors are subject to dynamic strains.

3.4 Sensor Response to Dynamic Strains

The piezoresistive characteristics of the inkjet-printed sensors are interrogated using electro-mechanical analysis and the responsive capability of the sensors is calibrated in a broad frequency range from quasi-static strain (uniaxial and mixed (uniaxial +

flexural) mode), through medium-frequency vibration, to acousto-ultrasonic waves up to 500 kHz.

3.4.1 Tensile Strain (quasi-static)

A series of epoxy dogbone samples (2.0 mm thick each) are prepared for quasi-static electro-mechanical analysis, each of which undergoes a uniaxial tensile test on a tensile machine (MTS Alliance RT/50), as shown in Figure 3.7. The speed of the crosshead is set to be 1 mm min^{-1}, while the tensile stress and strain (ε) are calculated according to the applied force, crosshead displacement and specimen dimensions. Surface-glued at the midpoint of each sample is a sensor printed on the PI film, respectively featuring 6, 9, 12 or 15 layers. Each sensor is silver-pasted with a pair of electrodes, and the gap (2 mm) between the two electrodes is the effective sensing area. Electrical resistance of the electrodes is neglectable compared with the resistance of the printed sensor which is of an order of several kΩ [141]. The electrodes are connected to a dynamic digital multimeter (Keithley® DMM 7510) via shielded cables. Using a two-probe method, the electrical resistance (R) of the sensor under the quasi-static loading is real-time measured, as depicted in Figure 3.7. For comparison and calibration, a commercial strain gauge with a gauge resistance of 120 Ω is mounted on the opposite side of the sample, to record the load-induced train simultaneously.

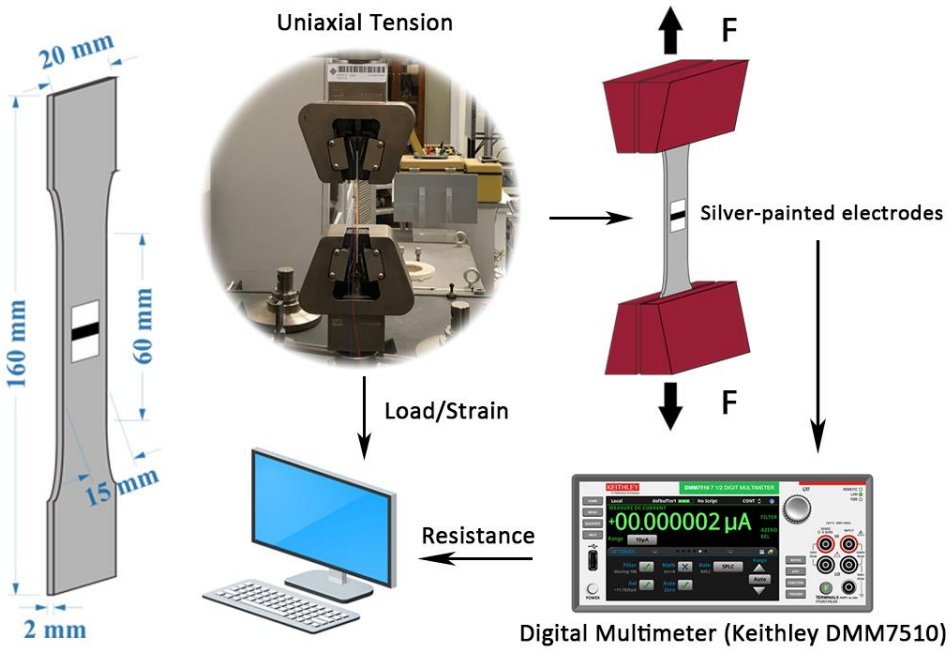

Figure 3.7 Experimental set-up of quasi-static tensile test.

Figure 3.8 shows the normalized change in electrical resistance of the printed sensors of different layers against the applied uniaxial quasi-static loads. The results reveal that the electrical resistance of the sensors increases exponentially with loading. To put it into perspective, the gauge factor (K), a key figure of merit to describe the sensitivity of the sensor, can be calculated as

$$K = \frac{\Delta R}{R_0} / \Delta\varepsilon \,, \tag{3.5}$$

where $\Delta R = R - R_0$, and R_0 is the initial sensor resistance. Using Equation (3.5), the gauge factor of the printed sensors is calculated using linear fitting of all the measured strains from 0.8% to 2.0%. Note that the pre-loading of the tensile machine at the beginning of the test up to 0.8% introduces measurement deviation, and data when the strain is below 0.8% are not included into fitting. As indicated by the fitted results (dash lines in Figure 3.8, the gauge factor of the sensors of 6 layers is 10.7, which is

much higher than that of a commercial strain gauge and also higher than those of the rest of the printed sensors. During the tests, it has been observed that a sensor of fewer printed layers has a higher resistance, and thus a higher gauge factor, a higher resistance change rate and a greater sensitivity to dynamic strains (to be detailed in Section 3.4). The total resistance of the conductive network formed in the prepared CB/PVP nanocomposite ink mainly includes (i) the intrinsic resistance of the conductive CB particles (R_{particle}); (ii) the contact resistance of the conductive CB particles (R_{contact}); and (iii) the tunneling resistance (R_{tunnel}) among adjacent nanoparticles induced by microstrains. The change in R_{particle} can be neglected because of the intrinsic good conductivity of CB particles (compared with the insulating PVP matrix). R_{contact} is mainly attributable to the breakage of electrical-conductive paths in the sensors. As the electrical conductivity of the printed sensors is within the regime of the percolation threshold of the nanofiller, it therefore postulates that the piezoresistive response of the sensors is induced dominantly owing to the change in R_{tunnel}. Under an external strain, the distance between two adjacent nanoparticles alters, leading to the tunneling of charged carriers and a consequent increase in local electrical conductivity, making it possible to generate quantum tunneling effect and consequently leading to the change of R_{tunnel} [142]. R_{tunnel} is described based on a tunneling model [143, 144], as:

$$R_{tunnel} = \left(\frac{8\pi h_{\text{p}} sQ}{3A^2\gamma_t s^2 N}\right)\exp(\gamma_t s), \tag{3.6}$$

$$\gamma_t = \frac{4\pi(2m\varphi)^{1/2}}{h}, \tag{3.7}$$

where h_{p} is the Plank's constant, s the least distance between conductive particles, Q the number of particles forming a single conducting path, A^2 the effective cross-section

of a tunneling current, N the number of conducting paths, m the mass of an electron, and φ the height of potential barrier between two adjacent particles.

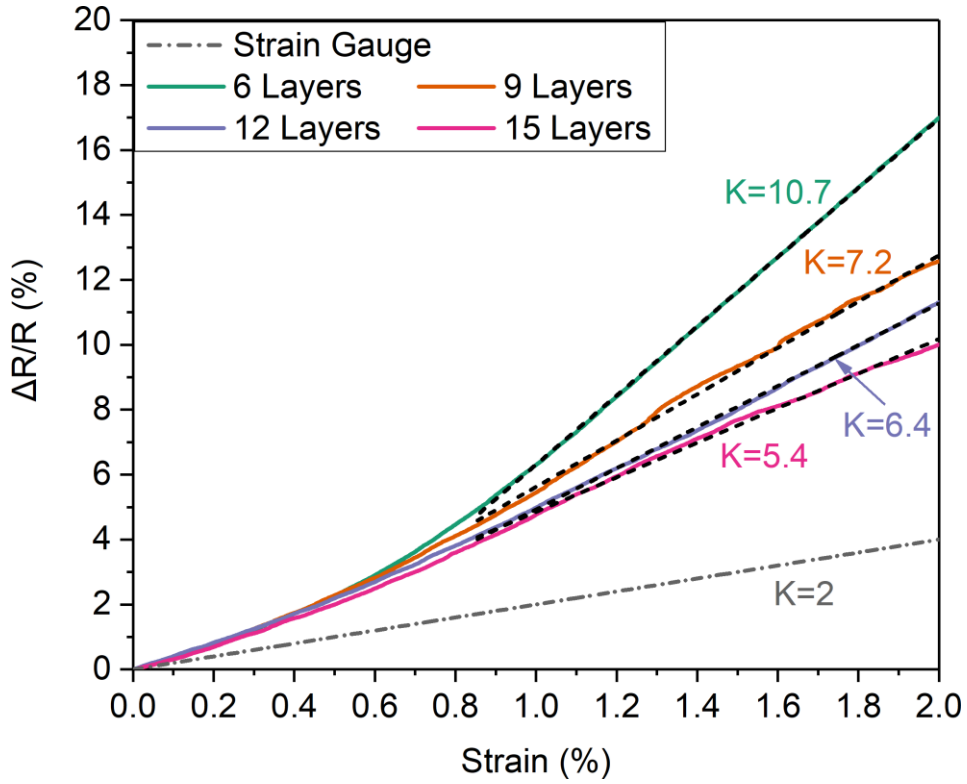

Figure 3.8 Normalized change in electrical resistance of printed sensors of different layers under quasi-static tensile loads.

When an external strain, ε, is applied on the sample, the electrical resistance measured by the sensors changes from s_0 (the initial particle separation) to s (the particle separation under ε), and the destruction of the tunnel-conducting pathway from N_0 (the initial number of tunnel-conducting path) to N [109, 145], as

$$s = s_0(1+\varepsilon), \tag{3.8}$$

$$N = N_0 \exp[-(\alpha_c\varepsilon + \beta_c\varepsilon^2 + \delta_c\varepsilon^3 + \tau_c\varepsilon^4)], \tag{3.9}$$

where, α_c, β_c, δ_c and τ_c are four constants related to the status of conducting path under

ε. Considering the variation of both the particle separation and tunnel-conducting path destruction, the resistance of the sensors changes from R_0 to R, and based on Equation (3.6), the resistance change ratio can be calculated as

$$\frac{\Delta R}{R_0} = \frac{R - R_0}{R_0} = \frac{R}{R_0} - 1 = \frac{sN}{s_0 N_0} \exp[\gamma_t (s - s_0)] - 1. \tag{3.10}$$

Substituting Equations. (3.8) and (3.9) into (3.10) yields

$$\frac{\Delta R}{R_0} = (1+\varepsilon) \exp\{-[(\alpha - \gamma_t s_0)\varepsilon + \beta\varepsilon^2 + \delta\varepsilon^3 + \tau\varepsilon^4]\} - 1. \tag{3.11}$$

Equation (3.11) can be simplified as

$$\frac{\Delta R}{R_0} = (1+\varepsilon) \exp(c_1\varepsilon + c_2\varepsilon^2 + c_3\varepsilon^3 + c_4\varepsilon^4) - 1 \tag{3.12}$$

where c_1, c_2, c_3 and are four constants linked to the resistance change under ε. The linear term c_1 is associated to both particle separation (tunneling gap) and destruction of conducting network, while the values of high-order coefficients c_2, c_3 and c_4 are correlated to the degree of conducting network destruction. These coefficients can be obtained with an ordinary least squares approach [93], and the calculated results for the printed sensors are shown in Table 3.1. Also included in Table 3.1 are the uncertainties of resistance changing ratio (U) which are smaller than 0.1% and the estimate of the coefficients of determination (C^2) which are close to 1, implying good agreement between the theoretical prediction and experimental measurement.

Table 3.1 Parameters, uncertainties of resistance changing ratio and coefficients of determination for sensors of different printed passes under quasi-static tensile loads.

No. of printed passes	c_1	c_2	c_3 ($\times 10^2$)	c_4 ($\times 10^4$)	U (%)	C^2
6	1.90	308.13	61.06	-46.16	0.04	0.9999
9	2.29	248.36	-18.43	-19.56	0.06	1.0000
12	2.59	191.53	-78.92	13.88	0.02	1.0000
15	1.81	288.91	-111.93	8.25	0.04	0.9998

3.4.2 Mixed (uniaxial + flexural) Strain (quasi-static)

In reality, strains undergone by an engineering structure, either static or dynamic, are usually not uniaxial only and their magnitude could be small (<0.3%). Considering this, the above electro-mechanical test is implemented using a mechanical analysis platform (METTLER TOLEDO Dynamic Mechanical Analysis DMA 1), via which quasi-static three-point bending is applied on samples made of epoxy (1.5 mm thick each), as shown in Figure 3.9. Knowing the span (l) of the two sample holders on the platform is 30 mm, under the bending, the strain (ε) of the sample can be obtained by [93]

$$\varepsilon = \frac{6Dt}{l^2}, \tag{3.13}$$

where D and t signify the maximum deflection of the centre of the sample and its thickness, respectively. Identical to the above quasi-static test, response of the sensors of 6, 9, 12 or 15 layers is respectively comparatively examined, and calibrated against commercial strain gauges using a two-probe method.

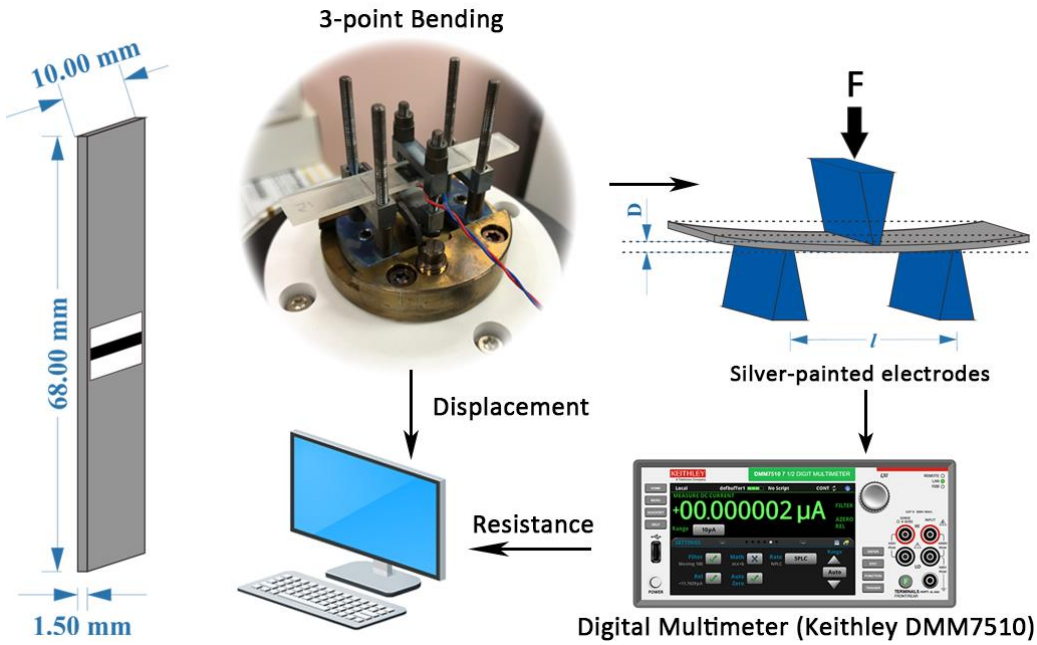

Figure 3.9 Experimental set-up of quasi-static three-point bending test.

Figure 3.10 shows the relative change (upon the slopes of linear fitted dash lines) of electrical resistance of the printed sensors of different printed passes when the bending-induced mixed strains vary from 0.10% to 0.30%, to note that the gauge factor of the sensors of 15 printed layers is ~31.0 – that is 15 times higher than that of a commercial strain gauge. Using the same theoretical model defined by Equation (3.12), four parameters (c_1, c_2, c_3 and c_4), uncertainties of resistance changing ratio (U) and coefficients of determination (C^2) are ascertained, as listed in Table 3.2. U is only around 0.1% and C^2 approximates 1 in Table 3.2, indicating good agreement between the theoretical prediction and experimental measurement.

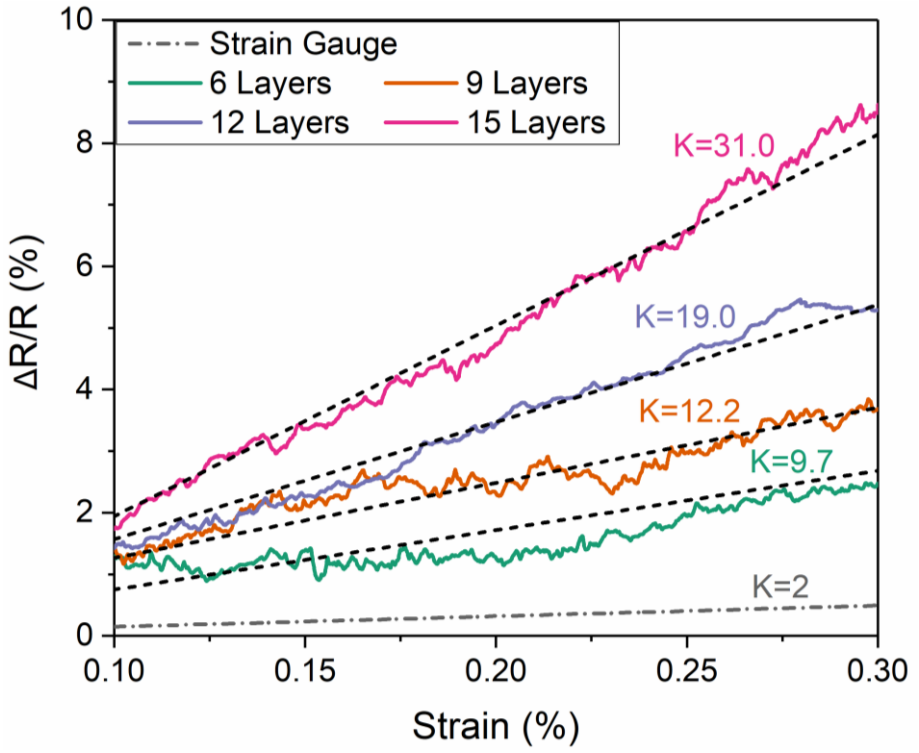

Figure 3.10 Normalized change in electrical resistance of printed sensors of different layers under quasi-static three-point bending test.

Table 3.2 Parameters, uncertainties of resistance changing ratio and coefficients of determination for sensors of different printed passes under quasi-static three-point bending loads.

No. of printed passes	c_1	c_2 ($\times 10^3$)	c_3 ($\times 10^5$)	c_4 ($\times 10^7$)	U (%)	C^2
6	14.43	-9.44	42.16	-46.60	0.09	0.9777
9	2.63	16.74	-91.18	142.58	0.11	0.9770
12	16.11	-9.60	75.05	-144.70	0.08	0.9976
15	-15.18	47.02	-198.07	294.42	0.14	0.9936

3.4.3 Vibration-induced Strain (medium-frequency)

The capability of the inkjet-printed sensors for sensing medium-frequency vibration loads is assessed by quantifying their response to dynamic strains using a dynamic vibration test system, in Figure 3.11. A set of four beams made of glass fibre/epoxy composites (280 mm long, 40 mm wide and 1.5 mm thick) is prepared, and each sample is clamped at one of its ends as a cantilever beam. An inkjet-printed sensor of 6, 9, 12 or 15 layers is adhered on the surface of each beam 70 mm from the clamped end. For comparison, a strain gauge is collocated to the printed sensors on the opposite side of the beam. An arbitrary waveform generator (HIOKI 7075) excites a continuous sinusoidal vibration signal (from 200 to 2000 Hz), which is applied on each beam 40 mm from its free end via an electro-mechanical shaker (B&K 4809). Each sensor is connected to a signal acquisition system comprising a Wheatstone bridge of which the resistor is compatible with the electrical resistance of the printed sensor, a commercial signal amplifier (KYOWA CDV-900A), and an oscilloscope (Agilent® DSO 9064A). The electrical resistances of electrical cables and connection in the measurement system are neglected.

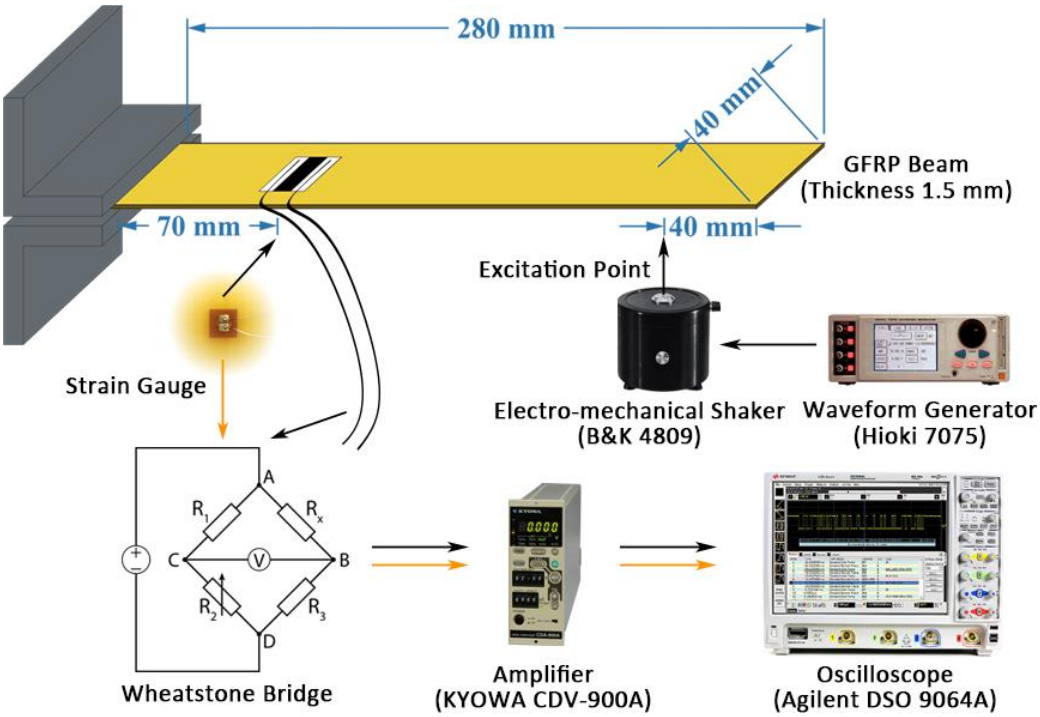

Figure 3.11 Experimental set-up of dynamic vibration test.

The vibration signals captured by the printed sensors along with those acquired by strain gauges, when the excitation frequency is 200 Hz, 800 Hz and 2000 Hz as examples, are shown in Figures 3.12(a)-(c), respectively, to observe good stability, reversibility and repeatability of the sensors in responding dynamic strains up to 2000 Hz without phenomenal hysteresis and deviation. Figure 3.12(d), showing the sensor response magnitude subjected to different degrees of excitation, accentuates that at given excitation frequency and a given printed pass (15 layers as an example for illustration), and argues a linear relationship between the magnitude of excitation and the response intensity of the sensor. Also revealed by Figures 3.12(a)-(c), is that a thicker printed sensor with more layers exhibits higher signal-to-noise ratio, the trend of which is the same as the observed in the quasi-static three-point bending test.

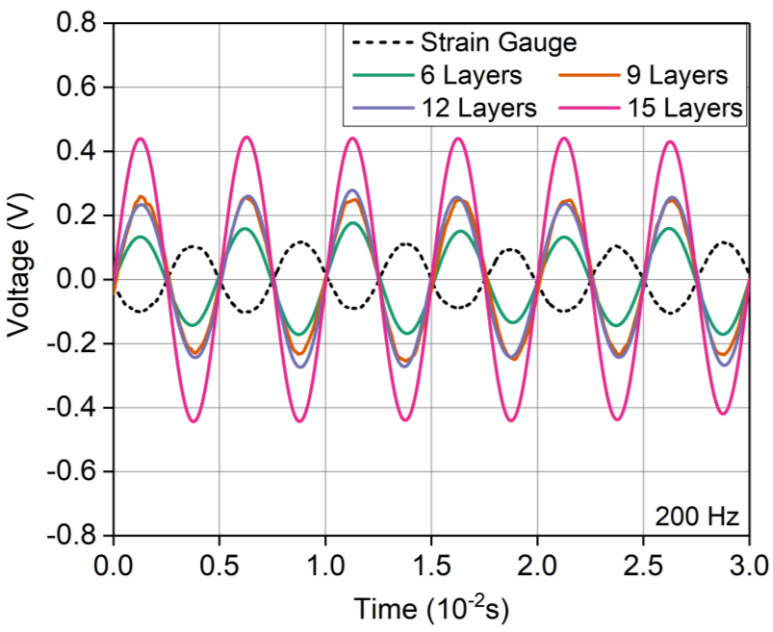

(a)

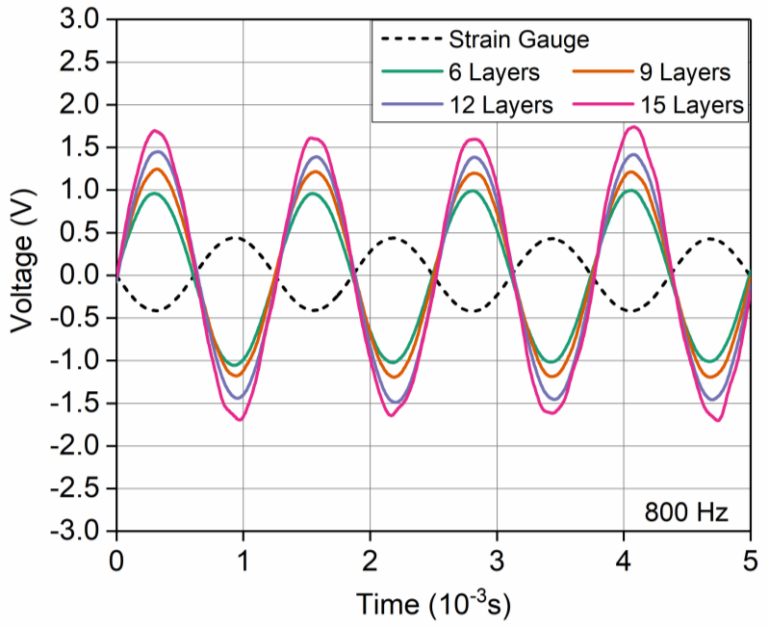

(b)

Figure 3.12 Response of printed sensors of 6, 9, 12 and 15 layers and strain gauges when the frequency excitation is (a) 200 Hz, (b) 800 Hz and (c) 2000 Hz; (d) response signals of the sensor of 15 layers under 200 Hz frequency of vibration with various excitation magnitudes (insert: signal amplitude *vs*. excitation magnitude).

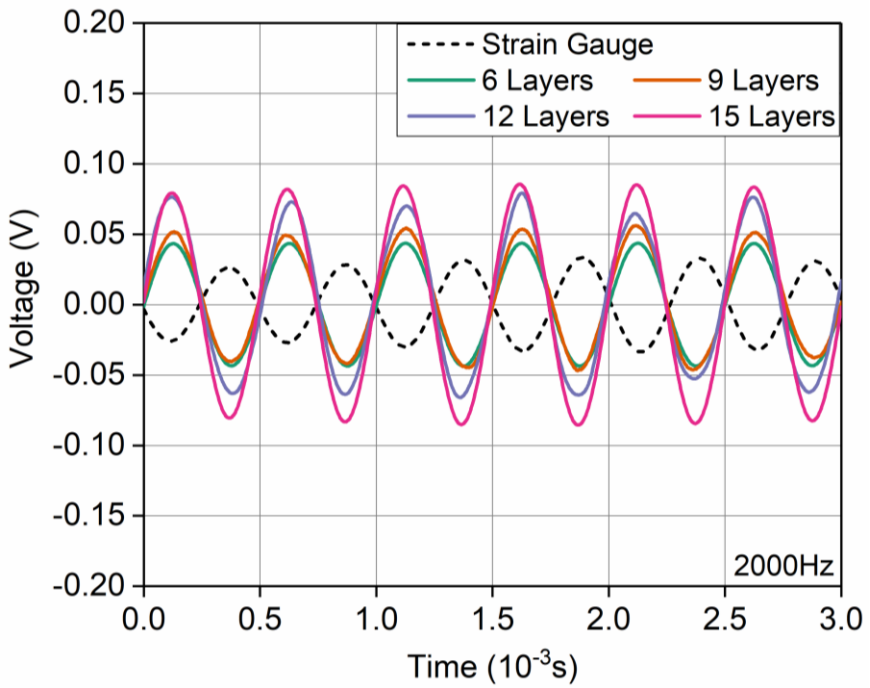

(c)

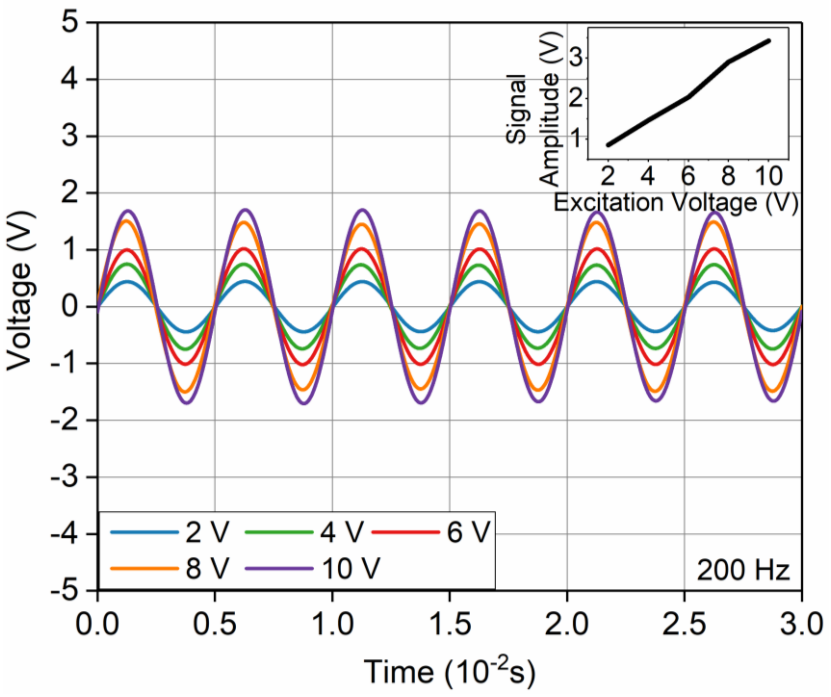

(d)

Figure 3.12 *Cont.*

The vibration-induced strain at the measurement point can be calculated according to the configuration and specification of the signal amplifier and the Wheatstone bridge by [100]

$$\varepsilon \approx \frac{4V_O}{MV_BK}, \tag{3.14}$$

where V_O, V_B and M are circuit parameters. V_O represents the output signal voltage and V_B the excitation voltage of Wheatstone bridge (2 V in this study). M denotes the amplification factor of the signal amplifier (×10000 in this study) and K is the gauge factor of the sensors. The sensors of 15 printed layers are chosen for further investigation due to its highest sensitivity to vibration excitation as observed in the test. With known output voltage V_O and gauge factor of the strain gauge ($K = 2$), the strains at the measurement points as well as the gauge factors of the sensors of 15 layers under different vibration frequencies can be ascertained by Equation (3.14), as presented in Table 3.3.

Table 3.3 Strains at measurement points and gauge factors of the sensor of 15 layers under different vibration frequencies.

Frequency (Hz)	Strain	Gauge factor
200	±20 με (±0.002%)	7.65
800	±100 με (±0.01%)	8.34
2000	±5 με (±0.0005%)	6.80

As asserted by Table 3.3, the measured strains (±0.0005% ~ ±0.01%) that is induced by vibration are significantly smaller than those (0.1% ~ 0.3%) induced by the quasi-static three-point bending. The strain under the vibration of 800 Hz is the highest

because the frequency is close to the resonance frequency of the beam. The gauge factor of the sensors (6.80 ~ 7.65) is smaller than that when used to measure mixed loads (31.0). Apparently, the smaller the strain, the lower the gauge factor of the printed sensors it will be.

3.4.4 Acousto-ultrasonic Wave-induced Strain (high-frequency)

By expanding the above vibration-type excitation from a medium-frequency range to a high-frequency ultrasonic regime, the responsive capability of the inkjet-printed sensors is examined using an ultrasonic measurement system, Figure 3.13. The acousto-ultrasonic wave signal excitation system consists of a waveform generator based on NI® PXIe-1071 platform, and a linear power amplifier (Ciprian US-TXP-3). A glass fibre/epoxy-composite laminate plate (400 mm long and wide, 1.5 mm thick) is prepared, and a PZT wafer (Ø12 mm, 1 mm thick) – used as the acousto-ultrasonic wave actuator – is surface-mounted at the centre of the laminate plate, and connected with the excitation system. The sensors printed on PI films are adhered on the surface of the plate, with a distance of 150 mm from the PZT actuator (shown in Figure 3.13). The sensors are connected to a self-developed amplification module via shielded cables, and the module consists of a resistor-adjustable Wheatstone bridge converting piezoresistive variation to electrical signals, and amplifiers and filters for reducing the contamination from ambient noise and measurement uncertainties. The amplification module is powered by a power supply (GW INSTEK® GPC-3030D), and the converted signals are recorded with an oscilloscope (Agilent® DSO 9064A). Alongside each printed sensor, a PZT wafer is collocated, functioning as an ultrasound sensor to capture signals simultaneously for signal calibration and comparison. The electrical

resistances of electrical cables and connection in the measurement system are neglected.

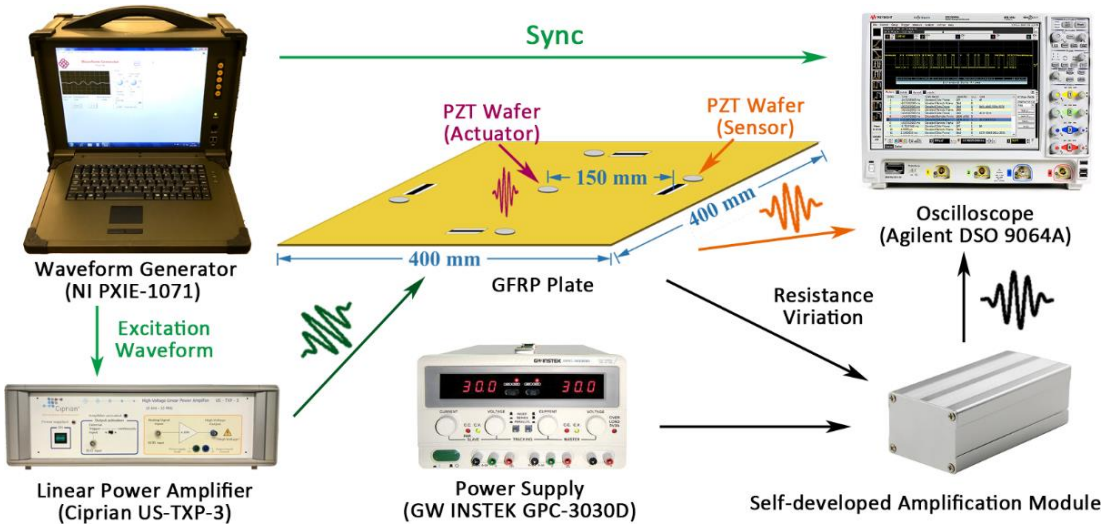

Figure 3.13 Experimental set-up of acousto-ultrasonic wave sensing test.

A series of five-cycle Hanning-function-modulated sinusoidal tonebursts with the central frequency varying from 50 kHz to 500 kHz (with a stepping of 25 kHz) are generated by the waveform generator, and applied on the PZT wafer (wave generator) via the power amplifier to emit acousto-ultrasonic waves into the laminate plate. The generated waves propagating in the laminate plate are captured by the printed sensors as well as the collocated PZT sensors. Figure 3.14 compares representative signals, at 175 kHz, captured by the inkjet-printed sensors of 6, 9, 12 or 15 layers, respectively, as well as the PZT sensors, to observe that the moments at which the first wave component (*viz*., the zeroth-order symmetric Lamb wave mode guided by the laminate, denoted by S_0 hereinafter) arrives are of the same in the signals acquired by the printed sensors and by the PZT sensors. Not only the S_0 mode, but other wave modes (*e.g.*, the zeroth-order anti-symmetric Lamb wave mode, A_0) are also faithfully captured by the

printed sensors, consistent with those by the PZT sensors in terms of the arrival moment and waveform. The inkjet-printed CB/PVP sensors of 12 layers and PZT sensors are of SNRs (S_0 mode) of 28.98 dB and 34.25 dB, respectively. To scrutinize the sensor performance at higher frequencies, Figure 3.15 comparatively displays the signals captured by the printed sensors of 12 layers and by the PZT sensors at 500 kHz, as an example for illustration. The signals captured by the printed sensors are filtered by a first-order Butterworth filter to mitigate noise, and good agreement between signals acquired by the printed sensors and PZT sensors is confirmed. Note that the crosstalk included in the signals at the zero moment, as highlighted in Figure 3.15, originates from the high-voltage power amplifier of the signal acquisition system.

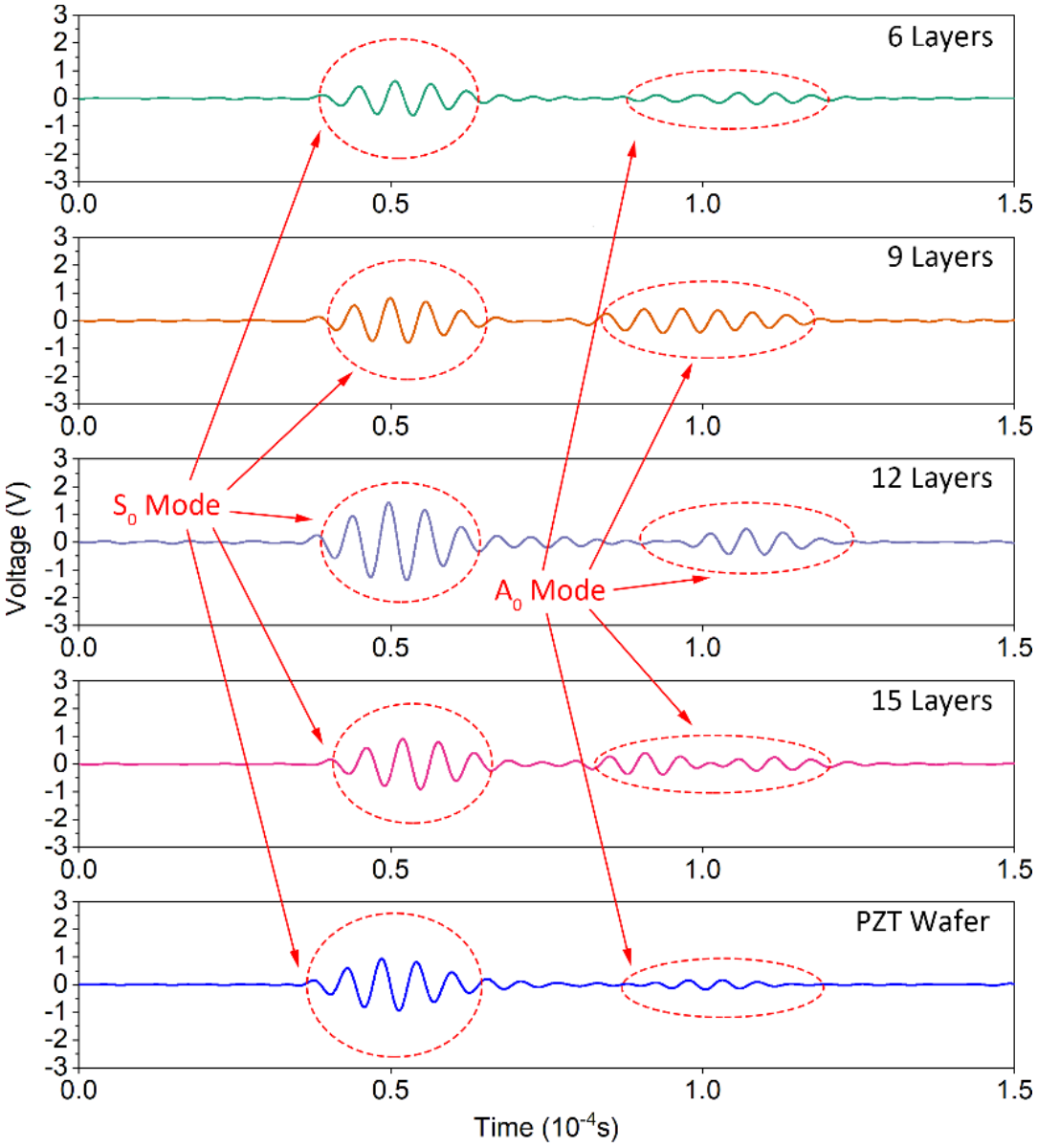

Figure 3.14 Raw acousto-ultrasonic wave signals captured by the inkjet-printed CB/PVP sensors of 6, 9, 12, or 15 layers, compared against counterpart signals captured by commercial PZT sensors at an excitation frequency of 175 kHz.

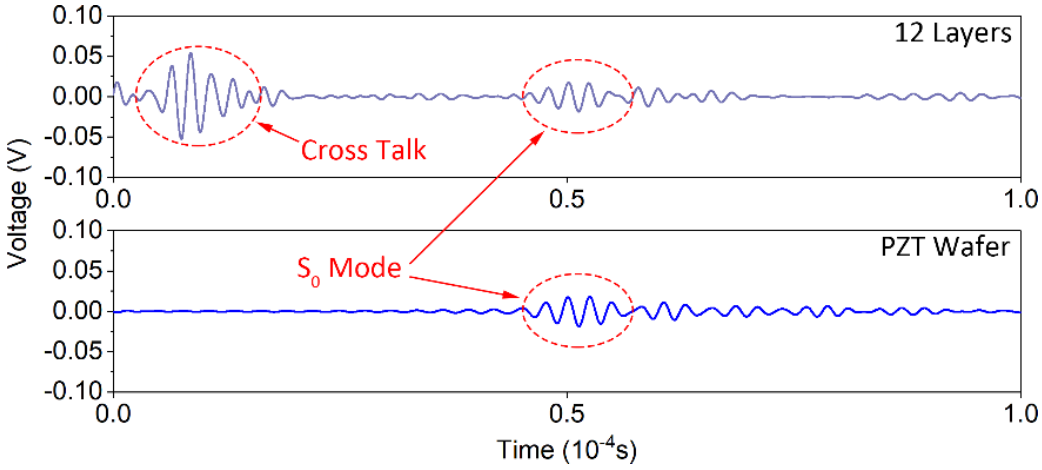

Figure 3.15 Noise-filtered acousto-ultrasonic wave signals captured by the inkjet-printed CB/PVP sensor of 12 layers and by PZT sensor at an excitation frequency of 500 kHz.

To put the comparison into perspective, Figure 3.16 depicts the sweep frequency responses over the time-frequency domain (from 50 kHz to 500 kHz), obtained using the printed sensors of 12 layers and PZT sensors, respectively, to observe no remarkable discrepancy in sensing performance between two types of sensors over a broad frequency regime. The results argue that the inkjet-printed sensors are of the capability to perceive dynamic strains in a broad frequency regime with a high signal-to-noise ratio up to 500 kHz, with precision similar to that of a commercial PZT sensor. It is also noteworthy that the magnitudes of the signals from two types of sensors are different – a finding attributed to the different sensing mechanisms: the printed sensor is a sort of piezoresistive sensor, while PZT sensor is based on piezoelectric measurement.

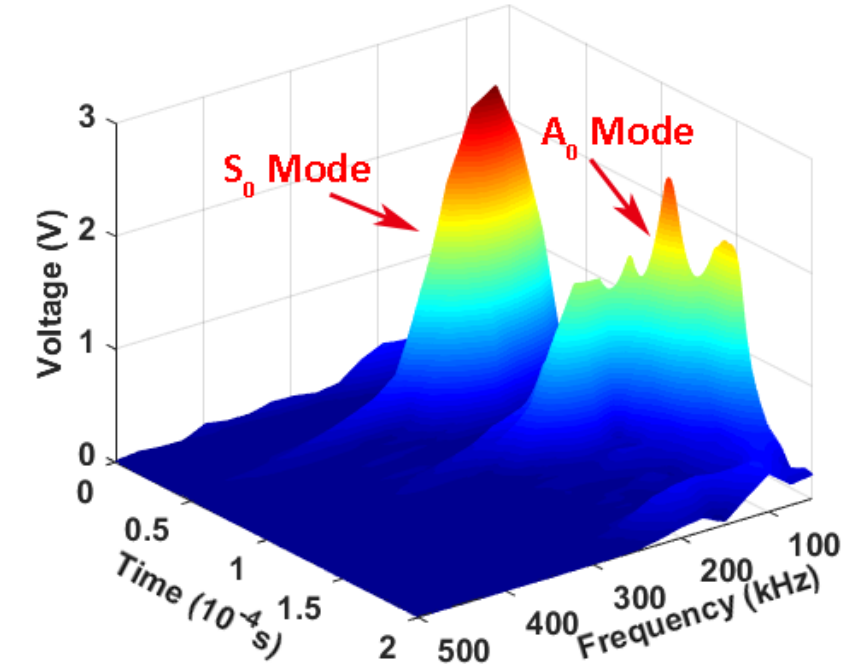

(a)

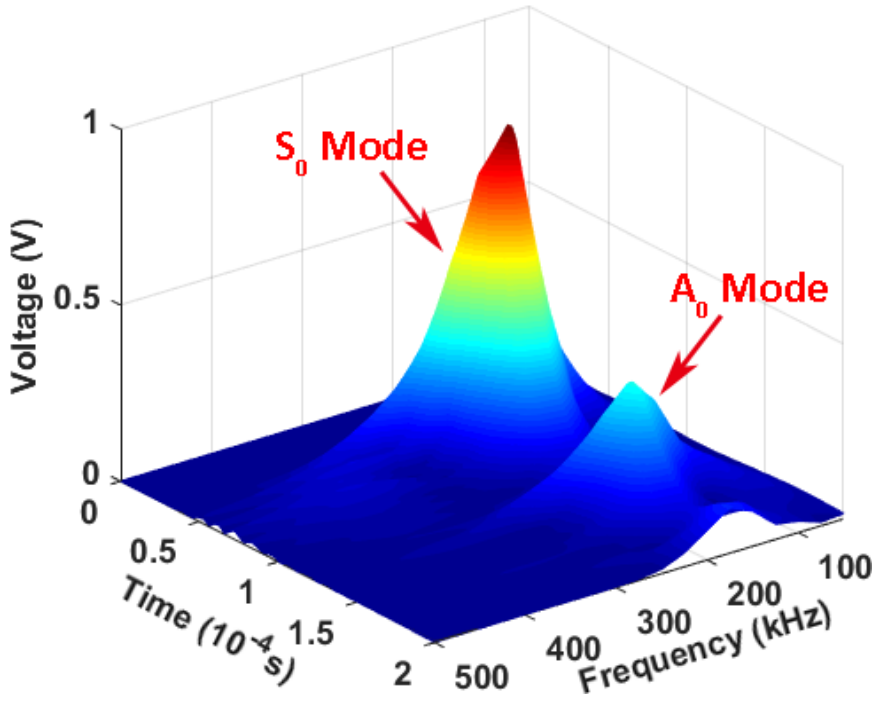

(b)

Figure 3.16 Sweep frequency responses obtained using (a) inkjet-printed CB/PVP sensors of 12 layers, and by (b) commercial PZT sensors.

3.5 Comparison of Different Sensors of Printed Passes

As commented earlier (in Section 3.4), the absolute values of high-order coefficients c_2, c_3 and c_4 in Equation (3.12) represent the degree of destruction in the nanofiller-formed conducting network of a sensor. In the tensile test when the sensors are used to measure a uniaxial strain – a relatively greater strain that is higher than 0.8%, there is no remarkable discrepancy and tendency in respective coefficient as noted in Table 3.1, regardless of the number of printed passes; while in the three-point bending test when the sensors are used to capture a mixed (uniaxial + flexural) strain – a relatively smaller strain that is lower than 0.3%, the respective absolute values of all three coefficients tend to augment as an increase in the number of printed passes, in Table 3.2. That is because for a printed sensor, a larger strain (>0.8%) suffices to introduce adequate destruction in tunnel-conductive paths, when a sensor is of different printed layers; on the other hand, under a greater strain, it is the original tunneling gap (*i.e.*, particle separation) rather than the tunnel-conductive path destruction that leads to the resistance change manifested by the sensor, and therefore a thinner printed sensor with fewer layers can achieve a higher gauge factor because of its higher degree of particle separation [146].

It is interesting to notice in Table 3.2 that the absolute values of coefficients c_2, c_3 and c_4 are correlated with the number of printed layers, highlighting that the conductive network of a thicker sensor (with higher electrical conductivity) is more sensitive to a smaller strain. This has also been proven in Figure 3.10, in which under the lower stains, a sensor with more printed passes shows higher sensitivity, which is in contrast

with the case that a greater strain is measured. This also echoes the conclusion drawn elsewhere [109]: a thicker film sensor usually induces more microcracks and larger crack openings in the sensor, especially under a smaller strain, so a thicker printed sensor has more conductive network destruction, exhibiting higher sensitivity to smaller strain.

The comparison between the quasi-static three-point bending test and the dynamic vibration test further verifies that a printed sensor with more layers tends to have higher sensitivity to small deformation due to a larger degree of tunnel-conductive path destruction. However, when the strain is smaller than tens of microstrain, the degree of tunnel-conductive path destruction shows a decreasing trend, and this results in the reduction of the gauge factor for the printed sensors. For acousto-ultrasonic wave sensing test, the findings from Figure 3.14 highlight that the inkjet-printed sensors are of high sensitivity to acousto-ultrasonic wave signals with high fidelity. It is noteworthy that under acousto-ultrasonic wave excitation, the sensors of 12 layers rather than the sensors of 15 layers (in vibration test) show the strongest response and thus the best sensitivity to the acousto-ultrasonic waves. The reason is that the load of acousto-ultrasonic waves with ultra-high frequency is much smaller than that of a medium-frequency vibration signal; when the strain is sufficiently small, the degree of tunnel-conductive path destruction shows a downward trend, and for a thicker sensor with a denser structure, it would be more difficult for the small strain induced by the acousto-ultrasonic waves to destruct the tunnel-conducting path. As a result, under the acousto-ultrasonic wave-induced load of ultra-low magnitude, the tunneling gap determined by the particle separation and the tunnel-conductive path destruction strike a balance when the sensors are of 12 printed layers.

In conclusion, the inkjet-printed sensors can be tailor-made towards specific signal acquisition demands by controlling the printed passes. To acquire uniaxial strains, especially when the strains are higher than 0.8%, the inkjet-printed sensors of 6 layers are suggested; to capture quasi-static mixed (uniaxial + flexural) strains or medium-frequency vibration signals, the sensors of 15 layers are preferred; to perceive high-frequency acousto-ultrasonic wave signal, a sensor of 12 printed passes shows the highest signal-to-noise ratio.

3.6 Comparison of Different Manufacturing Approaches: Inkjet-printed *vs.* Spray-coated *vs.* Hot-pressed

In earlier research [16, 17, 99], the nanocomposite-based sensors were fabricated using either the hot-pressing- or spray-coating-based approaches. During the hot pressing, the ingredients were pressed under a high temperature of 190 ºC, and it took 24 h for full curing of the hot-pressed films, after which the cured films were manually cut for preparing the sensors. Compared with the hot-pressing-based approach, the spray coating is conducive for rapid prototyping and scalable fabrication of sensors. However, the spray coating is a manual process, in which it is a challenging issue to precisely control the thickness and conductivity of the sensor. On the other hand, for the inkjet printing, a highly specific pattern of the sensor can be designed accurately, and the rigorously fabricated ink can be directly deposited with desired patterns onto

substrates through an automatic printing process. The thickness and conductivity of the sensors that are thus produced can also be tailor-made by controlling the number of printed passes, making it possible to customize the sensors for a specific application yet without a need to modify the ingredients of the ink. Compared with the hot-pressing- or spray-coating-based manufacturing approaches, the inkjet printing is of a high degree of versatility, simplicity, controllability, automaticity with high precision yet material-saving, low-cost and environmental-friendly.

To gain insight into the effect of different manufacturing approaches for sensor preparation on dynamic strain acquisition, the sensing performance of CB nanocomposite-based sensors that are prepared using hot press, spray coating and inkjet printing, respectively, is compared, in terms of their respective sensitivity to broadband dynamic strains and measurement stability. The same type of nanoparticle – CB, is selected and compounded with PVDF (for hot press) or PVP (for spray coating or inkjet printing) to produce CB nanocomposite-based sensors. In particular, without the loss of generality, 12 layers are printed for the inkjet-printed sensors. As some typical results, Figure 3.17 shows the signals respectively captured by three types of sensors at the excitation frequency of 175 kHz, to observe that the inkjet-printed sensors exhibit the highest sensitivity, as reflected by the largest magnitude and therefore the highest signal-to-noise ratio. To evaluate the stability of signal acquisition, for each type of sensors, under every single excitation frequency, 100 signals are extracted randomly from a large pool of acquired signals, when the excitation frequency varies from 50 kHz to 300 kHz with an interval of 50 kHz, on which basis the coefficients of variation (i.e., the relative standard deviations) of signal magnitude are calculated, in Figure 3.18 which confirms that throughout the whole frequency

range of interrogation, the coefficients of variation of inkjet-printed CB/PVP sensors are the lowest amongst three types of sensors and at higher frequencies in particular. Within 50 kHz-200 kHz, the relative standard deviation of the inkjet-printed sensors is ~0.1 only. The signal stability and reliability are of great significance for practical real-time SHM applications, and the much-lowered coefficients of variation of the inkjet-printed CB/PVP sensors under high frequency indicate great application potentials of the inkjet-printed sensors for *in situ* SHM. These findings indicate that the inkjet-printed sensors, with their even and uniform nanostructure, are conducive to maintain good stability, fidelity and sensitivity in dynamic strain acquisition, when compared with their peers that are fabricated using other manufacturing approaches such as hot press or spray coating.

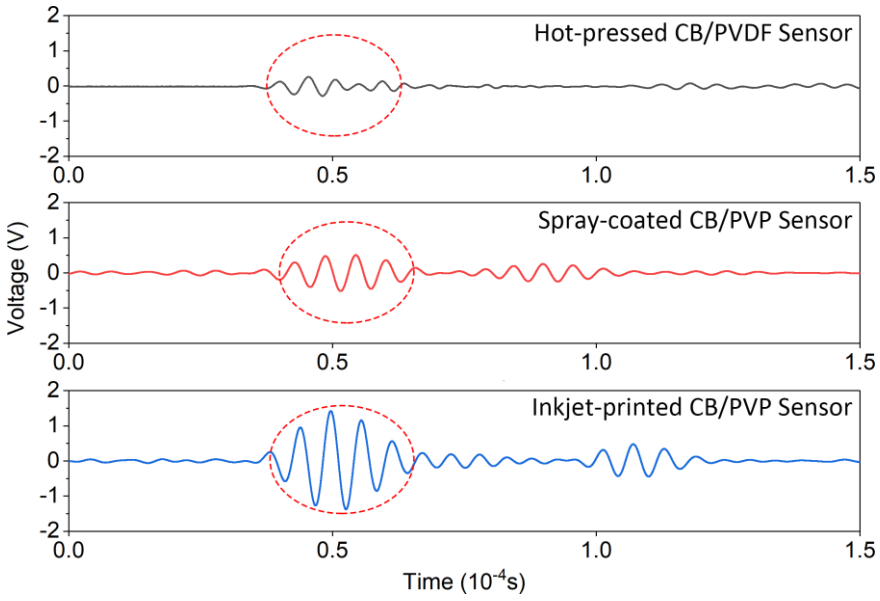

Figure 3.17 Acousto-ultrasonic wave signals at an excitation frequency of 175 kHz captured by sensors prepared using different manufacturing approaches.

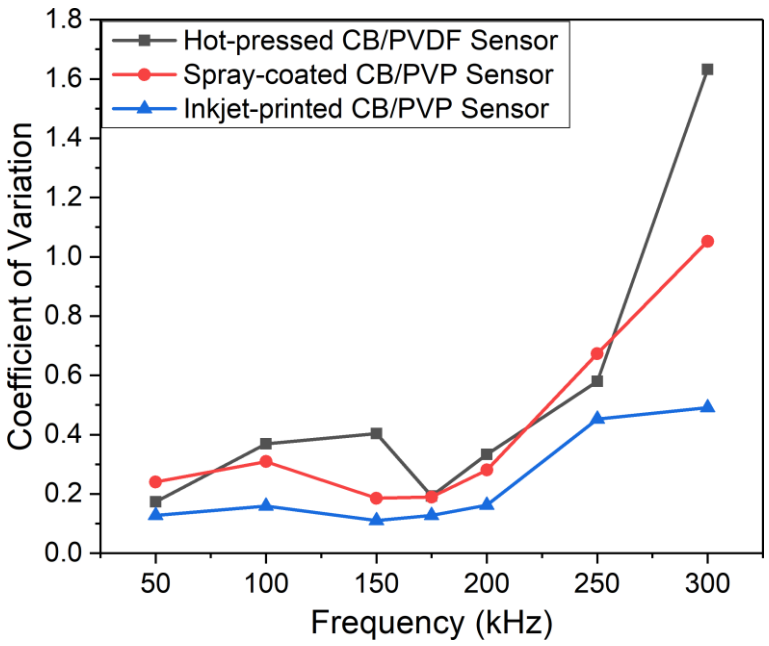

Figure 3.18 Coefficient of variation for acousto-ultrasonic wave signal acquisition (50-300 kHz) with sensors fabricated using hot press, spray coating and inkjet printing.

3.7 Summary

A new breed of nanocomposite thin film ultrasound sensors made of CB/PVP are developed using inkjet printing. The sensors are manufactured by drop-on-demand approach which deposits the integrated ink to fabricate sensors directly on flexible substrates. The sensing ink is rigorously designed and optimized, making it stable and printable and the signals captured by the printed sensors are compared against counterpart signals captured by traditional metal foil strain gauges (for quasi-static strain and vibration) and piezoelectric ceramic wafers (for strains induced by acousto-ultrasonic waves).

Taking advantage of the uniform and stable nanoparticle-based conductive network, the results reveal that the printed sensors are of significantly enhanced gauge factors than those of conventional metal foil strain gauges, and the sensors are able to capture ultrasonic signals precisely up to 500 kHz with high fidelity, stability and no obvious time delay. In addition, for dynamic strain of different frequencies (*e.g.*, quasi-static strain, vibration and acousto-ultrasonic waves), the sensitivity of the fabricated sensors can be precisely regulated by varying the degree of conductivity (controlled by the printed passes), which implies that the CB/PVP thin film ultrasound sensors can further be optimized to accommodate specific demands.

CHAPTER 4

Inkjet-printed NGP/PI Ultrasound Sensors

4.1 Introduction

Graphene – the two-dimensional (2D) allotrope of carbon, shows alluring intrinsic properties in terms of charge carrier concentration and mobility [147], thermal conductivity [148], mechanical strength [149], chemical stability [150], and flexibility [151]. With these appealing merits, graphene-based nanocomposites have opened up a new way for developing innovative electronic devices and sensors in particular [152]. To name but a few, the piezo-response of single-layer graphene (SLG) grown via chemical vapor deposition (CVD) on Si/SiO_2 calibration grating substrates was investigated, which demonstrates a high piezoelectric effect ($d_{33} \approx 1.4$ nm V^{-1}) of SLG on Si/SiO_2 substrates [153]. Graphene-based cellular elastomers with reduced rGO were fabricated, and thus-produced elastomers could provide instantaneous and high-fidelity electrical response to dynamic pressures up to 2 kHz [96]. GO/graphene resistive pressure sensors were produced, with proven capability of responding to transient signals up to 10 kHz [97]. These studies are among pioneering explorations in recent years, which has affirmed the capability of graphene-based nanocomposites in sensing dynamic strains, and paved a solid path leading to flexible, functional devices for acquiring high frequency acousto-ultrasonic wave signals.

In Chapter 3, CB/PVP film sensors are developed via inkjet printing, and the printed CB/PVP sensors have proven capability of *in situ*, precisely responding to acousto-ultrasonic wave signals up to 500 kHz. Thus-produced sensors, when compared against other CB-based sensors prepared by conventional fabrication approaches, feature enhanced sensing sensitivity, and expanded responsive range. However, due to the extremely low surficial area of the zero-dimensional (0D) CB nanoparticles, sphere-like CB nanoparticles intend to mingle together with others and form agglomerates in the sensors [154]. Such agglomerates lead to inadequate electrical conductivity of the sensors, impeding further improvement of the sensing capability.

In this chapter, flexible and ultrasensitive NGP /PI thin film ultrasound sensors are produced producing via drop-on-demand inkjet printing. The graphene-based ink is made with rigorously designed, morphologically optimized NGP/PAA hybrid nanocomposites that are prepared using novel high-shear LPE, in which few-layer NGPs are exfoliated from inexpensive bulk graphite. The ink features remarkable concentration of NGP as high as 13.1 mg mL^{-1}, and presents superb printability, storage stability, and functionality, with which the inkjet-printed flexible NGP/PI film sensors have an ultra-thin thickness of ~ 1 μm only, along with excellent thermal stability and adhesive strength reaching ASTM 5B level (*i.e.*, the highest level of adhesion grade). With a highly uniform and consolidated NGP/PI nanostructure in the sensor, quantum tunneling effect is triggered among NGPs and π-π interaction is formed between NGPs and PI polymer matrix, endowing the sensors with a gauge factor as high as 739 when responding to acousto-ultrasonic waves at 175 kHz, and a broad sensing band from zero to 1.6 MHz.

4.2 Ink Preparation and Sensor Fabrication

4.2.1 NGP Ink and NGP/PAA Sensing Ink Fabrication

Ethyl cellulose (EC, viscosity 4 cP, 5 % in toluene/ethanol, Aldrich Chemistry; 0.2 g) and PVP (PVP K-30, Sigma-Aldrich; 0.3 g) are dissolved in NMP (anhydrous, Aladdin; 100 mL) at a room temperature (25 °C). Then, bulk graphite powder (Aladdin®; 2.0 g) is mixed with the solvent using high shear laboratory mixer (L5M, Silverson®) at 6,000 rpm for 1 h, followed with centrifugation (H1850, Cence®) at 5,000 rpm (2,655 × *g*) for 20 min to remove unexfoliated graphite particles, and the supernatant containing exfoliated few-layer NGPs is collected as NGP ink. To produce the sensing ink, PAA solution (12.8 wt% (80% NMP/20% aromatic hydrocarbon), Sigma-Aldrich; 1.6 g) is added into the as-prepared NGP ink (20 mL). The mixture is magnetically stirred at 800 rpm for 30 min, and then filtered through a 0.22 μm-diameter PVDF micropore sieve to screen larger agglomerates.

The density of the NGP/PAA ink is estimated by weighing a certain volume of the filtered ink using a pipette, and its viscosity is measured by a viscosimeter (NDJ-5S, Lichen Technology). The surface tension measurement of the solvent and ink is conducted using a force tensiometer (K100, KRÜSS®). The NMP solvent surface energy (E_{Sur}^{Sol}) is calculated via $E_{Sur}^{Sol} = \gamma + TS_{Sur}^{Sol}$ [155], where γ refers to the measured surface tension of NMP solvent, T the temperature, and S_{Sur}^{Sol} the solvent surface entropy (universal value of ~ 0.1 mJ m^{-2} K^{-1}), respectively. The morphology of exfoliated few-layer NGPs is characterized by field emission scanning electron

microscopy (FESEM, MAIA 3, TESCAN®) and atomic force microscopy (AFM, AC mode, scan rate 0.8 Hz, MFP-3D Infinity, Asylum, OXFORD INSTRUMENTS®). For FESEM and AFM sample preparation, 0.02 vol% NGP ink (10 μL) is drop-casted onto pre-heated Si/SiO_2 substrates (250 ^oC), followed by annealing at 200 ^oC for 30 min. For UV-vis sample preparation, the ink is diluted to 0.1 vol% to avoid scattering loss [114], and the UV-vis spectra are obtained using a UV-vis double beam spectrophotometer (DB-20, Halo).

4.2.2 Sensor Printing and Imidization

NGP/PAA ink is directly printed on a Kapton (PI) film (25 μm thick) using a PiXDRO LP50 inkjet printer (OTB Solar-Roth & Rau) equipped with a DMC-11610 cartridge (Dimatix-Fujifilm Inc.). Before the printing process, the Kapton film is pre-treated with O_2 plasma using a plasma cleaner (PDC-002, Harrick Plasma, Inc.) for 2 min at 450 mTorr. The sensors are printed at a room temperature, under a driving voltage of 28 V with driving frequency of 4 kHz, and the printing resolution is set as 500 dpi in both in-scan and cross-scan directions. During the printing process, the printer substrate temperature is set as 40 ^oC to reduce "coffee-stain" effect. After printing, sensors are transferred onto a hot plate and annealed at 380 ^oC for 30 min, for complete solvent evaporation, stabilizer decomposition, and PAA imidization. The fabrication process of the inkjet-printed, film-type NGP/PI ultrasound sensors is recapped in Figure 4.1.

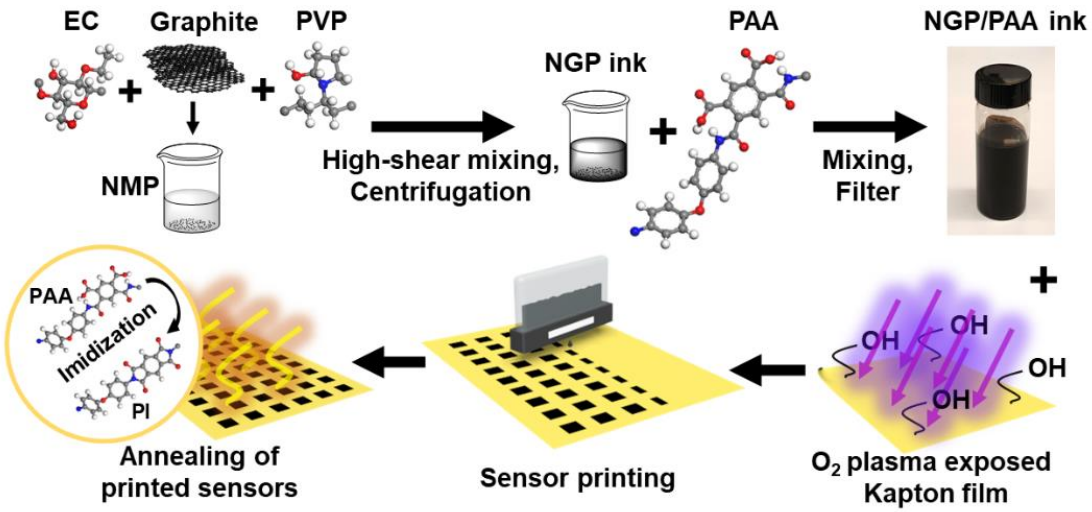

Figure 4.1 Schematic of the fabrication process of inkjet printing the film-type NGP/PI ultrasound sensors with optimized NGP/PAA nanocomposite ink.

The morphology of the printed sensors is characterized using FESEM (MAIA 3, TESCAN®). The thickness and surface roughness of the sensors are measured with a surface profiler (DektakXT surface optical profiler, Bruker®). The electrical resistance (R) of the sensors is measured using a four-probe method on a dynamic digital multimeter (4-wire resistance mode, DMM 7510, Keithley®), with a correction factor of 2.4575 [136]. The electrical conductivity (σ) of the sensors is calculated via $\sigma = l/(R \cdot A)$, where l and A are the length and effective cross-section area of the sensors, respectively. For Fourier-transform infrared spectroscopy (FTIR), Raman and X-ray photoelectron spectroscopy (XPS) characterization, the sensors are printed onto silicon wafer substrates with the same printing condition. FTIR spectra are obtained with a Bruker® VERTEX 70 FTIR spectrometer, and Raman spectra are recorded with a Raman spectrometer (488 nm excitation laser wavelength, LabRAM HR 800, HORIBA®). XPS spectra are obtained with an XPS system (Thermo Fisher® Nexsa). Thermogravimetric analysis (TGA) is performed using a TGA/DSC3+ (Mettler

Toledo®) system from room temperature to 800 °C under an argon or air flow at 80 mL min^{-1}, with a heating rate of 10 °C min^{-1}. ASTM D3359 adhesion test (cross-cut tape test) is conducted with Elcometer® ASTM D3359 adhesive tape [14].

4.3 Characterization of NGP Ink and NGP/PAA Sensing Ink

The nanocomposite ink is formulated with NGP/PAA, in which NMP is chosen as the solvent, due to the similarity in surface energy between NMP (74.5 mJ m^{-2}) and graphite (~ 70-80 mJ m^{-2}), leading to a near-to-zero enthalpy for exfoliation of graphite. As a result of the low enthalpy, a very small net energetic cost is required, making it possible to achieve effective exfoliation of graphite and stable dispersion of graphene through an LPE process [155]. Graphite is exfoliated and dispersed in the solvent via a high-shear LPE process. EC and PVP are selected as polymeric stabilizer and rheology modifier, to prevent re-aggregation and precipitation of exfoliated NGPs. Compared with conventional sonication-based LPE, this fabrication here shows additional merits including higher production quality and efficiency. The operation of high-shear LPE is precisely controlled, followed with a centrifugation process to minimize the possibility of printer nozzle clogging by unexfoliated particles of larger dimensions during the inkjet printing. Figures 4.2(a) and 4.2(b) depict the morphology of typical NGPs exfoliated from bulk graphite via FESEM and AFM. Figure 4.3 shows the statistic result of NGP dimensions via AFM measurement, to observe that most of the NGPs present a platelet length of 100-150 nm with an average thickness of ~ 2 nm

only – that is significantly smaller than 1/50 of the diameter of DMC-11610 printing nozzle (*i.e.*, 430 nm), adequate to avoid printing nozzle blockage. The thickness of monolayer graphene is ~ 1 nm via AFM measurement [156]. Considering the thickness of polymeric stabilizer, it can be concluded that most of the exfoliated NGPs are monolayer or double-layer.

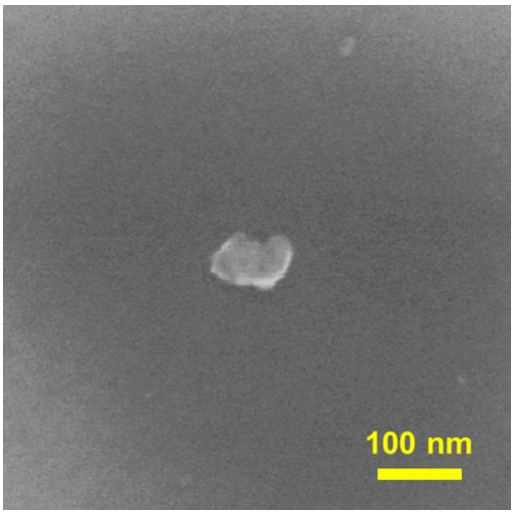

(a)

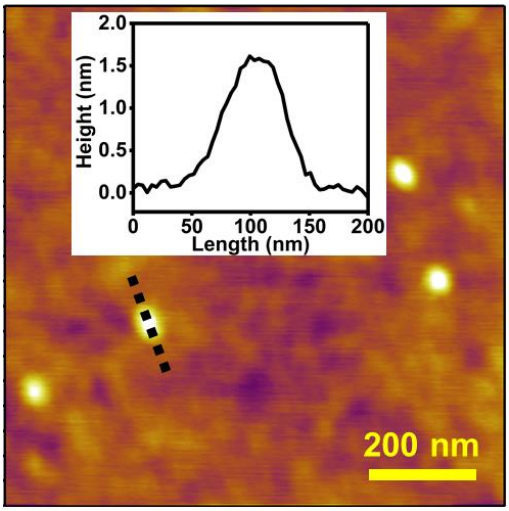

(b)

Figure 4.2 (a) FESEM and (b) AFM images of NGPs exfoliated by high-shear LPE (insert in (b): height profile of a typical NGP).

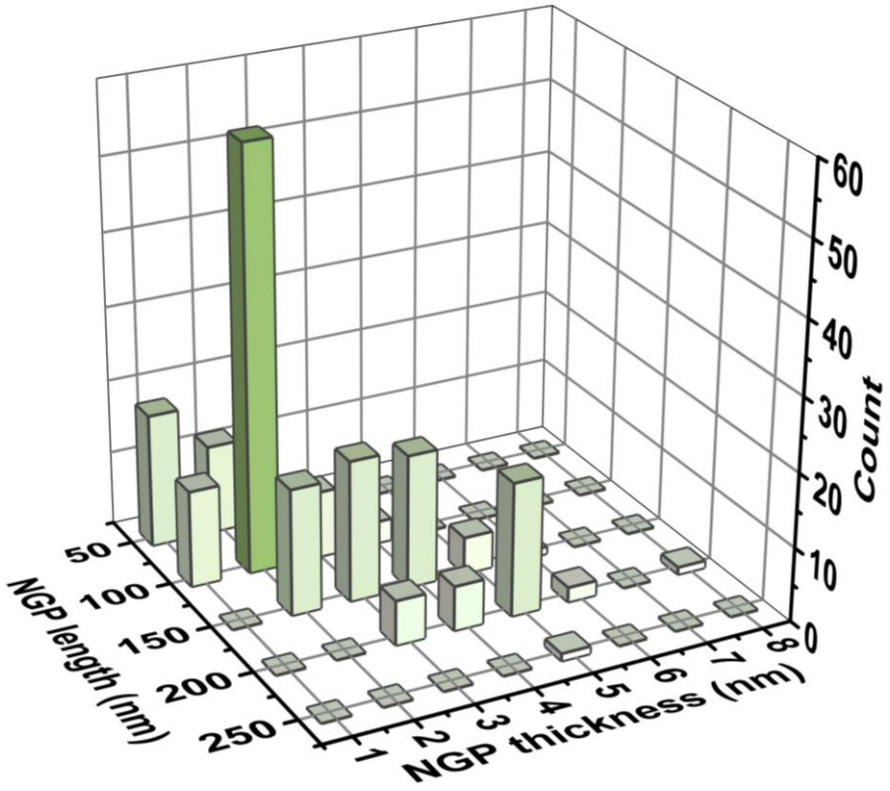

Figure 4.3 Statistic result of NGP dimensions via AFM measurement.

Targeting for an inkjet-printed sensor that is able to respond to acousto-ultrasonic waves in a broad regime, PI is selected as the polymeric matrix of the sensor with twofold consideration: (i) PI, a versatile polymer with aromatic structure connected with imide linkage in its backbone, is of good flexibility and heat resistance. Compared with conventional polymeric matrices used for developing ultrasound sensors (*e.g.*, PVDF and PVP), PI possesses lower dielectric constant, yet higher glass transition temperature and extraordinary thermal stability. The aromatic moieties of PI are of a high degree of similarity to that of the carbon structure in graphene, despite that PI is intrinsically insulative. The interaction between PI and graphene facilitates responsivity and sensitivity of the fabricated sensor to high frequency acousto-

ultrasonic waves (to be discussed later in this section); and (ii) PAA – the precursor of PI, is miscible with NMP solvent – a trait that is vitally important to warrant uniform, homogeneous and stable dispersion of NGPs in the ink.

With selected nanoparticles and polymetric matrix, the concentration of NGPs in NGP/PAA ink is estimated according to the UV-vis spectrum of the ink (Figure 4.4) with the Beer-Lambert law [157]

$$A_\lambda = \alpha_\lambda c l \,, \tag{4.1}$$

where A_λ signifies the absorption of ink at wavelength λ, α_λ the absorption coefficient at λ, c the concentration of NGPs, and l the path length of the spectroscopy. With $\alpha_{660\text{nm}}$ = 2,460 L g^{-1} m^{-1} [155], the NGP concentration of the prepared NGP/PAA ink is estimated, using Equation (4.1), to be 13.1 mg mL^{-1}, which remarkably exceeds the minimum threshold of the graphene concentration (*i.e.,* 1 mg mL^{-1}) to ensure adequate printing efficiency – as suggested elsewhere [158].

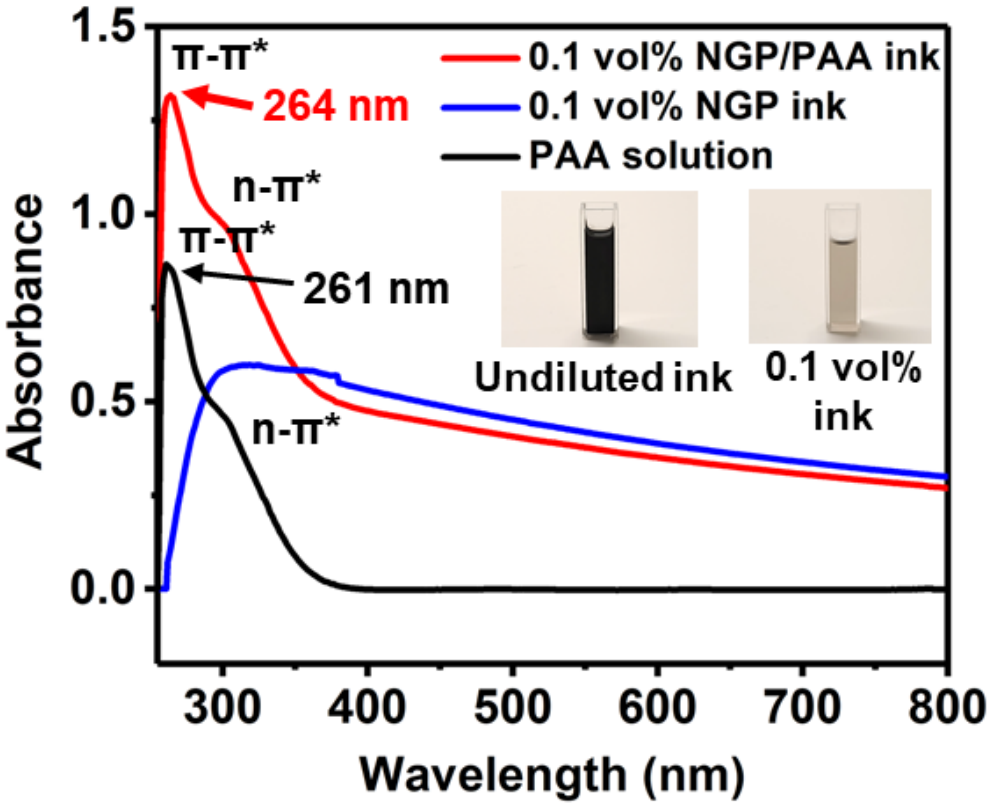

Figure 4.4 UV-vis spectra of the NGP/PAA nanocomposite ink (0.1 vol%), NGP ink (0.1 vol%) and PAA solution (inserts: undiluted and 0.1 vol% NGP/PAA inks in quartz cuvettes).

Notably, after 3-month of storage at a room temperature, the ink is observed to remain its original morphology with no obvious precipitation of NGP. Such excellent storage stability of the ink is verified by UV-vis spectroscopy (Figure 4.5), in which A_{660nm} of the NGP/PAA ink still remains 98% after three months of storage.

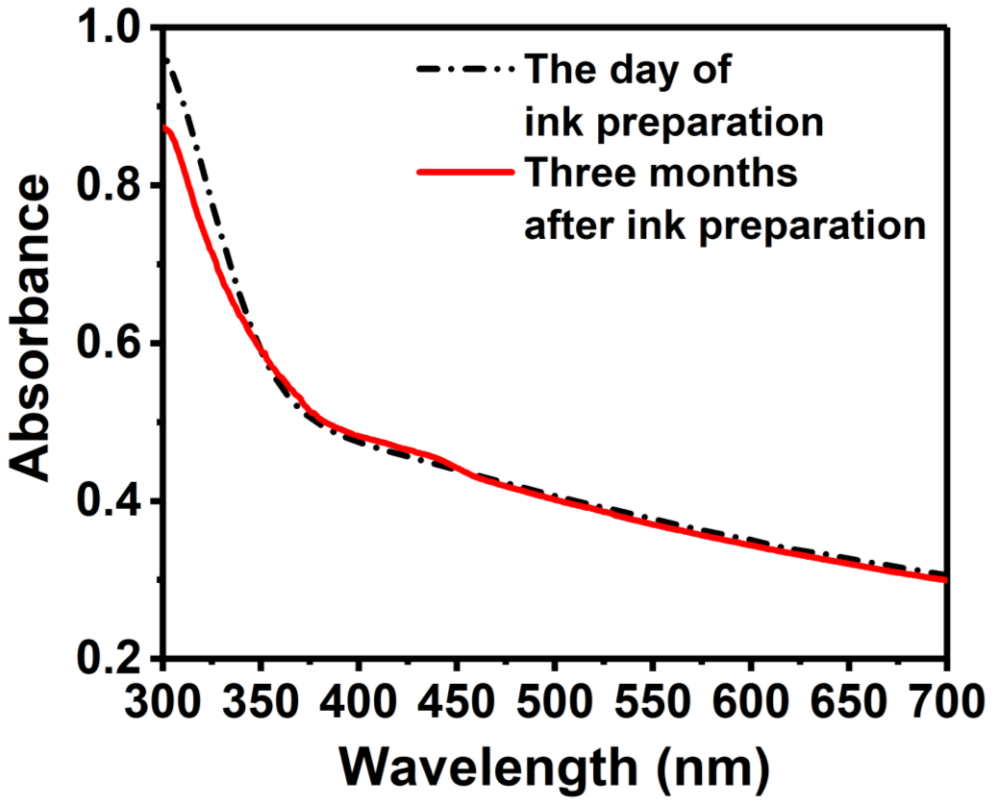

Figure 4.5 UV-vis spectra of NGP/PAA sensing ink at the day of preparation and after been placed for three months.

To evaluate the printability of the prepared nanocomposite ink, a figure of merit – Z which is the inverse of Ohnesorge number (O_h) [159], is introduced to calculate the capability of the ink of generating stable droplets during the inkjet printing process. Z reads

$$Z = \frac{1}{O_h} = \frac{(\gamma \rho d)^{1/2}}{\eta}, \tag{4.2}$$

where γ denotes the surface tension of the ink, ρ the ink density, η the ink viscosity, and d the nozzle diameter (21.5 μm for DMC-11610 nozzle used in this study). To ensure good printability of the ink, and in the meantime avoid viscosity dissipation and satellite drops, Z shall preferably fall into the optimal range between 1 and 10 [159].

Key physical properties of the NGP/PAA ink are listed in Table 4.1, and Z of the prepared ink is calculated to be 6.5 – a value that implies excellent compatibility and appropriateness of the NGP/PAA ink for inkjet printing. Thus-produced ink exhibits satisfactory concentration of NGPs, excellent stability yet good printability.

Table 4.1 Physical parameters of the NGP/PAA sensing ink.

Properties	Values
Surface tension (γ) [mN]	37.5
Density (ρ) [g mL^{-1}]	1.1
Viscosity (η) [cp]	4.6
Concentration (c) [mg mL^{-1}]	13.1

Thus-formulated and prepared NGP/PAA ink is directly printed on substrates using a PiXDRO LP50 inkjet printer. To demonstrate the printing performance of the ink with a better contrast, an illustrative paradigm printed with the ink on a piece of ordinary paper is shown in Figure 4.6, in which fine printing details are depicted clearly, demonstrating that excellent printing quality and fine resolution can be achieved with the optimized ink.

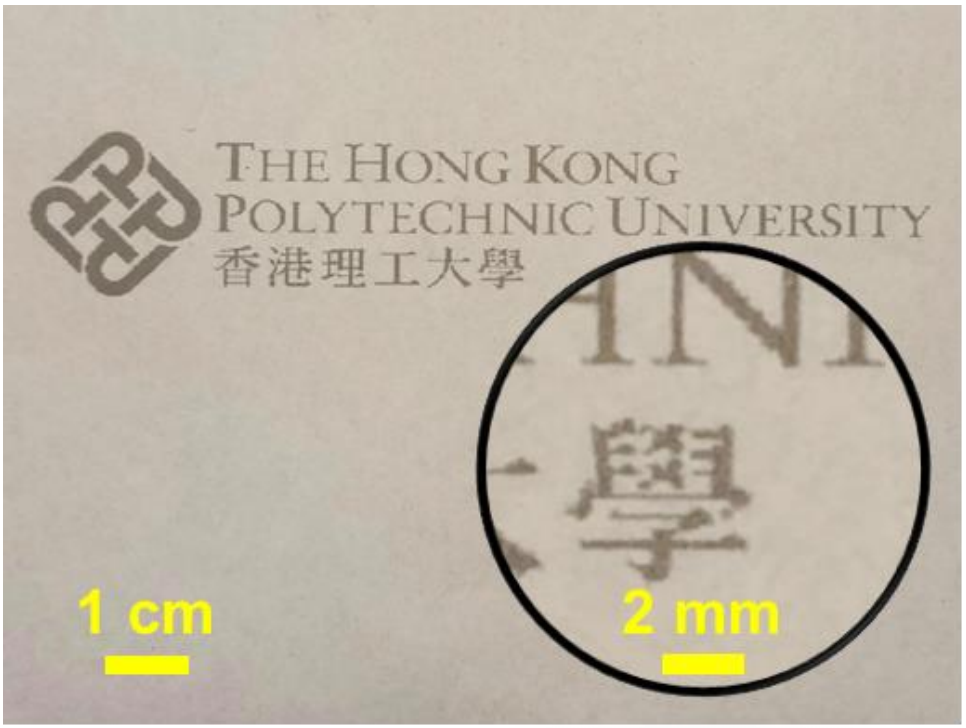

Figure 4.6 An illustrative pattern printed with the NGP/PAA ink on a piece of ordinary paper, showing fine printing details.

4.4 Characterization of Inkjet-printed NGP/PI Ultrasound Sensors

4.4.1 Morphological Characterization

Prior to sensor printing, a Kapton film substrate is pre-treated with O_2 plasma to create hydrophilic functional groups on the surface, increasing substrate surface energy and improving the wettability and printing quality of the ink when it is deposited on the substrate. As shown in Figure 4.7, the inkjet-printed NGP/PI nanocomposite sensors

deposited on the Kapton film substrate manifest good flexibility. After fully folding the sensors, the electrical resistance of the sensor slightly varies by 2.51% only, and no obvious defect or crack can be observed on the sensors. As can be seen from the FESEM images, Figures 4.8 and 4.9, NGPs are evenly distributed in PI matrix, in close proximity with others. Such a homogenous nanostructure serves as a building block for creating a stable and uniform electrical-conductive network in the sensors, conducive to triggering the tunneling effect when acousto-ultrasonic waves traverse the sensors.

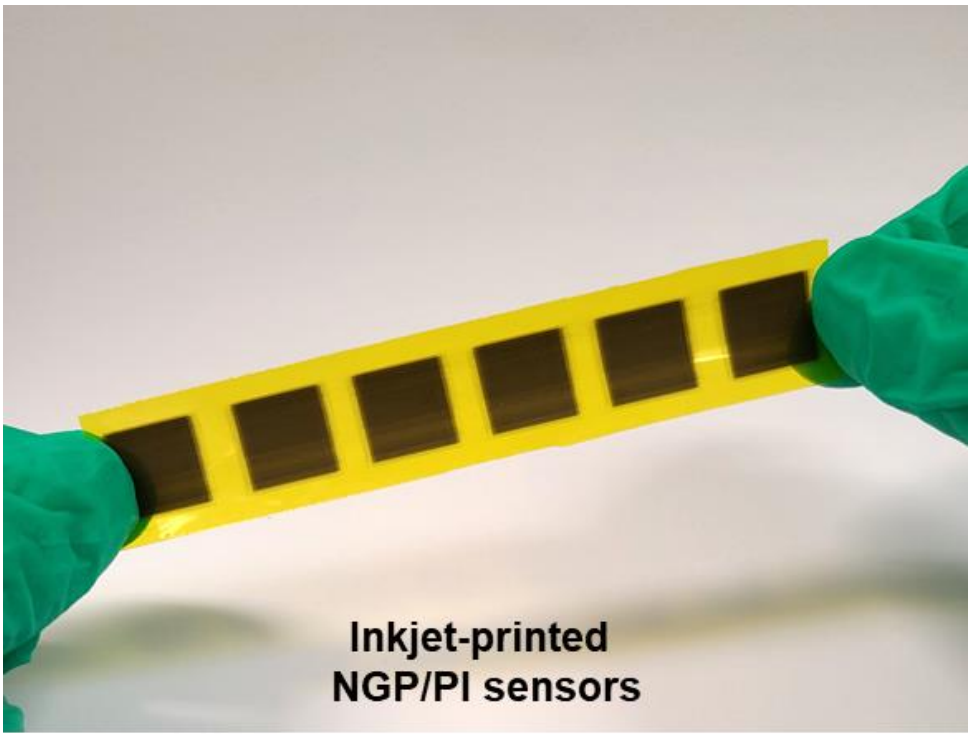

(a)

Figure 4.7 Inkjet-printed NGP/PI sensors on Kapton film substrate.

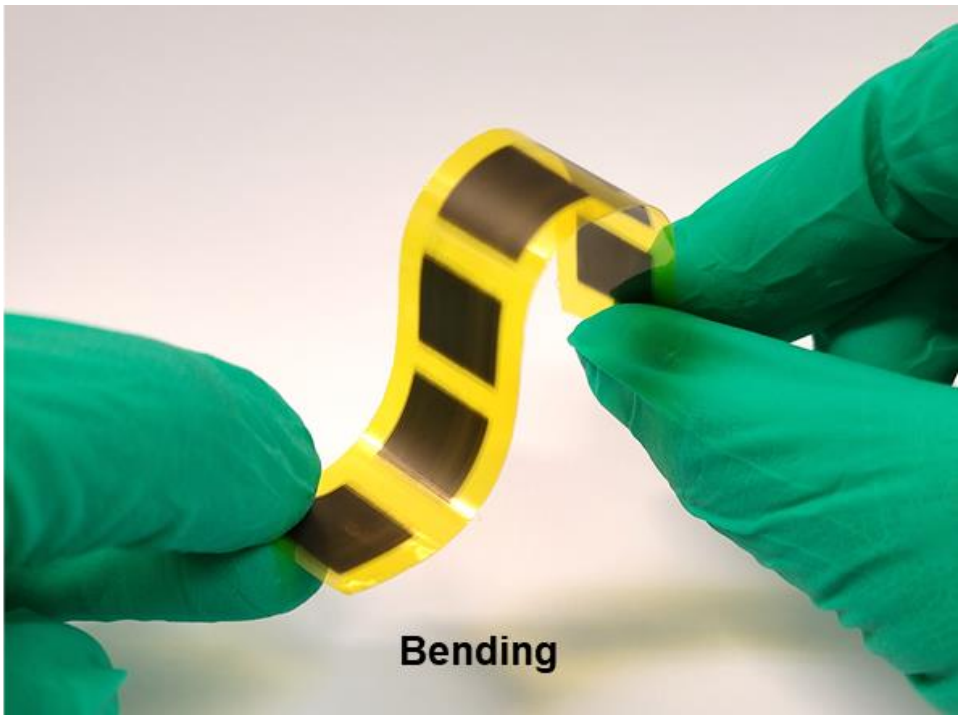

(b)

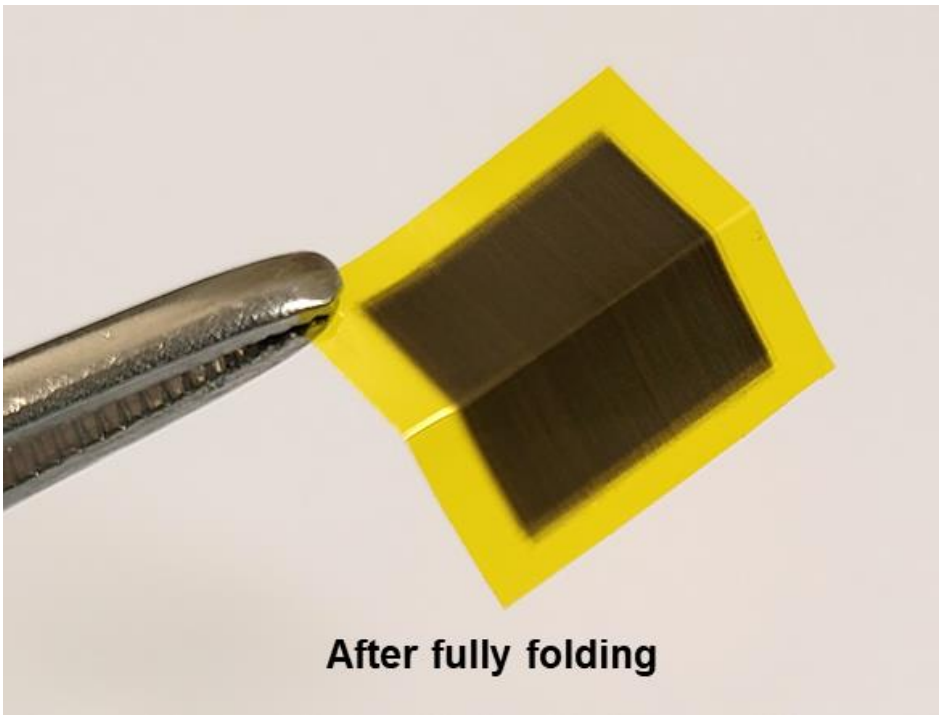

(c)

Figure 4.7 *Cont.*

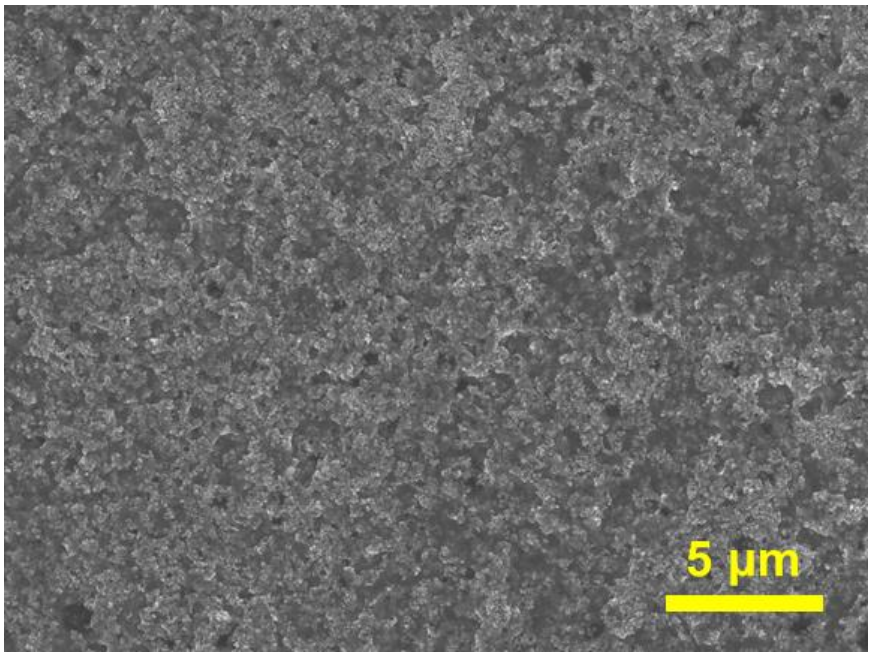

(a)

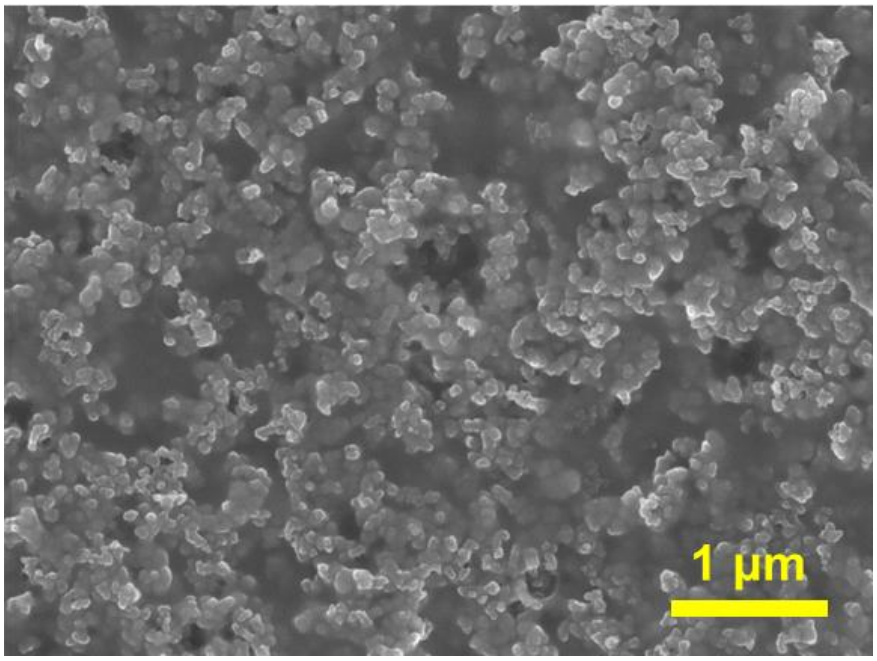

(b)

Figure 4.8 FESEM images of the inkjet-printed NGP/PI sensors.

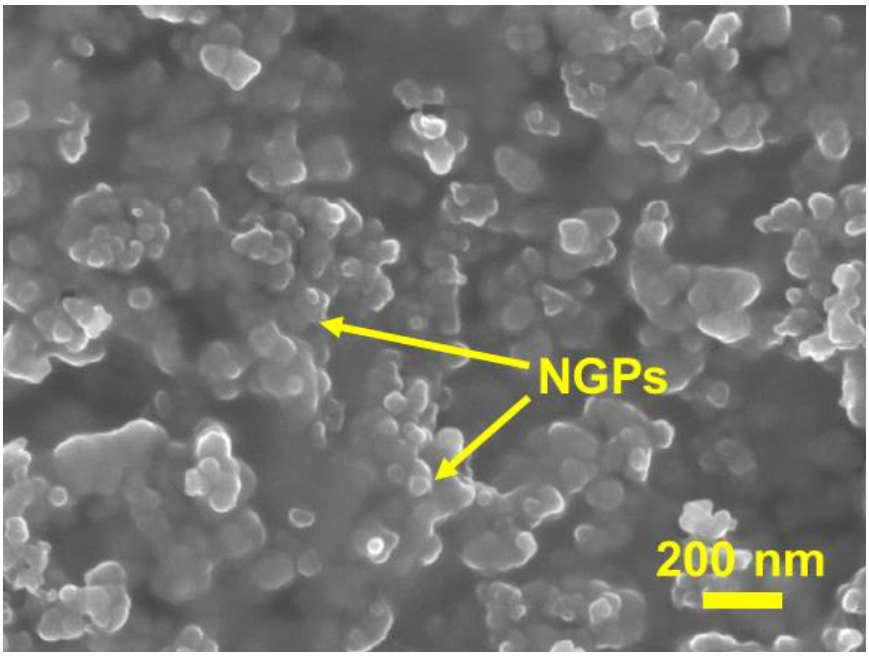

(c)

Figure 4.8 *Cont.*

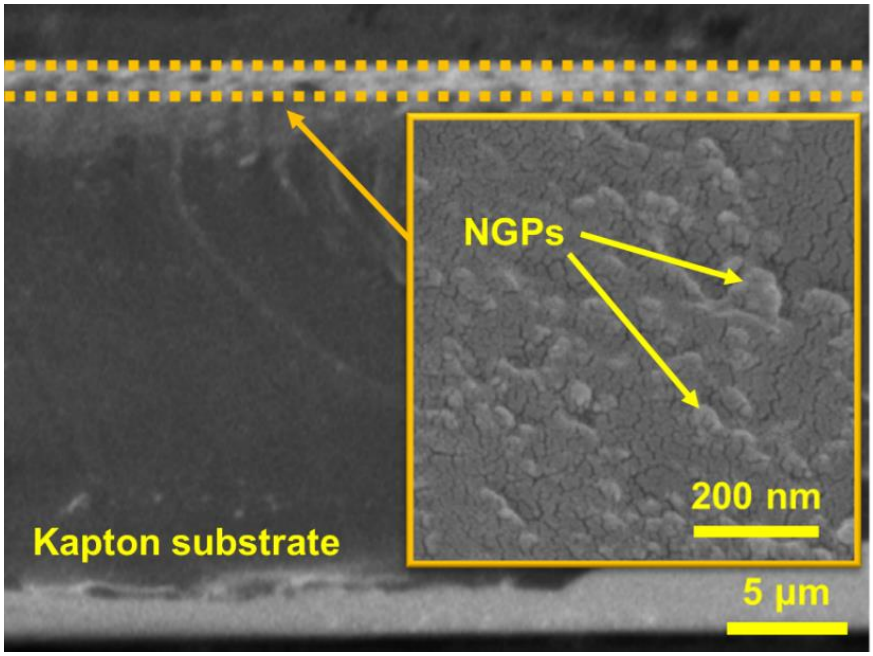

Figure 4.9 FESEM images of the cross-section of the inkjet-printed NGP/PI sensors on Kapton film substrate.

4.4.2 Microstructural Characterization

FTIR analysis is conducted for the printed NGP/PI sensors, and spectra obtained before and after annealing are compared in Figure 4.10(a). The FTIR spectrum before annealing shows typical characteristic infrared absorption bands of C=O (COOH) stretching vibration at 1713 cm^{-1}, C=O (CONH) stretching vibration at 1637 cm^{-1} (amide I band), C–NH vibration at 1540 cm^{-1} (amide II band), and symmetric C=C stretching vibration of aromatic ring at 1490 cm^{-1}; in the spectrum of annealed NGP/PI sensors, the characteristic bands at 1776 and 1712 cm^{-1} are assigned to symmetric and asymmetric C=O stretching vibration, respectively. Absorption band at 1492 cm^{-1} is attributed to the symmetric C=C stretching vibration of aromatic ring, and the band at 1361 cm^{-1} is due to the C–N stretching of imide ring [160]. The appearance of imide C–N band (1361 cm^{-1}) and absence of amide I and II bands articulate the complete *in situ* imidization of PAA in the annealed NGP/PI sensors. Raman spectra of the printed NGP/PI sensors before and after annealing are displayed in Figure 4.10(b), to observe two broad and intense peaks. Peak I of the NGP/PAA hybrid (1343 cm^{-1}) corresponds to the D peak of graphitic carbon atoms in NGPs, and it shifts to 1365 cm^{-1} after the annealing process, as peak I of the imidized NGP/PI sensor is the overlap of the D peak and the peak of C–N stretching vibration of the imide ring [94]. Peak II in the spectra is produced by the overlapping among G peak of graphitic carbon atoms in NGPs, and the peaks of original and imidized aromatic ring vibration of PI [161]. The intensity ratio of the peak II and peak I (I_{II}/I_I) increases after annealing, indicating reduced intrinsic microstructural defects in the printed sensors.

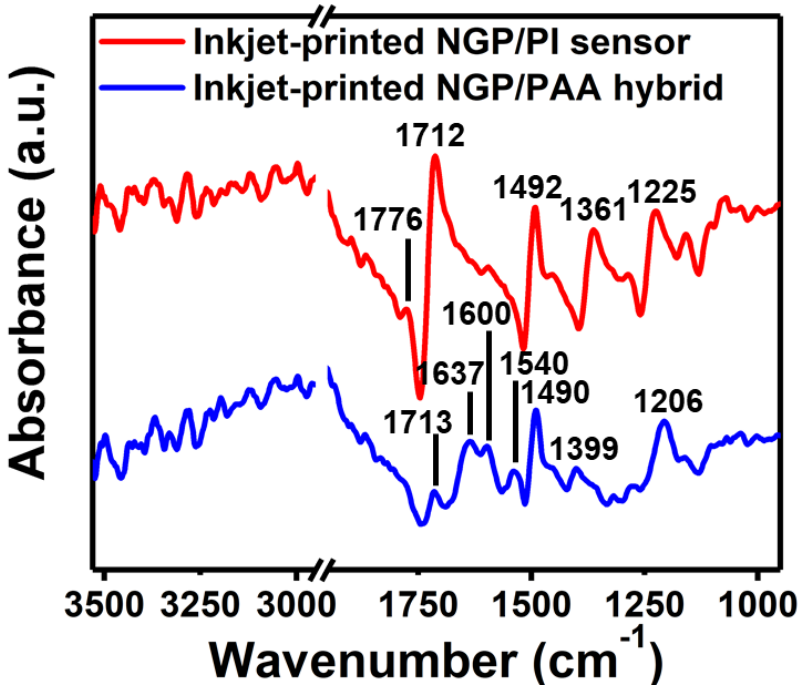

(a)

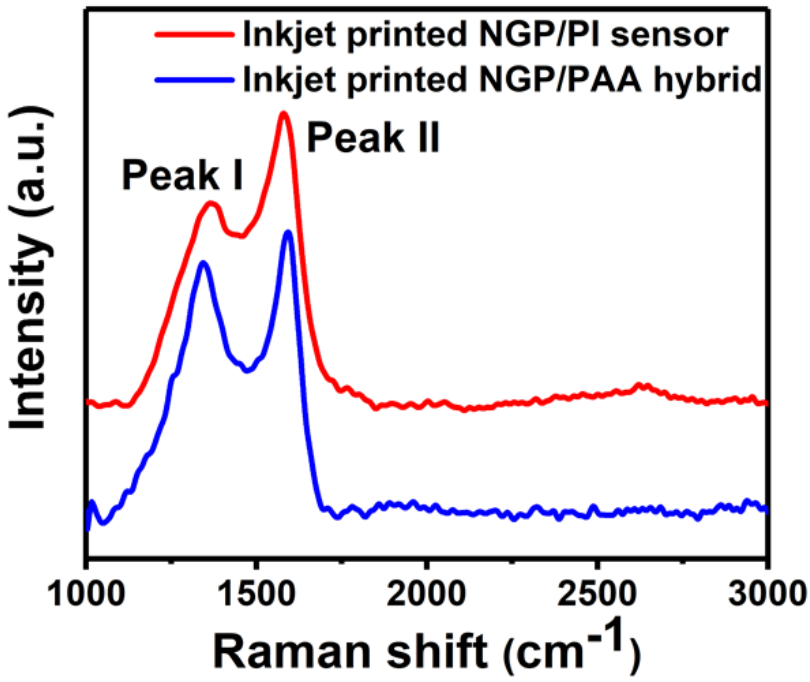

(b)

Figure 4.10 (a) FTIR, and (b) Raman spectra of inkjet-printed NGP/PAA hybrids (before annealing) and NGP/PI sensors (after annealing).

Aromatic moieties in PI chains are of a high degree of similarity to the hexagonal carbon structure of graphene, and when there is an overlap exist between aromatic groups, π-π stacking interaction occurs [162]. During ink preparation, after the high-shear LPE, the free surface of NGP becomes much larger and π-π interaction is consequently formed between the greatly extended NGP aromatic system and aromatic moieties of PAA. This can be verified from UV-vis spectroscopy, as shown in Figure 4.4. In Figure 4.4, both NGP/PAA ink and PAA solution exhibit an absorption peak, while there is no meaningful peak in the spectrum of NGP ink, as the peak is attributed to the electronic transitions of benzene. The maximum absorption wavelength (λ_{max}) of the NGP/PAA ink (264 nm) is larger than that of the pristine PAA solution (261 nm), and the red shift in the figure suggests the formation of π-π interaction between the high-shear exfoliated NGPs and PAA polymer [163]. The existence of π-π interaction also renders the ink with good storage stability. After sensor printing and annealing, by virtue of the non-destructive and reversible nature of π-π interaction, π-π interaction exists between the π-π* electron cloud of NGPs and the π electrons of aromatic moieties of PI (Figure 4.11).

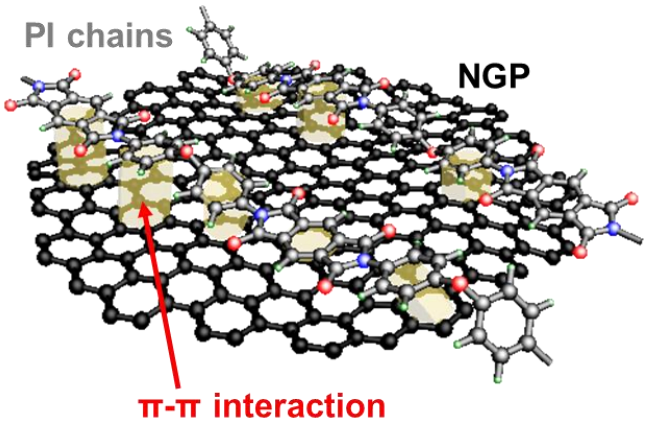

Figure 4.11 Schematic illustration of π-π interaction between NGPs and PI chains.

To gain a deeper insight into the chemical and structural characteristics of the printed NGP/PI sensors, the NGP/ PI sensors are characterized with XPS. EC, PVP and PI polymers are also characterized with XPS (Figure 4.12). The XPS spectrum of the printed NGP/PI nanocomposite sensors exhibits an intense C1s peak (Figure 4.13(a)), accompanied by a weaker O1s peak after annealing, suggesting a high sp^2-hybridized carbon content ratio. Figures 4.13(b) and 4.13(c) compare the C1s spectra of the sensor before and after annealing. As can be seen from the spectra, both the peak intensities of C–N and C–O bonds decrease remarkably after the annealing process, while the peak intensity of sp^2-hybridized carbon content augments, indicating the decomposition of EC and PVP stabilizer, as well as a consolidated NGP/PI nanostructure in the sensors. Key parameters including electrical conductivity, thickness, and surface roughness of the sensors before and after the annealing process are presented in Table 4.2. The printed sensors feature an ultra-thin thickness of ~ 1 μm (see Figure 4.14 for detailed results of thickness measurement). The annealed NGP/PI sensors present a thinner thickness and smaller surface roughness, yet a better electrical conductivity than the unannealed NGP/PAA hybrids (Table 4.2), as a result of the complete imidization of PAA and removal of EC and PVP after the annealing process.

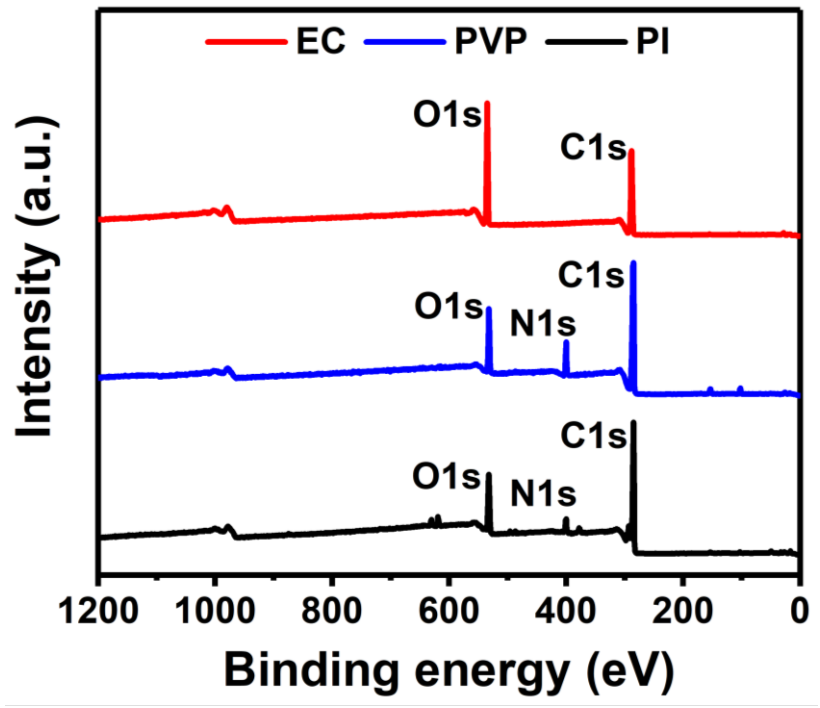

(a)

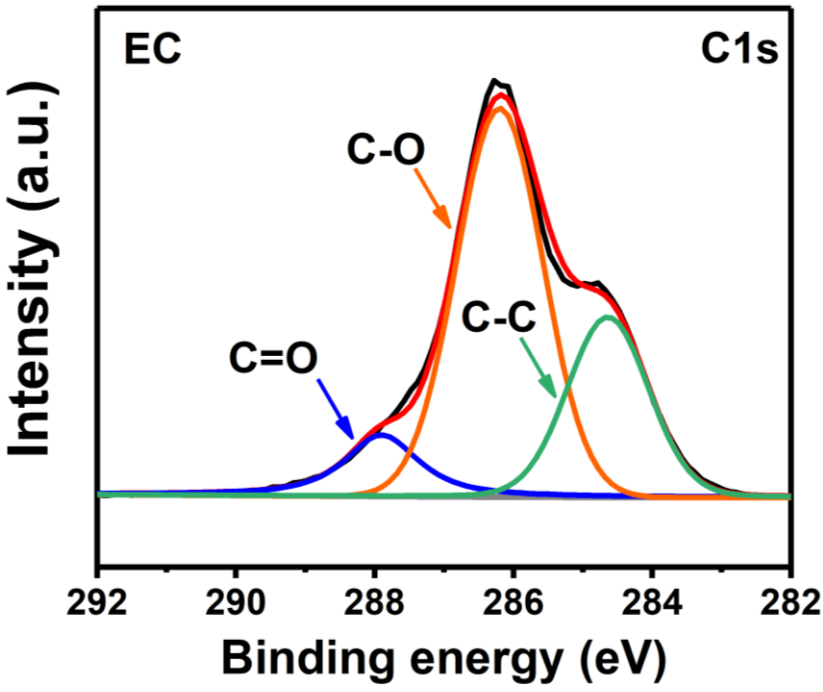

(b)

Figure 4.12 (a) XPS spectra of EC, PVP; (b) XPS spectrum for C1s of EC, (c) PVP, and (d) PI.

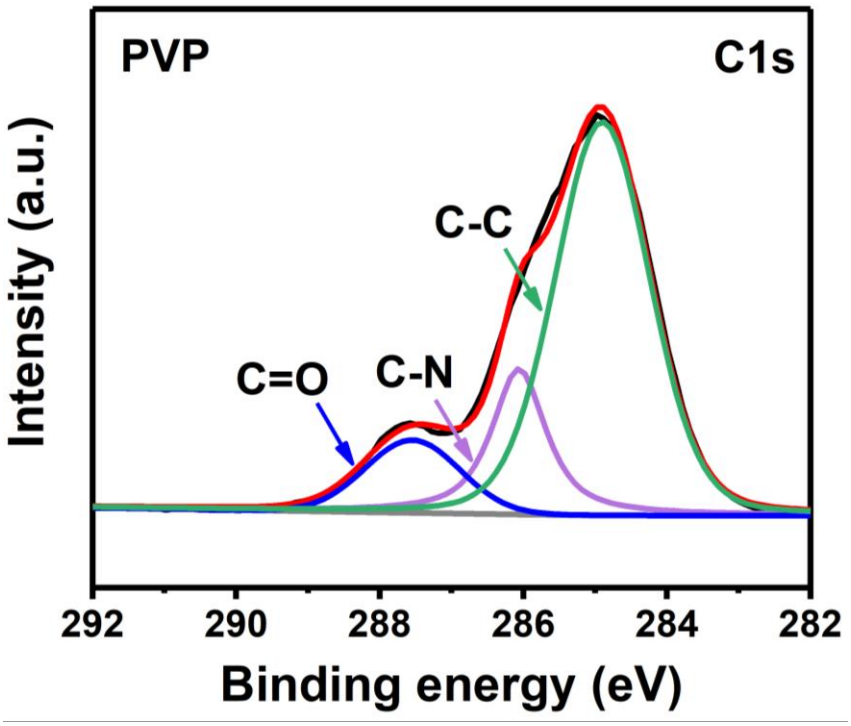

(c)

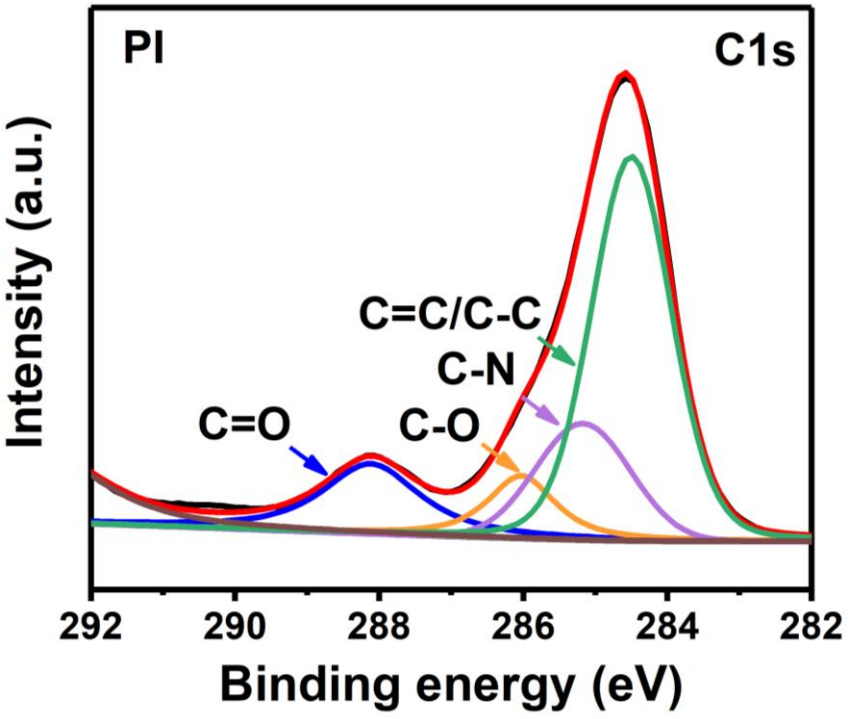

(d)

Figure 4.12 *Cont.*

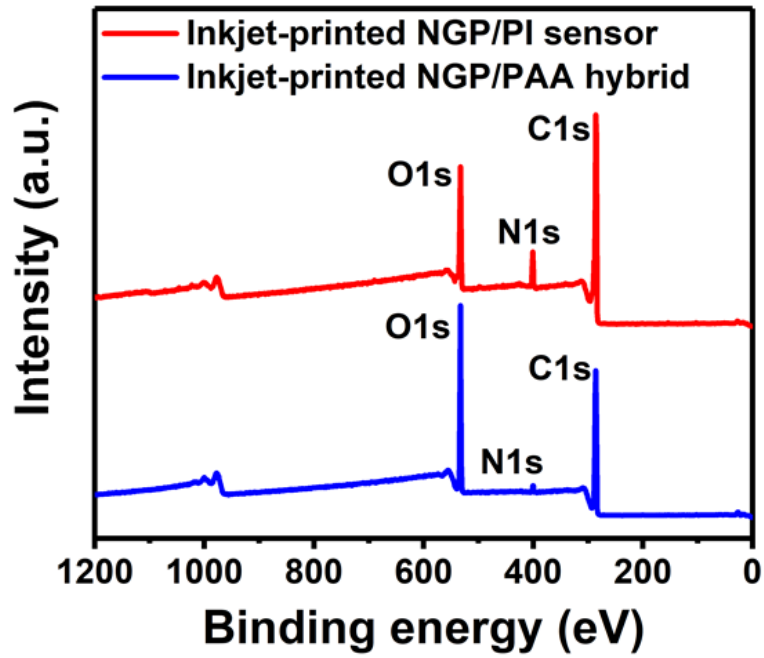

(a)

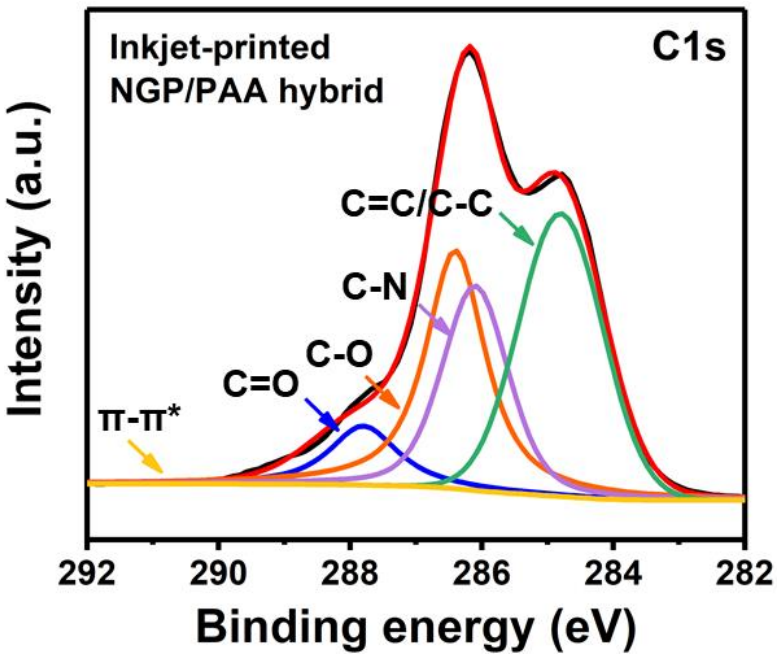

(b)

Figure 4.13 (a) XPS spectra of inkjet-printed NGP/PAA hybrids (before annealing) and NGP/PI sensors (after annealing); (b) XPS spectra for C1s of inkjet-printed NGP/PAA hybrids (before annealing) and (c) NGP/PI sensors (after annealing).

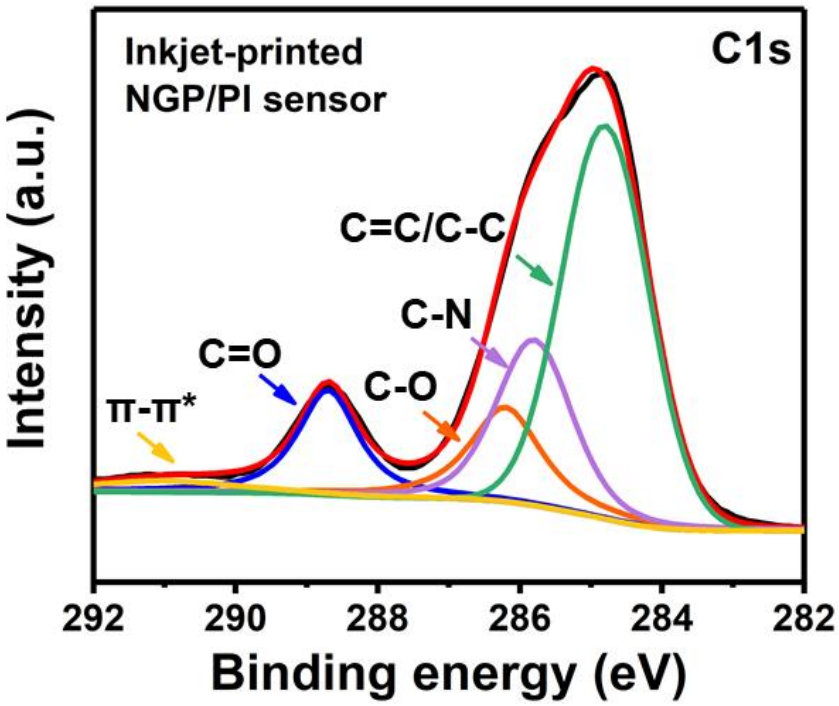

(c)

Figure 4.13 *Cont.*

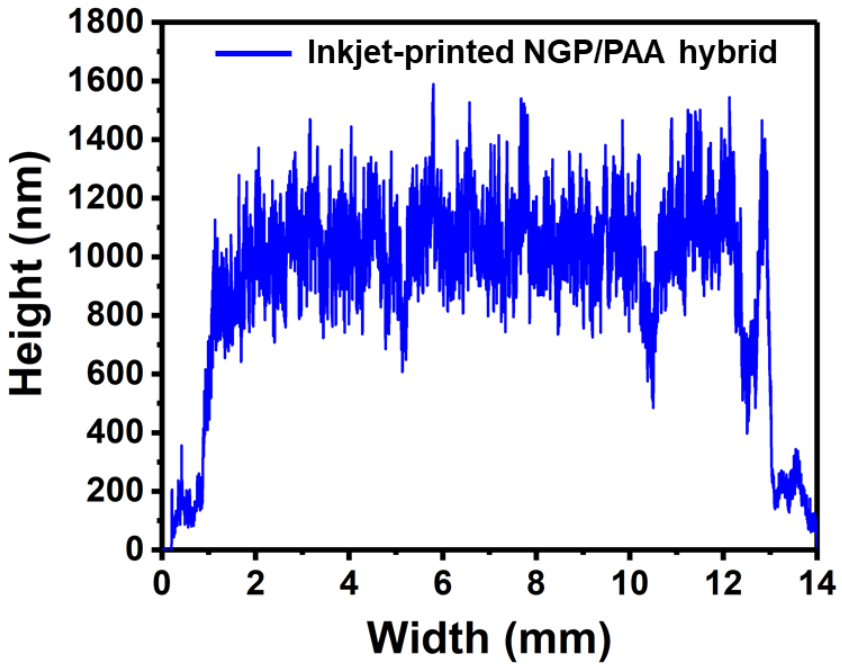

(a)

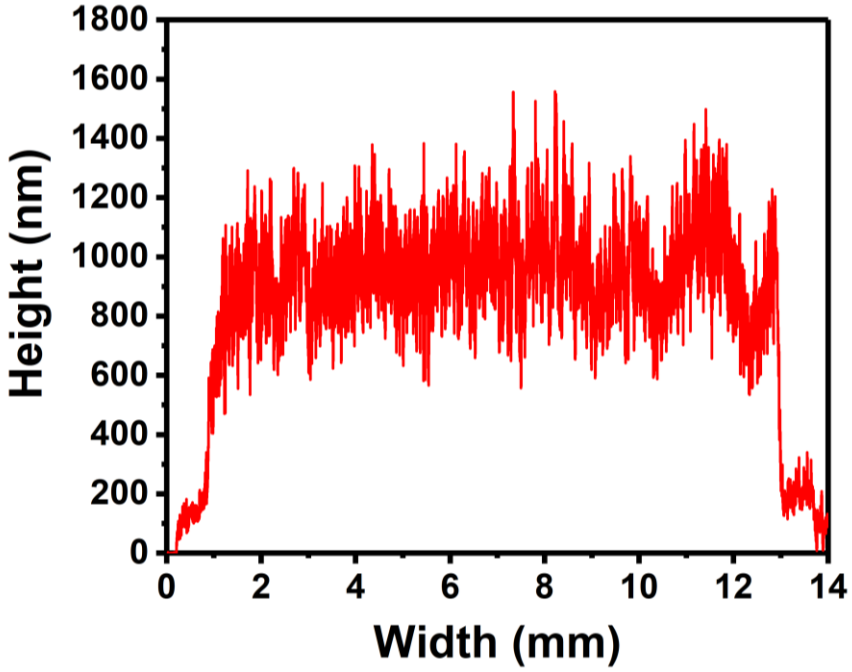

(b)

Figure 4.14 Surface profile of the inkjet-printed (a) NGP/PAA hybrids (before annealing) and (b) NGP/PI sensors (after annealing).

Table 4.2 Physical parameters of the inkjet-printed NGP/PAA hybrids and NGP/PI sensors.

	Conductivity [S cm^{-1}]	Thickness [μm]	Surface roughness [μm]	
			Ra[a)]	Rq[b)]
NGP/PAA hybrids (before annealing)	0.13	1.06	0.12	0.14
NGP/PI sensors (after annealing)	0.27	0.96	0.10	0.13

[a)] Average surface roughness; [b)] Root mean square roughness.

4.4.3 Thermal Stability and Adhesive Strength

Thermal stability of the inkjet-printed NGP/PI sensors is scrutinized with TGA, with results shown in Figure 4.15. With PI as the polymeric matrix, the onset degradation temperature of the printed sensors is as high as 500 and 560 °C, respectively in air and in argon, suggesting excellent intrinsic thermal stability of the sensors. Adhesive strength between the printed NGP/PI sensors and the Kapton substrates is evaluated with a standard adhesion test conforming with ASTM D3359 [14]. Figure 4.16 shows a sensor and the tape after the ASTM D3359 cross-cut tape test, to observe that no any content of the sensor is removed from the substrate after the tape is peeled off, arguing that adhesion has reached an ASTM 5B level, *viz.*, the highest level of adhesion grade. The superb adhesive strength of the sensors is attributed to the hydrogen bonds formed between carbonyl groups of PI matrix and hydrophilic functional groups on the O_2 plasma pre-treated Kapton substrates.

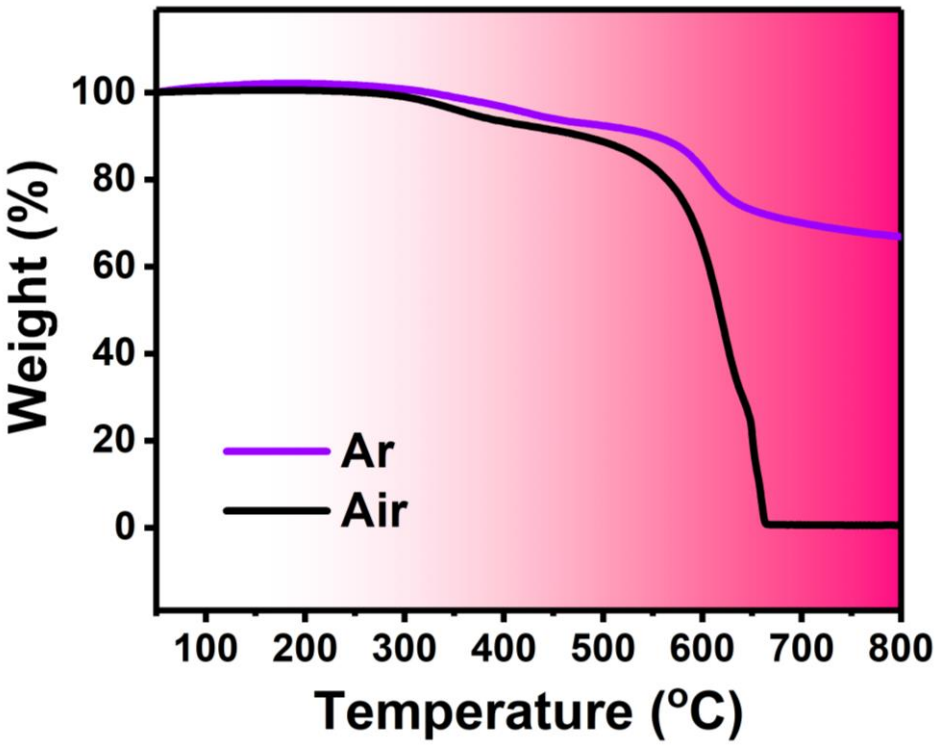

Figure 4.15 TGA curves of inkjet-printed NGP/PI sensors.

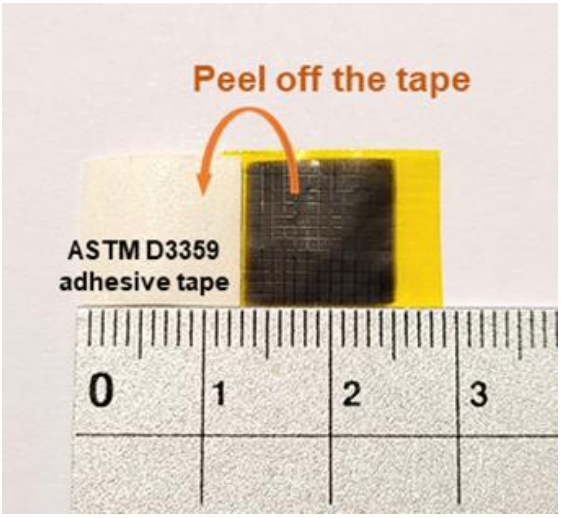

Figure 4.16 The inkjet-printed NGP/PI sensor and adhesive tape after ASTM D3359 cross-cut tape test.

4.5 Calibration of Sensing Capability

The sensing capability of the inkjet-printed NGP/PI nanocomposite sensors is interrogated and calibrated in a broad frequency range up to megahertz. The excitation acousto-ultrasonic wave signal is generated with a waveform generator based on NI® PXIe-1071 platform and amplified by a Ciprian® US-TXP-3 linear power amplifier, taking a waveform of five-cycle Hanning-function-modulated sinusoidal tone-bursts with the central frequency ranging from 100 to 1,600 kHz (with a stepping of 25 kHz). A glass fibre/epoxy composite laminate plate (600 mm long and wide, and 1 mm thick) is prepared, and a lead stibium niobium (PSN)-33 piezoelectric wafer as an acousto-ultrasonic wave actuator is surface-bonded at the centre of the plate (Figure 4.17). The excitation signal is applied on the PSN-33 wafer to introduce an acousto-ultrasonic wave signal into the plate. To examine the acousto-ultrasonic wave sensing capability of the inkjet-printed NGP/PI nanocomposite sensors, eight printed sensors are silver-pasted with electrodes and surface-mounted on the plate, and for each printed sensor, a PSN-33 wafer is collocated alongside the sensor for signal comparison and calibration. Each printed sensor is connected to a self-developed signal amplification module which comprises a resistance-voltage (R-V) transformation system [164]. Such a module converts piezoresistive variations to electrical signals (with 1,385 times gain amplification), and the converted acousto-ultrasonic wave signals and their counterpart signals captured by PSN-33 wafers are recorded simultaneously with an oscilloscope (DSO 9064A, Agilent®). The electrical resistances of electrical cables and connections in the measurement system are negligible.

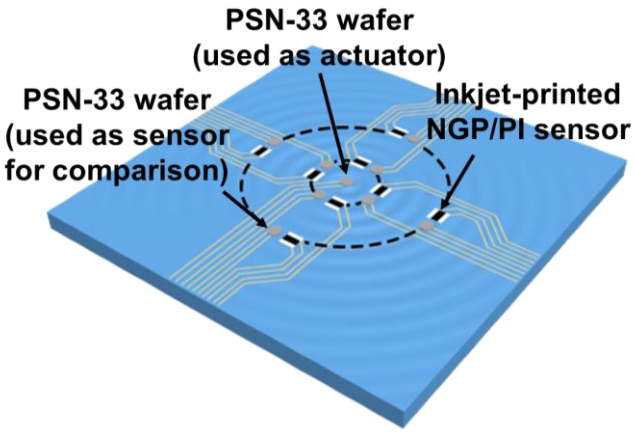

Figure 4.17 Schematic of experimental set-up for acousto-ultrasonic wave signal acquisition.

In the calibration experiment, for acousto-ultrasonic wave signals in the frequency range of 100-600 kHz, the sensing distance is 150 mm (using the four NGP/PI sensors and four PSN-33 sensors located along the outer circle, see Figure 4.17), while the sensing distance is decreased to 50 mm (both types of sensors along the inner circle) for signals beyond 600 kHz. The reason of selecting different measurement distances with regard to different acousto-ultrasonic wave frequencies is that an acousto-ultrasonic wave signals of higher frequency attenuate quicker than that of a lower frequency, and the shortened measurement distance for signals beyond 600 kHz is conducive to remain an adequate signal-to-noise ratio. As some representative results, Figure 4.18 comparably displays the raw acousto-ultrasonic wave signals captured by the printed NGP/PI sensors and the PSN-33 wafers at 175 kHz, to observe that the first-arrival wave component (*viz.*, the zeroth-order symmetric Lamb wave mode guided by the laminate, denoted by S_0 mode hereinafter) in the signals perceived by the printed sensors is in quantitative agreement with that captured by the PSN-33 wafer in terms of the arrival time. The printed NGP/PI sensors show an SNR of 35.62 dB (S_0

mode, 175 kHz), which is higher than that of the PSN-33 wafers (34.56 dB). In addition, the zeroth-order anti-symmetric Lamb wave mode (A_0) following the S_0 mode, is also perceived faithfully and accurately by the printed sensors. Figure 4.19 displays the signals captured by both types of sensors under an excitation of 1,600 kHz, which are filtered by a fast Fourier transformation-based algorithm to reduce crosstalk and noise. The printed sensors are observed to maintain their high degree of sensitivity, fidelity, and precision at such a high frequency.

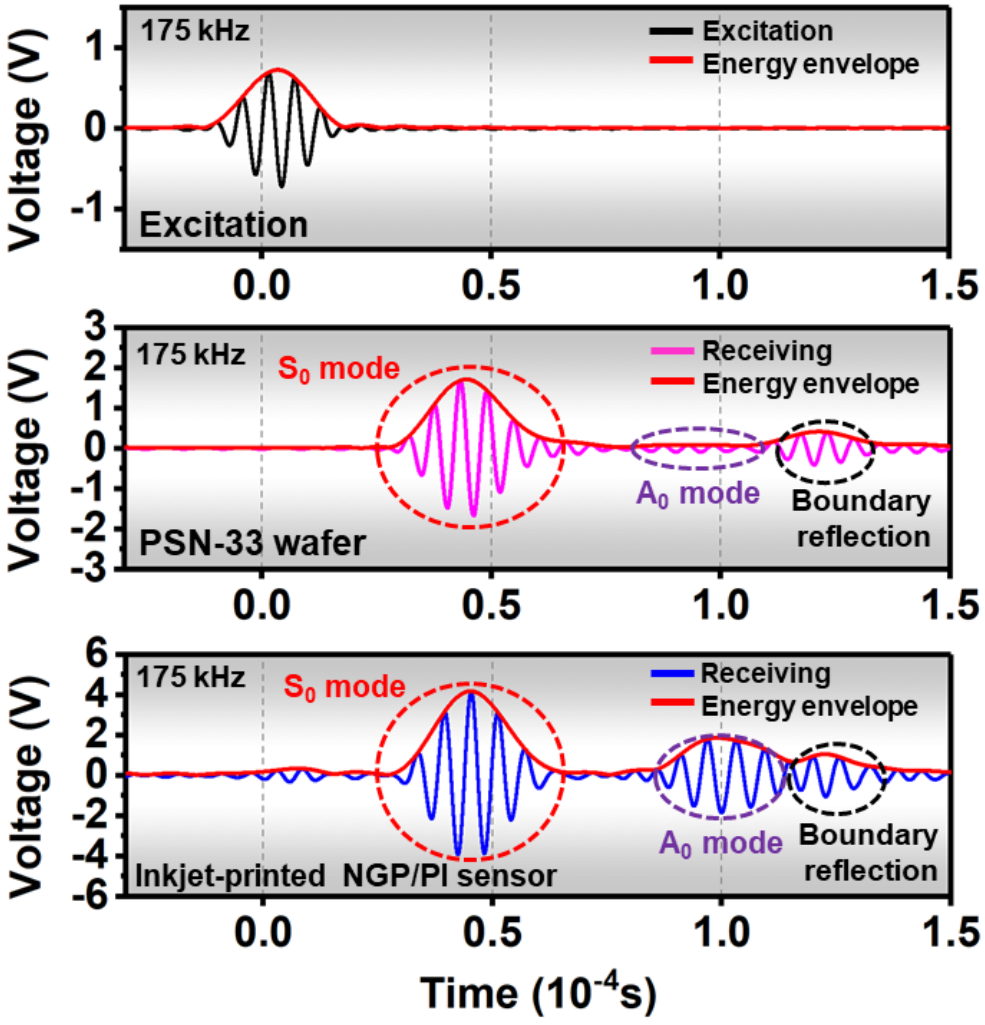

Figure 4.18 Excitation signal, and acousto-ultrasonic wave signals captured by the PSN-33 wafers and by inkjet-printed NGP/PI sensors at 175 kHz.

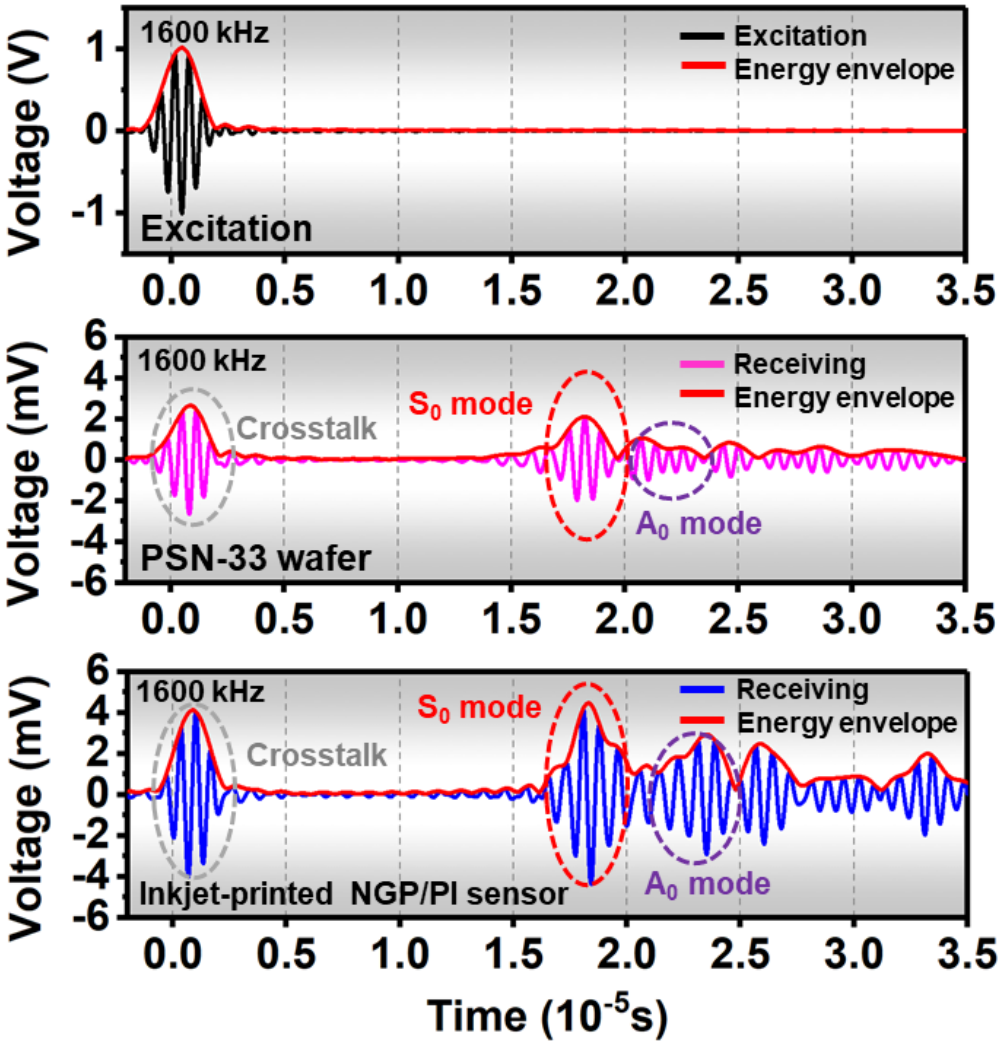

Figure 4.19 Excitation signal, and acousto-ultrasonic wave signals captured by the PSN-33 wafers and by inkjet-printed NGP/PI sensors at 1,600 kHz.

To examine the effect of annealing on sensing capacity, signals captured by the NGP/PAA hybrids (namely before annealing) and by the NGP/PI sensors (*viz.*, after annealing) are compared in Figure 4.20. As can be seen from Figure 4.20, the signal amplitude for NGP/PAA hybrids at 175 kHz is lower than that for NGP/PI sensors, implying that the consolidated nanostructure after imidization without residual solvent and polymer stabilizer (EC and PVP) plays a critical role in enhancing the performance of sensing acousto-ultrasonic wave signals.

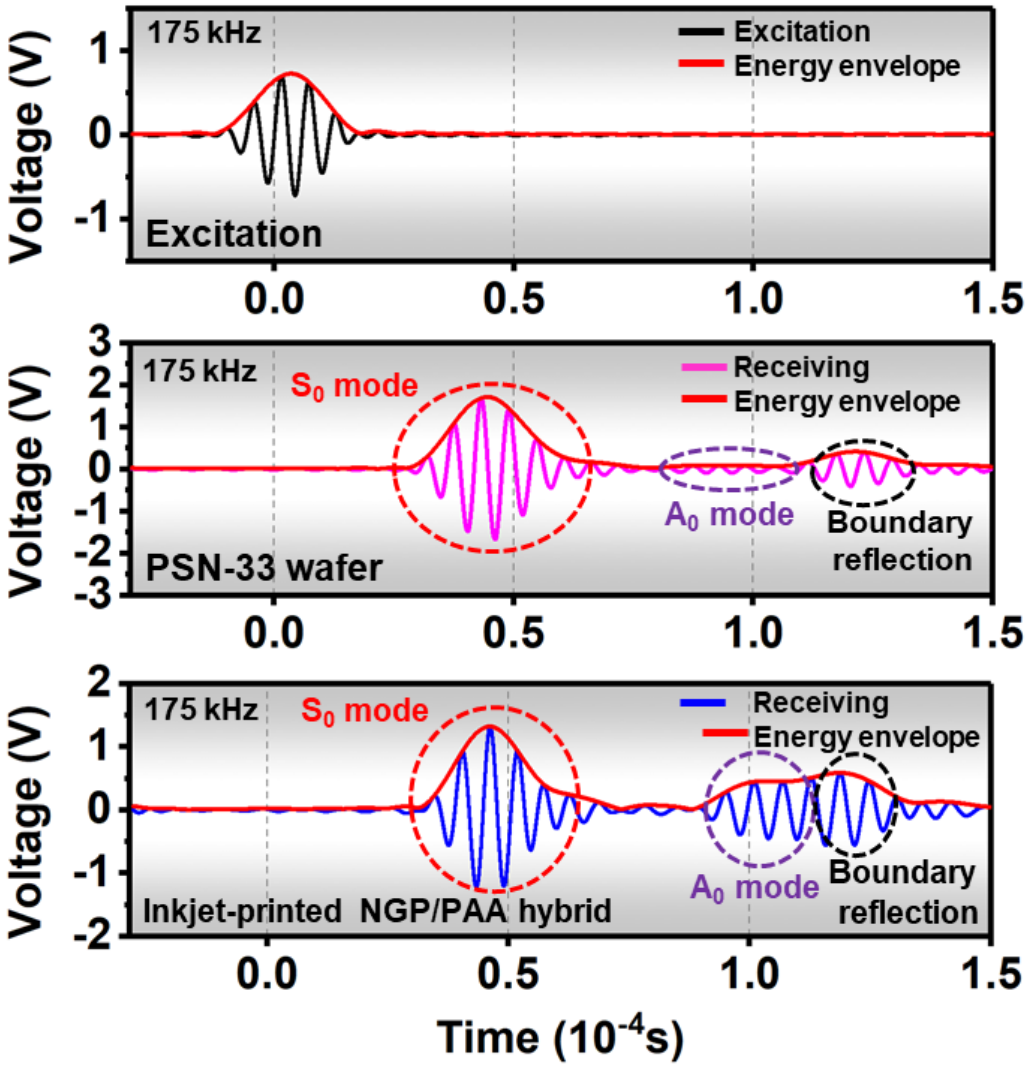

Figure 4.20 Excitation signal, and acousto-ultrasonic wave signals captured by the PSN-33 wafers and inkjet-printed NGP/PAA hybrids at 175 kHz.

Figures 4.21 and 4.22 compare signals captured by the NGP/PI sensors and PSN-33 wafers over the time-frequency domain, respectively, from 100 to 1,600 kHz. In such a broad frequency regime, both sensors show high consistency. These findings articulate that printed NGP/PI sensors faithfully perceive broadband acousto-ultrasonic wave signals, with comparable performance as that of commercial

piezoelectric sensors, yet with additional merits including flexibility, lightweight and rapid prototyping. Such excellent acousto-ultrasonic wave signal sensing performance is attributed to their consolidated nanostructure established by NGPs and PI. As commented earlier, with the developed NGP/PAA nanocomposite ink and the drop-on-demand inkjet printing fabrication process, NGPs are distributed evenly in PI polymeric matrix of the sensors, forming a stable and uniform electrical-conductive network. As is known that quantum tunneling effect can be triggered between adjacent conductive nanoparticles in an insulating polymer when the nanoparticles are in close proximity with others [138]. When the printed sensors are subject to acousto-ultrasonic wave-induced high-frequency dynamic strain, such a disturbance is usually too weak to break up the electrical-conductive network formed in the sensors, which, however, is adequate to alter the distance between adjacent NGPs, leading to the variation of tunneling condition of charged carriers and the change in tunneling resistance among NGPs. It is noteworthy that the π-π interaction formed in the sensors can accelerate the charge carrier transfer between NGPs and PI [165], but π-π interaction is not as strong as covalent bonding or electrostatic interaction. The consequence is that when acousto-ultrasonic waves traverse the sensor, the particulate movement of NGPs also affects the binding force and charge transfer of π-π interaction between NGPs and PI matrix (Figure 4.23), and this becomes an additional factor to amplify the variation of tunneling resistance between NGPs and engender the strong and accurate response of the NGP/PI sensors to high frequency acousto-ultrasonic waves.

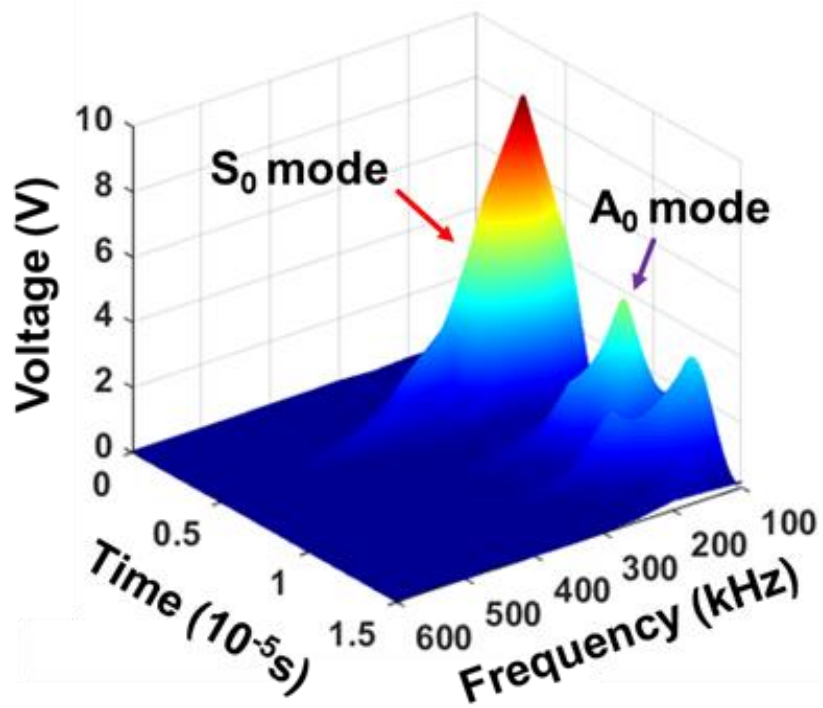

(a)

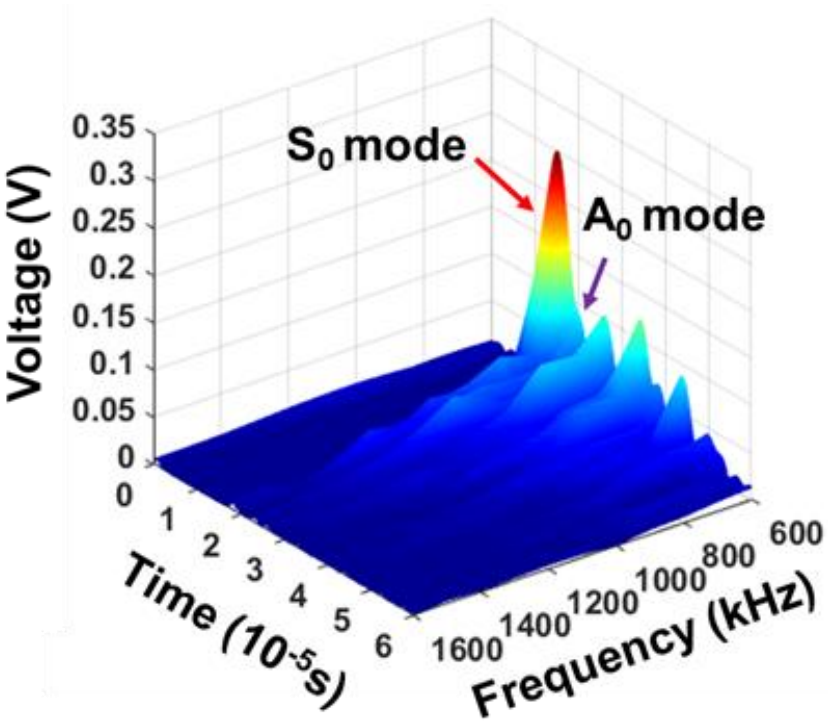

(b)

Figure 4.21 (a) Signals captured by NGP/PI sensors in a sweep range from 100 to 600 kHz, and (b) from 600 to 1,600 kHz.

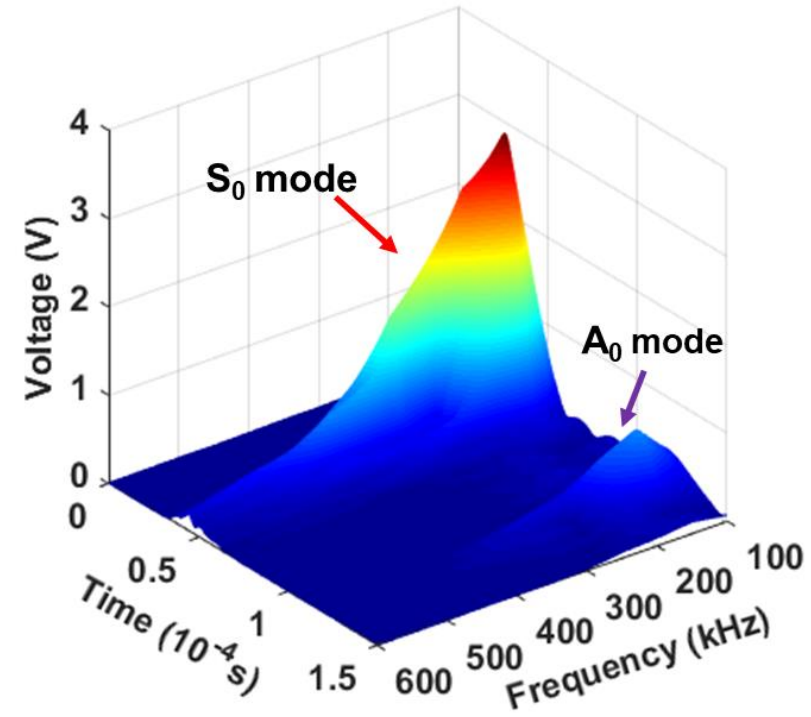

(a)

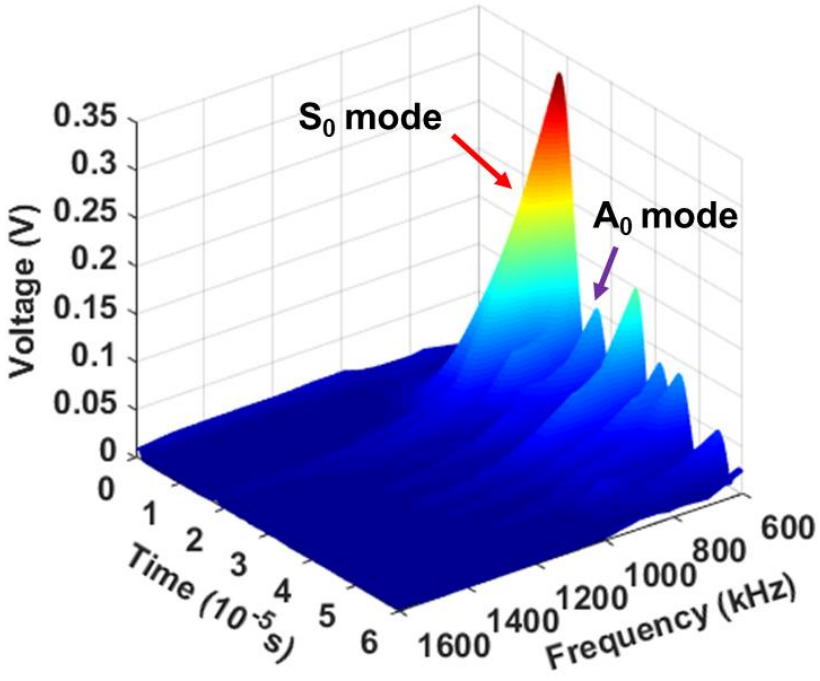

(b)

Figure 4.22 (a) Signals captured by the PSN-33 wafers in a sweep range from 100 to 600 kHz, and (b) from 600 to 1,600 kHz.

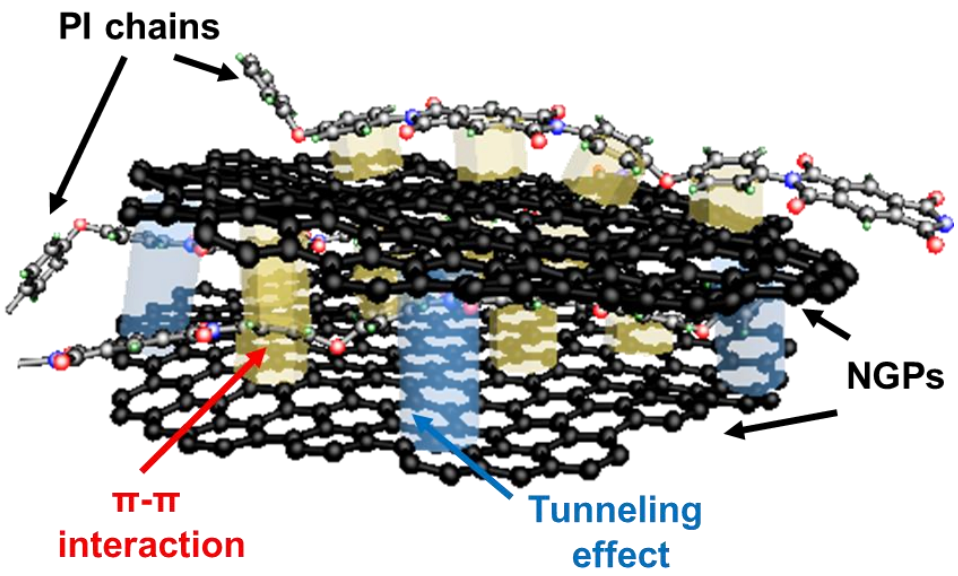

Figure 4.23 Schematic illustration of the sensing mechanism of the printed NGP/PI sensors.

To put into perspective, the gauge factor (K) of the printed sensors, in responding to acousto-ultrasonic waves, is calculated as [98]

$$K = \frac{\Delta R}{R_0} / \varepsilon \,, \tag{4.3}$$

where ΔR is the resistance change of the sensor, R_0 the intrinsic resistance of the printed NGP/PI sensors, and ε the acousto-ultrasonic wave-induced dynamic strain. In Equation (4.3), $\Delta R/R_0$ (2.89×10^{-3}) is calculated according to the acousto-ultrasonic wave signal magnitude of the sensors, by making reference to the amplification scale and principle of the R-V circuit in the self-developed signal amplification module at 175 kHz. ε is calculated via [61]

$$\varepsilon = \frac{Vd_{31}(1-k_{31}^2)}{tk_{31}^2}, \tag{4.4}$$

where V denotes the peak-to-peak value of the responsive voltage of PSN-33 wafers

adjacent to the NGP/PI sensors, d_{31} the in-plane piezoelectric coefficient of the wafers, k_{31} the electromechanical coupling coefficient of the wafers, and t the thickness of the wafers. With the key parameters of the PSN-33 wafer listed in Table 4.3, ε is determined to be 3.91×10^{-6} at 175 kHz, and K is calculated as high as 739 via Equation (4.3). Such an extraordinarily high gauge factor of the inkjet-printed NGP/PI sensors verifies their excellent sensing performance to high frequency acousto-ultrasonic wave signals – a result that has never been achieved by the prevailing nanocomposite sensors.

Table 4.3 Physical parameters of the PSN-33 piezoelectric wafers.

Properties	Values
Diameter (d) [mm]	12
Thickness (t) [mm]	1
In-plane piezoelectric coefficient (d_{31}) [pC N^{-1}]	-160
Electromechanical coupling coefficient (k_{31})	0.35

4.6 Summary

NGP/PI ultrasensitive thin film ultrasound sensors are developed using inkjet printing with rigorously designed and optimized NGP/PAA sensing ink. The novel graphene-based sensing ink is efficiently produced by facile high-shear LPE directly from inexpensive bulk graphite, exhibiting advantages of good functionality, high graphene concentration, excellent storage stability and inkjet printability. The printed film sensors are demonstrated with ultra-thin thickness (~ 1 μm), excellent thermal stability

and extraordinary adhesive strength (ASTM 5B level). By virtue of the uniform nanostructure in the sensors, quantum tunneling effect triggered among NGPs and π-π interactions formed between NGPs and PI allow the printed sensors to have a gauge factor of 739 in responding to acousto-ultrasonic waves at 175 kHz. The sensors have proven capability of accurately perceiving acousto-ultrasonic wave signals up to 1.6 MHz. The NGP/PI sensors feature not only extraordinary sensitivity, fidelity, and sensing precision that are comparable to popular commercial piezoelectric wafers, but also additional merits including light weight, low cost, large-scale production, and simplicity in fabrication, highlighting their alluring potentials in developing the next generation of wearable devices, ultrasound identification and acousto-ultrasonic wave-driven health monitoring.

CHAPTER 5

Temperature Effect on Inkjet-printed Ultrasound Sensors

5.1 Introduction

Aircraft and spacecraft are operated in extremely atrocious conditions with acute variation in ambient parameters including air pressure, humidity, and temperature, to name a few. Amongst various ambient parameters, temperature has been evidenced as the most influential factors to critically affect the performance of an SHM system and the sensors in particular [166]. The temperature of the operating environment for typical aircraft varies from –50 ºC when they fly at a high altitude to 60 ºC when park in a closed hangar. For spacecraft, tremendous heat flux induced during the re-entry to the Earth atmosphere elevates the temperature as high as ~1650 ºC. Even with the thermal protection systems, the temperature of internal components in spacecraft soars to 150 ºC. When orbiting, spacecraft undergo a drastic fluctuation in temperature (~70-100 ºC) within a day when facing towards or away from the sun [167]. On top of that, the internal heat radiation from cabin electronics is another unneglectable hostile thermal factor which can negatively affect structural performance.

The aggressive environmental exposures not only degrade the performance of sensors *per se*, but also weaken the adhesion between sensors and the host structures. A thermal cycle as a result of acute change of ambient temperature progressively fatigues adhesive layers, potentially leading to exfoliation of sensors. In addition, thermal fluctuation alternately expands and contracts a structure, and changes material phase or chemical composition, jointly leading to deviation in material geometry and material properties including Young's modulus, Poisson's ratio and acoustic parameters (*e.g.*, transmitting velocity of the acousto-ultrasonic waves) [168]. Consequently, under the interference from temperature variation, the changes of signal features extracted by an SHM system, such as the arrival time of ultrasonic waves, may not faithfully reflect the health status of the inspected structure, leading to false alarm or ignorance of damage *de facto* [169, 170].

With the temperature effect in mind, the sensors used to implement *in situ* SHM for aircraft or spacecraft must be rigorously selected, and sensor networks must be deliberately configured, so that a desired level of reliability and durability can be maintained within the entire range of temperature variation during operation. The rudimental requirements embrace:

(i) The sensors to accommodate *in situ* SHM of aircraft and spacecraft must be stable, durable and robust at severe operating temperature extremes, and able to withstand mechanical strain under severe operating conditions for a prolonged period;
(ii) The sensitivity and accuracy of the sensors must not be compromised within the entire range of temperature fluctuation for a complete flight;
(iii) Compensation must be applied to correct contaminated signal features due to

temperature variation;

(iv) Sensors should maintain an adequate level of reliability after environmentally harsh storage, transit, and operation [171].

Driven by this, Blaise and Chang investigated the performance of embedded piezoelectric wafers (PZT-5A) in capturing ultrasonic wave signals at low temperatures (–90 to 20 ºC), and concluded that in this temperature variation range, ultrasonic wave signals could be reconstructed using an empirical linear model [172]. Raghavan and Cesnik examined the ultrasonic signal features captured by PZT-5A piezoelectric wafers from spacecraft structures subjected to a varying temperature from 20 to 150 ºC, to reveal that under elevated temperature, time of flight (ToF) of the signals increased with temperature, and signal amplitude was affected by adhesion properties [167]. Lanza di Scalea and Salamone calibrated the responses of monolithic PZT patches and macrofibre composite (MFC) patches, when ambient temperature changed from –40 to 60 ºC which corresponds to that change during a normal flight, and argued that for both PZT and MFC, the variations in ultrasonic wave signal amplitude followed two opposite trends below and above 20 ºC, respectively [173]. Several temperature compensation methods have also been proposed, to minimize the temperature effect, as typified by baseline signal stretch (BSS) [174], optimal baseline selection (OBS) [175], combination of BSS and OBS [176, 177], and combination of OBS and adaptive filter [178].

Nevertheless, prevailing studies on temperature effect on sensor performance are restricted to piezoceramic-type sensors, which have gained prominent popularity in developing SHM approaches for aircraft and spacecraft. The sensing performance of

nanocomposite sensors under an extended range of temperature change has yet been attended hitherto. In this chapter, the temperature effect on nanocomposite piezoresistive sensors in acquiring broadband acousto-ultrasonic wave signals is investigated in an extensive temperature regime (–60 to 150 ºC) that spans the thermal extremes undergone by typical aircraft and spacecraft. To this end, the developed thin film ultrasound sensors are further printed with electrodes and insulating layers, to form AIP sensors. A theoretical model is developed to predict dispersive characteristics of acousto-ultrasonic waves at varying temperatures, against which the capability and accuracy of the sensors in perceiving broadband acousto-ultrasonic wave signals under harsh thermal cycles are examined experimentally. Results are also compared with commercial piezoelectric wafers. Taking a step further, a sensor network consisting of AIP sensors is configured to implement *in situ* characterization of damage in a typical aerospace structural component under acutely varying temperatures.

5.2 Fabrication of All-inkjet-printed Sensors

5.2.1 Printing of Sensing Ink

Central to the preparation of sensing ink for developing AIP sensors is the ink stability and printability, in addition to its functionality. Conductive CB powders (CABOT® Black Pearl 2000, average particle diameter: 30 nm, as nanofiller) are mixed with PVP (PVP K-30, Sigma-Aldrich, as polymer matrix) at a weight ratio of 1:2 (0.28 g and 0.56 g, respectively) in 40 mL NMP (J&K Scientific). The dispersion of CB and PVP

in NMP solvent is stabilized by adding 0.08 g SDBS (Sigma-Aldrich, as surfactant). The mixture is mechanically stirred at 400 rpm for 2 hours at a room temperature (25 ^{o}C), followed by a sonication for 1 hour in an ultrasonic bath. After sonication, the CB/PVP dispersion is filtered through a 0.45 μm-diameter PVDF micropore sieve, to remove large CB/PVP agglomerates so that blockage and clogging of the inkjet printer nozzle can be avoided.

Such produced CB/PVP ink shows good stability, printability, and wettability. The ink is printed directly onto a substrate using a PiXDRO LP50 inkjet printer (OTB Solar-Roth & Rau) equipped with a DMC-11610 cartridge (Dimatix-Fujifilm Inc.). The printing process allows a sensor to be customizable in different patterns and printed passes, to accommodate various needs of sensing. Details of the sensing or printing process can be referred to Chapter 3. In this study, each sensor, printed on the substrate with the sensing ink, measuring 10.0 mm in width and 20.0 mm in length, with 12 printed passes (leading to a total thickness of ~1.0 μm). The substrate is pre-treated with O_2 plasma prior to the printing process, endowing the substrate with high surface energy which is conducive to the improvement of wettability of the ink and good adhesion between sensors and the substrate. Figure 5.1 shows such produced sensors printed on a flexible heat-resistant PI film substrate, along with a typical SEM image of the printed sensors showing their morphology.

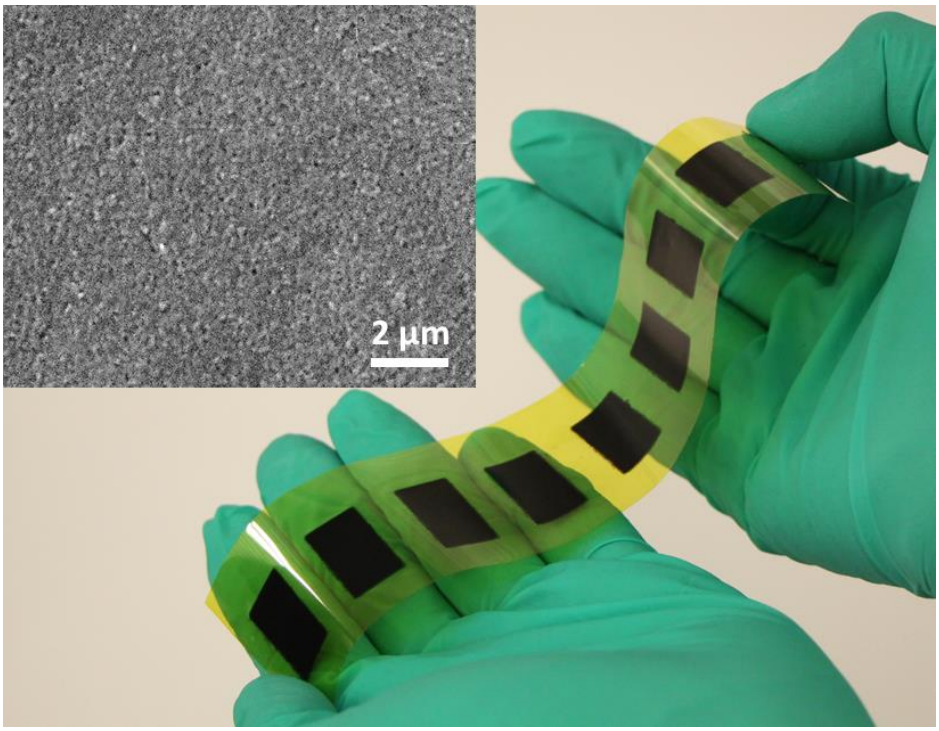

Figure 5.1 Inkjet-printed CB/PVP sensors on a PI film substrate (insert: SEM (20.00 k× magnification) image of the printed sensors).

Thermal stability of the printed sensors is calibrated through TGA, using a TGA/DSC3+ (Mettler Toledo) system, to show the intrinsic thermal stability of the fabricated nanocomposites. In TGA, the proportion of remained mass/weight is measured over time as the temperature changes. The sensors are heated under an argon flow at 80 mL min^{-1}, from room temperature to 800 ºC with a heating rate of 10 ºC min^{-1}. As can be seen from Figure 5.2, the sensors remain their stability at a temperature as high as ~370 ºC, since which the sensors tend towards initial decomposition, as ~370 ºC is the decomposition temperature of PVP polymer.

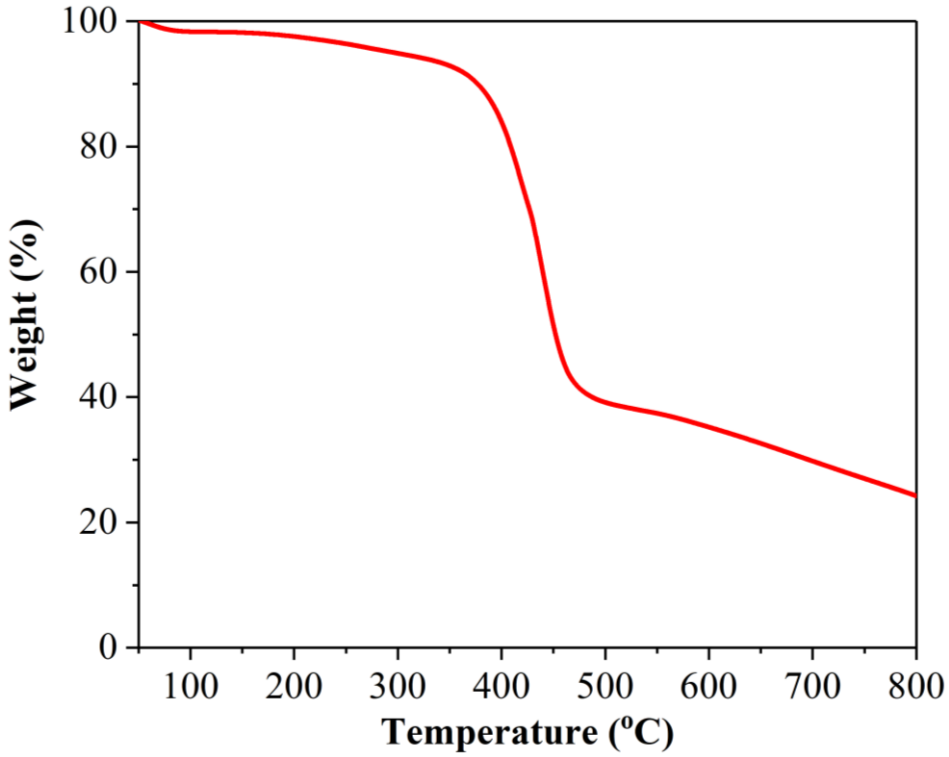

Figure 5.2 TGA curve of inkjet-printed CB/PVP sensors.

5.2.2 Electrode and Insulating Layer Printing

Silver electrodes and insulating layers are installed onto the printed CB/PVP sensors via the same inkjet printing process, as illuminated by the flowchart shown in Figure 5.3. A pair of silver electrodes is inkjet printed with commercial Metalon® JS-A211 silver ink (Novacentrix, 40.0 wt.% Ag, Average particle size: 36 nm) onto each sensor, with the gap of 2 mm between two electrodes. The printing resolution is set as 500 dpi in both cross-scan and in-scan directions (inkjet droplet spacing ~50 μm), which is the same as that of the sensor printing process, and the electrodes are fabricated with two printed passes. The AIP sensors with AIP electrodes are then heated on a hot plate at 140 °C for 10 mins, to accelerate the solvent evaporation and curing of the silver electrodes. Insulating layers are installed to prevent possible external interference or

damage, such as short circuit and scratch. To fabricate the insulating layers, PAA solution (12.8 wt.% (80% NMP/20% aromatic hydrocarbon), Sigma-Aldrich; 1g) is diluted in 19 mL NMP (J&K Scientific), followed with mechanical stirring at a room temperature for 15 mins at 800 rpm. The printing resolution is set as 600 dpi in both cross-scan and in-scan directions, higher than the sensor and electrode printing of 500 dpi, so that the inkjet droplet spacing is reduced to ~42 μm. The prepared PAA ink is then printed onto the surfaces of the sensors and electrodes using the same inkjet printing platform, after which the substrates are heated on a hot plate at 160 ^{o}C for 15 mins. Such a heating process is aimed at enabling the solvent evaporation and imidization of PAA and consequently forming the insulating layer [179]. The thermal imidization process of PAA is shown in Figure 5.4. With such a fabrication process, the nanocomposite-based AIP sensors are fabricated directly on either a flexible film or a structural surface. A multitude of such produced sensors can further be networked via inkjet-printed circuits developed with the same silver ink for electrodes, and Figure 5.5 displays a paradigm of the sensor network configured by six AIP sensors deployed on a glass fibre-reinforced plastic (GFRP) laminate.

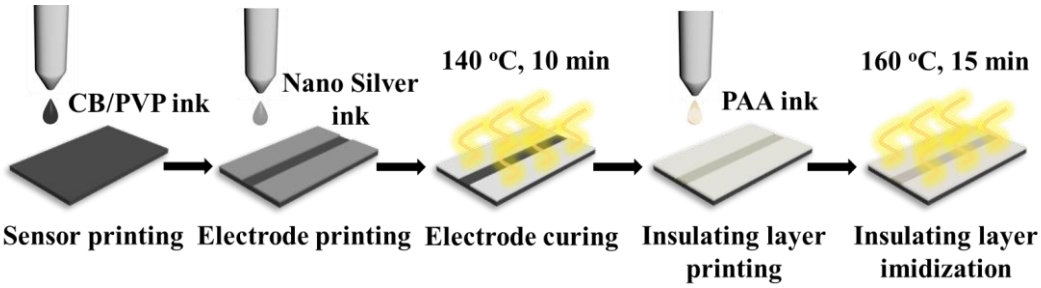

Figure 5.3 Process flow of electrode and insulating layer printing of AIP sensors.

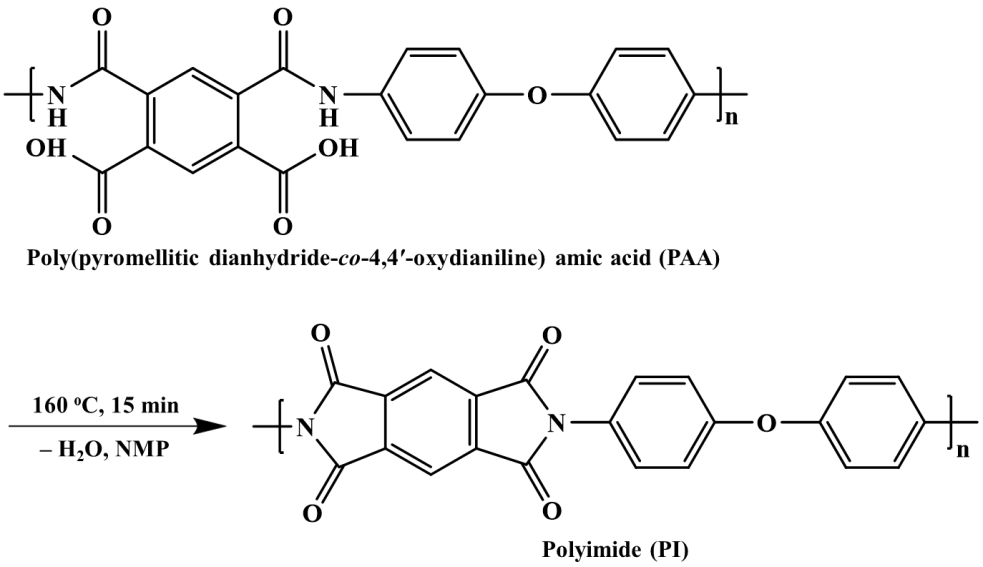

Figure 5.4 Thermal imidization process of PAA.

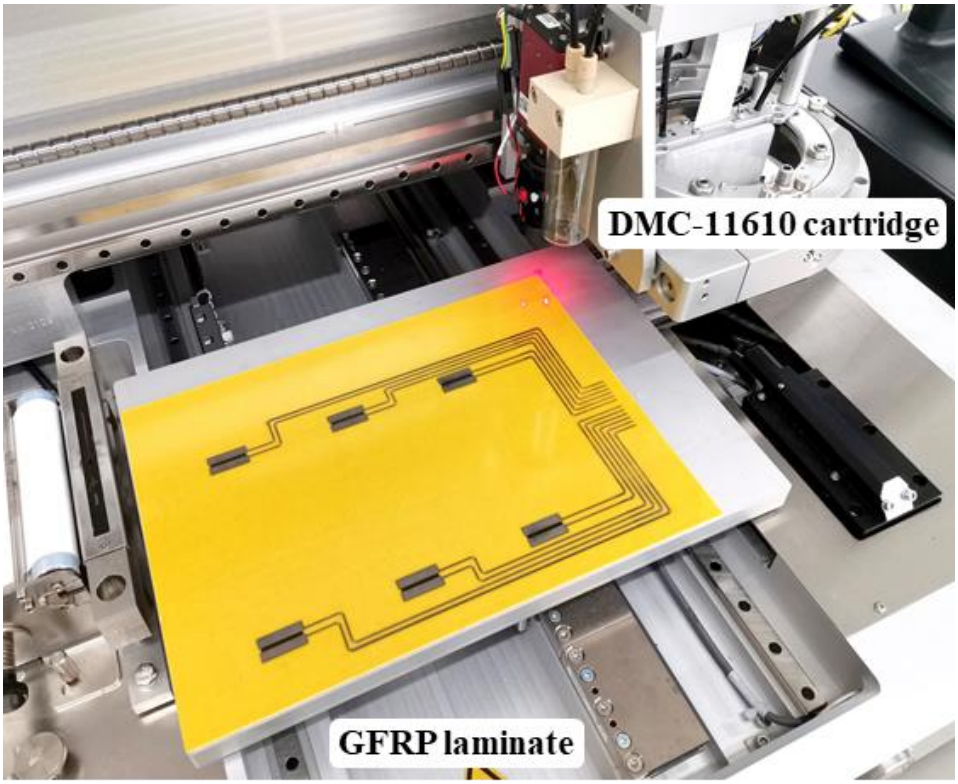

Figure 5.5 An AIP sensor network with printed circuits on a GFRP laminate.

5.3 Sensing Capability at Varying Temperatures

The sensing capability of the developed AIP sensors in responding to broadband acousto-ultrasonic waves is examined in an extensive temperature regime (–60 to 150 ^{o}C) that spans the thermal extremes undergone by typical aircraft and spacecraft. An aluminium alloy (6061-T6) plate (600 mm long and wide, 2 mm thick) is prepared, surface-bonded with a PZT wafer (Ø12 mm, 1 mm thick) that is used as an ultrasonic transmitter; an AIP sensor deposited on a PI film, produced as described in Section 5.2, is surface-glued on the plate, 210 mm apart from the PZT transmitter, for signal acquisition, as shown in Figure 5.6(a). Another surface-mounted PZT wafer is collocated alongside the AIP sensor, to capture counterpart signals for comparison. To securely bond the PZT wafers and the AIP sensor on the plate, the plate surface is roughened with light sanding and cleaned by acetone, and otherwise the weak bonding or bonding agent degradation under thermal cyclic loads can result in weak and inaccurate sensing or even exfoliation of sensors. The PZT wafers are adhered on the aluminium plate with a two-component epoxy (Epotek® 353ND, Epoxy Technology Inc.), while the AIP sensor is glued with single-component bonding agent (SELLEYS® Supa Glue Shock Proof) which is of a higher degree of operational simplicity. The use of different adhesives in this study is aimed at achieving the best bonding conditions for two different types of sensors. The adhesion and gluing are cured overnight at 20 ^{o}C, and a light weight (500 g) is applied on each wafer and sensor to warrant adequate bonding.

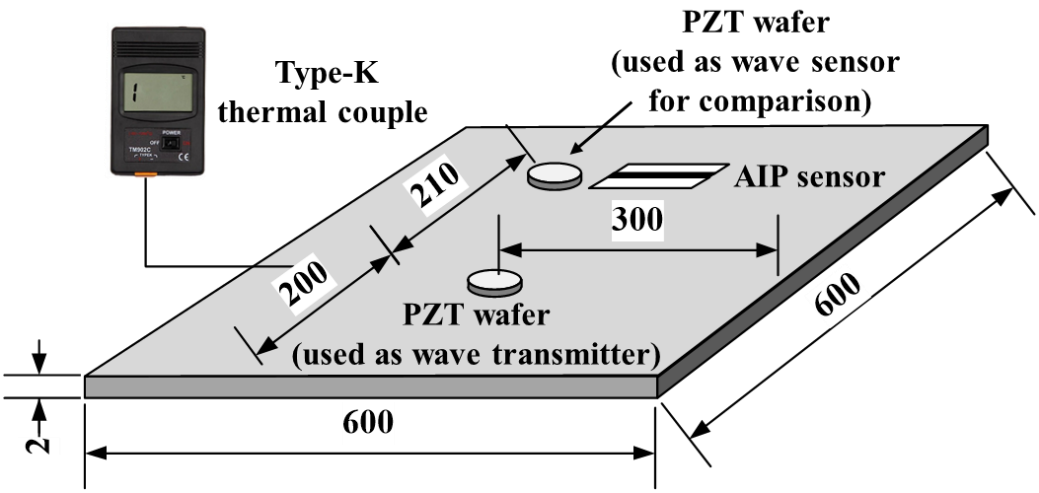

(a)

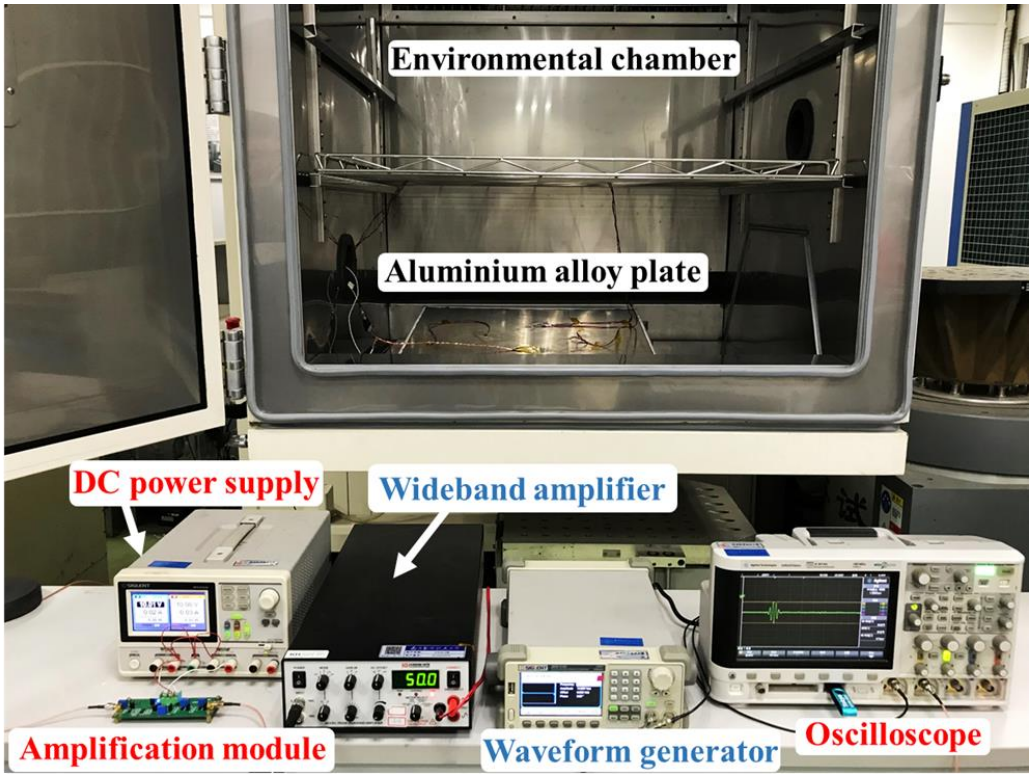

(b)

Figure 5.6 (a) Schematic of experimental set-up for broadband acousto-ultrasonic wave acquisition (unit: mm); and (b) measurement system for ultrasonic wave acquisition under varying temperatures.

Acousto-ultrasonic wave signals are acquired at varying temperatures in a computer-controlled environmental chamber (THV1070W, Hongrui) which regulates the ambient temperature between –60 and 150 ^{o}C precisely with a heating or cooling rate of 1 ^{o}C min^{-1}. The excitation signals are generated with an arbitrary waveform generator (SIGLENT SDG 5122) and amplified by a wideband amplifier (7602M, Krohn-Hite Corporation), taking a waveform of five-cycle Hanning-function-modulated sinusoidal tone-bursts with the central frequency ranging from 50 to 500 kHz (with an increment of 25 kHz). The excitation signals are applied on the PZT transmitter to emit acousto-ultrasonic waves into the aluminium plate. The signals are then captured by the AIP sensor. Temperature of the plate is measured with a type-K thermal couple (apuhua TM-902C), schematically illustrated in Figure 5.6(a). The sensor is connected to a self-developed amplification and signal conditioning module via shielded cables. In the module, a Wheatstone bridge converts piezoresistive variations to electrical signals. The converted signals and their counterpart signals captured by the PZT wafer are synchronously registered with a 4-channel digital oscilloscope (MSOX 3014A, Agilent® Technologies). The electrical resistances of electrical cables and connections in the measurement system are negligible, as copper electrical cables, adapters and connectors are used in the experiment, and no influence on sensing performance is observed.

To facilitate evaluation of the sensor stability under different temperatures and also the comparison against PZT wafer, key signal features, embracing ToF, signal phase and amplitude, are extracted from acquired signals. Here, ToF is defined as the time difference between (i) the peak of the first wave component (the zeroth-order symmetric Lamb wave mode guided by the aluminium plate, denoted by S_0 hereinafter)

in a signal and (ii) the peak of the excitation, either in the time domain or in the spectrogram obtained with the short-time Fourier transform, with an example, when the ambient temperature is 20 ºC, shown in Figure 5.7.

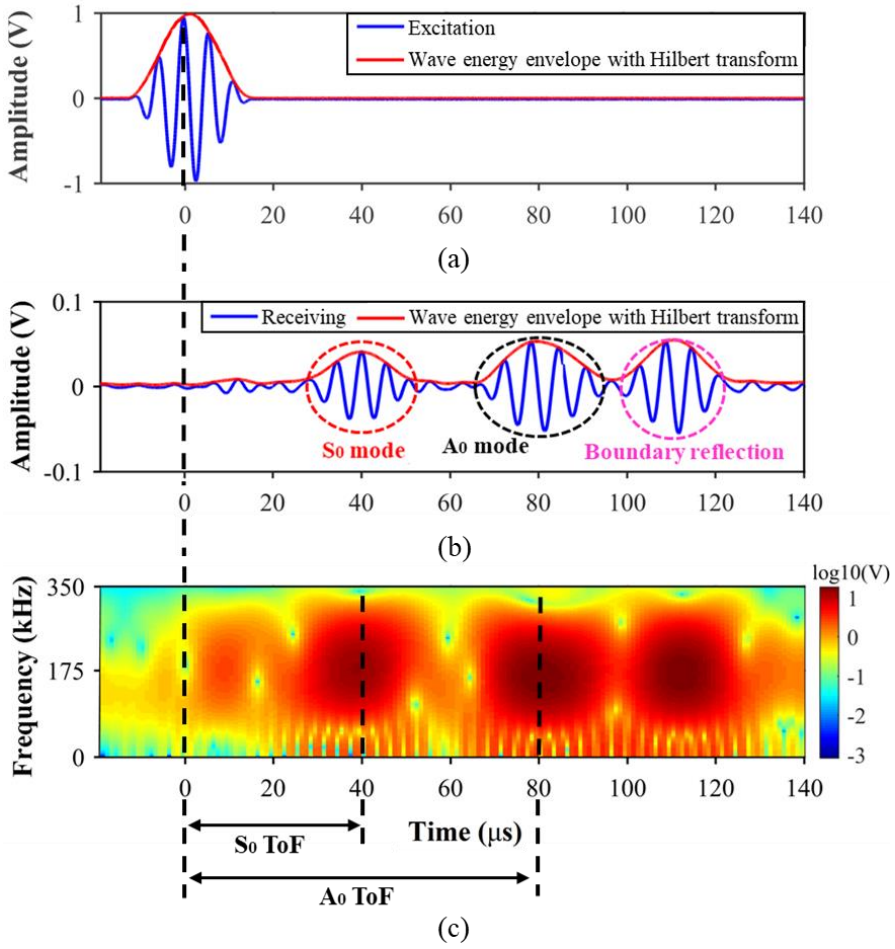

Figure 5.7 Measurement of ToF of acousto-ultrasonic wave signal captured by the AIP sensor at 20 ºC: (a) excitation signal with central frequency of 175 kHz; (b) signal captured by the AIP sensor; and (c) spectrogram of signal in (b) shown in a logarithmic scale.

Figure 5.8 compares signals, when the waves are excited at 175 and 500 kHz (heating or cooling), respectively – as two representative cases, and perceived by the AIP sensor

in a thermal cycle. For each signal depicted in Figure 5.8, the signal amplitude is normalized to the peak value of the S_0 mode. The AIP sensor is observed to maintain its high sensitivity to acousto-ultrasonic wave-induced strains in an extensive temperature regime from –60 to 150 °C, and also in a broad frequency band from static to half a megahertz (*viz.*, the frequency that is predominantly adopted by acousto-ultrasonic wave-driven SHM). During the thermal cycle, both the S_0 mode and the other wave modes (*e.g.*, the zeroth-order anti-symmetric Lamb wave mode guided by the aluminium plate, denoted by A_0 hereinafter), as well as reflected signals from the plate boundary, are faithfully perceived by the AIP sensor, with clear waveforms and high SNR.

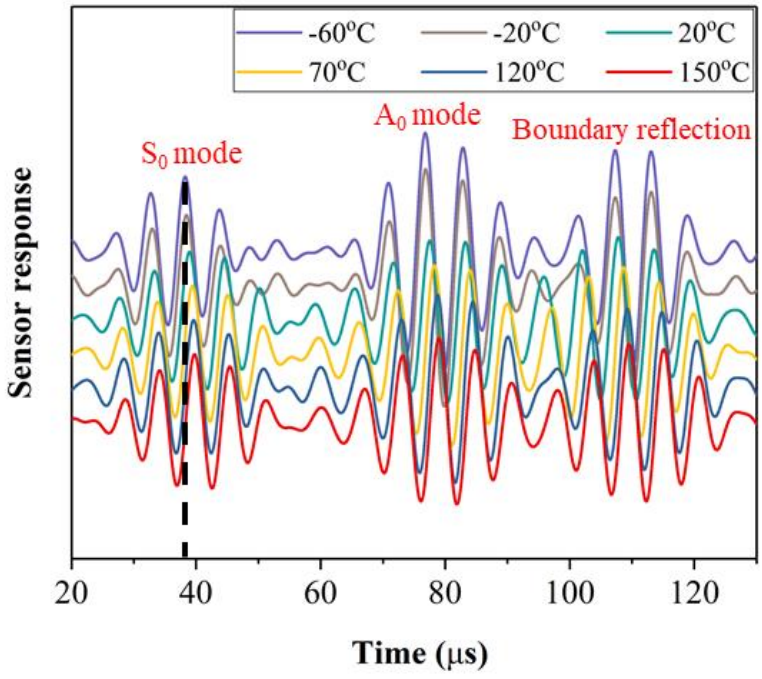

(a)

Figure 5.8 Acousto-ultrasonic wave signals captured by the AIP sensor under varying temperatures in a thermal cycle at an excitation frequency of: (a) 175 kHz (heating), (b) 175 kHz (cooling), (c) 500 kHz (heating) and (d) 500 kHz (cooling).

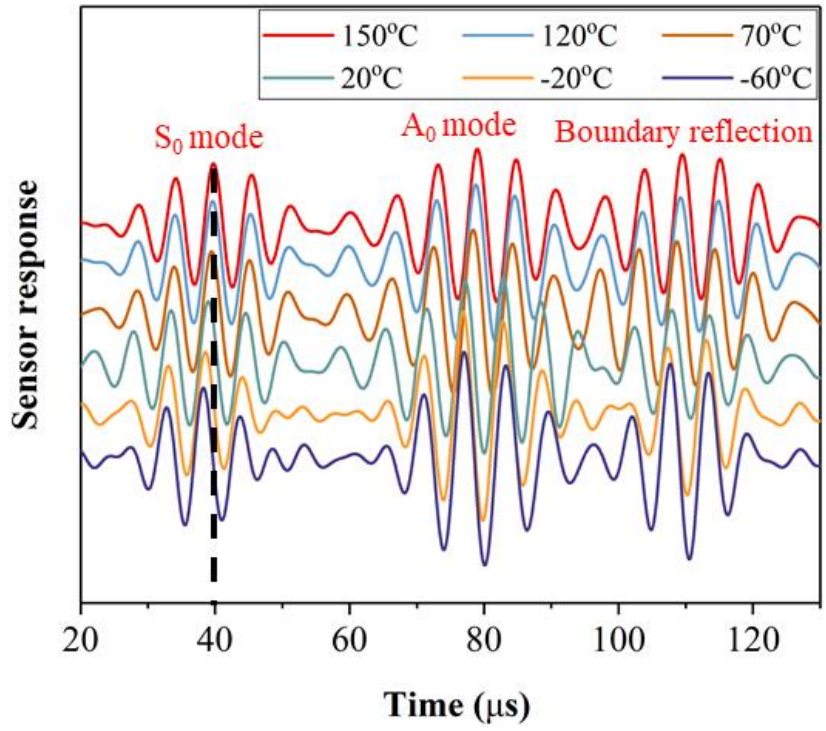

(b)

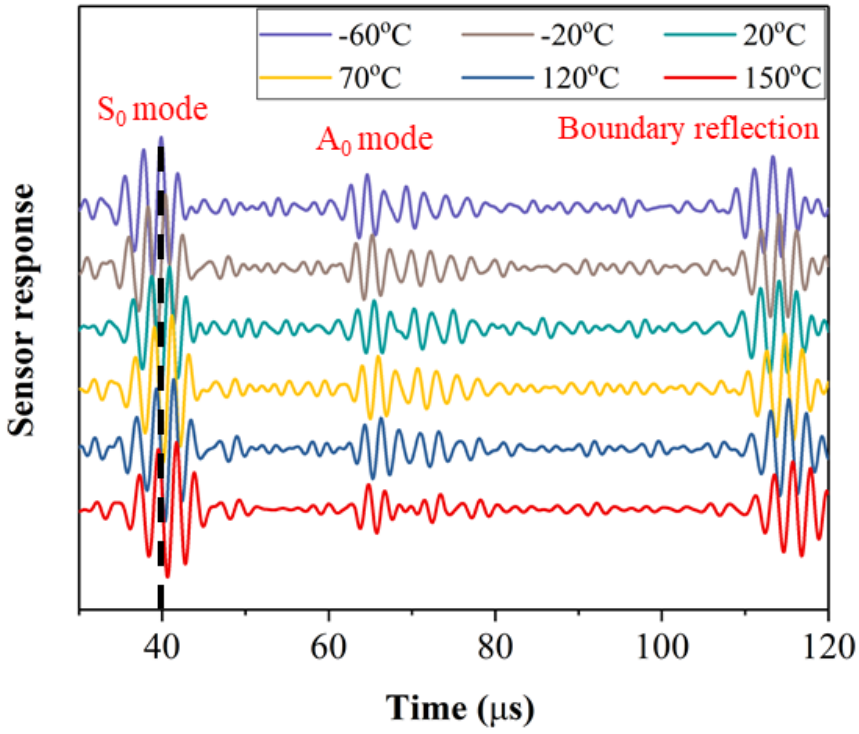

(c)

Figure 5.8 *Cont.*

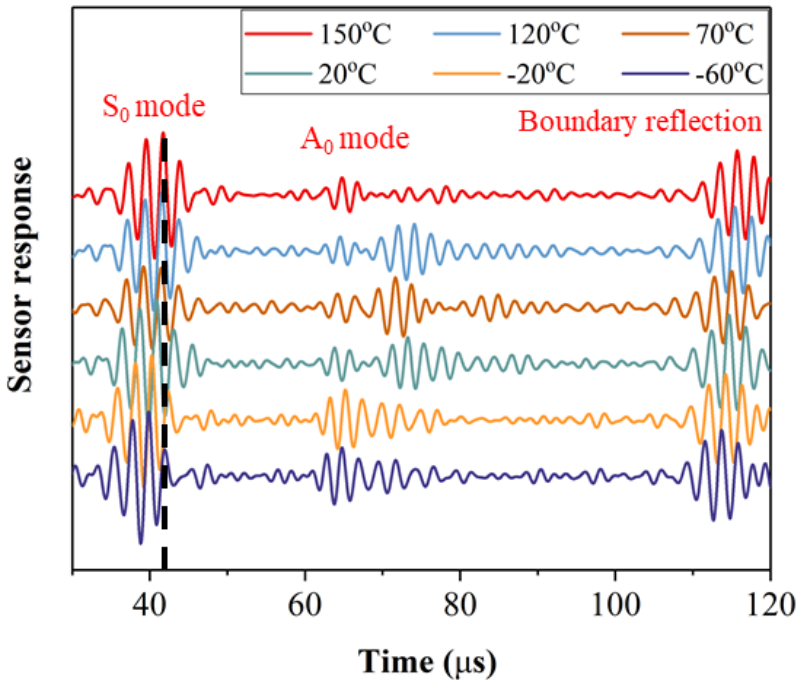

(d)

Figure 5.8 *Cont.*

It is interesting to note in Figure 5.8 that in a thermal cycle, either at its heating or cooling semi-period, a higher temperature leads to a greater ToF, and *vice versa*. To examine such a phenomenon in an extended range, Figure 5.9 compares the extracted ToFs of signals captured in three thermal cycles, when the waves are excited at 175 kHz as a typical case. The error bars in the figure illustrate the variation in ToF at a certain temperature in different thermal cycles. ToFs in Figure 5.9 show the same tendency as that when piezoelectric sensors are used for acousto-ultrasonic wave acquisition, as reported elsewhere [167, 173, 180].

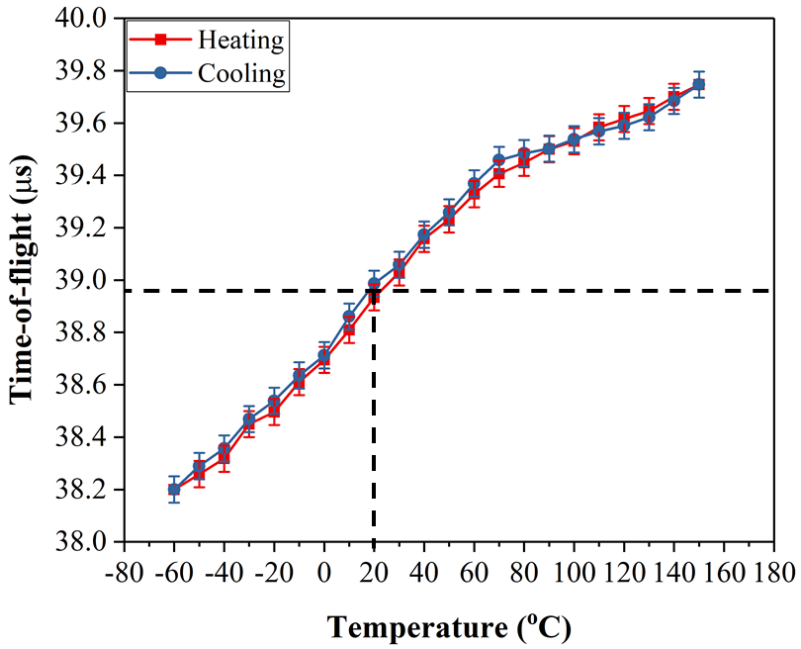

Figure 5.9 ToF of the AIP sensor-captured acousto-ultrasonic wave signals under varying temperatures (excitation frequency: 175 kHz).

As far as the signal amplitude concerned, Figure 5.10 depicts the change of signal amplitude in three thermal cycles, and the plot is normalized to the signal amplitude measured at 20 ºC before the thermal cycles for comparison. As can be seen from Figure 5.10, in both heating and cooling stages, a higher temperature leads to a larger signal amplitude, and *vice versa*. From the results shown in Figures 5.9 and 5.10, the ToF and magnitude of the signal perceived by the AIP sensor are observed highly consistent throughout the entire range of interested temperatures, indicating that not only the bonding is suitable and robust, but the fabricated sensors are stable and functional under an extreme thermal variation from –60 to 150 ºC, with comparable performance as commercial piezoelectric sensors.

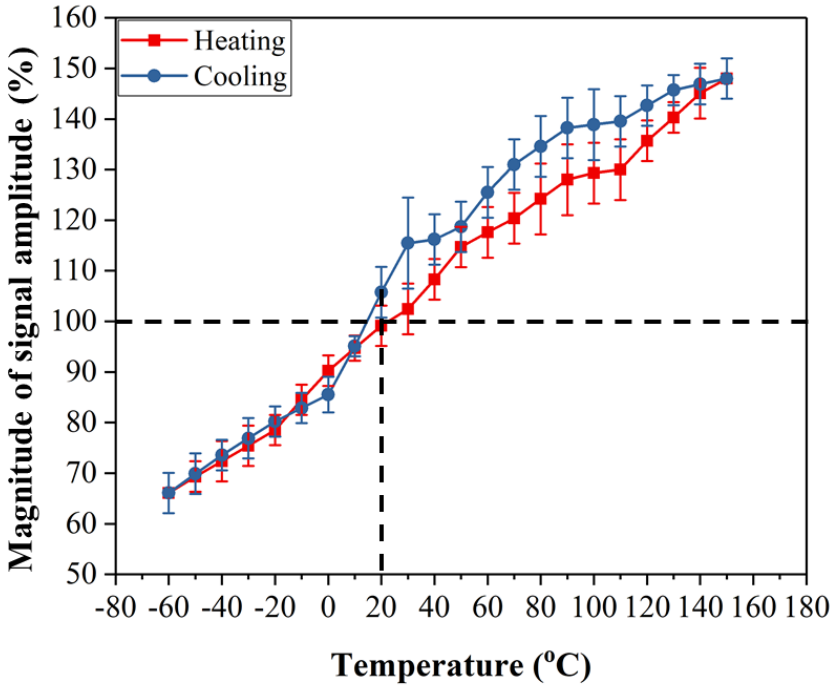

Figure 5.10 Magnitude of the AIP sensor-captured acousto-ultrasonic wave signals under varying temperatures (excitation frequency: 175 kHz).

The variation in signal amplitude at different temperatures, Figure 5.10, is attributed to the variation of piezoelectric coefficient of PZT wafers with temperature. For the PZT wafer used as wave transmitter in this study, the acousto-ultrasonic wave-induced dynamic strain ε generated by the converse piezoelectric effect of the wafer can be estimated via [181]

$$\varepsilon = -d_{31}\frac{V}{t}, \tag{5.1}$$

where d_{31} denotes the in-plane piezoelectric coefficient of the PZT wafer, K_3 the applied out-of-plane electric field, V the applied external voltage, and t the thickness of the wafer. When the operation temperature is no more than half of the Curie temperature (half the Curie temperature for the wafer used here is 167.5 °C), the wafer remains functional and the absolute value of d_{31} increases with temperature [182]. As

can be seen from Equation (5.1), the acousto-ultrasonic wave-induced strain increases with larger d_{31}, and the consequence is that within the temperature range from –60 to 150 ºC, the higher the temperature in the aluminium plate, the larger the strain will be generated. For the AIP sensor – a type of piezoresistive sensor, at a higher temperature, although the tunneling gap is narrowed [183], a larger strain induced by the wave causes more conductive network destruction within the CB-formed conductive network in PVP. A higher degree of tunnel-conductive path destruction in the sensor leads to higher sensitivity to external strains, and as a result, stronger signal amplitude is perceived at higher temperature.

It is noteworthy that in previous studies where piezoelectric sensors are used for acousto-ultrasonic wave acquisition [173, 180], at higher temperatures above 20 ºC, the captured signal magnitude becomes weaker as temperature increases, and this phenomenon is also observed in the present study: the amplitude of signal perceived by the PZT sensor at 175 kHz dropped by ~60% at 150 ºC, when compared to that measured at 20 ºC before the thermal cycles. This can be attributable to the competing interaction between the increasing absolute value of the piezoelectric coefficient and the dielectric permittivity in the PZT wafer [184, 185]. These findings argue that the developed AIP sensors can avoid the negative influence of increased dielectric permittivity in conventional piezoelectrical measurement at a high temperature – an advantage of the AIP sensors over those conventional piezoelectric sensors (such as PZT wafers) in acquisition of broadband acousto-ultrasonic waves at extensive thermal conditions.

5.4 Sensing Precision at Varying Temperatures

Sensing precision of the developed AIP sensors in responding to broadband acousto-ultrasonic waves, subjected to varying temperatures, is scrutinized. First, it is of relevance and necessity to advance the understanding of temperature effect of the measurement system. As discussed in Section 5.3, the bonding layer is proven stable and robust within the discussed temperature variation range (–60 to 150 ^{o}C). Therefore, the properties of the bonding layer can be considered to be constant, and the change of bonding layer thickness (less than 0.01 mm) by thermal expansion is negligible [180]. For the configured experiment in which the PZT wafer is used as a wave transmitter, the change of ambient temperature, according to Equation (5.1), only alters the strain magnitude of an excited wave. Altogether, the variation in transmitting velocity of the waves guided by the aluminium plate and then in the ToF of the wave propagation can be solely attributable to the changes in plate properties and geometry under varying temperatures. To put such changes into perspective, consider an infinite isotropic plate, in which the temperature-dependent acousto-ultrasonic wave motion is governed by [45]

$$(\lambda_e(T)+\mu_e(T))\nabla(\nabla\vec{u})+\mu_e(T)\nabla^2\vec{u}+\rho(T)\vec{f}=\rho(T)\ddot{\vec{u}}\,, \tag{5.2}$$

where

$$\lambda_e(T)=\frac{E(T)\nu(T)}{(1+\nu(T))(1-2\nu(T))}, \tag{5.3}$$

$$\mu_e(T)=\frac{E(T)}{2(1+\nu(T))}\,. \tag{5.4}$$

In the above, $\vec{u}$ denotes the displacement vector, $\vec{f}$ the body force, and T the temperature. μ_e the shear modulus of the plate, and λ_e signifies the Lame's constant that

is related to the Young's modulus E and Poisson's ratio v. $\nabla = \frac{\partial}{\partial x_1} + \frac{\partial}{\partial x_2} + \frac{\partial}{\partial x_3}$, and $\nabla^2 = \frac{\partial^2}{\partial x_1^{\,2}} + \frac{\partial^2}{\partial x_2^{\,2}} + \frac{\partial^2}{\partial x_3^{\,2}}$. ρ is the mass density, which is also temperature-dependent and can be ascertained by solving the differential equation that is defined as (valid at constant pressure P) [180]

$$(\frac{\partial \rho(T)}{\partial T})_P + \rho(T)\alpha_V = 0, \tag{5.5}$$

where α_V is the volumetric thermal expansion coefficient of the plate.

Guided to propagate in the plate, the propagating velocity of acousto-ultrasonic waves of various modes, including the above-mentioned S_0 and A_0 modes, are of a dispersive nature, showing strong dependence on wave excitation frequency, which can be depicted as [46]

$$\frac{\tanh(qh)}{\tanh(ph)} = -\left[\frac{4k^2pq}{(q^2-k^2)^2}\right]^{\pm 1}, \tag{5.6}$$

where

$$p = \sqrt{(\omega / c_L)^2 - k^2}, \tag{5.7}$$

$$q = \sqrt{(\omega / c_T)^2 - k^2}. \tag{5.8}$$

In Equation (5.6), +1 in the exponent is for the symmetric modes, and -1 for the antisymmetric modes. In Equations (5.6)-(5.8), ω is the angular frequency of the Lamb waves. k denotes the wavenumber, and h is the half-thickness of the plate. c_T is the bulk transverse propagating velocity of the Lamb waves and c_L represents the longitudinal propagating velocity of the Lamb waves. c_T and c_L are defined as

$$c_T = \sqrt{\frac{E}{2\rho(1+\nu)}}, \tag{5.9}$$

$$c_L = \sqrt{\frac{E(1-\nu)}{\rho(1+\nu)(1-2\nu)}}. \tag{5.10}$$

According to Equations (5.9) and (5.10), it is noteworthy that the wave dispersion lies jointly upon the Young's modulus, Poisson's ratio and density of the plate. All these properties vary with temperature in a linear manner as [173]

$$R(T) = R(T_0) + \frac{\partial R(T)}{\partial T}\Delta T, \tag{5.11}$$

where R signifies one of the three properties (*i.e.*, Young's modulus, Poisson's ratio or density of the plate), T_0 the original ambient temperature (20 ºC in this study), and $\partial R(T)/\partial T$ the sensitivity of the property with regard to the change of ambient temperature.

5.4.1 Theoretical Prediction

Without loss of generality, 6061-T6 aluminium plates discussed in Section 5.3 are considered. Key material properties of the plates at 20 ºC as well as their sensitivities to the change of ambient temperature (*i.e.*, $\partial R(T)/\partial T$) are listed in Table 5.1 [180, 186], and these parameters are recalled to analytically estimate the dispersive characteristics of waves via Equations (5.6) and (5.11).

The dispersion natures, reflected in terms of the phase and group velocities of the acousto-ultrasonic waves versus temperature variation, obtained using Equations (5.6) and (5.11), are shown in Figure 5.11, in the regime from –60 to 150 ºC. The phase velocity is referred to as the propagation speed of the phase of a particular frequency

contained in the wave, while the group velocity is the velocity with which the overall shape of the wave amplitude, which is the actual velocity captured in experiment. Phase and group velocities of both the fundamental S_0 and A_0 modes show a downward trend with higher temperatures. It is noteworthy that within the temperature range of interest, the changes in wave dispersion are remarkable – a phenomenon that is attributed to change of mechanical properties of the plate under temperature effect. A higher temperature leads to an increase of material compliance with a subsequent reduction of the acousto-ultrasonic wave propagating speeds, which in turn reduces the phase and group velocities of wave modes. The trend of the ToF variation shown in Figure 5.9 – a higher temperature leading to a greater change of ToF, can thus be explained by the velocity change of the dispersive waves.

Table 5.1 Key material properties of 6061-T6 aluminium plates at 20 ºC and their sensitivity to change of ambient temperature.

Material properties	Values at 20 ºC	Sensitivities to temperature
Young's modulus (E)	$E(T_0) = 71.16$ GPa	$\partial E(T)/\partial T = -27.00 \times 10^{-3}$ GPa °C^{-1}
Poisson's ratio (v)	$v(T_0) = 0.33$	$\partial v(T)/\partial T = 54.79 \times 10^{-6}$ °C^{-1}
Density (ρ)	$\rho(T_0) = 2700$ kg m^{-3}	$\partial \rho(T)/\partial T = -1.87 \times 10^{-6}$ kg m^{-3} °C^{-1}

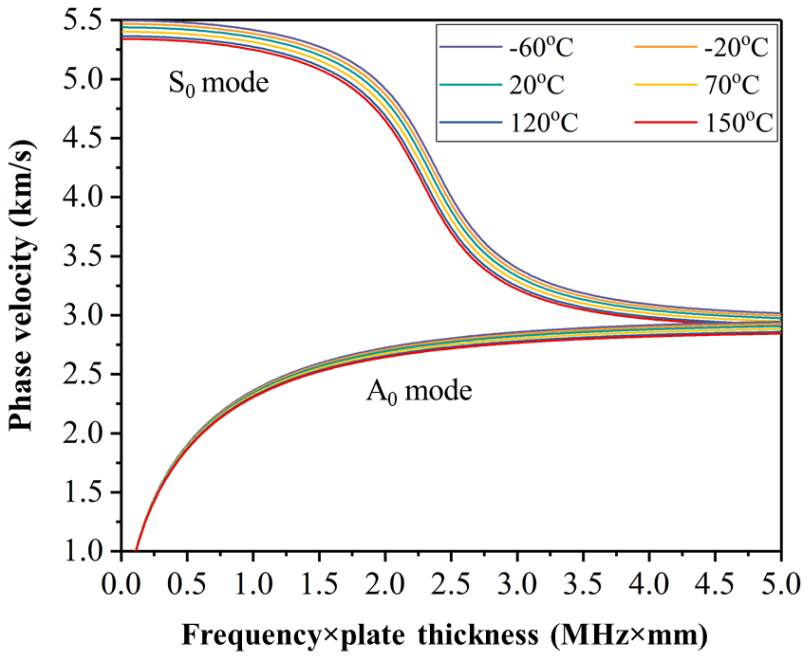

(a)

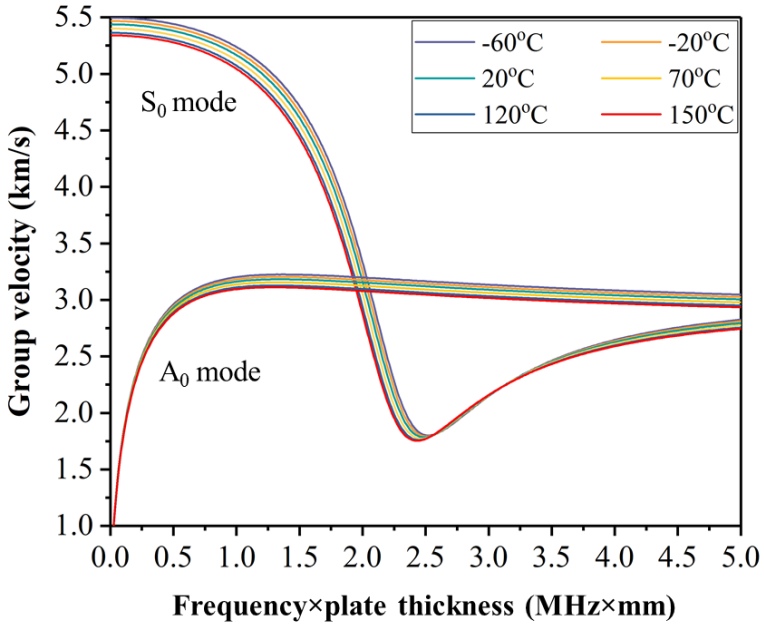

(b)

Figure 5.11 Dispersion curves of waves in an isotropic 6061-T6 aluminium plate at different temperatures: (a) phase velocity and (b) group velocity.

5.4.2 Experimental Validation

The above theoretical estimate of the propagation characteristics of acousto-ultrasonic waves subjected to temperature change (from –60 to 150 ºC) is further experimentally validated. With all parameters remained identical to those in the above theoretical prediction, the ToFs of S_0 and A_0 wave modes are measured using the experimental set-up shown in Figure 5.6(b), and the group velocities are calculated. Compared with experimental measurement using the collocated PZT sensor (for the purpose of comparison) and results from previous studies where piezoelectric wafers are used as wave sensors [167, 180, 186], the analytical prediction is proven accurate in estimating the dispersive characteristics of acousto-ultrasonic waves at varying temperatures. As shown in Figure 5.12, the experimentally obtained group velocities of both the S_0 and A_0 modes by the AIP sensor decrease as the temperature increases, showing good consistency with the trend of dispersion nature calculated theoretically in the preceding section. These findings have confirmed that the nanocomposite-based AIP sensors are able of acquiring broadband acousto-ultrasonic wave signals in an extensive temperature regime responsively, precisely and stably, with comparable performance as commercial piezoelectric sensors.

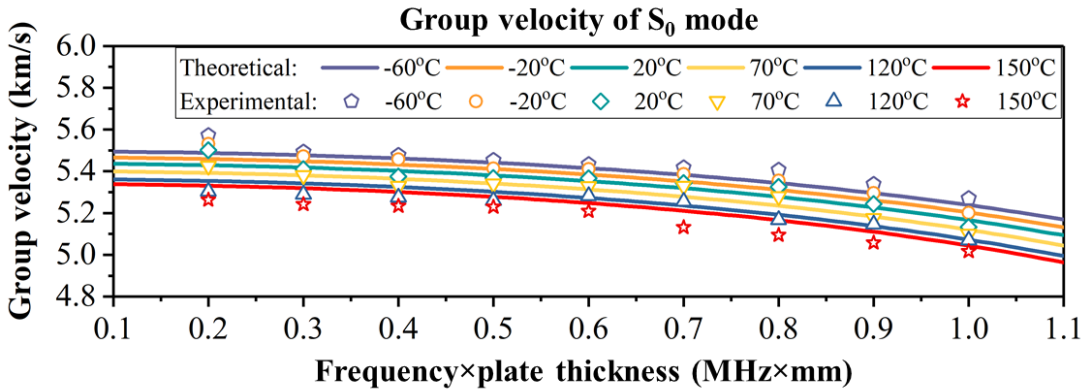

(a)

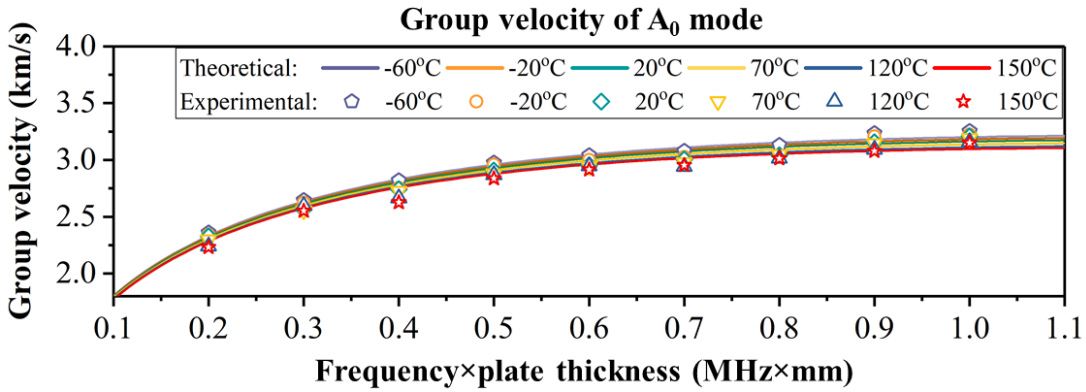

(b)

Figure 5.12 Comparison of theoretically obtained dispersion curves and experimentally obtained dispersion curves with the AIP sensor: (a) S_0 and (b) A_0 modes.

5.5 An Application Paradigm: Damage Characterization Using Acousto-ultrasonic Waves at Varying Temperatures

Upon material morphological investigation, nano-structural optimization and sensing

performance validation, the developed nanocomposite-based AIP sensors are extended to damage characterization using high-frequency elastic waves at varying temperatures. As shown in Figure 5.13, eight thus-produced AIP sensors (serving as broadband acousto-ultrasonic wave sensors) and two PZT wafers (used as wave actuators) are surface-mounted on an isotropic 6061-T6 aluminium plate, to configure a circular sensing network which renders in total 16 actuator-sensor paths. A through-thickness crack of 20 mm in length and 2 mm in width is pre-introduced to the plate using a fine blade, at the location of (-22.5 mm, 22.5 mm). A seven-cycle Hanning-windowed sinusoidal tone-burst at a central frequency of 175 kHz is applied to drive each PZT actuator in turn to generate probing acousto-ultrasonic waves via an arbitrary waveform generator and wideband amplifier. Measurement procedures remain the same as those described in Section 5.3.

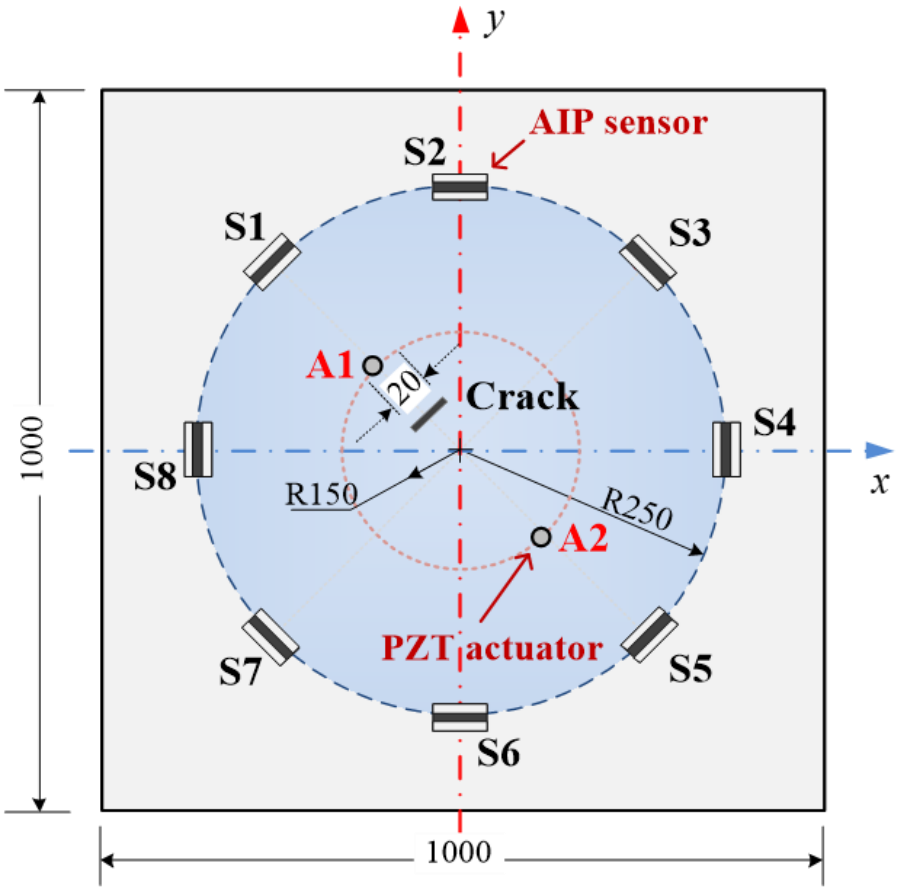

Figure 5.13 Schematic of the 6061-T1 aluminium plate with a fine crack, on which a sensing network is configured with eight AIP sensors and two PZT wafers (A*i* and S*i* denote PZT actuator and AIP sensor, respectively; unit: mm).

Two representative sets of signals acquired via the actuator-sensor path A2-S5, at 20 and 60 ºC, before and after introducing the crack to the plate, are presented in Figure 5.14. In these signals, the first and second wave packets are the incipient acousto-ultrasonic wave modes (*i.e.*, S_0 and A_0 modes). The third wave packet in the signals obtained in the damaged plate, but not observed in the baseline signals from the pristine plate, is the wave component converted from the incipient S_0 mode when it is scattered by the damage, and this wave packet is named as damage-scattered S_0 mode.

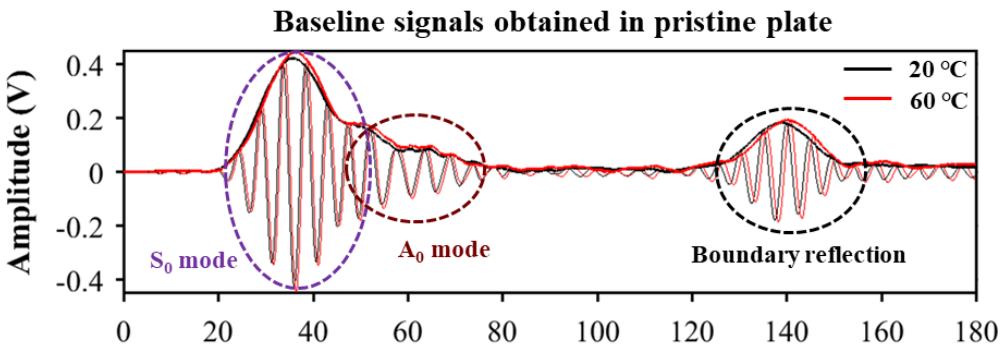

(a)

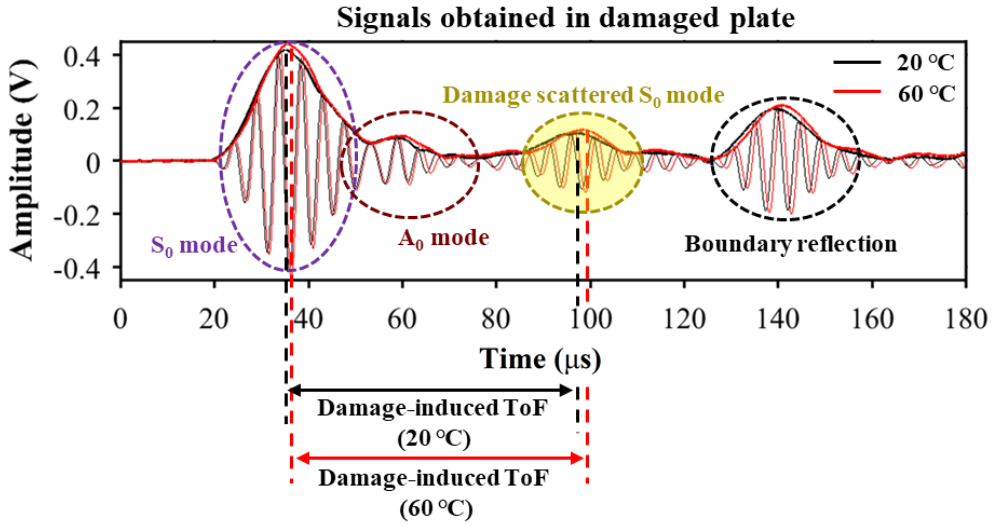

(b)

Figure 5.14 Signals captured via actuator-sensor path A2-S5: (a) before (baseline signals obtained in pristine plate) and (b) after a fine crack is introduced; and comparison of wave packets in signals captured at 20 and 60 °C; (c) S_0 mode and (d) damage-scattered S_0 mode.

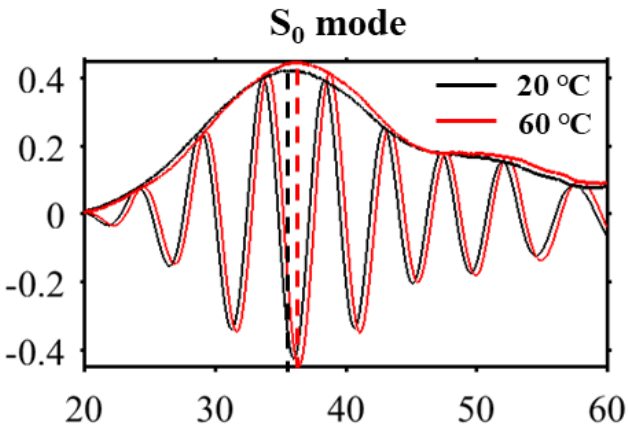

(c)

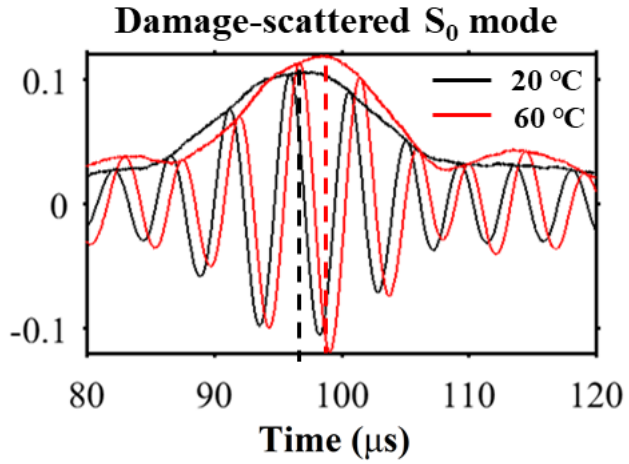

(d)

Figure 5.14 *Cont.*

Damage-induced ToF, as indicated in Figure 5.14(b), is extracted from the signals for damage localization via a triangulation algorithm [187], in terms of the relative position of the actuator Ai (x_{Ai}, y_{Ai}), AIP sensor Si (x_{Si}, y_{Si}) and damage D (x_D, y_D), as

$$\left(\frac{L_{A_i\text{-}D} + L_{D\text{-}S_i}}{v_0}\right) - \frac{L_{A_i\text{-}S_i}}{v_0} = \Delta t_i, \ (i = 1, 2, \ldots, N) \tag{5.12}$$

where

$$L_{\mathrm{A}_i\text{-D}} = \sqrt{(x_{\mathrm{A}_i} - x_{\mathrm{D}})^2 + (y_{\mathrm{A}_i} - y_{\mathrm{D}})^2}\,, \tag{5.13}$$

$$L_{\mathrm{D\text{-}S}_i} = \sqrt{(x_{\mathrm{D}} - x_{\mathrm{S}_i})^2 + (y_{\mathrm{D}} - y_{\mathrm{S}_i})^2}\,, \tag{5.14}$$

$$L_{\mathrm{A}_i\text{-}\mathrm{S}_i} = \sqrt{(x_{\mathrm{A}_i} - x_{\mathrm{S}_i})^2 + (y_{\mathrm{A}_i} - y_{\mathrm{S}_i})^2}\,. \tag{5.15}$$

In Equations (5.12)-(5.15), $L_{\mathrm{A}i\text{-D}}$, $L_{\mathrm{D\text{-}S}i}$ and $L_{\mathrm{A}i\text{-}\mathrm{S}i}$ denote the distances from the actuator Ai ($x_{\mathrm{A}i}$, $y_{\mathrm{A}i}$) to the damage centre D (x_{D}, y_{D}), from the damage centre to the sensor Si ($x_{\mathrm{S}i}$, $y_{\mathrm{S}i}$), and from the actuator to the sensor, respectively. v_0 is the group velocity of the incipient S_0 mode. Δt_i (*i.e.*, damage-induced ToF) is to be determined from the signals captured by the actuator-sensor path Ai-Si. By solving Equations (5.12) with the knowledge of v_0, ($x_{\mathrm{A}i}$, $y_{\mathrm{A}i}$) and ($x_{\mathrm{S}i}$, $y_{\mathrm{S}i}$), an elliptical locus with two foci at the actuator Ai and sensor Si can be ascertained (see Figure 5.15), implying all the possible locations of damage in this actuator-sensor path. With more elliptical loci from all the available 16 actuator-sensor paths, the damage location (x_{D}, y_{D}) can be determined by mathematically seeking the intersection of these ellipses.

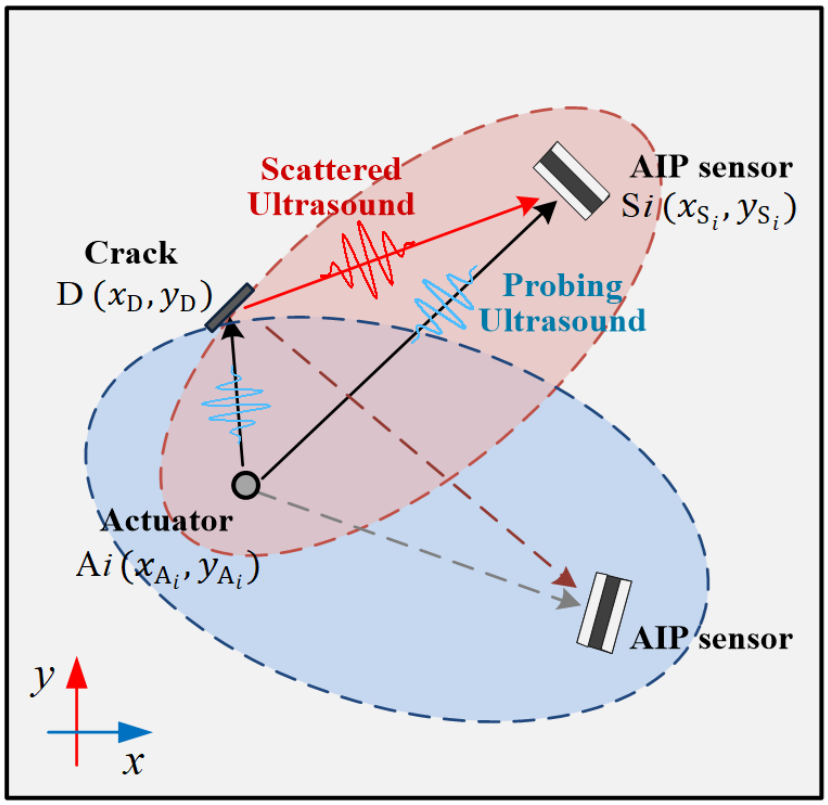

Figure 5.15 Relative positions of the actuator A*i*, AIP sensor S*i*, and damage D in an actuator-sensor path.

A probability-based diagnostic imaging (PDI) algorithm is recalled [188, 189], using all data from the two actuators for data fusion to visualize the identified damage in a two-dimensional greyscale image, with results shown in Figure 5.16 for two scenarios when the experiments are performed at 20 and 60 ºC. PDI presents the diagnostic results in terms of the probability of presence of damage in the inspected structure, with detailed description in the previous research [190]. Points on a particular locus that produced by an actuator-sensor path are of the highest degree of probability (100%) of damage presence, while for other points the probability of damage presence decreases with the distance to the locus. For a specific point in the diagnostic image, a higher field value with outstanding pixel suggests a higher probability of damage

presence, which gives users an intuitive and precise perception of the damage location.

In Figure 5.16(a), the diagnostic image constructed with the ToF-based PDI, when the group velocity of the waves obtained at 20 ºC is used, quantitatively tallies with the reality. However, as discussed in Section 5.4, the group velocity of waves varies as temperature changes, which may lead to pseudo or erroneous diagnostic results if the temperature effect is not taken into account and compensated. At 60 ºC, compensation for temperature-dependent wave group velocity is applied, based on the dispersion curves obtained at 60 ºC in Section 5.4. Only with such compensation can precise identification of the damage be achieved, with results shown in Figure 5.16(b) and (c). The imaging result in Figure 5.16(c) shows high coincidence with the true location and the crack orientation, affirming the performance of the developed AIP sensors in *in situ* SHM applications at varying temperature conditions.

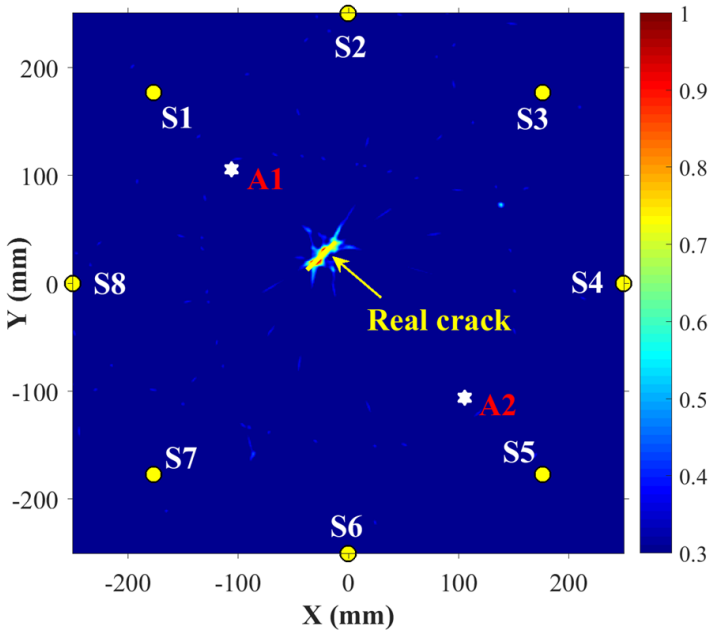

(a)

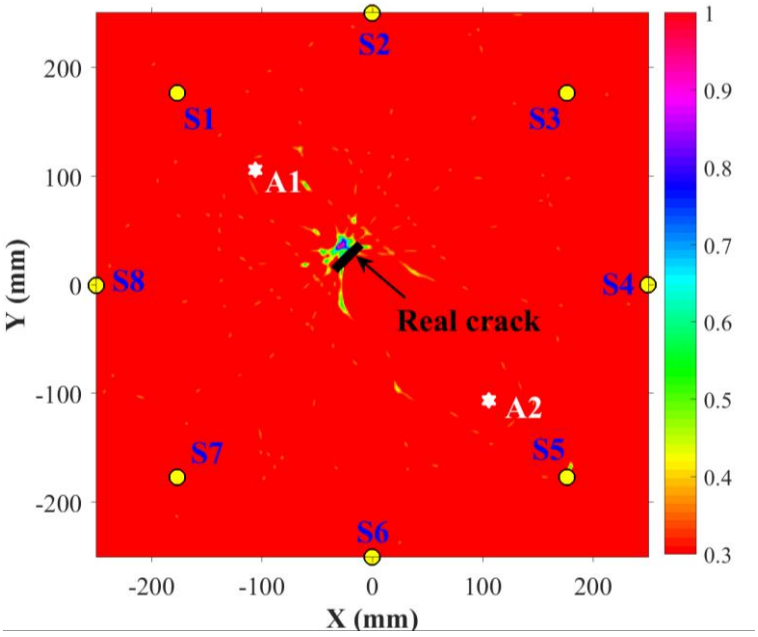

(b)

Figure 5.16 Diagnostic images obtained with ToF-based PDI algorithm at: (a) 20 ºC, (b) 60 ºC (without temperature compensation) and (c) 60 ºC (with temperature compensation).

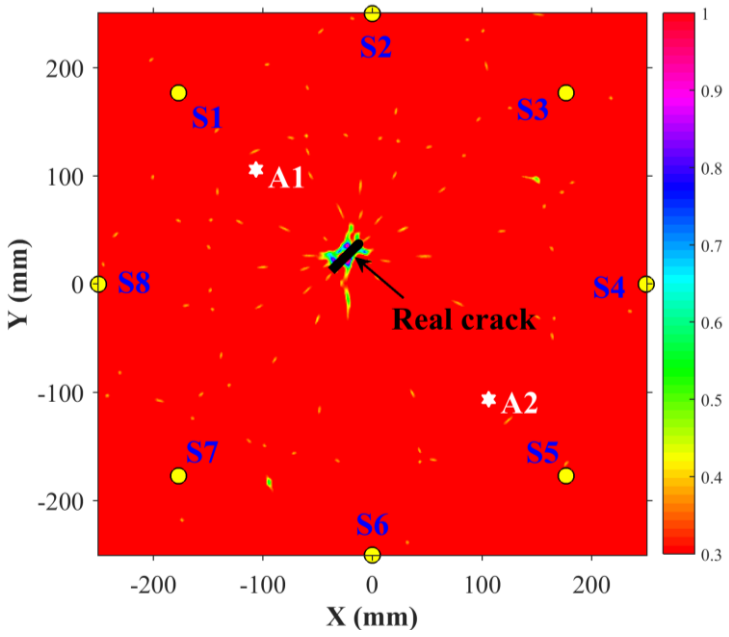

(c)

Figure 5.16 *Cont.*

5.6 Summary

In this chapter, silver electrodes and insulating layers are introduced onto the developed inkjet-printed thin film ultrasound sensors, by using inkjet printing with a layer-by-layer manner to develop AIP thin film ultrasound sensors. The fabrication process of AIP sensors features a high degree of automaticity, versatility, simplicity and controllability. The AIP nanocomposite film sensors are proven to be capable of perceiving acousto-ultrasonic wave signals up to half a megahertz under harsh thermal cycles ranging from –60 ºC to 150 ºC (this temperature range covers thermal extremes experienced by aircrafts and spacecraft), with satisfying stability, sensitivity, and precision. An additional merit of the AIP sensors is that unlike piezoelectric sensors (*e.g.*, PZT wafers), the piezoresistive AIP sensors can get rid of the influence of

dielectric loss in piezoelectrical acousto-ultrasonic wave-based measurement at a high temperature.

With proven capability of *in situ*, precisely and stably perceiving acousto-ultrasonic wave signals at different temperatures, the nano-engineered AIP sensors are further implemented to conduct damage evaluation at varying temperatures. A dense sensor network is configured using the AIP piezoresistive sensors, in lieu of conventional piezoelectric ceramic sensors with high mass density and dielectric loss. The AIP sensor network is demonstrated capable of identifying the crack accurately at different temperatures, indicating the promising application potentials of the AIP sensors in *in situ* SHM for aerospace structures.

CHAPTER 6

All-printed Nanocomposite Sensor Array for Ultrasonic Imaging of Composites

6.1 Introduction

With the ability of directional scanning and high-precision signal acquisition, phased array technique has secured its popularity in radar searching [191], sonar positioning [192], seismology study [193], telecommunication [194], and biomedical imaging [195], as well as NDT [21-23]. Particularly for NDT, with multiple, synchronized sensing elements, a phased array features merits including wave focusing, steerable inspection and enhanced signal-to-noise ratio, through which a broad region can be scanned, and rich information on material defect or structural anomaly can be obtained.

Despite proven effectiveness when used for ultrasonic imaging of composite structures [196, 197], conventional ultrasonic phased arrays are encountering problematic issues. With a bulky and unwieldy nature, phased arrays are of a low degree of coupling compatibility with inspection structures [198], limited adaptation to curved or geometrically complex structural surfaces [199], possible blind zones [200], and low inspection efficiency due to the need of manipulating arrays back and forth along the

inspected surfaces. In particular, the impossibility of integrating an array with the inspected structure precludes the phased array-based inspection from being extended from offline NDT to *in situ*, real-time SHM of composite structures.

Recognizing the deficiency that conventional phased arrays are facing, and extending the endeavours in developing inkjet-printed thin film ultrasound sensors, APNSA is fabricated via drop-on-demand inkjet printing, by directly writing NGP/PAA-based nanocomposite ink on Kapton film substrates. With novel NGP/PI sensors as individual sensing elements and by virtue of the quantum tunneling effect, APNSA is functionalized to substitute conventional ultrasonic phased arrays which are of a low degree of integrity with composites, for acquiring acousto-ultrasonic wave signals and implementing *in situ* ultrasonic imaging of composites.

6.2 APNSA: Principle and Fabrication

6.2.1 Direct-writable Sensing Ink

Individual sensing elements of APNSA are inkjet printed by directly writing NGP/PAA-based nanocomposite sensing ink on a Kapton film substrate. Taking printability, stability and functionality as the paramount consideration, the sensing ink solvent is prepared by dissolving 0.2 g EC (viscosity 4 cP, 5 % in toluene/ethanol, Aldrich Chemistry) and 0.3 g PVP (PVP K-30, Sigma-Aldrich®) into 100 mL anhydrous NMP (Aladdin®). EC and PVP are added to the NMP solvent as ink

stabilizer and rheology modifier. Graphite powder (Aladdin®; 2.0 g) is added to the prepared solvent, and processed via a high-shear LPE process using a high shear laboratory mixer (L5M, Silverson®) at 6000 rpm for 1 h, in which bulk natural graphite is exfoliated to few-layer NGPs and the NGP dispersion is regulated to best fit the printing process. Thus-prepared NGP dispersion is centrifuged at 5000 rpm for 20 min using a Cence® H1850 high speed centrifuge, and top 80% of the supernatant is collected. PAA (12.8 wt%, (80% NMP/20% aromatic hydrocarbon) Sigma-Aldrich; 1.6 g) – the polymeric precursor of PI, is mixed with 20 mL of the NGP dispersion, and the mixture is magnetically stirred at 800 rpm for 30 min, to form the NGP/PAA sensing ink.

6.2.2 Direct Write of APNSA

The above direct-writable NGP/PAA sensing ink is deployed onto a Kapton film, using a desktop inkjet printing platform which consists of a PiXDRO LP50 inkjet printer (OTB Solar-Roth & Rau) equipped with a DMC-11610 cartridge (Dimatix-Fujifilm Inc.). Prior to the printing process, the NGP/PAA sensing ink is filtered through a PVDF micropore sieve (with diameter of 0.22 μm) to screen out large NGPs, minimizing the probability of printing nozzle clogging. The Kapton film is pre-treated with O_2 plasma to introduce hydrophilic functional groups on the substrate surface beforehand, which is beneficial to warrant good adhesion between the ink and the O_2 plasma-processed substrate. Each sensing element of APNSA is printed on the substrate as a square (12 mm×12 mm), and the distance between the centres of two neighbouring elements (*viz.*, the pitch) is 16 mm. Such a pattern effectively avoids pseudo or erroneous imaging results caused by spatial aliasing (to be discussed in

Section 6.4). The printing process is accomplished in a resolution of 500 dpi in both the cross-scan and in-scan directions. Thus-printed APNSA is annealed at 400 ^{o}C for 20 min, to ensure complete imidization of PAA and removal of residual solvent and polymer stabilizers from printed APNSA. The number of sensing elements in an APNSA depends on specific applications, and a paradigm of an APNSA with 12 sensing elements deployed on Kapton film is pictured in Figure 6.1(a).

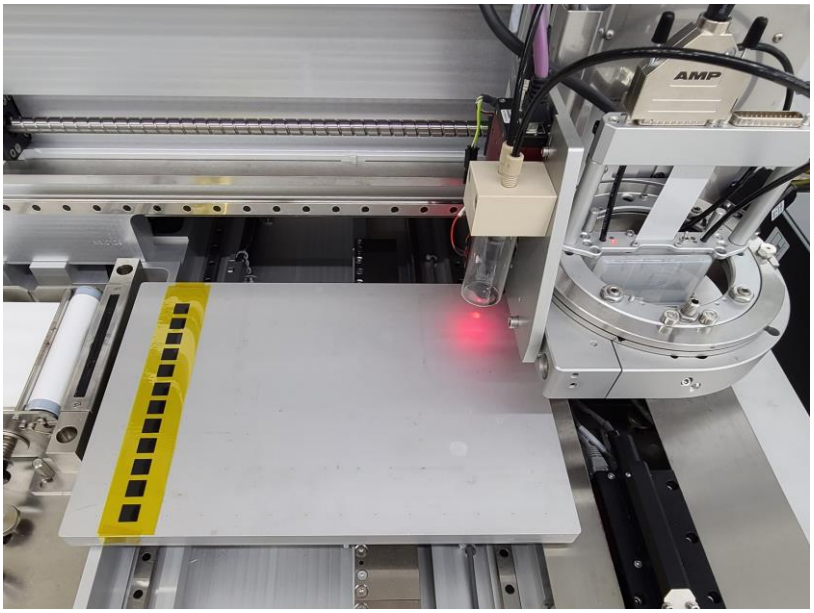

(a)

Figure 6.1 (a) APNSA on a Kapton film substrate, printed by a desktop inkjet printing platform; and (b) a typical NGP/PI sensing element of an APNSA.

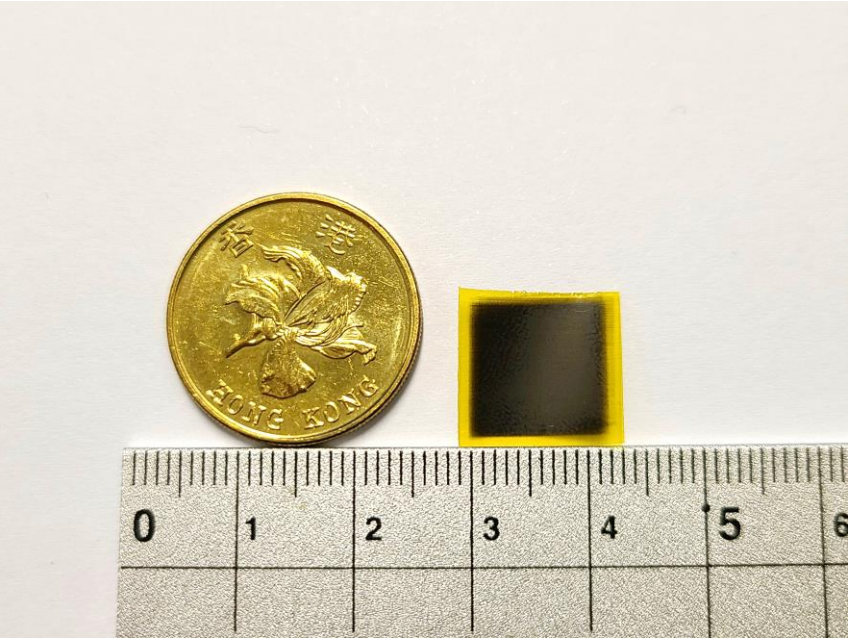

(b)

Figure 6.1 *Cont.*

6.3 Responsivity of APNSA

The responsivity of APNSA to broadband acousto-ultrasonic waves is examined and calibrated. To this end, a glass fibre/epoxy composite laminate plate (600 mm long and wide, 1 mm thick) is prepared, and a piezoelectric PZT (Ø12 mm, 1 mm thick) wafer is surface-bonded at the plate centre, functioning as an ultrasonic wave transmitter to emit waves into the laminate, as schematically illustrated in Figure 6.2. The waves, five-cycle Hanning-windowed tone-bursts of a central frequency from 50 to 500 kHz (with a stepping of 50 kHz), are generated with a NI® PXI-5412 waveform generator, amplified with a Ciprian® US-TXP-3 linear power amplifier, and applied on the PZT wafer. Four APNSA sensing elements are adhered on the plate, and each is 150 mm apart from the transmitter as shown in Figure 6.2, for signal perception. Alongside

each sensing element is a PZT wafer (Ø12 mm, 1 mm thick) which is used to capture wave signals for calibration and comparison with APNSA elements. Each NGP/PI sensing element is connected to a self-developed signal amplification and conditioning module via shielding cables. The module is powered by a GW INSTEK® GPC-3030D power supply, and consists of a resistance-adjustable R-V circuit that converts piezoresistive variations to electrical signals [164]. The signals captured by the APNSA sensing elements, as well as the counterpart signals acquired by PZT wafers, are simultaneously recorded using an Agilent® MSOX 3014A oscilloscope.

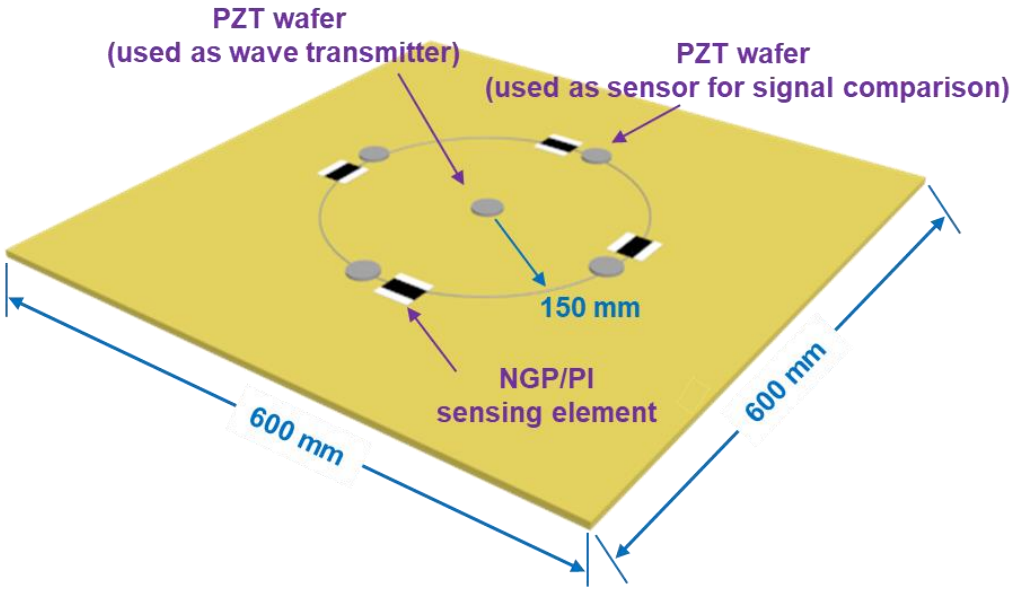

Figure 6.2 Experimental set-up for APNSA sensing element responsivity calibration (unit: mm).

Figure 6.3 exemplarily displays signals perceived at an excitation frequency of 200 kHz. As can be seen from Figure 6.3(b), the signal captured by the APNSA sensing element faithfully and explicitly exhibits wave components including S_0 (the zeroth-order symmetric plate wave mode guided by the laminate) and A_0 (the zeroth-order

anti-symmetric plate wave mode guided by the laminate) modes, with all waveforms in good coincidence with those acquired by the PZT wafers (Figure 6.3(c)). Figure 6.3(d) compares the wave energy envelopes obtained via Hilbert transform, to observe the same arrival time of S_0 mode captured by two different types of sensors. This has affirmed good sensitivity and sensing precision of the APNSA sensing element to ultrasonic waves.

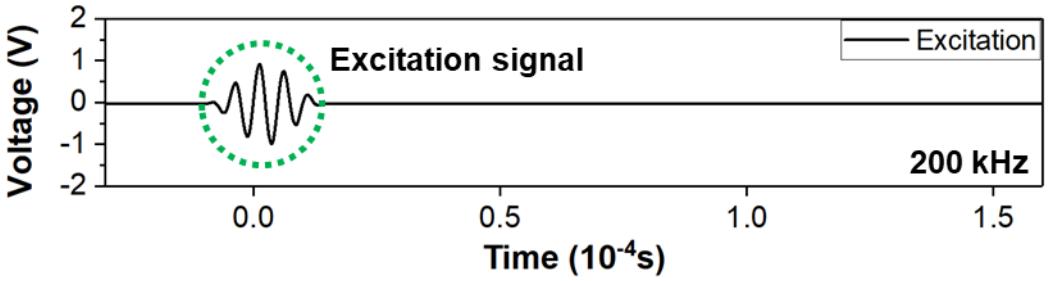

(a)

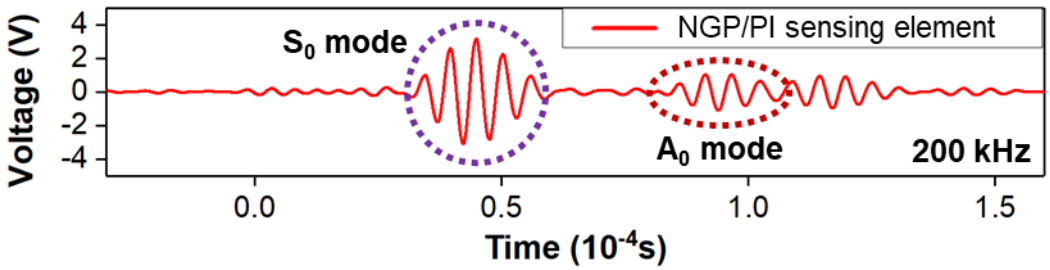

(b)

Figure 6.3 (a) Excitation signal at 200 kHz, as an example; wave signals acquired by (b) an APNSA sensing element, and (c) a PZT wafer; (d) comparison of wave energy envelopes.

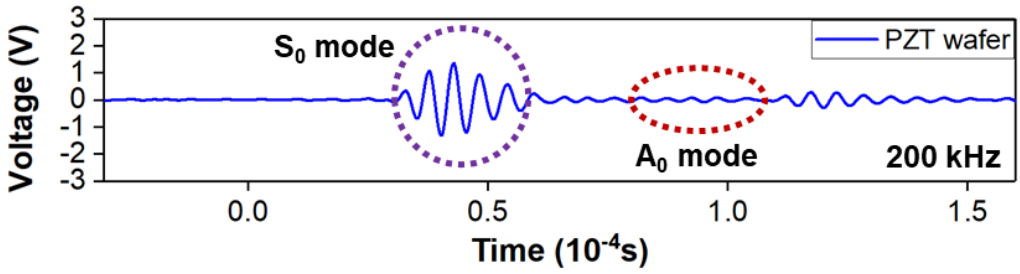

(c)

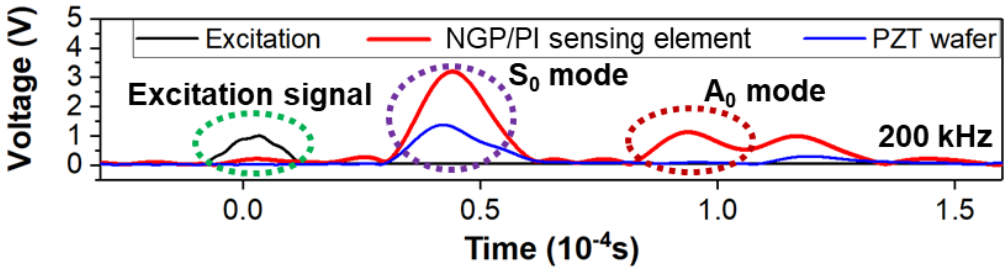

(d)

Figure 6.3 *Cont.*

The spectra of exemplary signals in Figures 6.3(b) and 6.3(c) are obtained via fast Fourier transform, and compared in Figure 6.4(a). In Figure 6.4(a), an energy peak at ~200 kHz is observed in both spectra, in consistence with the excitation frequency. Still using the excitation of 200 kHz as an example, the signal magnitude, as an increase in the excitation voltage, is shown in Figure 6.4(b), to reveal a linear increase, in good consistency with that captured by the PZT wafer. On the other hand, the magnitude of an elastic wave generated by a PZT wafer is in a linear relationship with the intensity of excitation, which echoes the linear increase of the acquired signal magnitude against excitation voltage, as observed in Figure 6.4(b). For an NGP/PI sensing element, a larger strain under higher wave excitation voltage can lead to greater particulate movement of NGPs in the sensing element, thus enlarging the variation of tunneling condition and the sensing element exhibits stronger

piezoresistive response.

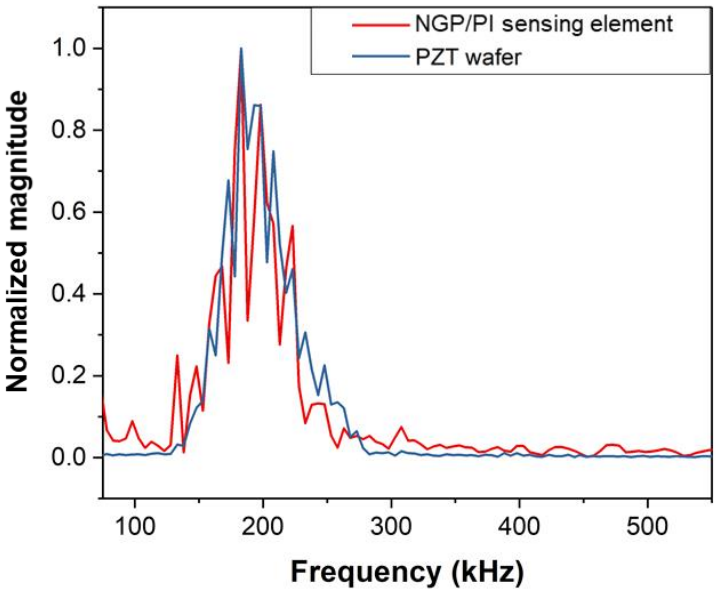

(a)

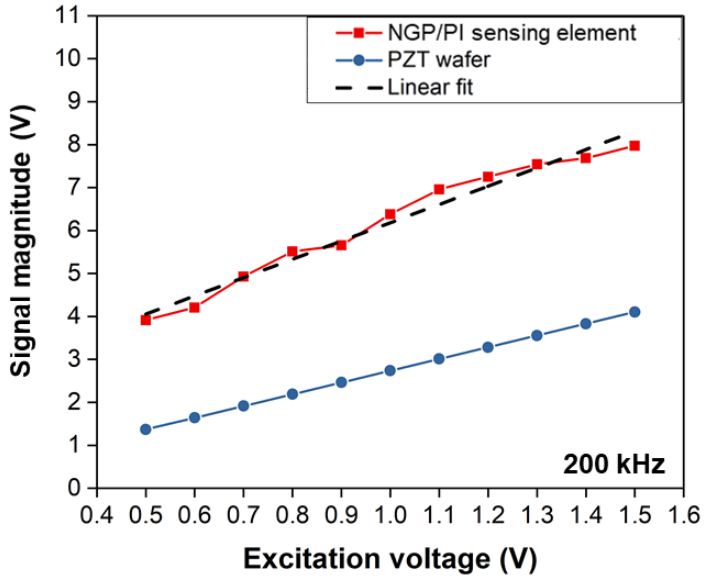

(b)

Figure 6.4 (a) Spectra of wave signals captured by an APNSA sensing element and PZT wafer, at 200 kHz; and (b) peak-to-peak wave signal magnitude acquired by an APNSA sensing element and PZT wafer under different excitation voltages.

Signal magnitudes captured by the APNSA sensing element and by PZT wafer in a sweep frequency from 50 to 500 kHz are compared in Figure 6.5(a), arguing consistent trend for the two types of sensors. The stronger magnitude sensed by the NGP/PI sensing element than that by the PZT wafer can be attributable to different sensing mechanisms of these two genres of sensors, *i.e.*, the piezoresistive effect induced by the quantum tunneling effect for the NGP/PI sensing element, while the piezoelectric effect for the piezoelectric sensor, respectively.

Taking a step further, the group velocity of wave propagation in the laminate is extracted from captured signals. The group velocity denotes the velocity of overall shape of the wave amplitude, indicates continuous movement of wave energy, and is the actual wave propagation velocity captured in experiment. The extracted group velocities of the waves, when the waves are excited in the range from 50 to 500 kHz, are shown in Figure 6.5(b), to observe no remarkable discrepancy in the velocities obtained by two types of sensors. These findings have demonstrated the prominent capability of the developed APNSA sensing elements for acquisition of broadband wave signals.

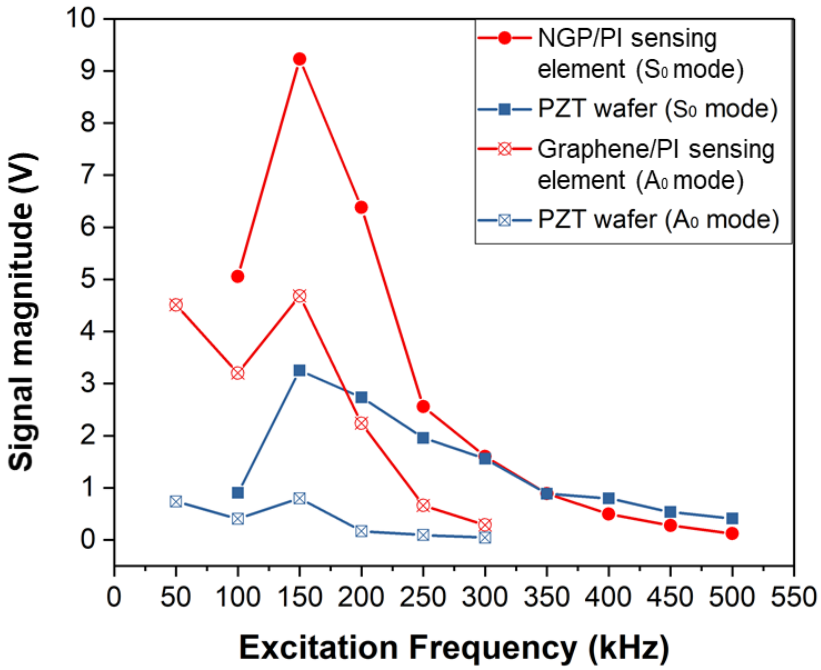

(a)

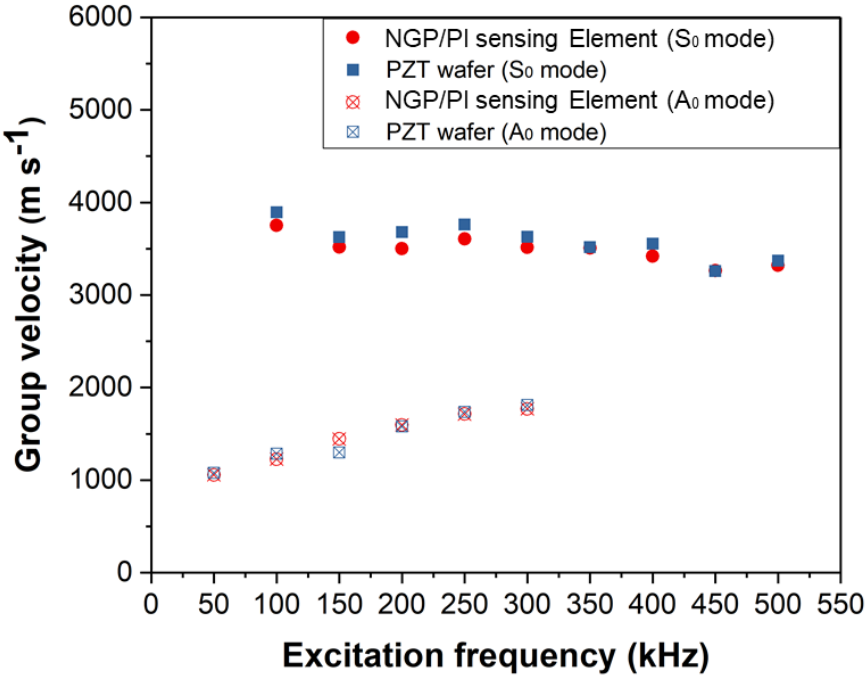

(b)

Figure 6.5 (a) Peak-to-peak wave signal magnitudes acquired by APNSA sensing elements and PZT wafers (50-500 kHz); and (b) comparison of group velocities acquired by APNSA sensing elements and PZT wafers (50-500 kHz).

6.4 Anomaly Imaging of Composites Using APNSA

With proven responsivity and sensing precision in responding to broadband acousto-ultrasonic wave signals, the fabricated APNSA is applied to implement *in situ* ultrasonic imaging for a glass fibre/epoxy composite laminate plate, pictured in Figure 6.6(a), as a proof-of-concept validation. An APNSA consisting of eight NGP/PI sensing elements (labelled as S1, S2, …, S8) is surface-mounted on the plate, and a PZT wafer (Ø12 mm, 1 mm thick) is mounted on the plate surface as a wave actuator. The locations of the APNSA and PZT wafer on the plate are indicated in Figure 6.6(b). A steel cylinder (Ø20 mm, 200 g weight) is bonded on the plate as a mock-up anomaly, at the location of (30 mm, 10 mm), in Figure 6.6(b). The experimental system and measurement procedures remain the same as those in Section 6.3. A five-cycle Hanning-windowed sinusoidal tone-burst at a central frequency of 100 kHz is applied to drive the PZT actuator, to generate a probing wave with wavelength (λ) of 37.2 mm in the laminate. In APNSA, the element pitch (*i.e.*, distance between the centres of neighbouring sensing elements) has been pre-set as 16 mm during inkjet printing, which is smaller than the half wavelength (*i.e.*, 18.6 mm) of the generated probing wave, and this will ensure the detection resolution and avoid false results caused by spatial aliasing [201].

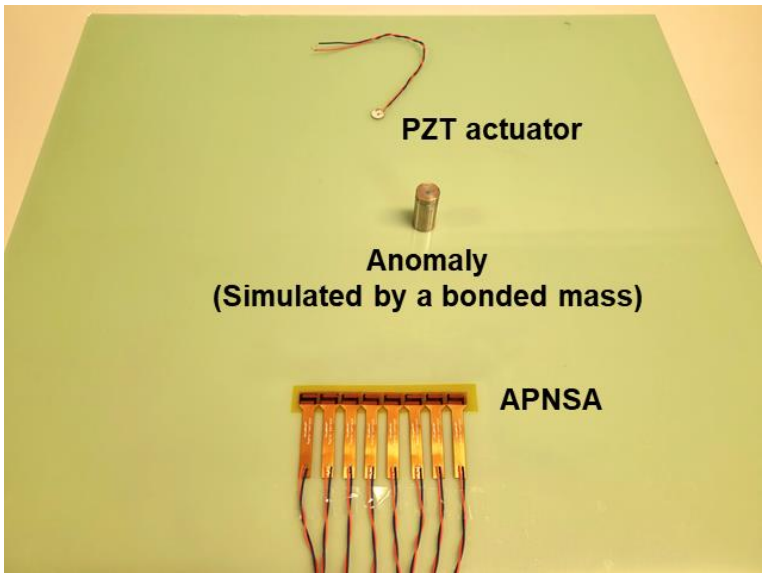

(a)

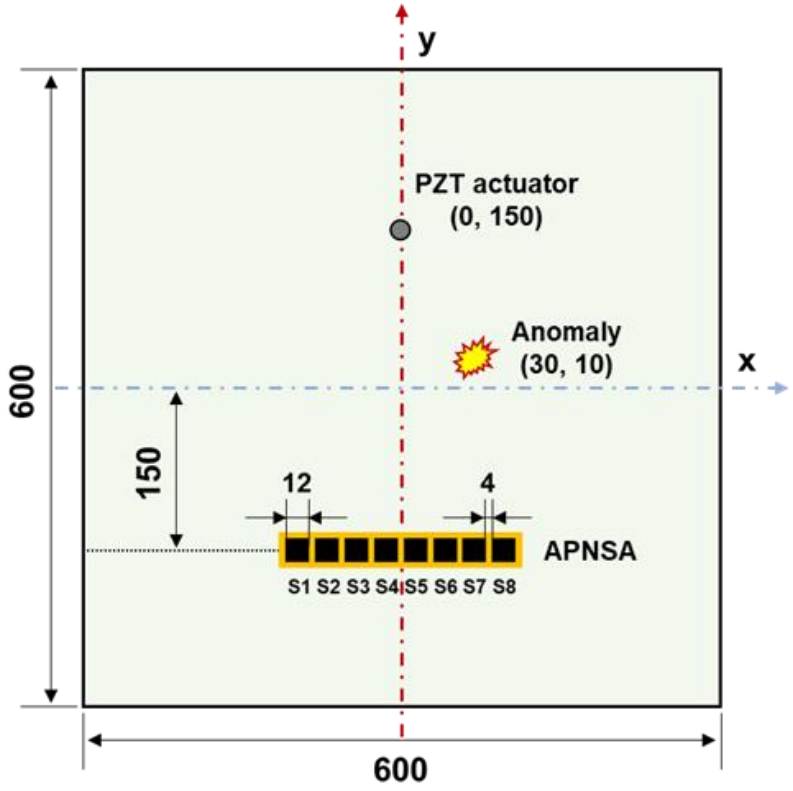

(b)

Figure 6.6 (a) Photograph and (b) schematic of the glass fibre/epoxy composite laminate plate with APNSA and a mock-up anomaly (unit: mm).

Figure 6.7(a) presents representative signals captured by sensing element S1 of APNSA, before and after that the mock-up anomaly is introduced to the laminate plate. The S_0 wave mode of the probing waves can be perceived clearly in both cases. After introducing the mock-up anomaly, an additional wave packet, following the original S_0 mode, is prominent and classified as the anomaly-induced wave component in the sensing element-captured signal. For anomaly imaging, this additional wave component is extracted, Figure 6.7(b), and named the anomaly-scattered S_0 mode ($S_0^{Anomaly}$).

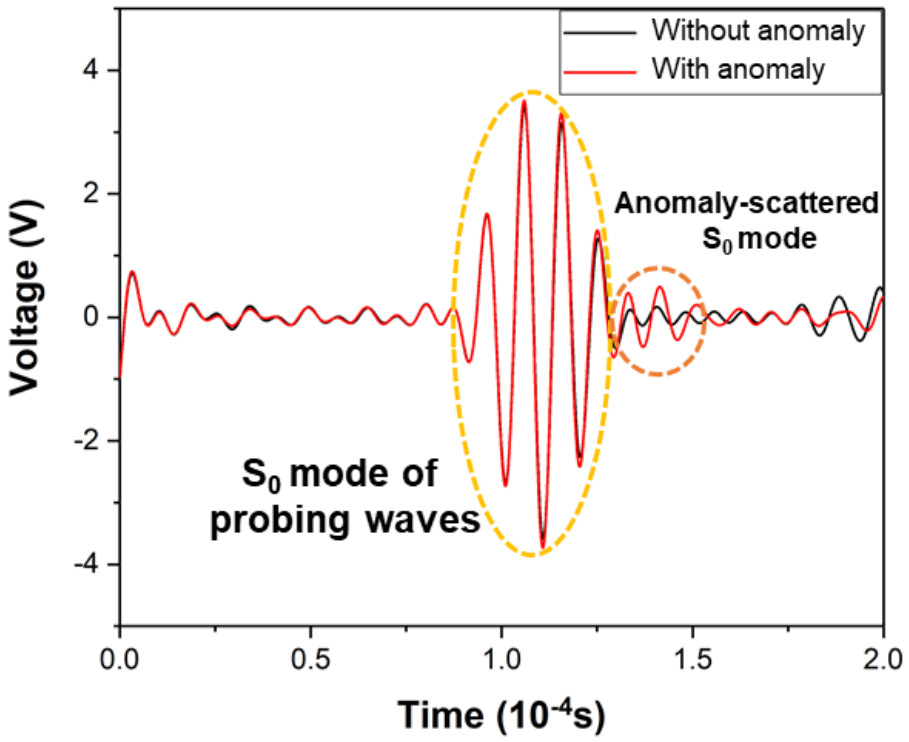

(a)

Figure 6.7 (a) Wave signals captured by S1 of APNSA, before and after the mock-up anomaly introduced; (b) $S_0^{Anomaly}$ in the signal captured by S1; and (c) $S_0^{Anomaly}$ in signals captured by all the sensing elements of APNSA.

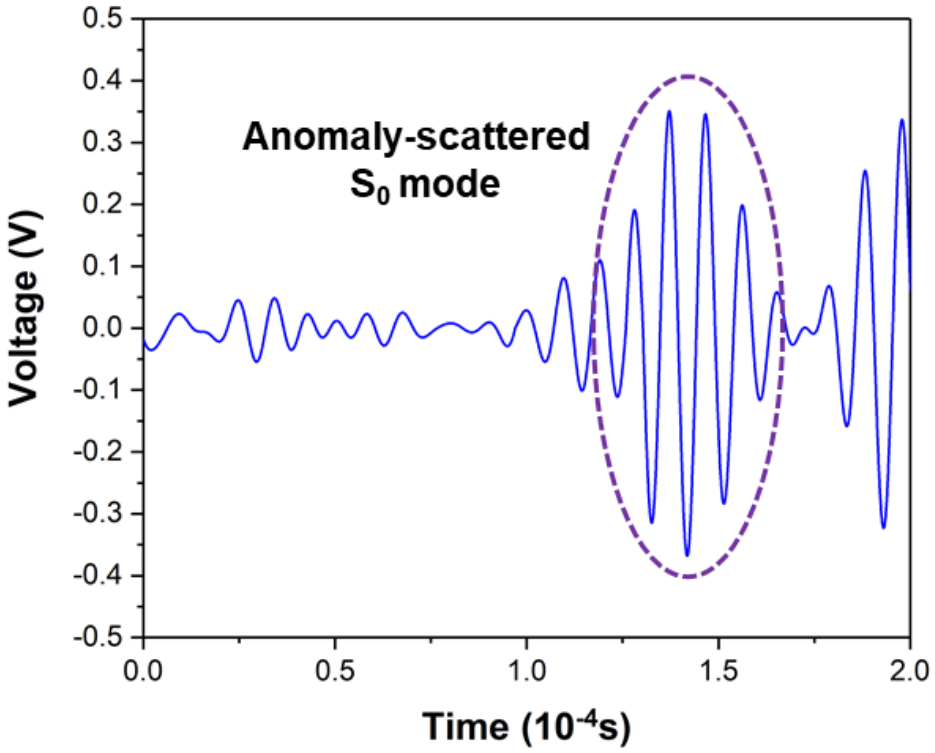

(b)

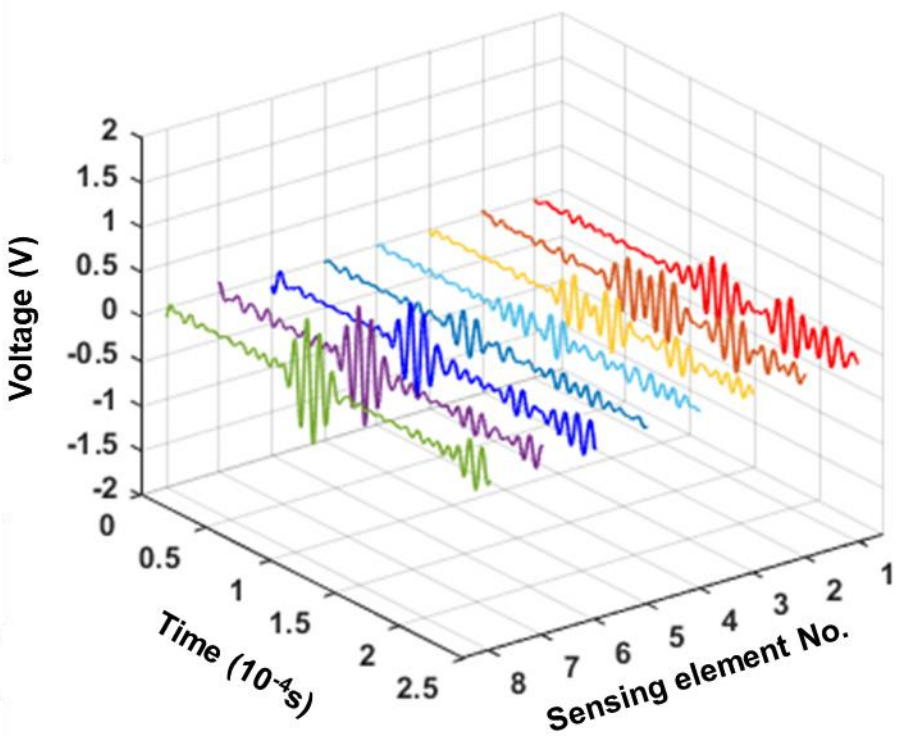

(c)

Figure 6.7 *Cont.*

Analogously, the $S_0^{Anomaly}$ is in turn extracted from the signal captured by each sensing element of APNSA, as shown in Figure 6.7(c). The *multiple signal classification* (MUSIC) – an array signal processing method for ultrasonic imaging, is applied. All extracted $S_0^{Anomaly}$ are written as a matrix form [202], as

$$\boldsymbol{R}^{S_0^{Anomaly}}(t) = [r_1(t), ..., r_m(t), ..., r_8(t)]^T, \tag{6.1}$$

where $\boldsymbol{R}^{S_0^{Anomaly}}(t)$ denotes the covariance matrix of signals acquired by all elements of APNSA, and $r_m(t)$ signifies $S_0^{Anomaly}$ captured via the m^{th} sensing element (Sm, m = 1, 2, …, 8). As indicated in Figure 6.8, the actuator is placed at position (x_0, y_0), and the m^{th} sensing element of APNSA is at (x_m, y_m). Assuming that a scanning position in the inspection region is at (x, y), the APNSA steering vector $\boldsymbol{A}(x, y)$ at this position can be defined as

$$\boldsymbol{A}(x, y) = [a_1(x, y), ..., a_m(x, y), ..., a_8(x, y)], \tag{6.2}$$

where

$$a_m(x, y) = e^{j\omega_0 \tau_m}, \tag{6.3}$$

$$\tau_m = \frac{d_1 - d_m}{c_w}, (m = 1, 2, \ldots, 8) \tag{6.4}$$

$$d_m = \sqrt{(x_0 - x)^2 + (y_0 - y)^2} + \sqrt{(x - x_m)^2 + (y - y_m)^2}. \tag{6.5}$$

In Equations (6.3)-(6.5), $a_m(x, y)$ is the steering vector of sensing element Sm, and τ_m is the difference in propagation time between two signals captured by sensing element S1 and element Sm. d_m signifies the wave propagation distance from the actuator to the scanning position, and then to Sm. c_w is the propagation velocity of the probing waves with central frequency of ω_0.

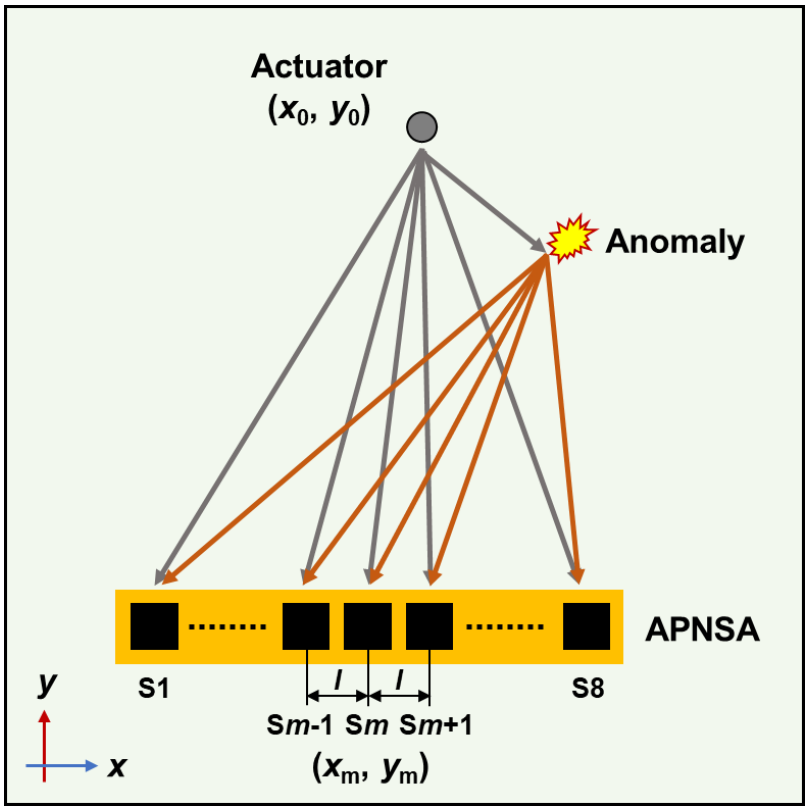

Figure 6.8 Use of MUSIC algorithm and APNSA for anomaly imaging.

The covariance matrix of the array signals $\boldsymbol{R}^{S_0^{Anomaly}}(t)$ can be decomposed into signal subspace $\boldsymbol{U}_S$ and noise subspace $\boldsymbol{U}_N$ via an eigenvalue decomposition. Based on the orthogonality between these two subspaces, the pixel value of the spatial spectrum at (x, y), $P_{MUSIC}(x, y)$, is formulated as

$$P_{MUSIC}(x,y) = \frac{1}{\boldsymbol{A}^H(x,y)(\boldsymbol{U}_N\boldsymbol{U}_N^H)\boldsymbol{A}(x,y)}. \tag{6.6}$$

Superscript H represents the complex conjugate transpose. By varying the scanning position (x, y), the spatial spectrum of the entire inspection region of the laminate is obtained. When the scanning position matches the anomaly location, the steering vector $\boldsymbol{A}(x, y)$ is orthogonal with regard to the noise subspace $\boldsymbol{U}_N$, and thus the denominator of Equation (6.6) approaches 0, resulting in a peak in the spatial

spectrum that corresponds to the anomaly location. The anomaly imaging result is shown in Figure 6.9, showing high coincidence with the true location of the mock-up anomaly, demonstrating the great application potential of the developed APNSA towards *in situ* composite structure health monitoring.

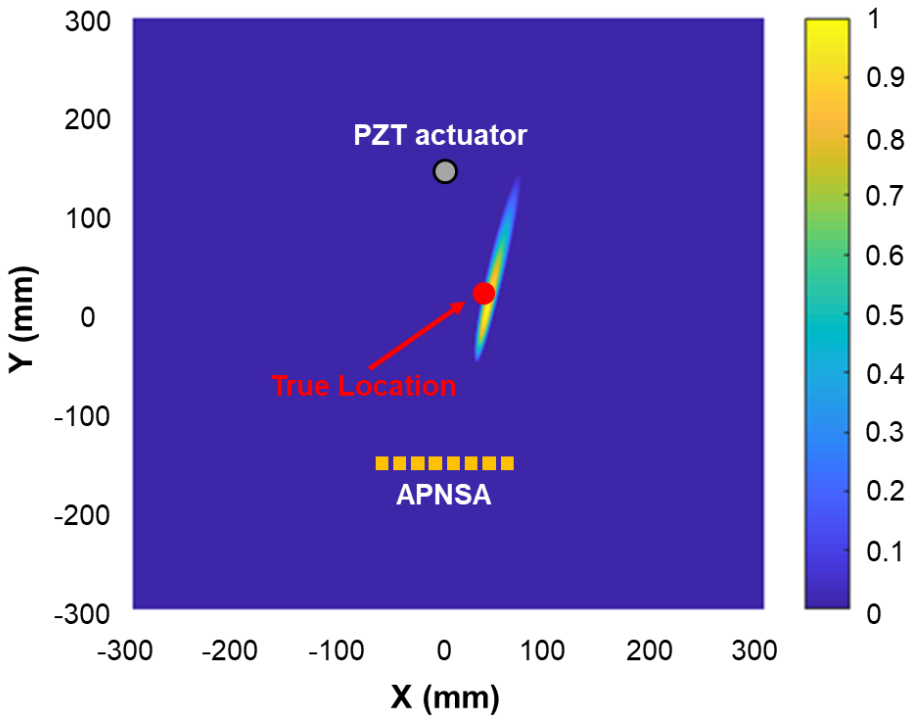

Figure 6.9 Anomaly image obtained via MUSIC algorithm and APNSA.

6.5 Summary

A new genre of nanocomposite-based APNSA is developed with graphene and PI, and fabricated by direct-write inkjet printing. Taking advantages of facile high-shear LPE and inkjet printing, by leveraging NGP/PAA nanocomposite sensing ink, APNSA is fabricated in a large-scale yet cost-effective manner. Each individual sensing element in APNSA (*i.e.*, NGP/PI sensor) features a homogenous and consolidated

nanostructure, and with quantum tunneling effect triggered by particulate movement of nanofillers in the NGP/PI sensor, the sensor has validated sensitivity, fidelity, and accuracy in responding to high-frequency acousto-ultrasonic wave signals in a broadband regime. APNSA is deployed to perform *in situ* anomaly imaging of composite laminates, well manifesting the full integration nature of APNSA with composites, and its great application prospects towards *in situ* SHM of composites.

CHAPTER 7

Conclusions and Recommendations for Future Study

7.1 Conclusions

Defects in engineering structures might not arouse sufficient attention until they deteriorate to a critical and irretrievable level, which may potentially result in catastrophic consequences, posing threat to the structural reliability, durability, and personal safety. Acousto-ultrasonic wave-based *in situ* SHM is demonstrated sensitive to damage of small dimension, and the damage information can be derived from the acousto-ultrasonic wave signals quantitively. Damage identification and health status perception in different structures can thus be achieved in an *in situ* manner with high accuracy, but without pausing the normal functionality of the structure. Central to the acousto-ultrasonic wave-based *in situ* SHM is perceiving acousto-ultrasonic wave signals, and sensors have become the most critical building block in an acousto-ultrasonic wave-driven SHM system. However, it is still challenging for prevailing sensors to concurrently achieve “sensing effectiveness” and “sensing cost”. In the meantime, ink-based AM has blazed a new trail in manufacturing new genre of electronic devices. In recognition of the drawbacks and development bottlenecks that

acousto-ultrasonic wave-driven SHM sensors are facing, in this PhD study, a series of sensors are designed and fabricated with direct-write ink-based AM approach (inkjet printing) to conform application demands of acousto-ultrasonic wave-driven SHM, with proven merits of superb ultrasound sensitivity, light weight, good flexibility, and excellent stability to aggressive environmental exposures.

Firstly, AM-driven thin film ultrasound sensors for acousto-ultrasonic wave-driven SHM are developed by directly printing CB/PVP ink on flexible substrates. The CB/PVP ink is rigorously designed and morphologically optimized, ensuring the good stability, printability and wettability of the ink. The great flexibility of the CB/PVP film sensors allows the sensors to conform with curve or non-planar surfaces. With uniform, even and stable nanofiller conductive networks formed inside the sensors, as well as the quantum tunneling effect triggered in the conductive networks of the sensors, the printed sensors show a much higher gauge factor than that of conventional metal foil strain gauges (when used for quasi-static strain or medium-frequency vibration measurement) and have proven responsivity and precision in responding to acousto-ultrasonic waves up to 500 kHz.

To further improve the sensitivity and responsivity of inkjet-printed thin film ultrasound sensors, NGP/PI-based film sensors are developed with NGP/PAA ink. The novel graphene-based ink is cost-effectively produced with facile high-shear LPE directly from inexpensive bulk graphite, exhibiting advantages of high graphene concentration, good storage stability, inkjet printability yet good functionality. The tailor-made printed film sensors feature an ultra-thin thickness (~ 1 μm), excellent thermal stability and extraordinary adhesive strength (ASTM 5B level). By virtue of

the uniform and compact nanostructure in the sensors, the quantum tunneling effect triggered among NGPs, and π-π interactions formed between NGPs and PI facilitate the printed sensors with a gauge factor as high as 739 (at 175 kHz). The sensors have proven capability of accurately sensing acousto-ultrasonic waves in a regime of megahertz (up to 1.6 MHz). The new flexible, ultrasensitive sensors feature not only extraordinary sensitivity, fidelity, and sensing precision that are comparable to commercial piezoelectric wafers, but also additional merits including light weight, low cost, large-scale production, and fabrication mildness and simplicity, accentuating their alluring potentials of being expanded to other application domains such as wearable healthcare devices for acousto-ultrasonic wave-based disease diagnosis.

As the inkjet-printed thin film ultrasound sensors have been demonstrated sensitive in perceiving acousto-ultrasonic wave signals, the film sensors are further printed with electrodes and protection layers, to form AIP sensors. The temperature effect on the AIP thin film ultrasound sensors in acquiring broadband acousto-ultrasonic wave signals is examined under harsh thermal cycles in an extensive temperature regime (–60 to 150 ^{o}C) that spans the thermal extremes undergone by typical aircraft and spacecraft. The dispersive characteristics of waves acquired by the sensors at varying temperatures exhibit good consistency with the theoretical model. With proven sensing accuracy and sensitivity comparable to commercial piezoelectric sensors, the AIP sensors outperform commercial piezoelectric sensors with an additional merit that the negative influence of increased dielectric permittivity during measurement of high-frequency signals at elevated temperatures can be prevented. These findings have confirmed that the AIP sensors are of good stability and a high degree of sensing precision within a wide range of temperature variation. An AIP sensor network

configured with a multitude of AIP sensors is deployed to perform *in situ* characterization of damage in a typical aerospace structural component under acutely varying temperatures, highlighting the application potentials of the developed AIP nanocomposite sensors in fulfilling *in situ* SHM for key aircraft and spacecraft components at harsh thermal conditions.

Lastly, the inkjet-printed thin film ultrasound sensors are further developed to APNSA by inkjet printing. Taking advantages of inkjet printing and numerous merits of thin film ultrasound sensors, APNSA can be fully integrated with the inspected composite structure, without degrading its original structural integrity – a task that is challenging to be fulfilled using conventional ultrasonic phased arrays. With a high degree of compatibility with the host structures, the APNSA manifests proven effectiveness in performing anomaly imaging of composite laminates, in lieu of conventional ultrasonic phased arrays, spotlighting its application prospects towards *in situ* SHM of composites.

In short, the merits of AM-driven thin film ultrasound sensors towards acousto-ultrasonic wave-driven SHM application developed in this PhD study can be summarized as follows:

- The AM-driven thin film ultrasound sensors are of ultrathin thickness, light weight, and good flexibility;
- The developed thin film ultrasound sensors feature excellent responsivity and sensitivity to high frequency ultrasonic waves, with a broad responsive spectrum up to megahertz;

- With proven stability to variation of ambient condition, the developed thin film ultrasound sensors are capable of maintaining their high degree of sensing accuracy to high frequency ultrasonic wave signals;
- The fabrication process (direct-write inkjet printing) of the thin film ultrasound sensors is of a high degree of automation, simplicity, and controllability;
- The responsive sensitivity of the sensors can be fine-tuned by adjusting the degree of conductivity via controlling the printed passes, making it possible to customize the sensors towards specific applications yet without a need to modify the ingredients of the inks;
- Lead-free, the developed thin film ultrasound sensors are of good biocompatibility when compared to lead-rich piezoelectric ceramic wafers, exhibiting attractive potentials for developing wearable health care devices.

7.2 Recommendations for Future Study

Although AM-driven thin film ultrasound sensors developed in this PhD study are of numerous merits, there are still several recommendations for extending research in the future.

First, there has been increasing demands of wearable health care devices in the past decades. For wearable devices, the stretchability, and maintaining the device performance under stretching are recognized as the most critical issues. Although the AM-driven thin film ultrasound sensors developed in this PhD study are non-toxic,

and show good flexibility, the stretchability of the sensors is yet to be investigated. Thus, the stretchability of the sensors and their acousto-ultrasonic wave sensing performance under stretching are two important problems to tackle in the future study, and stretchable polymeric materials such as polydimethylsiloxane (PMDS), poly(styrene-butadiene-styrene) (SBS), and Ecoflex can be considered as potential substrates of the sensors.

Second, the electrodes and supporting systems of the developed sensors including amplification modules are to be improved in future study. The sensitivity and responsivity of the sensors can be improved with the specifically optimized electrodes, as the shape and dimension of electrodes can be designed to select and magnify desired acousto-ultrasonic wave modes. For the supporting systems, they can be packaged with smaller physical sizes by adopting MEMS techniques, which is of critical significance for the development of the sensors towards wearable health care devices.

Third, inkjet printing features merits of high manufacturing precision, automation, controllability, and low cost. However, the limitations of inkjet printing also cannot be ignored. Inks have to be rigorously designed and optimized to be inkjet-printable, and it is difficult for the inks with viscosity higher than 20 cP to be deposited via inkjet printing. Restricted by this, inks with higher concentrations or formed with materials of higher viscosities are not compatible with inkjet printing. To overcome such a bottleneck, some other AM approaches such as aerosol printing can be considered in future study for producing new thin film ultrasound sensors.

Bibliography

[1] Wang K, Liu M, Su Z, Guo S, Cui F. Mode-mismatching enhanced disbond detection using material nonlinearity in guided waves at low frequency. Journal of Sound and Vibration. 2021;490:115733.

[2] Feng D, Feng MQ. Experimental validation of cost-effective vision-based structural health monitoring. Mechanical Systems and Signal Processing. 2017;88:199-211.

[3] Tzounis L, Zappalorto M, Panozzo F, Tsirka K, Maragoni L, Paipetis AS, *et al*. Highly conductive ultra-sensitive SWCNT-coated glass fiber reinforcements for laminate composites structural health monitoring. Composites Part B: Engineering. 2019;169:37-44.

[4] Tokognon CA, Gao B, Tian GY, Yan Y. Structural health monitoring framework based on Internet of Things: A survey. IEEE Internet of Things Journal. 2017;4(3):619-35.

[5] Hu N, Itoi T, Akagi T, Kojima T, Xue J, Yan C, *et al*. Ultrasensitive strain sensors made from metal-coated carbon nanofiller/epoxy composites. Carbon. 2013;51:202-12.

[6] Laflamme S, Kollosche M, Connor JJ, Kofod G. Robust flexible capacitive surface sensor for structural health monitoring applications. Journal of Engineering Mechanics. 2013;139(7):879-85.

[7] Loutas TH, Charlaftis P, Airoldi A, Bettini P, Koimtzoglou C, Kostopoulos V. Reliability of strain monitoring of composite structures via the use of optical fiber ribbon tapes for structural health monitoring purposes. Composite Structures.

2015;134:762-71.

[8] Seher M, Nagy PB. On the separation of Lorentz and magnetization forces in the transduction mechanism of Electromagnetic Acoustic Transducers (EMATs). NDT & E International. 2016;84:1-10.

[9] Abbasipour M, Khajavi R, Yousefi AA, Yazdanshenas ME, Razaghian F. The piezoelectric response of electrospun PVDF nanofibers with graphene oxide, graphene, and halloysite nanofillers: a comparative study. Journal of Materials Science: Materials in Electronics. 2017;28(21):15942-52.

[10] Ahn Y, Lim JY, Hong SM, Lee J, Ha J, Choi HJ, *et al*. Enhanced piezoelectric properties of electrospun poly(vinylidene fluoride)/multiwalled carbon nanotube composites due to high β-phase formation in poly(vinylidene fluoride). The Journal of Physical Chemistry C. 2013;117(22):11791-9.

[11] Liu M, Zeng Z, Xu H, Liao Y, Zhou L, Zhang Z, *et al*. Applications of a nanocomposite-inspired in-situ broadband ultrasonic sensor to acousto-ultrasonics-based passive and active structural health monitoring. Ultrasonics. 2017;78:166-74.

[12] Payo I, Hale JM. Dynamic characterization of piezoelectric paint sensors under biaxial strain. Sensors and Actuators A: Physical. 2010;163(1):150-8.

[13] Wang Y, Luo Y, Qiu L. Simulation method of an expandable Lamb wave sensor network for aircraft smart skin. IEEE Sensors Journal. 2020;20(1):102-12.

[14] Zhang Y, Jarosinski W, Jung Y-G, Zhang J. 2 - Additive manufacturing processes and equipment. In: Zhang J, Jung Y-G, editors. Additive manufacturing: Butterworth-Heinemann; 2018. p. 39-51.

[15] Xu S, Wu W. Ink-based additive nanomanufacturing of functional materials for human-integrated smart wearables. Advanced Intelligent Systems. 2020;2(10):2000117.

[16] Zeng Z, Liu M, Xu H, Liao Y, Duan F, Zhou L-m, *et al*. Ultra-broadband frequency responsive sensor based on lightweight and flexible carbon nanostructured polymeric nanocomposites. Carbon. 2017;121:490-501.

[17] Cao W, Zhou P, Liao Y, Yang X, Pan D, Li Y, *et al*. A spray-on, nanocomposite-based sensor network for in-situ active structural health monitoring. Sensors. 2019;19(9).

[18] Derby B. Inkjet printing ceramics: From drops to solid. Journal of the European Ceramic Society. 2011;31(14):2543-50.

[19] Jang D, Kim D, Moon J. Influence of fluid physical properties on ink-jet printability. Langmuir. 2009;25(5):2629-35.

[20] Lu Y, Xiang P, Dong P, Zhang X, Zeng J. Analysis of the effects of vibration modes on fatigue damage in high-speed train bogie frames. Engineering Failure Analysis. 2018;89:222-41.

[21] McKee JG, Bevan RLT, Wilcox PD, Malkin RE. Volumetric imaging through a doubly-curved surface using a 2D phased array. NDT & E International. 2020;113:102260.

[22] Kim G, Seo M-K, Kim Y-I, Kwon S, Kim K-B. Development of phased array ultrasonic system for detecting rail cracks. Sensors and Actuators A: Physical. 2020;311:112086.

[23] Lei X, Wirdelius H, Rosell A. Experimental validation of a phased array probe model in ultrasonic inspection. Ultrasonics. 2020;108:106217.

[24] Nesvijski EG. Some aspects of ultrasonic testing of composites. Composite Structures. 2000;48(1):151-5.

[25] Yuan F, Yu Y, Li L, Tian G. Investigation of DC electromagnetic-based motion induced Eddy current on NDT for crack detection. IEEE Sensors Journal.

2021;21(6):7449-57.

[26] Liao TW, Ni J. An automated radiographic NDT system for weld inspection: Part I – Weld extraction. NDT & E International. 1996;29(3):157-62.

[27] Zhu Y-K, Tian G-Y, Lu R-S, Zhang H. A review of optical NDT technologies. Sensors. 2011;11(8).

[28] Avdelidis NP, Almond DP, Dobbinson A, Hawtin BC, Ibarra-Castanedo C, Maldague X. Aircraft composites assessment by means of transient thermal NDT. Progress in Aerospace Sciences. 2004;40(3):143-62.

[29] Gomes GF, Mendez YAD, da Silva Lopes Alexandrino P, da Cunha SS, Ancelotti AC. A review of vibration based inverse methods for damage detection and identification in mechanical structures using optimization algorithms and ANN. Archives of Computational Methods in Engineering. 2019;26(4):883-97.

[30] Giurgiutiu V. Chapter 1 - Introduction. In: Giurgiutiu V, editor. Structural health monitoring with piezoelectric wafer active sensors (Second Edition). Oxford: Academic Press; 2014. p. 1-19.

[31] Wilson CL, Lonkar K, Roy S, Kopsaftopoulos F, Chang F-K. 7.20 Structural health monitoring of composites. In: Beaumont PWR, Zweben CH, editors. Comprehensive composite materials II. Oxford: Elsevier; 2018. p. 382-407.

[32] Abbas M, Shafiee M. Structural health monitoring (SHM) and determination of surface defects in large metallic structures using ultrasonic guided waves. Sensors. 2018;18(11).

[33] Fu H, Sharif-Khodaei Z, Aliabadi MHF. An energy-efficient cyber-physical system for wireless on-board aircraft structural health monitoring. Mechanical Systems and Signal Processing. 2019;128:352-68.

[34] Qiu L, Yuan S, Zhang X, Wang Y. A time reversal focusing based impact imaging

method and its evaluation on complex composite structures. Smart Materials and Structures. 2011;20(10):105014.

[35] Aggelis DG, Barkoula NM, Matikas TE, Paipetis AS. Acoustic structural health monitoring of composite materials : Damage identification and evaluation in cross ply laminates using acoustic emission and ultrasonics. Composites Science and Technology. 2012;72(10):1127-33.

[36] Xu K, Ta D, Su Z, Wang W. Transmission analysis of ultrasonic Lamb mode conversion in a plate with partial-thickness notch. Ultrasonics. 2014;54(1):395-401.

[37] Yuan S, Lai X, Zhao X, Xu X, Zhang L. Distributed structural health monitoring system based on smart wireless sensor and multi-agent technology. Smart Materials and Structures. 2005;15(1):1-8.

[38] Wang Q, Yuan S. Baseline-free imaging method based on new PZT sensor arrangements. Journal of Intelligent Material Systems and Structures. 2009;20(14):1663-73.

[39] Wang Y, Qiu L, Luo Y, Ding R. A stretchable and large-scale guided wave sensor network for aircraft smart skin of structural health monitoring. Structural Health Monitoring. 2019:1475921719850641.

[40] Shi J-X, Natsuki T, Lei X-W, Ni Q-Q. Wave propagation in the filament-wound composite pipes conveying fluid: Theoretical analysis for structural health monitoring applications. Composites Science and Technology. 2014;98:9-14.

[41] Rayleigh L. On waves propagated along the plane surface of an elastic solid. Proceedings of the London Mathematical Society. 1885;s1-17(1):4-11.

[42] Lamb H. On waves in an elastic plate. Proceedings of the Royal Society of London Series A, Containing Papers of a Mathematical and Physical Character. 1917;93(648):114-28.

[43] Felice MV, Fan Z. Sizing of flaws using ultrasonic bulk wave testing: A review. Ultrasonics. 2018;88:26-42.

[44] Introduction. In: Rose JL, editor. Ultrasonic guided waves in solid media. Cambridge: Cambridge University Press; 2014. p. 1-15.

[45] Waves in plates. In: Rose JL, editor. ultrasonic guided waves in solid media. Cambridge: Cambridge University Press; 2014. p. 76-106.

[46] Shen Z, Chen S, Zhang L, Yao K, Tan CY. Direct-write piezoelectric ultrasonic transducers for non-destructive testing of metal plates. IEEE Sensors Journal. 2017;17(11):3354-61.

[47] Lee YH, Oh T. The simple Lamb wave analysis to characterize concrete wide beams by the practical MASW test. Materials. 2016;9(6).

[48] Su Z, Ye L. Fundamentals and analysis of Lamb waves. In: Su Z, Ye L, editors. Identification of damage using Lamb waves: from fundamentals to applications. London: Springer London; 2009. p. 15-58.

[49] Wan X, Tse PW, Zhang X, Xu G, Zhang Q, Fan H, *et al*. Numerical study on static component generation from the primary Lamb waves propagating in a plate with nonlinearity. Smart Materials and Structures. 2018;27(4):045006.

[50] Michaels JE. Detection, localization and characterization of damage in plates with anin situarray of spatially distributed ultrasonic sensors. Smart Materials and Structures. 2008;17(3):035035.

[51] Peng T, Saxena A, Goebel K, Xiang Y, Sankararaman S, Liu Y. A novel Bayesian imaging method for probabilistic delamination detection of composite materials. Smart Materials and Structures. 2013;22(12):125019.

[52] Zhou C, Su Z, Cheng L. Quantitative evaluation of orientation-specific damage using elastic waves and probability-based diagnostic imaging. Mechanical Systems

and Signal Processing. 2011;25(6):2135-56.

[53] Zhu R, Huang GL, Yuan FG. Fast damage imaging using the time-reversal technique in the frequency–wavenumber domain. Smart Materials and Structures. 2013;22(7):075028.

[54] Zhao X, Gao H, Zhang G, Ayhan B, Yan F, Kwan C, *et al*. Active health monitoring of an aircraft wing with embedded piezoelectric sensor/actuator network: I. Defect detection, localization and growth monitoring. Smart Materials and Structures. 2007;16(4):1208-17.

[55] Moll J, Schulte RT, Hartmann B, Fritzen CP, Nelles O. Multi-site damage localization in anisotropic plate-like structures using an active guided wave structural health monitoring system. Smart Materials and Structures. 2010;19(4):045022.

[56] Ostachowicz W, Kudela P, Malinowski P, Wandowski T. Damage localisation in plate-like structures based on PZT sensors. Mechanical Systems and Signal Processing. 2009;23(6):1805-29.

[57] Kim SB, Sohn H. Instantaneous reference-free crack detection based on polarization characteristics of piezoelectric materials. Smart Materials and Structures. 2007;16(6):2375-87.

[58] Solodov I, Wackerl J, Pfleiderer K, Busse G. Nonlinear self-modulation and subharmonic acoustic spectroscopyfor damage detection and location. Applied Physics Letters. 2004;84(26):5386-8.

[59] Dutta D, Sohn H, Harries KA, Rizzo P. A nonlinear acoustic technique for crack detection in metallic structures. Structural Health Monitoring. 2009;8(3):251-62.

[60] Stetsovych O, Mutombo P, Švec M, Šámal M, Nejedlý J, Císařová I, *et al*. Large converse piezoelectric effect measured on a single molecule on a metallic surface. Journal of the American Chemical Society. 2018;140(3):940-6.

[61] Giurgiutiu V. Chapter 7 - Piezoelectric wafer active sensors – PWAS transducers. In: Giurgiutiu V, editor. Structural health monitoring with piezoelectric wafer active sensors (Second Edition). Oxford: Academic Press; 2014. p. 357-94.

[62] PI Piezo Technology. Piezoelectric Materials. https://www.piceramic.com/en/products/piezoelectric-materials/, retrieved by May 26, 2021.

[63] Lin M, Kumar A, Beard SJ, Qing X. Built-in structural diagnostic with the SMART Layer™ and SMART Suitcase™. Smart Materials Bulletin. 2001;2001(4):7-11.

[64] Qing XP, Beard SJ, Kumar A, Chan H-L, Ikegami R. Advances in the development of built-in diagnostic system for filament wound composite structures. Composites Science and Technology. 2006;66(11):1694-702.

[65] Bekas DG, Sharif-Khodaei Z, Aliabadi MHF. An innovative diagnostic film for structural health monitoring of metallic and composite structures. Sensors. 2018;18(7).

[66] Wang Y, Qiu L, Luo Y, Ding R, Jiang F. A piezoelectric sensor network with shared signal transmission wires for structural health monitoring of aircraft smart skin. Mechanical Systems and Signal Processing. 2020;141:106730.

[67] Nishiyama T, Sumihara T, Sasaki Y, Sato E, Yamato M, Horibe H. Crystalline structure control of poly(vinylidene fluoride) films with the antisolvent addition method. Polymer Journal. 2016;48(10):1035-8.

[68] Ohigashi H, Koga K, Suzuki M, Nakanishi T, Kimura K, Hashimoto N. Piezoelectric and ferroelectric properties of P(VDF-TrFE) copolymers and their application to ultrasonic transducers. Ferroelectrics. 1984;60(1):263-76.

[69] Karan SK, Sriramdas R, Kang M-G, Yan Y, Priya S. Small-scale energy harvesting devices for smart electronics. In: Pomeroy M, editor. Encyclopedia of materials:

technical ceramics and glasses. Oxford: Elsevier; 2021. p. 391-425.

[70] Li Z, Wang Y, Cheng ZY. Electromechanical properties of poly(vinylidene-fluoride-chlorotrifluoroethylene) copolymer. Applied Physics Letters. 2006;88(6):062904.

[71] Neese B, Wang Y, Chu B, Ren K, Liu S, Zhang QM, *et al*. Piezoelectric responses in poly(vinylidene fluoride/hexafluoropropylene) copolymers. Applied Physics Letters. 2007;90(24):242917.

[72] Zhang S, Zhang N, Huang C, Ren K, Zhang QM. Microstructure and electromechanical properties of carbon nanotube/poly(vinylidene fluoride–trifluoroethylene–chlorofluoroethylene) composites. Advanced Materials. 2005;17(15):1897-901.

[73] Anwar S, Hassanpour Amiri M, Jiang S, Abolhasani MM, Rocha PRF, Asadi K. Piezoelectric nylon-11 fibers for electronic textiles, energy harvesting and sensing. Advanced Functional Materials. 2021;31(4):2004326.

[74] Lu Z, Dorantes-Gonzalez DJ, Chen K, Yang F, Jin B, Li Y, et al. A four-quadrant PVDF transducer for surface acoustic wave detection. Sensors. 2012;12(8).

[75] Di Sante R. Fibre optic sensors for structural health monitoring of aircraft composite structures: recent advances and applications. Sensors. 2015;15(8).

[76] Lam P-M, Lau K-T, Ling H-Y, Su Z, Tam H-Y. Acousto-ultrasonic sensing for delaminated GFRP composites using an embedded FBG sensor. Optics and Lasers in Engineering. 2009;47(10):1049-55.

[77] Betz DC, Thursby G, Culshaw B, Staszewski WJ. Identification of structural damage using multifunctional Bragg grating sensors: I. Theory and implementation. Smart Materials and Structures. 2006;15(5):1305-12.

[78] Takeda N, Okabe Y, Kuwahara J, Kojima S, Ogisu T. Development of smart

composite structures with small-diameter fiber Bragg grating sensors for damage detection: Quantitative evaluation of delamination length in CFRP laminates using Lamb wave sensing. Composites Science and Technology. 2005;65(15):2575-87.

[79] Kahandawa GC, Epaarachchi J, Wang H, Lau KT. Use of FBG sensors for SHM in aerospace structures. Photonic Sensors. 2012;2(3):203-14.

[80] Attarian VA, Cegla FB, Cawley P. Long-term stability of guided wave structural health monitoring using distributed adhesively bonded piezoelectric transducers. Structural Health Monitoring. 2014;13(3):265-80.

[81] Ribichini R, Cegla F, Nagy PB, Cawley P. Study and comparison of different EMAT configurations for SH wave inspection. IEEE Transactions on Ultrasonics, Ferroelectrics, and Frequency Control. 2011;58(12):2571-81.

[82] Vasile CF, Thompson RB. Excitation of horizontally polarized shear elastic waves by electromagnetic transducers with periodic permanent magnets. Journal of Applied Physics. 1979;50(4):2583-8.

[83] Jeong K, Lee J, Kim T, Cho Y. Aircraft component defect monitoring by the use of patch magnetostrictive EMAT. Journal of Visualization. 2017;20(4):847-58.

[84] Thompson RB. Generation of horizontally polarized shear waves in ferromagnetic materials using magnetostrictively coupled meander-coil electromagnetic transducers. Applied Physics Letters. 1979;34(2):175-7.

[85] Miao H, Dong S, Li F. Excitation of fundamental shear horizontal wave by using face-shear (d36) piezoelectric ceramics. Journal of Applied Physics. 2016;119(17):174101.

[86] Innerspec. EMAT technology. https://www.innerspec.com/emat-technology, retrieved by 28 May, 2021.

[87] García D, Trendafilova I, Inman DJ. A study on the vibration-based self-

monitoring capabilities of nano-enriched composite laminated beams. Smart Materials and Structures. 2016;25(4):045011.

[88] Osho S, Wu N, Aramfard M, Deng C, Ojo O. Fabrication and calibration of a piezoelectric nanocomposite paint. Smart Materials and Structures. 2018;27(3):035007.

[89] Wang L, Loh KJ, Chiang W-H, Manna K. Micro-patterned graphene-based sensing skins for human physiological monitoring. Nanotechnology. 2018;29(10):105503.

[90] Augustin T, Karsten J, Kötter B, Fiedler B. Health monitoring of scarfed CFRP joints under cyclic loading via electrical resistance measurements using carbon nanotube modified adhesive films. Composites Part A: Applied Science and Manufacturing. 2018;105:150-5.

[91] Liu Y, Zhang D, Wang K, Liu Y, Shang Y. A novel strain sensor based on graphene composite films with layered structure. Composites Part A: Applied Science and Manufacturing. 2016;80:95-103.

[92] Yan C, Wang J, Kang W, Cui M, Wang X, Foo CY, *et al.* Highly stretchable piezoresistive graphene–nanocellulose nanopaper for strain sensors. Advanced Materials. 2014;26(13):2022-7.

[93] Spinelli G, Lamberti P, Tucci V, Vertuccio L, Guadagno L. Experimental and theoretical study on piezoresistive properties of a structural resin reinforced with carbon nanotubes for strain sensing and damage monitoring. Composites Part B: Engineering. 2018;145:90-9.

[94] Qin Y, Peng Q, Ding Y, Lin Z, Wang C, Li Y, *et al.* Lightweight, superelastic, and mechanically flexible graphene/polyimide nanocomposite foam for strain sensor application. ACS Nano. 2015;9(9):8933-41.

[95] Wu S, Peng S, Han ZJ, Zhu H, Wang CH. Ultrasensitive and stretchable strain sensors based on mazelike vertical graphene network. ACS Applied Materials & Interfaces. 2018;10(42):36312-22.

[96] Qiu L, Bulut Coskun M, Tang Y, Liu JZ, Alan T, Ding J, *et al.* Ultrafast dynamic piezoresistive response of graphene-based cellular elastomers. Advanced Materials. 2016;28(1):194-200.

[97] Liu S, Wu X, Zhang D, Guo C, Wang P, Hu W, *et al.* Ultrafast dynamic pressure sensors based on graphene hybrid structure. ACS Applied Materials & Interfaces. 2017;9(28):24148-54.

[98] Gullapalli H, Vemuru VSM, Kumar A, Botello-Mendez A, Vajtai R, Terrones M, *et al*. Flexible piezoelectric ZnO–paper nanocomposite strain sensor. Small. 2010;6(15):1641-6.

[99] Zeng Z, Liu M, Xu H, Liu W, Liao Y, Jin H, *et al*. A coatable, light-weight, fast-response nanocomposite sensor for the in situ acquisition of dynamic elastic disturbance: from structural vibration to ultrasonic waves. Smart Materials and Structures. 2016;25(6):065005.

[100] Xu H, Zeng Z, Wu Z, Zhou L, Su Z, Liao Y, *et al*. Broadband dynamic responses of flexible carbon black/poly (vinylidene fluoride) nanocomposites: A sensitivity study. Composites Science and Technology. 2017;149:246-53.

[101] Liao Y, Duan F, Zhang H, Lu Y, Zeng Z, Liu M, *et al*. Ultrafast response of spray-on nanocomposite piezoresistive sensors to broadband ultrasound. Carbon. 2019;143:743-51.

[102] Zhang T, Chen Z, Yang D, Wu F, Zhao X, Yang X. Fabricating high performance polymer photovoltaic modules by creating large-scale uniform films. Organic Electronics. 2016;32:126-33.

[103] Wang T, Scarratt NW, Yi H, Dunbar ADF, Pearson AJ, Watters DC, *et al*. Fabricating high performance, donor–acceptor copolymer solar cells by spray-coating in air. Advanced Energy Materials. 2013;3(4):505-12.

[104] Kavadiya S, Biswas P. Electrospray deposition of biomolecules: Applications, challenges, and recommendations. Journal of Aerosol Science. 2018;125:182-207.

[105] Gao M, Li L, Song Y. Inkjet printing wearable electronic devices. Journal of Materials Chemistry C. 2017;5(12):2971-93.

[106] Jabari E, Toyserkani E. Micro-scale aerosol-jet printing of graphene interconnects. Carbon. 2015;91:321-9.

[107] Wallin TJ, Pikul J, Shepherd RF. 3D printing of soft robotic systems. Nature Reviews Materials. 2018;3(6):84-100.

[108] Muth JT, Vogt DM, Truby RL, Mengüç Y, Kolesky DB, Wood RJ, *et al*. Embedded 3D printing of strain sensors within highly stretchable elastomers. Advanced Materials. 2014;26(36):6307-12.

[109] Casiraghi C, Macucci M, Parvez K, Worsley R, Shin Y, Bronte F, *et al.* Inkjet printed 2D-crystal based strain gauges on paper. Carbon. 2018;129:462-7.

[110] Zirkl M, Sawatdee A, Helbig U, Krause M, Scheipl G, Kraker E, *et al.* An all-printed ferroelectric active matrix sensor network based on only five functional materials forming a touchless control interface. Advanced Materials. 2011;23(18):2069-74.

[111] Sirringhaus H, Kawase T, Friend RH, Shimoda T, Inbasekaran M, Wu W, *et al.* High-resolution inkjet printing of all-polymer transistor circuits. Science. 2000;290(5499):2123.

[112] He P, Brent JR, Ding H, Yang J, Lewis DJ, O'Brien P, *et al*. Fully printed high performance humidity sensors based on two-dimensional materials. Nanoscale.

2018;10(12):5599-606.

[113] Molina-Lopez F, Briand D, de Rooij NF. All additive inkjet printed humidity sensors on plastic substrate. Sensors and Actuators B: Chemical. 2012;166-167:212-22.

[114] Juntunen T, Jussila H, Ruoho M, Liu S, Hu G, Albrow-Owen T, *et al*. Inkjet printed large-area flexible few-layer graphene thermoelectrics. Advanced Functional Materials. 2018;28(22):1800480.

[115] Chen B, Kruse M, Xu B, Tutika R, Zheng W, Bartlett MD, *et al.* Flexible thermoelectric generators with inkjet-printed bismuth telluride nanowires and liquid metal contacts. Nanoscale. 2019;11(12):5222-30.

[116] Sun Y, Zhang Y, Liang Q, Zhang Y, Chi H, Shi Y, *et al.* Solvent inkjet printing process for the fabrication of polymer solar cells. RSC Advances. 2013;3(30):11925-34.

[117] Eggenhuisen TM, Galagan Y, Biezemans AFKV, Slaats TMWL, Voorthuijzen WP, Kommeren S, *et al.* High efficiency, fully inkjet printed organic solar cells with freedom of design. Journal of Materials Chemistry A. 2015;3(14):7255-62.

[118] Singh R, Singh E, Nalwa HS. Inkjet printed nanomaterial based flexible radio frequency identification (RFID) tag sensors for the internet of nano things. RSC Advances. 2017;7(77):48597-630.

[119] Borgese M, Dicandia FA, Costa F, Genovesi S, Manara G. An inkjet printed chipless RFID sensor for wireless humidity monitoring. IEEE Sensors Journal. 2017;17(15):4699-707.

[120] Huang T-T, Wu W. Scalable nanomanufacturing of inkjet-printed wearable energy storage devices. Journal of Materials Chemistry A. 2019;7(41):23280-300.

[121] Gu Y, Wu A, Sohn H, Nicoletti C, Iqbal Z, Federici JF. Fabrication of

rechargeable lithium ion batteries using water-based inkjet printed cathodes. Journal of Manufacturing Processes. 2015;20:198-205.

[122] Martin GD, Hoath SD, Hutchings IM. Inkjet printing - the physics of manipulating liquid jets and drops. Journal of Physics: Conference Series. 2008;105:012001.

[123] Derby B. Inkjet printing of functional and structural materials: fluid property requirements, feature stability, and resolution. Annual Review of Materials Research. 2010;40(1):395-414.

[124] Haque RI, Vié R, Germainy M, Valbin L, Benaben P, Boddaert X. Inkjet printing of high molecular weight PVDF-TrFE for flexible electronics. Flexible and Printed Electronics. 2015;1(1):015001.

[125] Derby B. Additive manufacture of ceramics components by inkjet printing. Engineering. 2015;1(1):113-23.

[126] Reis N, Derby B. Ink jet deposition of ceramic suspensions: modeling and experiments of droplet formation. MRS Proceedings. 2000;625:117.

[127] Shin K-Y, Hong J-Y, Jang J. Flexible and transparent graphene films as acoustic actuator electrodes using inkjet printing. Chemical Communications. 2011;47(30):8527-9.

[128] Loffredo F, Mauro ADGD, Burrasca G, La Ferrara V, Quercia L, Massera E, *et al.* Ink-jet printing technique in polymer/carbon black sensing device fabrication. Sensors and Actuators B: Chemical. 2009;143(1):421-9.

[129] Pabst O, Perelaer J, Beckert E, Schubert US, Eberhardt R, Tünnermann A. All inkjet-printed piezoelectric polymer actuators: Characterization and applications for micropumps in lab-on-a-chip systems. Organic Electronics. 2013;14(12):3423-9.

[130] Fic K, Platek A, Piwek J, Frackowiak E. Sustainable materials for

electrochemical capacitors. Materials Today. 2018;21(4):437-54.

[131] He P, Derby B. Inkjet printing ultra-large graphene oxide flakes. 2D Materials. 2017;4(2):021021.

[132] Fromm JE. Numerical calculation of the fluid dynamics of drop-on-demand jets. IBM Journal of Research and Development. 1984;28(3):322-33.

[133] Mionić M, Pataky K, Gaal R, Magrez A, Brugger J, Forró L. Carbon nanotubes–SU8 composite for flexible conductive inkjet printable applications. Journal of Materials Chemistry. 2012;22(28):14030-4.

[134] Calvert P. Inkjet printing for materials and devices. Chemistry of Materials. 2001;13(10):3299-305.

[135] Inagaki N, Tasaka S, Hibi K. Surface modification of Kapton film by plasma treatments. Journal of Polymer Science Part A: Polymer Chemistry. 1992;30(7):1425-31.

[136] Smits FM. Measurement of sheet resistivities with the four-point probe. The Bell System Technical Journal. 1958;37(3):711-8.

[137] Michelis F, Bodelot L, Bonnassieux Y, Lebental B. Highly reproducible, hysteresis-free, flexible strain sensors by inkjet printing of carbon nanotubes. Carbon. 2015;95:1020-6.

[138] Hu N, Karube Y, Yan C, Masuda Z, Fukunaga H. Tunneling effect in a polymer/carbon nanotube nanocomposite strain sensor. Acta Materialia. 2008;56(13):2929-36.

[139] Pawlyta M, Rouzaud J-N, Duber S. Raman microspectroscopy characterization of carbon blacks: Spectral analysis and structural information. Carbon. 2015;84:479-90.

[140] Saito R, Hofmann M, Dresselhaus G, Jorio A, Dresselhaus MS. Raman

spectroscopy of graphene and carbon nanotubes. Advances in Physics. 2011;60(3):413-550.

[141] Vertuccio L, Guadagno L, Spinelli G, Lamberti P, Tucci V, Russo S. Piezoresistive properties of resin reinforced with carbon nanotubes for health-monitoring of aircraft primary structures. Composites Part B: Engineering. 2016;107:192-202.

[142] Li Y, Wang K, Su Z. Dispersed sensing networks in nano-engineered polymer composites: from static strain measurement to ultrasonic wave acquisition. Sensors. 2018;18(5).

[143] Zhang X-W, Pan Y, Zheng Q, Yi X-S. Time dependence of piezoresistance for the conductor-filled polymer composites. Journal of Polymer Science Part B: Polymer Physics. 2000;38(21):2739-49.

[144] Al-solamy FR, Al-Ghamdi AA, Mahmoud WE. Piezoresistive behavior of graphite nanoplatelets based rubber nanocomposites. Polymers for Advanced Technologies. 2012;23(3):478-82.

[145] Sadasivuni KK, Ponnamma D, Thomas S, Grohens Y. Evolution from graphite to graphene elastomer composites. Progress in Polymer Science. 2014;39(4):749-80.

[146] Zhao J, He C, Yang R, Shi Z, Cheng M, Yang W, *et al.* Ultra-sensitive strain sensors based on piezoresistive nanographene films. Applied Physics Letters. 2012;101(6):063112.

[147] Yoonessi M, Gaier JR, Sahimi M, Daulton TL, Kaner RB, Meador MA. Fabrication of graphene–polyimide nanocomposites with superior electrical conductivity. ACS Applied Materials & Interfaces. 2017;9(49):43230-8.

[148] Wu T, Xu Y, Wang H, Sun Z, Zou L. Efficient and inexpensive preparation of graphene laminated film with ultrahigh thermal conductivity. Carbon. 2021;171:639-

45.

[149] Lee G-H, Cooper RC, An SJ, Lee S, van der Zande A, Petrone N, *et al.* High-strength chemical-vapor-deposited graphene and grain boundaries. Science. 2013;340(6136):1073.

[150] Torrisi F, Carey T. Graphene, related two-dimensional crystals and hybrid systems for printed and wearable electronics. Nano Today. 2018;23:73-96.

[151] Mu Z, Liu T, Ji X, Luo H, Tang L, Cheng S. A facile and cost-effective approach to fabricate flexible graphene films for aqueous available current collectors. Carbon. 2020;170:264-9.

[152] Tran MT, Tung TT, Sachan A, Losic D, Castro M, Feller JF. 3D sprayed polyurethane functionalized graphene/carbon nanotubes hybrid architectures to enhance the piezo-resistive response of quantum resistive pressure sensors. Carbon. 2020;168:564-79.

[153] da Cunha Rodrigues G, Zelenovskiy P, Romanyuk K, Luchkin S, Kopelevich Y, Kholkin A. Strong piezoelectricity in single-layer graphene deposited on SiO_2 grating substrates. Nature Communications. 2015;6(1):7572.

[154] Jäger K-M, McQueen DH. Fractal agglomerates and electrical conductivity in carbon black polymer composites. Polymer. 2001;42(23):9575-81.

[155] Hernandez Y, Nicolosi V, Lotya M, Blighe FM, Sun Z, De S, *et al.* High-yield production of graphene by liquid-phase exfoliation of graphite. Nature Nanotechnology. 2008;3(9):563-8.

[156] Novoselov KS, Geim AK, Morozov SV, Jiang D, Zhang Y, Dubonos SV, *et al.* Electric field effect in atomically thin carbon films. Science. 2004;306(5696):666.

[157] Pandhi T, Kreit E, Aga R, Fujimoto K, Sharbati MT, Khademi S, *et al.* Electrical transport and power dissipation in aerosol-jet-printed graphene interconnects.

Scientific Reports. 2018;8(1):10842.

[158] Majee S, Song M, Zhang S-L, Zhang Z-B. Scalable inkjet printing of shear-exfoliated graphene transparent conductive films. Carbon. 2016;102:51-7.

[159] Torrisi F, Hasan T, Wu W, Sun Z, Lombardo A, Kulmala TS, *et al.* Inkjet-printed graphene electronics. ACS Nano. 2012;6(4):2992-3006.

[160] Diaham S, Locatelli ML, Lebey T, Malec D. Thermal imidization optimization of polyimide thin films using Fourier transform infrared spectroscopy and electrical measurements. Thin Solid Films. 2011;519(6):1851-6.

[161] Seo Y, Lee SM, Kim DY, Kim KU. Kinetic study of the imidization of a poly(ester amic acid) by FT-Raman spectroscopy. Macromolecules. 1997;30(13):3747-53.

[162] Grimme S. Do special noncovalent π–π stacking interactions really exist? Angewandte Chemie International Edition. 2008;47(18):3430-4.

[163] Wang Q, Bai Y, Chen Y, Ju J, Zheng F, Wang T. High performance shape memory polyimides based on π–π interactions. Journal of Materials Chemistry A. 2015;3(1):352-9.

[164] Su Z, Zhou L, Qiu L, Xu H, Zeng Z, Liu M. Resistance-voltage transformation system for sensors in dynamic strain measurement and structural health monitoring. US Patent. 2018; 9 863 824 B1.

[165] Su HY, Wu YK, Tu SL, Chang S-J. Electrostatic studies of π–π interaction for benzene stacking on a graphene layer. Applied Physics Letters. 2011;99(16):163102.

[166] Sohn H. Effects of environmental and operational variability on structural health monitoring. Philosophical Transactions of the Royal Society A: Mathematical, Physical and Engineering Sciences. 2007;365(1851):539-60.

[167] Raghavan A, Cesnik CES. Effects of elevated temperature on guided-wave

structural health monitoring. Journal of Intelligent Material Systems and Structures. 2008;19(12):1383-98.

[168] Li W, Dichiara A, Zha J, Su Z, Bai J. On improvement of mechanical and thermo-mechanical properties of glass fabric/epoxy composites by incorporating CNT–Al_2O_3 hybrids. Composites Science and Technology. 2014;103:36-43.

[169] Qing X, Li W, Wang Y, Sun H. Piezoelectric transducer-based structural health monitoring for aircraft applications. Sensors. 2019;19(3).

[170] Mohimi A, Gan T-H, Balachandran W. Development of high temperature ultrasonic guided wave transducer for continuous in service monitoring of steam lines using non-stoichiometric lithium niobate piezoelectric ceramic. Sensors and Actuators A: Physical. 2014;216:432-42.

[171] Baker A, Rajic N, Davis C. Towards a practical structural health monitoring technology for patched cracks in aircraft structure. Composites Part A: Applied Science and Manufacturing. 2009;40(9):1340-52.

[172] Blaise E, Chang F. Built-in diagnostics for debonding in sandwich structures under extreme temperatures. Proceedings of the 3rd international workshop on structural health monitoring: Stanford, California, USA; 2001. p. 154-63.

[173] Lanza di Scalea F, Salamone S. Temperature effects in ultrasonic Lamb wave structural health monitoring systems. The Journal of the Acoustical Society of America. 2008;124(1):161-74.

[174] Lu Y, Michaels JE. A methodology for structural health monitoring with diffuse ultrasonic waves in the presence of temperature variations. Ultrasonics. 2005;43(9):717-31.

[175] Konstantinidis G, Drinkwater BW, Wilcox PD. The temperature stability of guided wave structural health monitoring systems. Smart Materials and Structures.

2006;15(4):967-76.

[176] Clarke T, Cawley P, Wilcox PD, Croxford AJ. Evaluation of the damage detection capability of a sparse-array guided-wave SHM system applied to a complex structure under varying thermal conditions. IEEE Transactions on Ultrasonics, Ferroelectrics, and Frequency Control. 2009;56(12):2666-78.

[177] Clarke T, Simonetti F, Cawley P. Guided wave health monitoring of complex structures by sparse array systems: Influence of temperature changes on performance. Journal of Sound and Vibration. 2010;329(12):2306-22.

[178] Wang Y, Gao L, Yuan S, Qiu L, Qing X. An adaptive filter–based temperature compensation technique for structural health monitoring. Journal of Intelligent Material Systems and Structures. 2014;25(17):2187-98.

[179] Fukukawa K-i, Ueda M. Recent progress of photosensitive polyimides. Polymer Journal. 2008;40(4):281-96.

[180] Marzani A, Salamone S. Numerical prediction and experimental verification of temperature effect on plate waves generated and received by piezoceramic sensors. Mechanical Systems and Signal Processing. 2012;30:204-17.

[181] Su Z, Ye L. Activating and receiving lamb waves. In: Su Z, Ye L, editors. Identification of damage using lamb waves: from fundamentals to applications. London: Springer London; 2009. p. 59-98.

[182] Lee H-J, Saravanos DA. The effect of temperature dependent material properties on the response of piezoelectric composite materials. Journal of Intelligent Material Systems and Structures. 1998;9(7):503-8.

[183] Zhang R, Bin Y, Chen R, Matsuo M. Evaluation by tunneling effect for the temperature-dependent electric conductivity of polymer-carbon fiber composites with visco-elastic properties. Polymer Journal. 2013;45(11):1120-34.

[184] Lanza di Scalea F, Matt H, Bartoli I. The response of rectangular piezoelectric sensors to Rayleigh and Lamb ultrasonic waves. The Journal of the Acoustical Society of America. 2007;121(1):175-87.

[185] Sukesha, Vig R, Kumar N. Effect of electric field and temperature on dielectric constant and piezoelectric coefficient of piezoelectric materials: a review. Integrated Ferroelectrics. 2015;167(1):154-75.

[186] Dodson JC, Inman DJ. Thermal sensitivity of Lamb waves for structural health monitoring applications. Ultrasonics. 2013;53(3):677-85.

[187] Su Z, Ye L. Lamb wave propagation-based damage identification for quasi-isotropic CF/EP composite laminates using artificial neural algorithm: Part II - implementation and validation. Journal of Intelligent Material Systems and Structures. 2005;16(2):113-25.

[188] Sohn H, Lim HJ, DeSimio MP, Brown K, Derriso M. Nonlinear ultrasonic wave modulation for online fatigue crack detection. Journal of Sound and Vibration. 2014;333(5):1473-84.

[189] Wang Q, Hong M, Su Z. An in-situ structural health diagnosis technique and its realization via a modularized system. IEEE Transactions on Instrumentation and Measurement. 2015;64(4):873-87.

[190] Li Y, Liao Y, Su Z. Graphene-functionalized polymer composites for self-sensing of ultrasonic waves: An initiative towards “sensor-free” structural health monitoring. Composites Science and Technology. 2018;168:203-13.

[191] Wang C, Chen M, Lei H, Yao K, Li H, Wen W, *et al.* Radar stealth and mechanical properties of a broadband radar absorbing structure. Composites Part B: Engineering. 2017;123:19-27.

[192] Pan X, Jiang J, Wang N. Evaluation of the performance of the distributed phased-

MIMO sonar. Sensors. 2017;17(1).

[193] Huda MM, Langston CA. Coherence and variability of ground motion in New Madrid Seismic Zone using an array of 600 m. Journal of Seismology. 2021.

[194] Blanco D, Rajo-Iglesias E, Benito AM, Llombart N. Leaky-wave thinned phased array in PCB technology for telecommunication applications. IEEE Transactions on Antennas and Propagation. 2016;64(10):4288-96.

[195] Wong C-M, Chen Y, Luo H, Dai J, Lam K-H, Chan HL-w. Development of a 20-MHz wide-bandwidth PMN-PT single crystal phased-array ultrasound transducer. Ultrasonics. 2017;73:181-6.

[196] Morozov M, Jackson W, Pierce SG. Capacitive imaging of impact damage in composite material. Composites Part B: Engineering. 2017;113:65-71.

[197] Flora F, Boccaccio M, Fierro GPM, Meo M. Real-time thermography system for composite welding: Undamaged baseline approach. Composites Part B: Engineering. 2021;215:108740.

[198] Brizuela J, Camacho J, Cosarinsky G, Iriarte JM, Cruza JF. Improving elevation resolution in phased-array inspections for NDT. NDT & E International. 2019;101:1-16.

[199] Nsengiyumva W, Zhong S, Lin J, Zhang Q, Zhong J, Huang Y. Advances, limitations and prospects of nondestructive testing and evaluation of thick composites and sandwich structures: A state-of-the-art review. Composite Structures. 2021;256:112951.

[200] Yuan C, Xie C, Li L, Zhang F, Gubanski SM. Ultrasonic phased array detection of internal defects in composite insulators. IEEE Transactions on Dielectrics and Electrical Insulation. 2016;23(1):525-31.

[201] Giurgiutiu V. Chapter 13 - In situ phased arrays with piezoelectric wafer active

sensors. In: Giurgiutiu V, editor. Structural health monitoring with piezoelectric wafer active sensors (Second Edition). Oxford: Academic Press; 2014. p. 707-805.

[202] Zuo H, Yang Z, Xu C, Tian S, Chen X. Damage identification for plate-like structures using ultrasonic guided wave based on improved MUSIC method. Composite Structures. 2018;203:164-71.